DEVELOPMENT OF MULTIVARIATE CURVE RESOLUTION AND ASSOCIATED SYSTEM IDENTIFICATION TOOLS FOR IR EMISSION, CHIROPTICAL, AND FAR-INFRARED AND FAR-RAMAN SPECTROSCOPIES

CHENG SHUYING

NATIONAL UNIVERSITY OF SINGAPORE

2007

DEVELOPMENT OF MULTIVARIATE CURVE RESOLUTION AND ASSOCIATED SYSTEM IDENTIFICATION TOOLS FOR IR EMISSION, CHIROPTICAL, AND FAR-INFRARED AND FAR-RAMAN SPECTROSCOPIES

CHENG SHUYING

(B. Eng. &, M .Eng., (Tianjin University))

A THESIS SUBMITTED

FOR THE DEGREE OF DOCTOR OF PHILOSOPHY

DEPARTMENT OF CHEMICAL & BIOMOLECULAR ENGINEERING

NATIONAL UNIVERSITY OF SINGAPORE

2007

ACKNOWLEDGEMENT

This thesis is the result of four and half years of work whereby I have been accompanied, supported and inspired by many people. It is a pleasant aspect that I have now the opportunity to express my gratitude for all of them.

I want to thank the National University of Singapore for giving me permission to commence this thesis in the first instance, to do the necessary research work and to use departmental facilities. I have furthermore to thank Institute of Chemical and Engineering Sciences (ICES) for the constant supports of their researchers which help me tremendously to overcome many of the obstacles during this thesis work.

The first person I would like to thank is my supervisor Prof. Marc Garland. His perpetual energy and enthusiasm in research had motivated all his students, including me. In addition, he was always accessible and willing to help his students with their research. His overly enthusiasm and integral view on research and his mission for providing 'only high-quality work ', has made a deep impression on me. I owe him lots of gratitude for having me shown this way of research.

I especially want to thank Prof. Shamsuzzaman Farooq, for his willingness to be my co-supervisor. He was always willing to help me so that my research life became smoother. I would also indebted to the members of my PhD committee members who took efforts in reading and providing me with valuable comments on the early work of this thesis: Prof. Simo Olavi Pehkonen and Prof. Iftekhar A. Karimi.

I would also like to gratefully acknowledge Dr. Dharmarajan Rajarathnam and Dr. Ilya Lyapkalo for their collaboration in emission studies. I am grateful to Prof. Liya Yu for her collaboration in the FT-Raman solid state studies. Also I am indebted to Mr. Ng Kim

Poi and his employees at the workshop for their help on machining my designed spectroscopic cells.

I would like to express my thanks to all my NUS and ICES colleagues, particularly, Dr. Guo Liangfeng, Mr. Ayman D. Allian, Mr. Martin Tjahjono, Dr. Effendi Widjaja, Dr. Li Chuanzhao, Dr Gao Feng. Mr. Karl Irwin Krummel, Dr Chacko Jacob, Mr. Zhang Huajun and Dr. Srilakshmi Chilukoti for their friendship, enriching conversation and help in the past four and half years.

My deepest gratitude goes to my family for their love and care through out my Ph.D: my parents and my sister. I am greatly indebted to my husband, Luo Jijun, for his love and support. He also provided much useful information on coding some programs for my research work. One of the best experiences that we lived through in this period was the expecting for the birth of our baby, who accompanied me during the thesis writing period and provided an additional and joyful dimension to our life mission. This thesis is simply impossible without all of them.

TABLE OF CONTENTS

SUMMARY

Multivariate curve resolution (MCR) techniques are primarily used to recover pure contributions due to the individual species in the system from the multivariate experimental instrumental response such as multivariate spectroscopic data. Such techniques provide valuable tools for solving one of the most difficult problems, i.e. system identification, in analytical spectroscopy. Consequently, algebraic system identification generally comprises both the qualitative and quantitative characterization of mixtures. This thesis is devoted to develop a model-free MCR method to solve the important system identification problems associated with the resolution of pure component spectra and their associated concentration profiles without any prior knowledge of the system.

The current dissertation studies the system identification problems associated with IR emission spectroscopy (IRES), chiroptical spectroscopy including ultra-violet circular dichroism (UV CD) and Raman Optical Activity (ROA), and Far-IR and Far-Raman spectroscopy. This thesis focuses on solving the qualitative and quantitative analysis of multivariate data arrays with various chemometric methods.

1. IRES: Both experimental and chemometric studies were involved. With respect to the experimental measurements, studies of both solid and liquid phase non-reactive samples as well as a cyclo-addition organic synthesis in the liquid phase were carried out with an in-house designed cell. Emission mode BTEM (Band-Target Entropy Minimization) was successfully applied to resolve the pure component emission spectra from the mixture data for both the non-reactive as well as reactive systems. The large signal contribution due to black-body radiation was effectively eliminated. Subsequently, first approximations of concentration profiles for the reactive system were achieved.

This development of Emission mode BTEM should open new possibilities for (a) studying complex organic syntheses, particularly those possessing low transparency due to suspended salts etc., (b) strongly absorbing heterogeneous catalytic systems under reaction conditions which cannot presently be studied by techniques such as diffuse reflectance and (c) remote analysis of combustion and other extreme processes.

2. Chiroptical spectroscopy: Chiral-BTEM, an extension of current BTEM (allowing non-positive spectral features), was developed and applied to chiroptical spectroscopic data from UV CD and ROA spectroscopies. (a) An organometallic ligand substitution reaction (involving $Rh_4(CO)_{12}$ with a chiral ligand, (S)-BINAP) was successfully followed with UV CD. Both the pure component CD spectra and the concentration profiles for each reactant and product were obtained with Chiral-BTEM methods. (b) ROA was combined with Chiral-BTEM and DFT (density functional theory) to determine the absolute configurations and the enantiomeric purity of a chiral system. Good agreement was obtained between DFT calculations and processed experimental ROA spectra. The enantiomeric excess of the enantiomeric solutions was estimated.

This development of Chiral-BTEM should open new possibilities for rapid purity determination without the requirement of a stereo-pure standard as calibration in many enantio-selective syntheses of pharmaceutical products and other biological active substances. Moreover, in addition to UV CD and ROA already mentioned, Chiral-BTEM should be applicable to vibrational circular dichroism (VCD), fluorescence CD, x-ray CD, luminescence CD and magnetic circular dichroism (MCD).

3. Far-IR and Far-Raman spectroscopy: M-C and M-M vibrations of some neutral metal carbonyl complexes at very high dilution were successfully characterized with these two techniques. All pure component spectra were recovered using BTEM methods and

good agreement between the resolved spectra and theoretical spectral predictions with DFT was founded.

Such a combined approach of far-vibrational spectroscopy, BTEM and DFT should be a useful tool for a wide range of structural identification problems in reactive organometallic systems, such as homogeneously catalyzed systems, in order to identify new species and intermediates in solution. In particular, due to the pronounced differences in regio-isomers in this spectral window, the monitoring of regio-selectivities should become possible.

The present work represents the successful development and application of modified BTEM-type methods to some unusual and complicated spectroscopies in order to obtain satisfactory deconvolution of pure variables without a priori information. This contribution will help to open more possibilities for in-situ spectroscopic studies of a variety of reactive systems containing chiral/achiral compounds in homogenous or heterogeneous syntheses.

NOMENCLATURE

Abbreviations

ppm	part per million
ee	enantiomeric excess
ALS	Alternating Least Square
BTEM	Band-Target Entropy Minimization
CD	Circular Dichroism
DFT	Density functional theory
ECD	Electrical Circular Dichroism
EFA	Evolving Factor Analysis
Eq	Equation
HELP	Heuristics Evolving Latent Projections
FA	Factor Analysis
FTIR	Fourier Transform Infrared
IRES	Infrared Emission Spectroscopy
ITTFA	Iterative Target-Testing Factor Analysis
IE	Imbedded Error
LC-DAD	Liquid Chromatography – Diode Array Data
LCP	Left Circularly Polarized
MCR	Multivariate Curve Resolution
NIPALS	Non-Linear Iterative Partial Least-Squares
NMR	Nuclear Magnetic Resonance
OPA	Orthogonal Projection Approach
PCA	Principal Component Analysis

PCR	Principal-Component Regression
PLS	Partial Least Squares
RCP	Right Circularly Polarized
ROA	Raman optical activity
SA	Simulated Annealing
SIMCA	Soft Independent Modeling of Class Analogy
SIMPLISMA	Simple-to-use Interactive Self-Modelling Mixture Analysis
SMCR	Self-Modelling Curve Resolution
S/N	Signal-to-Noise
SSR	Sum squared Residual
SVD	Singular Value Decomposition
TFA	Target Factor Analysis
UV	Ultraviolet
VCD	Vibrational circular dichroism
VOA	Vibrational optical activity
WFA	Window Factor Analysis

Symbols

$a_{s\times\tilde{\nu}}$	pure component spectra matrix
$\hat{a}_{1\times\tilde{\nu}}$	pure component spectrum estimate
$\hat{a}_{s\times\tilde{\nu}}$	pure component spectral estimates matrix
d_{sxs}	a multiplier matrix for the normalized pure component spectra matrix
$ds_{\tilde{\nu}}$	derivative of resolved pure component spectrum estimate
$\hat{i}^{Raman}_{1\times\tilde{\nu}}$	pure component Raman spectrum estimate

$\hat{i}_{1\times\tilde{\nu}}^{ROA}$	pure component ROA spectrum estimate
k	number of spectra in one experiment
l	path length
m	degree of spectrum differentiation
s	number of species
v_m	step size value for optimization
xub	upper variable bound for optimization
xlb	lower variable bound for optimization
w	maximum number of species
w_{ij}	determinant-based weight function
z	number of right singular vectors taken more than number of observable species
$\mathbf{A}_{k\times\tilde{\nu}}$	absorbance data matrix
$\mathbf{C}_{k\times s}$	concentration matrix
$\hat{C}_{kxs}$	relative concentration
F_{obj}	Objective function value
H	information entropy
I_L	intensity of the left circularly polarized components \
I_R	intensity of the right circularly polarized components
I_{Raman}	unpolarized Raman scattering intensity
I_{ROA}	ROA intensity
P	penalty function value
T	temperature
$T_{1\times z}$	transformation matrix
$\mathbf{U}_{k\times k}$	matrix of left singular vectors

$\mathbf{V}^{\mathrm{T}}_{\widetilde{\nu}\times\widetilde{\nu}}$ transposed matrix of right singular vectors

Greek Letters

α maximum absorbance of resolved pure spectrum

γ_a penalty coefficient to ensure positivity of pure component spectrum estimate

γ_c penalty coefficient to ensure positivity of corresponding relative concentration

$\gamma_{\max}$ penalty coefficient to ensure maximum absorbance of resolved pure spectrum less than α

ς_a determinant of covariance matrix of pure component spectral estimates

θ angle between two vector-spectra

λ_1 lower bound for the absorptivity constraint

λ_2 upper bound for the absorptivity constraint

$\widetilde{\nu}$ number of data channels / wavenumber

$\Sigma_{k\times\widetilde{\nu}}$ diagonal matrix of singular values

LIST OF FIGURES

LIST OF TABLES

Chapter 1

Introduction

Spectroscopy has played a vital role in the development of modern chemical and engineering science. Spectroscopic techniques have provided perhaps the most widely used tools for the elucidation of molecular structure as well as further quantitative information for both inorganic and organic compounds. With the advances in modern instrumentation, overwhelming amounts of numerical and graphical experimental data are generated from on-line and in-situ analytical measurements. The analytical chemist or spectroscopist has to face the problem of recovering useful chemical information from the large amount spectroscopic data available. The development of chemometrics has provided us with powerful mathematical and statistical methods for handling, interpreting and predicting chemical data (Malinowski, 1991). Chemometrics has continued to mature and gain greater acceptance due to its success in extracting useful chemical information from complex experimental data, particularly spectroscopic signals.

1.1 A Typical System

The issue mentioned above might be related to a more fundamental inverse problem or system identification problem. In many branches of the physical sciences and engineering, the term “inverse problem” holds a very important and precise meaning. Assume that we have a reactive system in the liquid-phase on a batch scale. A possible future configuration of a series of spectrometers used to make on-line measurements in a liquid reactor is shown in Figure 1.1.

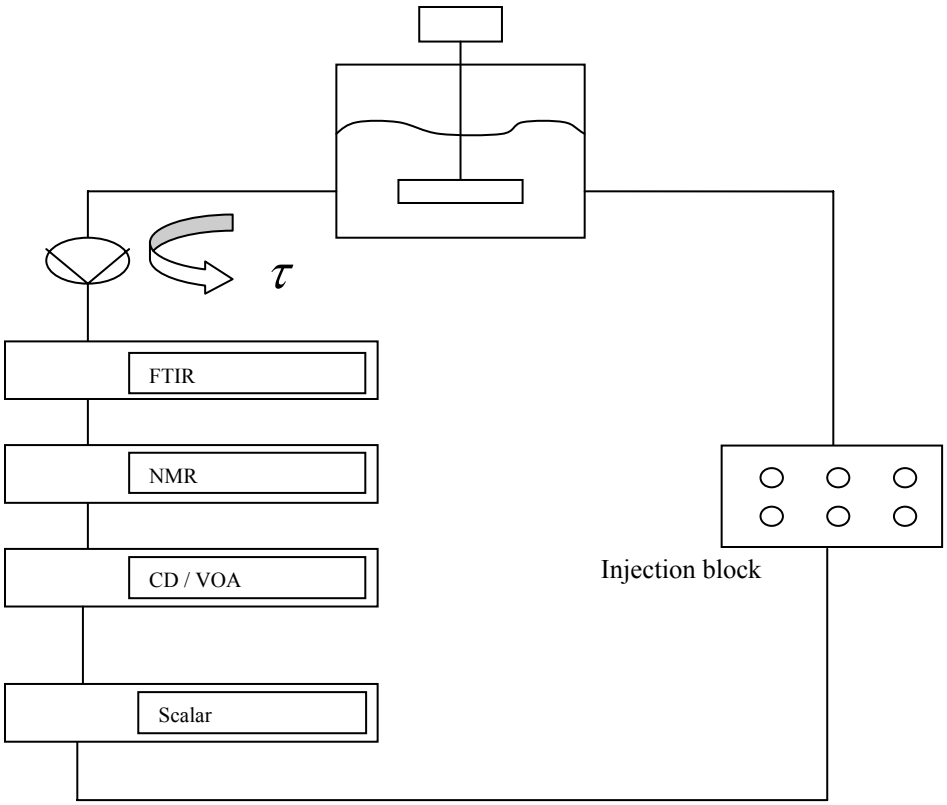

Figure 1.1 An experimental setup for characterization of a reactive system through in-situ measurements

In Figure 1.1, a batch reactor is connected online, under isobaric and isothermal conditions to an array of sophisticated analytical instruments. In general, a fluid element has a short residence time τ in the instruments before it returns to the reactor. A number of possible physico-chemical and spectroscopic quantities can be measure on line or in-situ by the experimentalist. The spectroscopic techniques can be grouped according to the format of the data measured, i.e. the un-polarized spectrometers such as FTIR and NMR and the polarized spectrometers such as circular dichroism (CD) and vibrational optical activity (VOA). The scalar valued quantities are associated with physico-chemical

properties including density, dielectric constant, heat flux, and viscosity. With an adequate experimental design, these on line or in-situ measurements produce sufficient experimental data for the analytic chemist to characterize the system in considerable detail.

The system identification for both academic and industrial synthetic chemistry has similar problems. These include: (1) determination of the number of observable species present and their pure component spectra, (2) determination of all the moles of all species, the number of reactions, and the reaction stoichiometries, (3) the system kinetics, (4) the partial molar properties of all the new species, and (5) the reaction related quantities, for instance, heat of reaction. In order to get start, one usually has to be able to get the pure component spectra. This means taking the in-situ spectroscopic data and inverting it using chemometric methods.

1.2 Problem Statements

One of the fastest growing areas of chemometrics is self-modeling curve resolution (SMCR) multivariate calibration, which is a certain mathematic decomposition of two-way signals from instrumentally unresolved multi-component mixtures resulting in deconvoluted spectra. In principle, with any SMCR technique you can resolve the pure component spectra. The assumptions might involve Beer's law or a certain bilinear model for the data. In 1960, Wallace developed a method to find the number of components in a multi-component system. It was perhaps the first member of the SMCR family. The starting point of the new term SMCR is in 1971 when Lawton and Sylvester discussed a method based on factor analysis to resolve a two-component system.

Later many techniques for SMCR were extensively studied and all these methods were primarily based on the progress of factor analysis (FA) or principal component analysis (PCA).

The SMCR techniques, alternating least square (ALS) (Andrew and Hancewicz, 1998; Frenich *et al.*, 2000; Sasic *et al.*, 2002), simple-to-use interactive self-modeling mixture analysis (SIMPLISMA) (Windig, 1991, 1992, 1993, 2002), modified SIMPLISMA, namely Interactive Principal Component Analysis (IPCA) (Bu and Brown, 2000) and orthogonal projection analysis (OPA) (Sanchez *et al.*, 1996, 1997; Braekeleer and Massart, 1997; Gourvenec *et al.*, 2002) are widely used. Most other methods are evolved by the modification or combination of the routines of ALS, SIMPLISMA, IPCA and OPA. Some priori knowledge about the pure variables is required when applying both SIMPLISMA and IPCA, such as the computational identification of a pure wavelength for each component, followed by spectral reconstruction using least squares approaches. The SIMPLISMA technique determines the pure wavelength from the set of mixture spectra by itself, and the IPCA technique finds them from the significant principal components or from significant singular vectors.

Recently, a new method based on Shannon Entropy and a constrained optimization technique, called Band-Target Entropy Minimization (BTEM), was introduced for retrieving the spectra of pure components from mixture spectra without any a priori knowledge. It has been successfully applied to spectral reconstruction and qualitative and quantitative analysis of pure components from mixture spectra using many types of spectrometers such as FTIR, UV-Vis, MS and Raman (Widjaja *et al.*, 2002; Li *et al.*, 2002, 2003). Guo (2005) extended the BTEM chemometrics methods for signal

processing from 1D spectroscopy to 2D spectroscopy, specifically for Nuclear Magnetic Resonance (NMR). It is important to mention at this point that these spectroscopies are un-polarized, and therefore, can only be used to differentiate achiral molecules.

The above mentioned success lead us to consider the development of BTEM for new and additional applications in this thesis: (1) for more advanced spectroscopies – namely chiroptical spectroscopies such as electrical circular dichroism (ECD), vibrational circular dichroism (VCD) and Raman Optical Activity (ROA) and (2) for some unusual spectroscopies with low signal-to-noise ratio such as IR emission spectroscopy (IRES).

Chiral-BTEM is an extension of the current BTEM algorithm to chiroptical spectroscopic data. It would allow the determination of the species pure component circularly polarized spectra as the first step and then further system identification for reactions involving stereo-isomers in pharmaceutical and fine chemical reactive systems. Some new physico-chemical constraints need to be satisfied in the mathematical solutions in order to extend analysis to polarized radiation.

Consequently, the primary goals of this thesis are: (1a) the development of new and broadly-applicable algorithm, namely Chiral-BTEM (1b) the application of this new algorithm to 2 types of polarized spectroscopies and to systems containing stereo-isomers and (1c) the use of Chiral-BTEM as a starting point for further liquid system identification of stereochemical mixtures i.e. enantiomeric excess (ee) determination; (2) The application of BTEM to a new area, namely, to the interpretation of IRES data from pure systems as well as from liquid phase reaction.

1.3 Outline of This Thesis

The thesis consists of seven chapters.

Chapter 2 presents a brief review of recent and related literature associated with this multi-disciplinary thesis. The basic concept of chemometrics and a variety of chemometric techniques, in particularly the self-modeling curve resolution, will be described. BTEM and its application will be highlighted. In addition, related information on the emission spectroscopy will be introduced.

Chapter 3 provides an experimental investigation for obtaining good quality emission spectra using IRES and the application of emission mode BTEM to deconvolute the pure component emission spectra. Pure solid and liquid samples and one liquid-phase reaction will be involved in this study. Moreover, further analysis in order to calculate the relative concentration profiles will be discussed.

Chapter 4 presents the first application of Chiral-BTEM. The spectroscopy used is UV-CD and two different organometallic ligand substitution reactions are successfully studied.

Chapter 5 describes an experimental study carried out on neutral metal carbonyl complexes using Far-Infrared and Far-Raman spectroscopies. Analysis of the spectroscopic data sets was then performed with BTEM. Subsequently, density functional theory (DFT) calculations were carried out in order to determine optimized geometries and frequency predictions. Comparison of the BTEM spectral estimates with the DFT predictions allows the assignment of the M-C vibrations in the IR and Raman as well as the M-M vibrations in the Raman.

Chapter 6 provides a second application of chiral-BTEM, this time, to ROA spectroscopic data. Firstly, experimental studies aimed at measuring good Raman optical activity (ROA) spectra for chiral solutions will be discussed. Secondly, Chiral-BTEM will be applied. Thirdly, further system identification for chiral systems such as the determination of the absolute configurations of chiral compounds (by comparison to DFT calculations) and the determination of the concentration or the enantiomeric excess will be addressed.

Chapter 7 provides a summary of the obtained results and their implications. In addition, recommendations for future experiments will be presented.

Chapter 2

Literature Review

The huge increase in the number and sophistication of computers and chemical instruments particular in spectroscopy has resulted in a dramatic increase in the amount of data available. This has triggered the current activities of many chemometricians, which involve the development of chemometric techniques for multivariate data analysis to provide maximum relevant chemical information from large arrays of chemical data. The main focus in this study is the application of chemometric techniques to quantitative and qualitative analysis of multivariate spectroscopic data. In spectroscopy, multivariate calibration is achieved by using the spectra as multivariate descriptors to predict quantitative estimation of chemical concentrations of constituents of interest using well-known statistical approaches such as partial least squares (PLS), principal-component regression (PCR), soft independent modeling of class analogy (SIMCA), and many others.

This chapter provides an overview of the theoretical background and literature relevant to this study. The related chemometric and spectroscopic issues will be addressed.

2.1 Chemometrics

Chemometrics is a relatively new and separate branch of chemistry that has no strict definition. Swedish scientist S. Wold, together with B. Kowalski, introduced the

terminology ‘chemometrics’ in the early 1970s. A reasonable definition of chemometrics (Wold, 1995) would be: ‘How to get chemically relevant information out of measured chemical data, how to represent and display this information, and how to get such information into data’. In a word, chemometrics is a data analysis methodology which applies mathematical, statistical and logical methods to elucidate the concealed information embedded inside the observable data set. The extracted relevant information from measured data commonly forms the basis for new understanding of the studied system for the chemist or chemical engineer.

Being conceived as a branch of analytical chemistry, chemometrics now is a general approach after more than thirty years of rapid development. It has been applied in many different areas, with the most successfully applications in multivariate calibration, pattern recognition, classification and discriminant analysis, multivariate modeling, and monitoring of processes. The methodologies and practice of data analysis in chemometrics have been reviewed in the biennial *Fundamental Review of Chemometrics* issue of the journal *Analytical Chemistry* (Brown *et al.*, 1988, 1990, 1992, 1994, 1996; Lavine, 1998, 2000, 2002, 2004, 2006).

As pointed by Brown (1998), many of the methods employed in chemometrics are based on the concept of soft modeling. It is worthy to note that soft modeling provides a more realistic framework for many of the chemometric methods than the traditional modeling derived from first principles (hard models) in chemistry. A hard model usually describes the system in terms of traditional chemical and physical relationships using just one or a very few variables at the same time. Because most interesting chemical systems or processes are complex, the applications of hard modeling have been limited to the

simple systems. However, soft model is used to describe the variation and correlation between the dependent variables and the latent variables which are linear combinations of the measured variables in the covariance matrix of data. In particular, soft modeling approaches attempt to describe a system without a priori information or any kind of model assumption. In this work, all developed chemometric approaches take soft modeling approaches. The achievement of these methods allows the identification of the number of data variance sources, the qualitative and quantitative estimations, i.e. the algebraic system identification inverse problem (as mentioned previously in chapter 1). The main purpose of soft modeling data analysis is the resolution of mixture data sets. Details of multivariate curve resolution techniques will be given in the next sub-section.

2.2 Self-modeling Multivariate Curve Resolution (SMCR) Techniques

The common goal for all the resolution techniques is to recover pure contributions due to the individual species in the system from the multivariate experimental instrumental response (the measured spectra signals) (Brown, 1998). Self-modeling multivariate curve resolution (SMCR) methods are often applied to resolve such multivariate spectroscopic data. Such techniques address one of the most difficult problems in analytical spectroscopy, the qualitative and quantitative characterization of mixtures containing unknown amounts of an unknown number of unknown components. In principle, SMCR does not need any spectra libraries or any a priori information on the number of components or concentration profiles.

2.2.1 History of SMCR

The starting point of SMCR goes back to the realization that the number of chemical components in a mixture might be determined by the matrix rank of the data matrix if each component has a different spectrum and corresponding concentration profile. SMCR was first introduced to resolve two-component mixture spectra by Lawton and Sylvester in 1971. Their approach was based on principal component analysis and non-negativity constraints on both the spectral estimates and their corresponding concentrations. Later, Gemperline (1984, 1986, 1987) and Vandeginste *et al.* (1985) came up with the resolution of three-component mixtures by use of a new SMCR method called iterative target transformation factor analysis (ITTFA). Since then, many different SMCR methods or their variations have been widely studied in the chemometrics literature. These techniques include evolving factor analysis (EFA) (Maeder, 1987; Keller and Massart, 1992), window factor analysis (WFA) (Malinowski, 1992; Manne, 1995; Liang and Kvalheim, 2001), subwindow factor analysis (SFA) (Manne *et al.*, 1999; Shen *et al.*, 1999), fixed size window evolving factor analysis (FSW-EFA) (Keller and Massart, 1991), heuristic evolving latent projection (HELP) (Kvalheim and Liang, 1992; Keller *et al.*, 1992; Leung *et al.*, 2000), simple-to-use interactive self-modeling mixture analysis (SIMPLISMA) (Windig and Guilment, 1991; Windig, 1997; Windig and Markel, 1993; Windig *et al.*, 2002), alternating least squares (ALS) (Karjlainen, 1989; auler *et al*., 1992), orthogonal projections analysis (OPA) (Sanchez *et al*., 1996, 1997) and simplex-based methods (SIMPLEX) (Jiang *et al.*, 2003) and etc. These methods differ in (1) whether the number of significant components is determined automatically, (2) whether the solution is unique, (3) how initial estimates for the calculation are obtained, and (4) whether the

matrix decomposition is performed in an iterative manner, and so on.

2.2.2 Basic Theory of SMCR

Self-modeling curve resolution comprises a set of mathematical tools for estimating pure-component spectra and composition profiles from a set of unknown mixture spectra. 'Self-modeling' implies that SMCR is model-free so that under ideal circumstances, SMCR provides the resolution of pure variables without any prior knowledge of the system. The only premises are the validity of the bilinear Lambert-Beer-Bougeur-Law model for the data and some constraints related to chemical features of system such as (1) non-negativity, this constraint requires the values in the pure-component profiles and spectra should be equal to or greater than zero; (2) unimodality, this constraint forces composition profiles of each component to be unimodal; and (3) closure, this constraint is applicable to closed reaction systems. In terms of mass balance, it is often assumed that there is no net transport of species into or out of the system.

Consider multiple experimental runs (each run having different reaction conditions) and the measurement of the associated in-situ spectra. For given multivariate measurements associated with in-situ spectra, let A represent the consolidated measured spectra matrix, where each row corresponds to a spectrum of a mixture. Then the bilinear model can be expressed as:

$$\mathrm{A}_{k\times\tilde{\nu}} = \mathrm{C}_{k\times s}\,\mathrm{a}_{s\times\tilde{\nu}} + E_{k\times\tilde{\nu}} \tag{2.1}$$

where k denotes the number of spectra recorded, $\tilde{\nu}$ is the number of data channels associated with the spectroscopic wavenumbers and s is the number of observable species involved in the chemical mixture. Eq.2.1 assumes that the

Lambert-Beer-Bougeur-Law model is valid, hence $\mathbf{A}_{k\times\tilde{\nu}}$ is a linear combination of concentration matrix $\mathbf{C}_{k\times s}$ (which incorporates the path length *l*) and the pure component absorptivities $\mathrm{a}_{s\times\tilde{\nu}}$ are constants, and *E* is simply instrumental and experimental error comprising mainly noise.

The basic procedures of SMCR is first to use factor analysis (FA) or principal component analysis (PCA) methods to abstract the eigenvectors of the covariance matrix A and then to use either iterative or non-iterative resolution methods to elucidate the pure variables. The first step can be achieved using PCA or SVD (singular value decomposition). The ultimately goal of SMCR is to find the best bilinear model to fit the experimental data. The good bilinear model is usually obtained by minimizing the error criterion of sum squared residual (SSR):

$$SSR = \left\| A - C'\mathrm{a}' \right\|^2 \tag{2.2}$$

where C' and a' are the estimations of pure variables by SMCR.

2.2.3 Factor Analysis

Factor analysis is a mathematical technique for investigating complex multivariate data to estimate chemical rank of a data matrix. It is applicable whenever the observables of a system can be represented by a bilinear model. As spectroscopic measurements often generate large size data, it is highly desirable to decompose the data matrix into several independent and orthogonal vectors which can be use to represent the system with a smaller set of basis vectors. Such independent and orthogonal principal components will be related to the number of the species involved in the mixture.

Many techniques have been proposed for factor analysis. The non-linear iterative partial least-squares (NIPALS) (Winter, 1992) was widely used earlier. Recently, the most generally used method is singular value decomposition (SVD) or PCA. Golub and Kahan published the first practical algorithm to compute SVD in 1965. Later Golub and Reinsch (1970) developed a variant of that algorithm and it is still used today. SVD can be computed with MATLAB using the embedded program (in this work all SVD computations were performed with MATLAB). Mathematical, SVD can be expressed as follows:

$$\mathbf{A}_{k\times\tilde{\nu}} = \mathbf{U}_{k\times k}\Sigma_{k\times\tilde{\nu}}\mathbf{V}^{\mathrm{T}}_{\tilde{\nu}\times\tilde{\nu}} \tag{2.3}$$

The experimental matrix $\mathbf{A}_{k\times\tilde{\nu}}$ is subjected to Singular Value Decomposition (SVD). The main purpose of SVD is to obtain the abstract orthonormal matrices $\mathbf{U}_{k\times k}$ and $\mathbf{V}^{\mathrm{T}}_{\tilde{\nu}\times\tilde{\nu}}$ with their diagonal singular matrix $\Sigma_{k\times\nu}$. The columns of $\mathbf{U}_{k\times k}$ are called the left singular vectors which form an orthonormal basis for pure concentration profiles and the rows of $\mathbf{V}^{\mathrm{T}}_{\tilde{\nu}\times\tilde{\nu}}$ contain the elements of the right singular vectors which form an orthonarmal basis for the pure spectra. $\Sigma_{k\times\tilde{\nu}}$ is a diagonal matrix whose elements are the non-negative square root of the eigenvalues of the covariance matrix $A\cdot A^T$ (transpose of A). By convention, the eigenvalues are ranked in descending order of magnitude, with the highest eigenvalues in the upper left part of the $\Sigma_{k\times\tilde{\nu}}$ matrix.

In fact, performing PCA is the equivalent of performing SVD for the covariance matrix of the data. There is a direct relation between PCA and SVD. The right singular vectors are the same as the principal components of PCA. The eigenvalues of $A\cdot A^T$ are equivalent to $\Sigma_{k\times\tilde{\nu}}{}^2$, which are proportional to the variances of the principal components.

The matrix $\mathbf{U}_{k\times k}\Sigma_{k\times\tilde{v}}$ then contains the principal component scores.

The next step is often finding the chemical rank which is defined as the number of species *s* in a multi-component sample. The determination of the number of significant eigenvalues can provide an estimate of the chemical rank in the data. There are sources of error altering the simple relationship between chemical rank and the number of significant eigenvalues (Toft, 1995). With a normal signal-to-noise ratio (for IR spectra, S/N is often better than 100/1), the chemical rank can reasonably be estimated by statistical or empirical methods such as Imbedded Error function, IE (Malinowski, 1977, 1991), Factor Indicator function, IND (Malinowski, 1977, 1991), F-test (Malinowski, 1977, 1991), Faber-Kowalski F-test (Faber and Kowalski, 1997), and Modified Faber-Kowalski F-test (Malinowski, 1999). Basically, the number of significant species *s* is determined by subjecting the singular values in the $\sum$ matrix to these various statistical tests. It is assumed that the primary singular values correspond to the number of significant factors, while the secondary singular values correspond to noise signals. However, data with bad noise behavior or spectral nonlinearities can lead to a too high or too low chemical rank estimation. It is clear that in order to have a good estimate of chemical rank one must minimize the effects of measurement noise and reduce the spectral nonlinearities.

2.2.4 SMCR Solutions Are Not Unique

In general, most curve resolution techniques cannot guarantee a unique solution to the pure variables. Tauler *et al.* (1993) identified two classes of ambiguity in SMCR results: rotational ambiguity and intensity ambiguity. The rotational ambiguity accounts

for the possibility of reproducing the correct concentration profiles and spectra by rotating the concentration profiles and spectra to their linear combinations without changing the residual errors associated with the model of the data. The intensity ambiguity refers to a scaling problem for both the resolved concentration profiles and spectra for the model. Various possible solutions can be easily obtained because each concentration profile can be multiplied by a non-zero number and this can be compensated by dividing its associated spectrum by the same number.

As mentioned above, various constraints such as non-negativity of spectra and concentration, unimodality and closure are usually imposed on the solution of the curve resolution problem in order to decrease the ambiguity. Although imposing a closure constraint is sufficient to solve the intensity ambiguity the rotational ambiguity is only partly removed. Therefore under most conditions, non-unique SMCR solutions are obtained.

Typically, some effects that can contribute to the uncertainty in SMCR include (1) high degree of spectral overlap of some components and (2) spectral nonlinearities due to shifting band position and changing band shape. These two points are ubiquitous in the chemical sciences or spectroscopy.

2.2.5 Methodologies in SMCR

In the literature, SMCR methods are usually classified in two different ways: (1) according to the non-iterative and iterative resolution methods used and (2) according to the unique or non-unique solutions for the SMCR results. Generally, most unique resolution methods fall into the category of non-iterative curve resolution methods and

most non-unique resolution methods can be found in the group of the iterative curve resolution methods.

The non-iterative resolution methods are usually fast but these techniques often require certain features to be present in the data set such as a unique maximum in the selected concentration profiles or zero-concentration regions. Such featured regions are used to facilitate the estimation of the chemical rank and can lead to a unique solution.

The group of non-iterative resolution methods comprises EFA (Maeder, 1987; Keller and Massart, 1992), WFA (Malinowski, 1992; Liang and Kvalheim, 1994), SFA (Manne et al, 1999), FSW-EFA (Keller and Massart, 1991), and HELP (Kvalheim and Liang, 1992; Liang *et al*., 1992; Keller *et al*., 1992; Liang and Kvalheim, 2001). Among these methods, WFA and HELP are probably the most studied and have a wide range of applications.

Window factor analysis, WFA, is a kind of modification of EFA using a different approach to identify the 'windows' for the components. This method requires that each component has a distinguishable spectrum and that the concentration profile of the component does not completely encase the profile of any other component (Zhao and Malinowski, 1999). The 'window' of a component refers to the region where the formation and decay of concentration profiles along the evolutionary axis is sequential, i.e. each component lying in such region is called the 'window' and all other components have signals outside this window. In essence, WFA estimates the spectral subspace for all the interesting species using the zero-concentration region and this identification of the window in turn leads to the uniqueness of the solution. WFA has been successfully applied to a variety of problems involving spectroscopy and chromatography

(Malinowski, 1996).

Heuristic evolving latent projections, HELP, like most SMCR methods was originally developed and applied to the resolution of overlapped liquid chromatography with photodiode array detection (LC-DAD). It was successfully applied to resolve the two-component mixtures of isomers characterized by LC-DAD although the resolution of the very similar spectra of the isomers was difficult. This multifunctional approach targets the identification of selected spectral regions where each component has a distinguishable spectral feature as well as a component wise resolution of the pure variables. HELP differs from WFA or EFA by using both the selective spectral region and the zero-concentration region of the component in the computation. It is noted that both HELP and WFA use the zero-concentration region for the resolution of concentration profiles. WFA saw wilder applications than HELP since the strategy used in WFA is more convenient for the implementation by a user. However, using both spectral and concentration selective regions is the major advantage of HELP in obtaining good results. Its main contribution is the ability to detect, in a sophisticated manner, the potential selected spectral zones and the application of statistical methods of chemical rank analysis techniques such as F-test to confirm the presence of the selected spectral zones and the zero-concentration regions.

Iterative resolution methods usually see more applications to diverse data than non-iterative resolution methods. The main process involved in an iterative resolution method includes the optimization of the initial profiles in either the spectra or concentration data matrix or in both the spectra and concentration data matrices with some selected constraints. Such constraints will help to select the elements which satisfy

a certain condition better than other candidates. The initial profiles can generally be estimated by some chemical rank analysis methods based on PCA or obtained directly from the real reference variables.

The group of iterative resolution methods mainly comprises ITTFA (Gemperline, 1984; Vandeginste, 1985), SIMPLISMA (Windig and Guilment, 1991), MCR/ALS (Tauler *et al.*, 1991, 1993; Jaumot *et al*., 2005; Zachariassen *et al.*, 2006), OPA (Sanchez *et al.*, 1996) and simplex-based methods (SIMPLEX) (Jiang and Ozaki, 2003) and etc. ITTFA, SIMPLISMA and MCR/ALS are probably the most representative and used iterative resolution methods.

Iterative target transformation factor analysis, ITTFA, was inspired by a TFA non-iterative method which was used to inspect the validity of initial profiles. Gemperline (1986) first proposed ITTFA for spectral reconstruction from LC-DAD data. This technique normally starts with an initial guess of either the concentration profiles or pure component spectra and then iteratively improves the resolution by incorporating non-negativity constraints and unimodality of the elution profiles. However, good ITTFA results often depend on appropriate initial estimates of potential concentration profiles or spectra. In practice, such information in some situation cannot be fully provided.

Another widely used SMCR is MCR/ALS, multivariate curve resolution / alternating least squares. It uses an alternative approach based on constrained alternating least squares to iteratively optimize the concentration profiles and pure component spectra. In contrast to ITTFA, MCR/ALS tries to find both optimized concentration profiles and pure component spectra at each iteration, and neither of them has priority over each other. The first estimates of concentrations and spectrum profiles can be obtained from other

pure-variables detection methods such as EFA and WFA. Again the constraints applied to this resolution are based on natural chemical features, such as the non-negativity of concentration and spectra estimates, unimodality of concentrations, selectivity (only one or some of the species present in the selected regions) and closure. In this way, at each iteration of the MCR/ALS procedure, the solutions are improved not only from a least-squares sense but also from the contribution of such constraints. MCR/ALS has been applied to many types of spectroscopic data and mixture systems, such as chromatography, spectroscopic titrations, protein folding, FTIR, NMR, UV and etc. (Tauler *et al.*, 1993, 1994, 1995, 1998, 1999; Esteban *et al.*, 2000; Vives *et al*., 2001, 2002; Jaumot *et al.*, 2002).

Simple-to-use interactive self-modeling mixture analysis, SIMPLISMA, is a popular method based on pure variables that attempts to determine the selected concentration or spectral variables. The algorithm was first proposed by Windig in 1991 to properly resolve spectra with wide and narrow peaks and minimize baseline problems by resolving them as separate components. The basic principle of SIMPLISMA is to resolve a pure variable which has intensity contribution from only one of the components in the mixture. However, in practice, some species are not independent of the others at one or more of the wavelength channels in the multivariate data set. A combination of KSFA and SIMPLISMA approach was able to eliminate the need of arbitrary offset values required by SIMPLISMA (Bu and Brown, 2000). The incorporation of an ALS-based iterative algorithm into SIMPLISMA can further refine the pure variables (Du *et al.*, 2003). Some modifications on the original SIMPLISMA algorithm have also been performed. Windig (1992, 1994) proposed the use of inverted second derivative spectra to determine the pure

variables in order to handle the high degree of spectral overlap, the background effects and the presence of a nonzero baseline.

Many SMCR methods have been proposed and implemented but most SMCR techniques have not reached the desired level of sophistication needed to handle really complex multivariate spectroscopic data from reactive systems. This is mainly due to the really tough spectroscopic problems associated with algebraic system identification. The main problems include: (1) high spectral overlap and similarity of spectral features, (2) low signal-to-noise ratio, (3) weak signals resulted from minor components, and (4) spectral nonlinearities related to the changes in band shapes and positions during measurements. Hence, it would be worthwhile to overcome these mentioned difficulties, as this will open up new opportunities of curve resolution methods for in-situ spectroscopic investigations of new and highly complex reaction systems where no a priori information exists.

In our research group, it has taken ten years to develop a curve resolution method based on the concept of information entropy, and one that is robust enough to resolve spectra from very complex reaction systems. At the early stage, Zeng and Garland (1998) explored a method base on the modification of Sasaki's method (1983, 1984) by using fourth order derivatives instead of second order, as part of the entropy function to enhance resolution in systems with highly overlapping features. Their results provide good spectral estimations. Pan *et al.* (2000) employed piecewise-continuous variance-weighted spectral measurements combined with entropy minimization to overcome the problem of spectral windows having significantly different variance. They were able to obtain good pure component spectral estimates. The next stage involved the

combination approach of entropy minimization, simulated annealing and spectral dissimilarity. It was applied to resolve 7 pure component spectra having high degree of spectral overlap using synthetic data as well as 6 pure component spectra using real in-situ reaction data (Widjaja and Garland, 2002; Chen *et al.*, 2003). From these studies, the group concluded that a one-spectrum-at-a-time resolution algorithm was indeed an important factor. This approach would allow a reduction in the amount of computation required and eradication of the problem associated with over-resolution. This was the birth of a new curve resolution method named band target entropy minimization (BTEM). BTEM algorithm originally appeared in Widjaja's thesis (2002) and in two publications in 2002 (Chew *et al*., 2002; Widjaja *et al*., 2002) and later other members of the group have applied this method to a variety of spectroscopic fields.

2.3 Band-Target Entropy Minimization (BTEM)

Band-Target Entropy Minimization, BTEM, is a quite special type of SMCR technique. This method is based on Shannon Entropy and a constrained optimization technique for retrieving the spectra of pure component from mixture spectra. Many features present in BTEM make it significantly different from the other SMCR techniques. (1) The estimated profiles (pure component spectra) are evaluated by the minimization of the Shannon entropy of the spectral matrix in BTEM but the other SMCR techniques usually minimize an error criterion such as sum squared residual. This difference enables BTEM to search the pure component spectrum one at a time without considering the other spectra or concentration profiles. (2) The use of targeting the interested band is a unique idea in BTEM. With the different target bands which can be

observed in the right singular vectors of SVD, all the observable pure component spectra can be resolved. It is evident that the above mentioned features of BTEM provide a simple and convenient curve resolution method such that one can focus on only the interesting solutions instead of all resolution problems. Hence, BTEM has a strong ability to cope with the large scale data sets from a complex chemical system. For example, (1) BTEM has been used to reconstruct the pure component spectra of more than 10 species from reactive syntheses, on a number of occasions (Li *et al.*, 2003) and (2) good signal-to-noise estimates (S/N is 25/1 or better) for minor species, i.e. species whose signal intensity is less than 0.1%, can also be obtained (Li *et al.*, 2002, 2003).

2.3.1 Entropy Minimization

Claude Shannon (1948) published the seminal paper to introduce the concept of information theory. The concept of Shannon entropy plays a central role in information theory. The meaning of information entropy in the signal processing field is a measure of the degree of randomness of the observed variables. Kawata, Sasaki and co-workers (1983) first introduced a minimum information entropy concept to retrieve pure component spectra from mixtures. This approach worked by minimizing the entropy of the second derivative of the transformed basis vectors. Entropy measures the degree of information dispersion across the frequency range. Thus, minimizing entropy will localize spectral features while smoothing the spectral baseline.

According to the original statistical property of information entropy, entropy can be expressed as disorder, therefore minimizing the entropy of transformed eigenvectors means maximizing the spectrum simplicity. In other words, minimizing entropy localizes

the spectral information around the major bands and maximizes the number of zero elements in the spectrum.

The entropy value is defined as:

$$H = -\sum_{\tilde{\nu}} h_{\tilde{\nu}} \ln\left(h_{\tilde{\nu}}\right) \tag{2.4}$$

$$\text{where} \quad h_{\tilde{\nu}} = \frac{\left|\frac{d^m \hat{a}_{\tilde{\nu}}}{d\nu^m}\right|}{\sum_{\tilde{\nu}}\left|\frac{d^m \hat{a}_{\tilde{\nu}}}{d\nu^m}\right|} \tag{2.5}$$

where H is the information entropy and $h_{\tilde{\nu}}$ denotes a discrete probability distribution function of the estimated pure spectrum $\hat{a}_{1\times\tilde{\nu}}$. Sasaki *et al*. used the second derivative (m=2), and our group has found through much practice that m=1 is effective for very noisy data, m=2 is effective in most cases, but very highly overlapping spectra are best resolved using m=4 (the spectra should have good S/N for 4th order derivatives).

2.3.2 Methodology of BTEM

BTEM algorithm is initiated by vector-space decomposition of data observations into orthonormal basis vectors. Then, from these basis vectors, via visual inspection, significant spectral features of interest are identified. Usually, such features appear only in the first few vectors as they represent most of the variance in the data matrix. The chosen spectral features will be retained during pure component spectral reconstruction. Simulated annealing (SA), a stochastic method, is the chosen optimization method.

The important conceptual starting point in BTEM is the realization that the pure component absorptivities $a_{s\times\tilde{\nu}}$ are really not very constant. Consequently, the bilinear

Lambert-Beer-Bougeur-Law model is only a first approximation for the measured absorbance. Accordingly, the experimental absorbance can be expressed as shown in Eq.2.6, where $E_{k\times\tilde{\nu}}$ * is explicitly assumed to be a combination of the instrumental / experimental error *plus* the spectral nonlinearities resulting from band position changes and band shape changes.

$$\mathrm{A}_{k\times\tilde{\nu}} = \mathrm{C}_{k\times s}\,\mathrm{a}_{s\times\tilde{\nu}} + E_{k\times\tilde{\nu}}\,* \tag{2.6}$$

The first computational step in BTEM is singular value decomposition (SVD) which is the most generally used matrix decomposition technique. The details of SVD can be found in section 2.2.3. According to Eq.2.3, a set of eigenvectors and eigenvalues can be extracted from an arbitrary matrix data using SVD. It gives us important information on the basis vectors present, and hence provides abstract information on the pure component spectra.

Notice that the spectral problem is not linear (see Eq.2.6). In order to eliminate the non-linearity problem due to shifting band position and changing band shape, BTEM uses *z* (*z*>*s*) right singular vectors for spectral reconstruction. This is a main idea of BTEM to take many more orthogonal basis vectors than the number of observable species (*s*). By doing so, it is possible to recover trace components which have very weak signals. Thus the matrix $A_{k\times\tilde{\nu}}$ can be approximately formulated as shown in Eq.2.7.

$$\mathbf{A}_{k\times\tilde{\nu}} = \mathbf{U}_{k\times z}\Sigma_{z\times z}\mathbf{T}^{+}_{z\times s}\mathbf{T}_{s\times z}\mathbf{V}^{\mathrm{T}}_{z\times\tilde{\nu}} \qquad k \geq z \geq s \tag{2.7}$$

The right singular vectors $\mathbf{V}^{\mathrm{T}}_{z\times\tilde{\nu}}$, obtained from the SVD of $A_{k\times\tilde{\nu}}$ contain all the necessary information on pure components, and therefore $\mathbf{V}^{\mathrm{T}}_{z\times\tilde{\nu}}$ is an abstract

representation of pure component spectra. For BTEM, each pure component is always a linearly optimum combination of those right singular vectors. As such, no a priori information is required concerning the type and the number of species present. The reconstruction is performed by the projection of *z* right singular vectors onto one single vector $\hat{a}_{1\times\tilde{\nu}}$ associated with the pure component spectrum estimate (see Eq.2.8) and the transformation is governed by a constrained non-linear objective function (Eq.2.9).

$$\hat{a}_{1\times\tilde{\nu}} = T_{1\times z}\, V^{T}_{z\times\tilde{\nu}} \tag{2.8}$$

During the optimization, simulated annealing (SA) optimization method is employed to optimize $T_{1\times z}$ so that the minimum value of objective function can be obtained. SA is generally used to determine the optimum of a multivariate response surface in many types of engineering problems (Metropolis *et al.*, 1953; Corana *et al.*, 1987).

The objective function includes two items: an information entropy function (*H*) and a penalty function (*P*).

$$F_{obj} = H + P \tag{2.9}$$

H is formulated by Eq. 2.4. The entropy minimization approach can produce a simplest or smoothest spectrum by reducing the spectral disorder and smoothing the range where peaks are absent.

The penalty ensures the non-negativity of $\hat{a}_{s\times\tilde{\nu}}$ or $\hat{C}_{kxs}$. Such constraints of non-negative characteristics of the real spectral and their corresponding concentrations can help to reduce the solution space. Thus, the purpose of adding a penalty in the objective function is to obtain more exact pure component spectra. The penalty works because if a minimum value of the objective function is achieved, it is expected that P is

near to zero or approaches zero (Eqs.2.10~2.15). The penalty function is divided into 3 parts, where F_1 and F_2 represent the contributions for negative absorptivities and concentrations and $\gamma_{\max}$ helps to control the maximum value of an absorptivity.

$$P(\hat{a}_{1\times\tilde{\nu}}, \hat{C}_{k\times 1}, \hat{a}^{\max}_{1\times\tilde{\nu}}) = \gamma_a F_1(\hat{a}) + \gamma_c F_2(\hat{C}_k) + \gamma_{\max} \tag{2.10}$$

where $F_1(\hat{a}) = \sum_{\tilde{\nu}} (\hat{a})^2 \qquad \forall\ \hat{a} < 0$ (2.11)

$$F_2(\hat{C}_k) = \sum_{k} (\hat{C}_k)^2 \qquad \forall\ \hat{C}_k < 0 \tag{2.12}$$

$$\gamma_{\max} = \begin{cases} 10^4 & \hat{a}^{\max}_{1\times\tilde{\nu}} < \alpha \\ 0 & \hat{a}^{\max}_{1\times\tilde{\nu}} \geq \alpha \end{cases} \tag{2.13}$$

$$\gamma_a = \begin{cases} 0 & F_1(\hat{a}) < \lambda_1 \\ 10 & \lambda_{1\leq} F_1(\hat{a}) < \lambda_2 \\ 10^4 & F_1(\hat{a}) \geq \lambda_2 \end{cases} \tag{2.14}$$

$$\gamma_c = 10^3 \qquad \forall\ F_2(\hat{C}_k) \tag{2.15}$$

Together with the penalty function there are three sets of associated scalar parameters: (1) $\gamma_{\max}$, γ_a, *and* γ_c are penalty coefficients for constraints defined by Eqs.2.13~2.15, (2) α is set to be the maximum absorbance of resolved pure spectrum, in relation to the target band peak absorbance, defined in Eq.2.13, and (3) λ_1 and λ_2 are the bounds for the absorptivity constraint defined in Eq.2.14. And the corresponding expectation of the relative concentration $\hat{\mathrm{C}}_{kxs}$, can be calculated by: Eq.2.16.

$$\hat{\mathbf{C}}_{k\times s} = \mathbf{U}_{k\times z}\Sigma_{z\times z}\mathbf{T}^{+}_{z\times s} = \mathbf{A}_{k\times\tilde{\nu}}\hat{\mathbf{a}}^{\mathrm{T}}_{\tilde{\nu}\times s}\left(\hat{\mathbf{a}}_{s\times\tilde{\nu}}\hat{\mathbf{a}}^{\mathrm{T}}_{\tilde{\nu}\times s}\right)^{-1} \tag{2.16}$$

One of the important advantages of BTEM is that it can eliminate some difficulties in signal processing such as spectra nonlinearities arising from shifting band

positions and changing band shapes due to the imbedded mathematical constructs (Chew *et al.*, 2001). Another attractive characteristic of BTEM is its capability to retrieve a pure component with very low concentration as well as having extremely weak signals. Thus, it is quite useful for trace component analysis. This merit of BTEM makes it useful to understand intermediates species that are usually present in very low concentrations in a reaction system. For example, in one study, the mean concentration $Rh_4(\sigma\text{-}CO)_{12}$ was only 7 ppm but a good pure component spectrum is obtained using BTEM (Widjaja *et al.*, 2002; Li *et al.*, 2003).

2.3.3 Applications of BTEM

BTEM has been successfully applied to the resolution of a wide variety of spectroscopic data, such as FTIR, (Chew *et al.*, 2002; Widjaja *et al.*, 2002; Widjaja and Garland, 2002; Chen *et al.*, 2002, 2003; Widjaja *et al.*, 2003), Raman (Sin *et al.*, 2003; Ong *et al.*, 2003), NMR (Widjaja and Garland, 2005; Guo *et al.*, 2005), MS (Zhang *et al.*, 2003) and fluorescence (Guo and Garland, 2007).

In this thesis, BTEM algorithm will be first applied to IR emission spectroscopy (IRES). Due to the spectral problems of IRES, mainly associated with low signal-to-noise ratio and large background radiation effects, this work is not a trivial. In addition, Chiral-BTEM that is a special extension of BTEM to the application of chiroptical spectroscopies. In this context, chiroptical spectra of UV CD and ROA will be examined. For chiroptical spectroscopic data, the constraints such as the non-negativity of spectra will not hold any more.

As another important development in this thesis, BTEM spectral estimates from complex systems are compared to first principal spectral estimates obtained from Density Functional Theory calculations. The uses include vibrational assignments to confirm the identity of solutes, as well as the determination of the absolute stereochemistry of solutes present in complex systems. Thus the combination of BTEM and DFT appears to be a powerful tool with considerable potential.

2.4 IR Emission Measurements and Experimental Difficulties

In the following sections, the history of IR emission spectroscopy and special problems associated with emission measurements and emission spectral analysis will be reviewed.

2.4.1 Developments in Infrared Emission Spectroscopy (IRES)

IR emission spectroscopy is an alternative to the analytical technique of IR absorption/transmittance spectroscopy. The earliest experiments in infrared emission spectroscopy stretch back to the work done by Coblentz in 1902. Low and Coleman (1965) first attempted to apply FT-IR-EMS to mineralogical surface analysis. A few years later, Griffiths (1972) further applied IRES to the studies of solid samples near ambient temperature. He measured the emission spectra of thick and thin films of silicone grease on aluminum sheets. He found that the characteristic bands of silicone were distorted by the re-absorption in the thick film. This result showed that sample thickness plays an important role in emission spectra. In the 1990s, numerous applications of emission spectroscopy were found for gas phase studies. The more recent developments in IR emission spectroscopy include Hancock and co-workers' work on gas phase emission of

methyl radicals (Heard *et al.*, 1993; Morrell *et al.*, 2002; Carvalho *et al.*, 2006) and King *et al.* (2004) on surface emission on an oxide surface. Although there are many studies on the IR emission of solid and gas-phase samples, literature or the study of liquid samples by IRES is less frequently been found in literature.

Multivariate calibration methods have been applied to IRES data analysis. However, due to the bad behavior of IRES spectra, the multivariate data analysis can only be applied to simple systems. In other words, there are opportunities to improve multivariate resolution of IRES spectra.

2.4.2 Problems in Measurement of Emission IR Spectra

The principal problem in measurement of emission IR spectra is the low signal-to-noise ratio resulting from the large background radiation relative to sample emission (Chalmers and Griffiths, 2002; DeBlase and Compton, 1991). Many researchers made efforts to reduce the effect of the large background radiation using different techniques, for instance, by cooling the spectrometer and sample chamber in liquid nitrogen, by polarization-modulation and by collecting the spectra over large solid angles with an ellipsoidal mirror (Handke and Harrick, 1986; Chalmers and Griffiths, 2002).

The thickness of the sample is an important factor for the measurement of IRES. Systematic measurements have shown that the ideal sample thickness for IR emission spectroscopy is circa 1-10μm for condensed matter (Chalmers and Griffiths, 2002; DeBlase and Compton, 1991). With large thickness, emission bands will become broadened gradually and thus less characterization of the sample can be obtained.

Re-absorption is also a severe problem. Significant re-absorption occurs when the

samples are thick and a temperature gradient exists between the emitting surface and the bulk sample (Chalmers and Griffiths, 2002). Surface reflectivity can also distort IRES spectral. The dispersion in refractive index at strong absorption or emission peaks serves to distort the emission bands.

In this thesis, one major objective is to experimentally investigate the application of infrared emission spectroscopy to liquid phase samples and the organic synthesis in the liquid phase, as well as to apply various new multivariate techniques.

Chapter 3

The Measurements of FTIR Emission Spectroscopic Data and The Development of a Chemometric Method for Emission Spectra

In this chapter, Infrared Emission Spectroscopy (IRES) experimental measurements and a chemometric method based on entropy minimization to reconstruct high-quality pure component emission spectra will be presented.

There are a number of difficulties encountered when trying to obtain a good emission spectrum of a sample. These include, the large superimposed background radiation, the low signal-to-noise ratio, the presence of self-absorption and internal reflection of the sample. All these issues introduce problems when trying to record a good emission spectral pattern. This chapter will mainly describe the application of a combination of experimental configurations and chemometric methods in order to eliminate these experimental difficulties and hence obtain good emission spectra of the individual species of interest in a system.

In this chapter, experimental studies on IRES focus on (1) a single component solid film and a single component liquid film and (2) a multi-component liquid-phase organic reactive system. The later case of IRES probably represents the first time that a liquid-phase reaction has been studied by infrared emission spectroscopy. A chemometric method, namely emission band-target entropy minimization (emission BTEM) is developed in order to deconvolute the Planck

function and instrument response function from the experimental raw data. Consequently, the pure component emission spectra can be reconstructed using emission BTEM. After obtaining the results of the estimated pure component emission spectra further analysis can be performed to obtain the relative concentration profiles.

3.1 Introduction of Infrared Emission Spectroscopy

3.1.1 Nomenclature

Emissivity Emissivity is a property of a sample measured at standard conditions. It is not composition or geometry dependent.

Emittance, ε Emittance is a property of the sample dependent on composition and geometry. It contains spectral characteristics of the species of interest and is defined as the ratio of a sample luminance (or radiant flux) to that of a blackbody at a given temperature.

Luminance, L Luminance is the intensity of emitted radiance per unit solid angle and frequency. It is sometimes called spectral radiance, or radiant flux. This quantity is dependent on both frequency and temperature according to Planck's distribution function and Wein's radiation law.

Blackbody Source The blackbody source is a wideband infrared source whose luminance, L, follows Planck's distribution law. It is often used as a reference in calculating emittance.

3.1.2 Infrared Emission Spectroscopy (IRES)

IR emission spectroscopy is a well-established analytical technique and often considered as an alternate to IR absorption/transmittance spectroscopy. Significant use of emission spectroscopy has been found in astrophysics to assess the chemical constituents in distant space, in remote monitoring of effluent industrial gases, in studying photochemical initiated reactions as well as in regular laboratory analysis of thin layer/metal oxide deposits and polymers (Rogers and Leone, 1993; Mink and Keresztury, 1993; Deming *et al*., 2004). For example, it has been used to characterize the molecular structures of various minerals involving carbonates, sulfates, phosphates, arsenates and chlorides as well as to study the lattice vibrations of the crystals and to investigate the vibrations of adsorbed molecules on metal surfaces and metal supported catalysts (Hamilton, 2000; Frost and Vassallo, 1996; Li *et al.* 1991). In particular, IRES has been used for the study of heterogeneous catalysts, since in general, such solids absorb too strongly for transmission or even reflectance experiments. In addition, time-resolved Fourier transform emission spectroscopy has proved to be a valuable tool for the study of the vibration states of gases during photolysis experiments such as N_2O, vinyl bromide and vinyl chloride, etc (Heard *et al.*, 1993; Letendre *et al.*, 2000; Morrell *et al.*, 2002; Carvalho *et al.*, 2006). However, getting a well-defined IR emission spectrum is still a major challenge. The main difficulties are the large background radiation, the self-absorption of the sample and the internal reflection at the sample surface. All of these complications lead to low signal-to-noise ratios for the sample studied.

A large number of experimental studies on IRES have been concerned with obtaining good quality IR emission spectra for solid samples. Such investigations have mainly involved the modification of experimental configurations and the testing of different conditions for sampling. Several factors such as sample temperature, sample thickness, and sample arrangement (such as the tilting of the sample) could affect the emission spectrum of the solid samples (Kember and Sheppard, 1975; Hvistendahl *et al.*, 1983; DeBlase and Compton, 1991; Mink, 1992, 2002). It should also be mentioned that in contrast to the large number of studies on the IR emission of solid and gas-phase samples, much less attention has been paid to the study of liquid samples, and the study of liquid-phase reactive systems is rare. In this chapter, a liquid-phase reaction was monitored using IRES.

A number of investigations have been conducted on the analysis of emission data in order to obtain the emissivities from the measured emittance (Kember and Sheppard, 1975; Hvistendahl *et al.*, 1983; Chase, 1981; Compton *et al.*, 1991; DaBlase and Compton, 1991; Tochigi *et al.*, 1992). Many of these studies have approached the problem by taking measurements of the sample, the blackbody reference, the background and other references then using a modified ratio method. In this context, it should also be mentioned that various chemometric techniques, such as digital filtering and multivariate calibration, are increasingly being used to treat emission spectra, particularly for pollutant monitoring and industrial stack emissions. Since the intensity of the background radiation is usually much larger than that from the sample itself, most analytical methods need references in order to correct for the

background signal and spectral patterns of the compounds of interest. In other words, application to unknown systems where reference spectra can not be obtained, presents a difficult challenge. In this chapter, a new analytical method was developed to reconstruct pure component emission spectrum without the use of any a-priori data.

3.2 Experimental Section

3.2.1 General Experiment Configuration

The main objectives of the experiments in this chapter are to use the IR emission spectrometer and apply the emission technique to study (1) a single component solid film and a single component liquid film and (2) a liquid phase reaction (such as the cyclo-addition involving cyclopentediene and dimethyl acetylenedicarboxylate used in this work).

The measurements of emission were conducted on a conventional FT-IR spectrometer (Bruker Equinox-55) equipped with an external emission accessory which was set up next to the spectrometer. The emission accessory consisted of an optical table with a parabolic mirror and sample holder on the bench top. This optical table allows the accurate and secure positioning of the mirror so that the emitting sample holder was in focus. The configuration of the optical path for the emission attachment is given in Figure 3.1. The sample serves as the radiation source, and the infrared emission is collected by the parabolic mirror and focused on the detector. The emission samples in our experiment were heated from the back side. The heat is transmitted to the sample via conduction from the heated circulating water to the steel sample holder and finally to the sample. Photographs of the emission bench with cell

and parabolic mirror are shown in Figure 3.2.

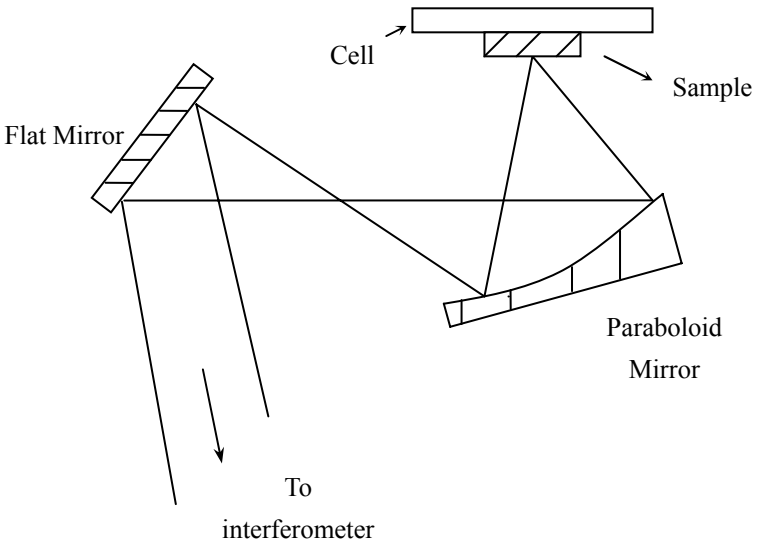

Figure 3.1. Schematic configuration of the optical arrangement for the IR emission attachment.

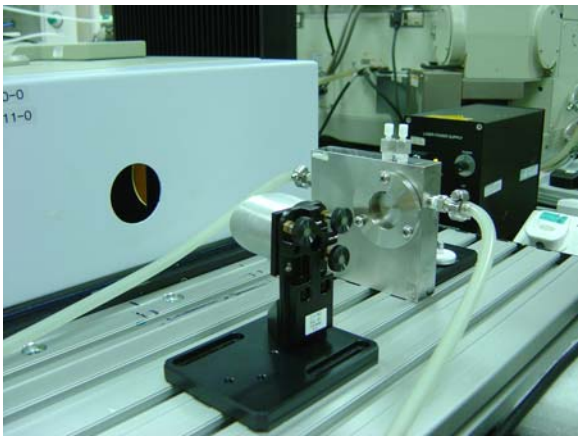

Figure 3.2. The experimental set-up: emission bench with cell and the parabolic mirror.

3.2.2 Design of Emission Cell

Emission cells are usually made of highly-reflecting (low emissivity) metals or can be backed with a reflector plate. In this work, the stainless steel thermostated emission cell was designed and constructed in-house. The newly designed stainless

steel cell is used in the present study. The cell has provisions for holding a thin solid film on one side and a liquid film sample on the other side. Close up Photographs of the solid sample holder and the liquid sample holder are shown in Figure 3.3. The three screws are used to secure the solid samples in place and it allows for various thicknesses to be examined. No optical window was used in the case of solid samples. For liquid phase sampling, there are two holes drilled on the metal plate which are connected to the two openings found on the top surface to allow circulation of the liquid sample of interest when performing in-situ studies. An optical window was placed in front of the metal plate in the case of liquid phase samples. To prevent the breakage of expensive windows when tightening the screws, a Viton® 'o'-ring is put in place to cushion the effect and to provide good sealing. A network of channels within the cell acts like a heat exchanger since heating or cooling fluid is circulated throughout. This will help to control the temperature of the sample. The temperature of the cell was maintained by an external circulating water bath with circa $\pm 0.1^0$ C accuracy. With the exception of the exposed sample area, the entire surface of the cell was masked with black paper to avoid the thermal signature from steel body during the measurements. The entire sample holder was tilted at an angle of approximately 15^0 facing towards the parabolic mirror in order to achieve a maximum throughput during the measurements.

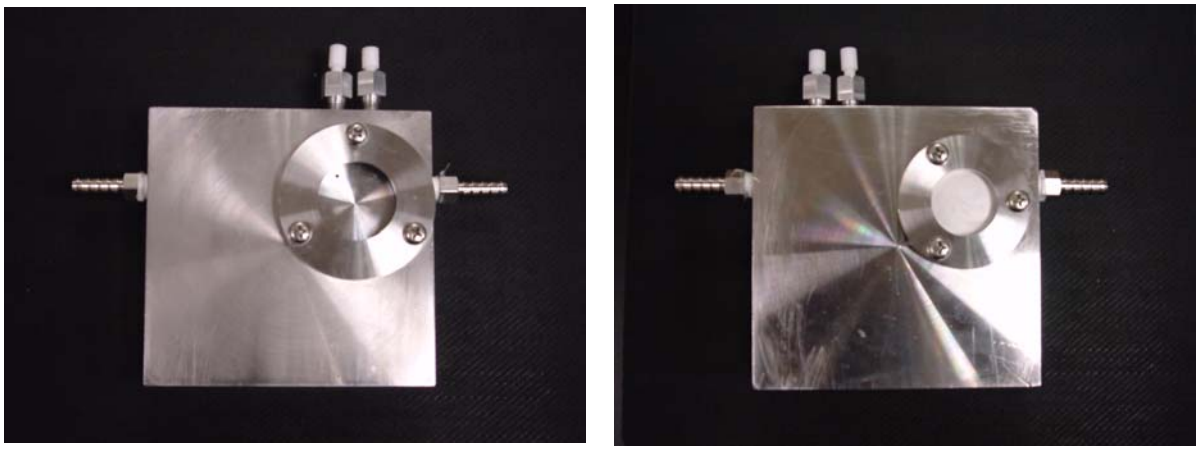

Figure 3.3. The left photograph is a close up of the liquid sample holder (without window present) and the right photograph is a close up of the solid sample holder (with polymer sample present).

3.2.3 Pure Solid Film and Pure Liquid Film Samples

Solid parafilm and liquid isopropanol were the samples used in this study. Both have good vibrational bands in the lower wavenumber range.

The parafilm, with a thickness 0.05mm was wrapped around the aluminum pellet and then fixed into the cell. The other side of the aluminum pellet was painted black and was employed as the blackbody reference. Emission spectra were recorded for the black body, aluminum pellet and for the film stretched around the aluminum pellet at temperatures from 298 K to 348 K in 10 K increments.

For liquid samples, a ZnSe window was used and the sample was injected between the cell and the window. The thickness of ZnSe window was 4mm. Similarly the emission spectra for isopropanol were recorded with the empty cell, ZnSe window, and with the injected liquid sample at temperatures from 298 K to 338 K in 10 K increments (the boiling point of isopropanol is 355.7 K).

Emission spectra were recorded using two different detectors, namely an air-cooled DTGS detector (450 cm^{-1} cut-off) and a liquid nitrogen cooled MCT

detector (750 cm^{-1} cut-off). The experimentally obtained emission spectra were the result of 400 co-added scans, at a resolution of 6 cm^{-1}. All the measurements were done without purging the emission bench.

3.2.4 Liquid-Phase Organic Reaction System

In the present work, a cyclo-addition reaction between conjugated cyclopentadiene and a di-substituted alkyne in the liquid phase was studied by IRES. Specifically, the reaction between cyclopentadiene (CP) and dimethyl acetylenedicarboxylate (DMAD) generates the product dimethyl bicyclo[2.2.1]-2,5-heptadiene-2,3-dicarboxylate (DBHD):

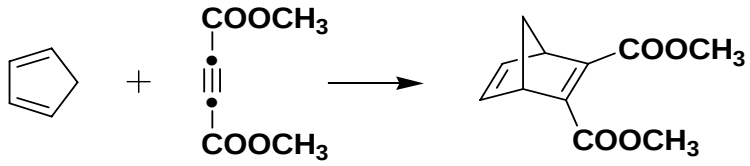

Cyclopentadiene was prepared from distillative dissociation of dicyclopentadiene (Aldrich)*. The resulting product was checked by ^{1}H NMR, found to be circa 99% pure, and stored at -80 ^{o}C. Chloroform (Aldrich 99%) was used as solvent, and the reactant dimethyl acetylenedicarboxylate (Aldrich 99%) were used as received.

Two semi-batch cycloaddition reactions were performed at 308 K. Circa 25 ml of solvent chloroform was used in each experiment, and then various quantities of the

* Thanks are extended to Dr. Ilya Lyapkalo for preparing this sample.

reactants DMAD and CP were added according to the experimental design given in Table 3.1. The two semi-batch experiments differ due to the order in which the reactants were added.

Table 3.1. Experimental design of the injections for cycloaddition reaction.

Number	Experiment 1		Experiment 2	
	Perturbation	**Spectra #**	**Perturbation**	**Spectra #**
1	Empty cell	1	Empty cell	29
2	Add 25 ml CHCl3	2-14	Add 25 ml CHCl3	30-32
3	Add 1ml DMAD	15-16	Add 0.3 ml CP	33-34
4	Add 1 ml DMAD	17-18	Add 0.3 ml CP	35-36
5	Add 1 ml DMAD	19-21	Add 1ml DMAD	37-41
6	Add 0.6ml CP	22-24	Add 2ml DMAD	42-44
7	Add 0.3 ml CP	25-26	Add 0.6 ml CP	45-48
8	Add 0.3 ml CP	27-28	Add 1ml DMAD	49-55

The reactions were conducted in the experimental setup shown in Figure 3.4. A Schlenk tube with magnetic stirring was immersed in a cryostat set to the reaction temperature of 308K. The liquid phase in the Schlenk tube was circulated to the emission cell using a hermetically sealed membrane pump (Cole Parmer) at the flow rate of 5 ml/min via PEEK tubes of 1/16” outer diameter. The temperature of the cell was maintained by a circulating water bath at 308K.

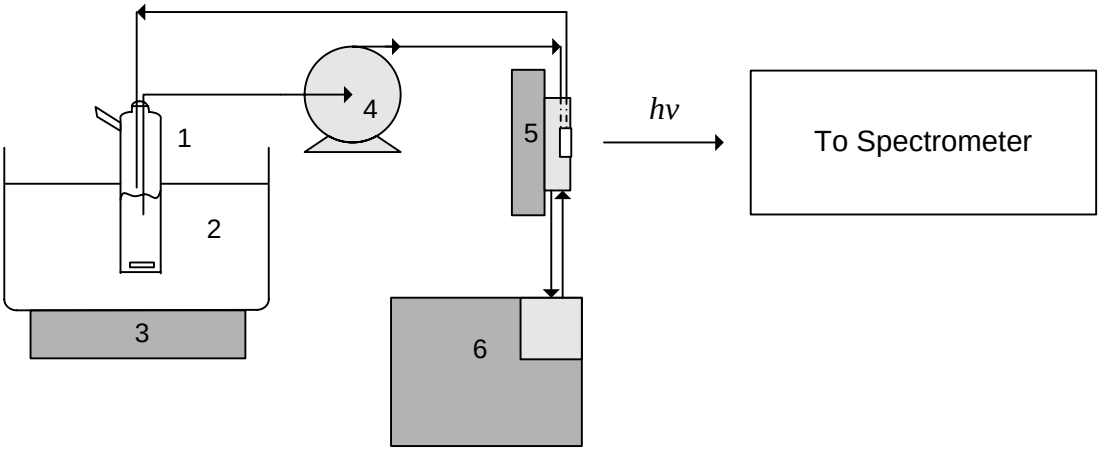

Figure 3.4. Schematic configuration of experimental set-up: 1. Schlenk tube; 2. Silicon oil; 3. IKA RCT Basic; 4. Pump; 5. Emission cell with window; 6. Water bath.

Ten minute co-added scans were accumulated for each emission spectrum at resolution of 6 cm^{-1} using an air-cooled DTGS detector. The raw experimental spectra were used in all calculations, and no background subtractions were performed. Emission spectra of the empty cell, the solvent, the reactant DMAD in the solvent and the reaction after injecting the second reactant CP were all recorded. A total of 55 emission spectra from two semi-batch reactions were obtained from the two semi-batch experiments.

Additionally, independent cycloaddition experiments were conducted in FTIR transmission mode in order to acquire reference FTIR spectra of DMAD, CP and DBHD for comparison with the present emission results.

3.3 Emission Model

3.3.1 Emission Spectral Presentation

The intensity of emission measured in the conventional way can usually be presented in the following forms: (1) single beam intensity, (2) single beam intensity

ratioed to sample holder, (3) single beam ratioed to blackbody, (4) single beam ratioed to optically opaque and thick reference sample. Keresztury *et al.* (1995) have drawn attention to the difficulties surrounding these different forms. They note that spectral presentation (1), single beam measurement, is not a good form since most useful spectral information of samples is modulated by the large Planck blackbody radiation and the instrument responses. From a theoretical viewpoint intensity forms (3) and (4) are preferred forms to ensure true emission band intensities. In this context, it is worth noting that the spectral presentation (3) holds the same definition as emittance and the spectral presentation (4) can be referred to as reflection-corrected emittance.

3.3.2 Lambert-Beer Law for Emission Spectroscopy

3.3.2.1 Lambert-Beer Law

A Lambert-Beer type law for emission spectroscopy is analogous to that of the Beer-Lambert IR absorbance law. Thus a brief introduction to the Lambert- Beer law for the absorption spectroscopy is given in order to facilitate understanding of the deducted Lambert- Beer law for emission spectroscopy. There are two ways in which the Lambert- Beer law of the absorption spectroscopy can be expressed:

$$A = \alpha \cdot l \cdot c \tag{3.1}$$

$$-\log_{10} T = \alpha \cdot l \cdot c \tag{3.2}$$

where A and T are the absorbance and transmittance of the sample respectively, α is molar absorptivity, l is the path length and c is the concentration.

In essence, the law states that (1) there is a logarithmic dependence between

the transmission of light through a substance and the concentration of the substance and (2) absorbance of light by a substance is a linearly proportional to *l* the path length and *c* the concentration.

3.3.2.2 Thermal Emission of the Sample (Non-Blackbody)

In order to obtain the Lambert-Beer law of emission spectroscopy, it is necessary to understand the relationship between transmittance and emission. The basic relation of optical emission spectroscopy for a sample can be expressed as:

$$E(\tilde{\nu}) + R(\tilde{\nu}) + T(\tilde{\nu}) = 1 \tag{3.3}$$

where E, R and T are the emittance, reflectance and transmittance of the sample, respectively. In most cases, the surface effects (reflectance) are usually neglected in the emission spectroscopy (Mink, 2002). In this case the equation can be simplified as:

$$E(\tilde{\nu}) + T(\tilde{\nu}) = 1, \qquad (R(\tilde{\nu}) = 0) \tag{3.4}$$

This equation shows the complementary nature of emittance and transmittance spectrum. $E(\tilde{\nu})$ can have different spectral representations as mentioned in subsection 3.3.1. However, it is often obtained from form (3), i.e. ratioing the single-beam emission spectrum to that of the blackbody reference.

3.3.2.3 Lambert-Beer Law of Emission Spectroscopy

The emittance spectrum $E(\tilde{\nu})$ in emission spectroscopy is analogous to transmittance in the absorption spectroscopy. Consequently, the Lambert-Beer law of emission spectroscopy can be deduced as follows:

$$T(\tilde{\nu}) = 1 - E(\tilde{\nu}) \tag{3.5}$$

$$-\log_{10}[1 - E(\tilde{\nu})] = lc\varepsilon(\tilde{\nu}) \tag{3.6}$$

where $E(\tilde{\nu})$ is the emittance of the sample, $\varepsilon(\tilde{\nu})$ is the molar emission coefficient, $\tilde{\nu}$ is wavenumber of electromagnetic radiation, l is the path length (or the thickness of the solid sample) and c is the concentration.

A series of steps were performed to simplify Eq.3.6 to obtain a linear dependence between emittance and an effective thickness. The Taylor expression at 0 for the natural logarithm (Eq.3.7) was used to simplify Eq.3.6:

$$\ln(1+x) = \sum_{n=1}^{\infty} \frac{(-1)^{n+1}}{n} x^n = x - \frac{x^2}{2} + \frac{x^3}{3} - \frac{x^4}{4} + \cdots\cdots \qquad for \quad |x| \langle 1 \tag{3.7}$$

In this work, the intensity scales of emission spectra are on the order of 10^{-4} for the measurements with the DTGS detector and 10^{-2} for the measurements with the MCT detector. Thus the Taylor expression can be reduced to:

$$\ln(1+x) \approx x \qquad for \quad |x| < 1 \tag{3.8}$$

Combining Eq.3.8 and Eq.3.6, the approximate Lambert-Beer law for emission spectroscopy can be obtained:

$$E(\tilde{\nu}) = lc\varepsilon(\tilde{\nu}) \cdot (\log_{10} e)^{-1} \tag{3.9}$$

This equation is used to construct the basic model for multi-component emission measurements.

3.3.3 Emission Model

For each set of emission spectroscopic data, a single matrix of dimension $E_{k\times\nu}$ comprises all individual experimental emission spectra $E_{1\times\nu}$ where k is the

number of spectra measured and ν is the number of data channels.

According to Eq.3.9, each measured emission spectrum $E_{1\times\tilde{\nu}}(T,P,l)$ at temperature T, pressure P and pathlength *l*, can be represented as a weighted contribution of the individual emissivities $\varepsilon_{1\times\tilde{\nu}}(T,P,l)$ where ω represents the weighting and $\Phi_{1\times\tilde{\nu}}$ represents the associated instrumental and experimental error.

$$E_{1\times\tilde{\nu}}(T,P,l) = (\omega\varepsilon(T,P,l) + \Phi_{1\times\tilde{\nu}}) \times (\log e)^{-1} \tag{3.10}$$

Then in matrix notation, each set of measured emission spectra are related to the mean value of the emissivities $\varepsilon_{s\times\tilde{\nu}}(\overline{T},\overline{P},\overline{l})$ and the error :

$$E_{k\times\tilde{\nu}}(T,P,l) = (\omega_{k\times s}\varepsilon_{s\times\tilde{\nu}}(\overline{T},\overline{P},\overline{l}) + \Phi'_{k\times\tilde{\nu}}) \times (\log e)^{-1} \tag{3.11}$$

It is assumed that *k* measurements are made, *s* species are present and $\tilde{\nu}$ channels of spectroscopic data are measured. In this equation, the error $\Phi'_{k\times\tilde{\nu}}$ contains (1) instrumental and experimental error as well as (2) model error due to variations in the emissivities at slightly different temperatures, pressures and small variations in pathlength. In the same manner, the model for the multi-component measurements at the same temperature and pressure can be rewritten as Eq.3.12:

$$E(\tilde{\nu})_{k\times\tilde{\nu}} = (l_{k\times k}c_{k\times k}\varepsilon_{s\times\tilde{\nu}} + \Phi''_{k\times\tilde{\nu}}) \times (\log e)^{-1} \tag{3.12}$$

where *l* is the path length (or the thickness of the solid sample), *c* is the concentration, and similarly, Φ'' is associated with the random experimental error as well as non-linearities in the bilinear model.

The bilinear models (Eqs.3.11 and 3.12) were used as emission models in further chemometric analyses.

3.4 Emission Mode Band-Target Entropy Minimization

In this subsection, a relatively new methodology for pure component emission spectral reconstruction based on the information entropy concept will be presented. The pure component spectral reconstruction is actually a system identification problem (inverse problem). In this context, using only a knowledge of $E(\tilde{\nu})$, one attempts to determine the individual $\varepsilon(\tilde{\nu})$.

3.4.1 Formulation of Emission BTEM

The basic idea of BTEM and its algorithm was previously given in chapter 2. BTEM analysis is performed after taking the SVD of the full data set. Once the right singular vectors are obtained, model-free deconvolution is performed to obtain one spectrum at a time. This deconvolution is achieved by optimizing the transformation of the right singular vectors, and is guided by the user's choice of spectral features to target. In contrast to other SMCR techniques, BTEM does not rely on statistical tests. Instead, enough latent vectors $z<k$ are chosen so that practically all physically meaningful data are used and only vectors consisting of more-or-less noise are discarded.

The first step of BTEM is singular value decomposition (SVD) which is one of the most generally used matrix decomposition techniques. Using SVD, a set of eigenvectors and eigenvalues can be extracted from an arbitrary matrix data, for instance $E(\tilde{\nu})_{k\times\tilde{\nu}}$, which possesses a bilinear form (Eq.3.11 or 3.12). The SVD gives us important information on the basis vectors present, and hence provides abstract

information on the pure component spectra.

In this work, SVD is used to decompose the experimental emission data, $E(\nu)$, into three matrices according to Eq.3.13:

$$E(\tilde{\nu})_{k\times\tilde{\nu}} = \mathrm{U}_{k\times k}\Sigma_{k\times\tilde{\nu}}\mathrm{V}^{\mathrm{T}}_{\tilde{\nu}\times\tilde{\nu}} \tag{3.13}$$

The main purpose of SVD is to obtain abstract orthonormal matrices $\mathbf{U}_{k\times k}$ and $\mathrm{V}^{\mathrm{T}}_{\tilde{\nu}\times\tilde{\nu}}$ with their diagonal singular matrix $\Sigma_{k\times\tilde{\nu}}$. $\Sigma_{k\times\tilde{\nu}}$ is a diagonal matrix whose elements are the non-negative square root of the eigenvalues of the covariance matrix $E\cdot E^{T}$ (transpose of *E*). The right singular vectors, $\mathrm{V}^{\mathrm{T}}_{\tilde{\nu}\times\tilde{\nu}}$, contain all the necessary spectral information on the species present such as individual emissivities as well as the thermal background (blackbody effects etc). Reconstruction is performed by the projection of *z* right singular vectors onto one single estimate of emissivity $\hat{\varepsilon}_{1\times\tilde{\nu}}$.

The primary equation for estimating the pure component emissivities by BTEM is given by Eq.3.14. It should be noted that this transformation returns estimates which are actually *normalized* emissivities. This is due in part to the scaling ambiguity previously mentioned in section 2.2.4.

$$\hat{\varepsilon}_{1\times\tilde{\nu}} = \mathrm{T}_{1\times z}\mathrm{V}^{\mathrm{T}}_{\tilde{\nu}\times\tilde{\nu}} \tag{3.14}$$

In the BTEM algorithm for emission spectroscopy the estimated emissivity, $\hat{\varepsilon}_{1\times\tilde{\nu}}$, is an optimized combination of *z* right singular vectors $\mathrm{V}^{\mathrm{T}}_{z\times\tilde{\nu}}$. *z* is typically much greater than the number of species present and is smaller than or equal to *k*. Accordingly, many noisy singular vectors can be discarded prior to optimization and this improves the resulting spectral estimates. From *z* right singular vectors, local

spectral features can be identified and in further step these local spectral features are targeted one-at-a-time. In other words, for BTEM, each estimated pure component spectrum is always an optimized linear combination of those major right singular vectors. As such, no a priori information is required concerning the type and the number of species present. It is clearly seen that the most important practical issue is the determination of the transformation matrix $T_{1\times z}$. This is achieved by a constrained non-linear optimization using simulated annealing.

Simulated annealing is generally used to determine the optimum of a multivariate response surface in engineering problems. It is a stochastic technique. As such, this global optimization method tries to avoid local minima by jumping out of them early in the computation. The chance of finding an optimal or near-optimal solution can be traded off with computation time by slowing down the cooling schedule. The origins of the algorithm are based on statistical mechanics (Metropolis algorithm) and it was presented as a search algorithm (Kirkpatrick *et al.*, 1983). Corona's (1987) SA method has found growing acceptances as an efficient method for global optimization. It has been frequently used and has proven capability for obtaining global solutions for highly nonlinear optimization problems. In this work, Corana's simulated annealing algorithm was employed to final optimal solution for the highly nonlinear BTEM objective function.

The objective function for this non-linear optimization is composed of a term for information entropy function (*H*) and a term for penalty function (*P*) as indicated in Eq.2.9.

The entropy function *H* is defined by Eq.2.4, where the entropy is evaluated as the spectral derivative (smoothness) at each wavenumber (Eq.2.5).

The corresponding penalty function takes the form of Eq.3.15. The purpose of adding a penalty in the objective function is to obtain more exact pure component spectra by preventing reconstruction of physically non-meaningful emissivities, in particular, non-positive values for the emissivities. Thus the non-negative characteristics of the real emissivities and their corresponding concentrations can be considered as a constraint to further reduce the solution space. The penalty *P* is frequently expected to be near zero for good solutions (Eqs.3.15~3.18).

$$P(\hat{\varepsilon}_{1\times\tilde{\nu}}, \tilde{\varepsilon}^{\max}_{1\times\tilde{\nu}}) = \gamma_a F_1(\hat{\varepsilon}_{1\times\tilde{\nu}}) + \gamma_{\max} \tag{3.15}$$

where

$$F_1(\hat{\varepsilon}) = \sum_{\nu} (\hat{\varepsilon})^2 \qquad \forall\ \hat{\varepsilon} < 0 \tag{3.16}$$

Together with the penalty function there are three sets of associated scalar parameters: (1) γ_a, $\gamma_{\max}$ are penalty coefficients, (2) α is set to be the maximum emissivity of the resolved pure spectrum, in relation to the target band peak emissivity, and (3) λ_1, λ_2, are the bounds for the emissivity constraint.

$$\gamma_a = \begin{cases} 0 & F_1(\hat{\varepsilon}) < \lambda_1 \\ 10 & \lambda_{1\le} F_1(\hat{\varepsilon}) < \lambda_2 \\ 10^4 & F_1(\hat{\varepsilon}) \ge \lambda_2 \end{cases} \tag{3.17}$$

$$\gamma_{\max} = \begin{cases} 10^4 & \hat{\varepsilon}_{1\times\tilde{\nu}}^{\max} < \alpha \\ 0 & \hat{\varepsilon}_{1\times\tilde{\nu}}^{\max} \geq \alpha \end{cases} \tag{3.18}$$

3.4.2 Quantitative Analysis: Concentration Profiles

By performing BTEM on the experimental spectroscopic data, the reconstructions of the possible pure component emissivities (*normalized*) associated with the studied system can be achieved. The next step of system identification for a multi-component system is to determine the concentration profiles of each species in the system. The corresponding *relative* concentration profiles can be calculated by using the reconstructed pure component spectra with Eq.3.19:

$$\hat{C}_{k\times s} = E(\nu) \times (\hat{\varepsilon}_{s\times\tilde{\nu}})^{-1} \tag{3.19}$$

Where s is the number of species (s might include the background, the blackbody, the cell and the instrumental response) present in the studied system. The pseudo inverse of the matrix of the reconstructed pure component spectra is calculated using a function provided in MATLAB.

3.5 Results and Discussion: Emission of Pure Solid Films and Pure Liquid Films

In this section, the experimental data from both parafilm and isopropanol were analysis by BTEM. In order to assess the importance of inclusion / exclusion of blackbody type spectra in the data sets, as well as other issues, eight data sets were analyzed using BTEM. Table 3.2 lists each set of consolidated spectra, the total

number of spectra taken *k*, the primary sample measured, any auxiliary measurements, the detector used and finally the number of right singular vectors *z* used in analysis.

Table 3.2. The different combinations of consolidated data and the number of the right singular vectors was used in BTEM for each of them.

Consoli-dated data set, No.	**Total number of the spectra taken, k**	**Primary sample measurements**	**Auxiliary measurements**	**Detector**	**Number of the used right singular vectors, z**
1	6	Parafilm	−	DTGS	4
2	18	Parafilm	Blackbody, Aluminum pellet	DTGS	8
3	6	Parafilm	−	MCT	4
4	18	Parafilm	Blackbody, Aluminum pellet	MCT	8
5	5	Isopropanol	−	DTGS	4
6	15	Isopropanol	Empty cell, Window	DTGS	8
7	5	Isopropanol	−	MCT	4
8	15	Isopropanol	Empty cell, Window	MCT	8

3.5.1 Pure Solid Films: Parafilm

3.5.1.1 Experimental Data Sets

The series of spectra for the parafilm samples obtained using both the DTGS and MCT detectors are shown in Figure 3.5 and Figure 3.6 respectively.

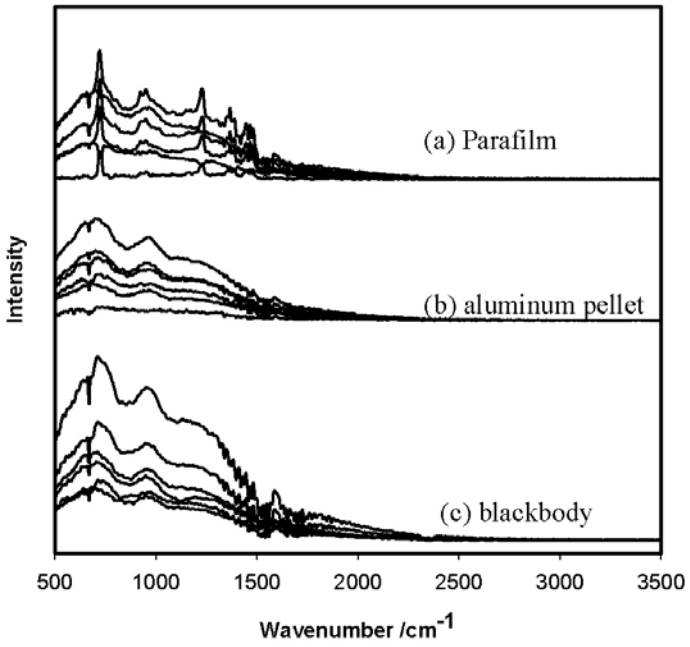

Figure 3.5. The emission spectra of (a) parafilm; (b) the aluminum pellet; (c) the blackbody taken at six temperatures (348, 338, 328, 318, 308, 298 K) using DTGS detector.

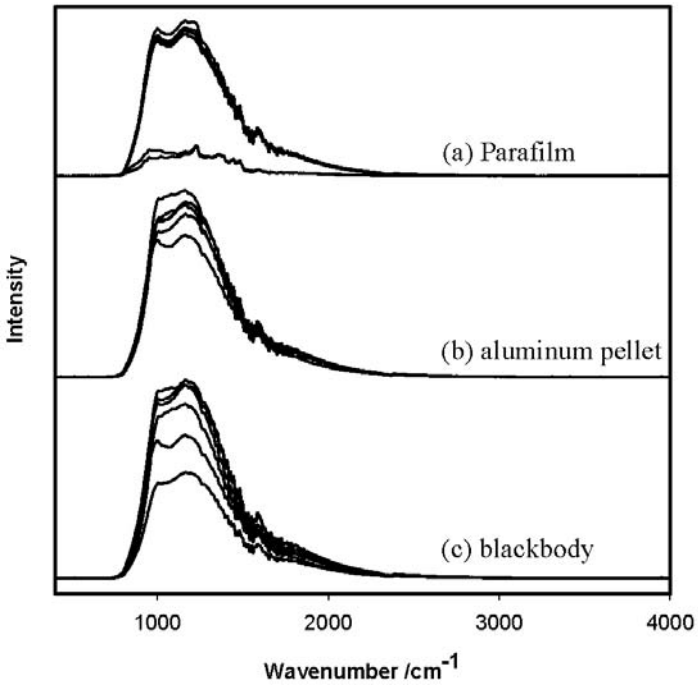

Figure 3.6. The emission spectra of (a) parafilm; (b) the aluminum pellet; (c) the blackbody taken at six temperatures (348, 338, 328, 318, 308, 298 K) using MCT detector.

Figure 3.5 (DTGS data) shows physically significant signals in the

characteristic fingerprint region at low wavenumbers, while at the high wavenumber region (above 2500 cm^{-1}) little signal is observed. This is consistent with the Planck function that blackbody radiation will show a maximum in the range of 600 cm^{-1} at circa 300 K. Figure 3.6 shows significant radiant emission down to 750 cm^{-1} which is the optical cut-off for the MCT detector. In contrast to the DTGS data, all the emission spectra from MCT have significantly higher signal intensity as evidenced by the relatively smooth quality of the spectra. In both Figure 3.5 and 3.6, the series of aluminum pellet emission spectra show the same generic characteristics as the corresponding blackbody series, and in addition the emission intensity of this series is less than the blackbody at any given temperature.

The DTGS data in Figure 3.5 show significant radiant emission down to 500cm^{-1}. The absorbance of the radiant energy by atmospheric moisture can be seen in all emission spectra as a series of bands at circa 1400-1800 cm^{-1} and the absorbance of the radiant energy by atmospheric carbon dioxide can be seen by a band at 670 cm^{-1}. The series of blackbody emission spectra do not follow a perfect Planck function due to (1) the above mentioned absorbance (2) the fact that the blackbody background is not perfect and (3) the absorbance/transmission/reflection characteristics of the optical components in the spectrometer. Finally, the series of parafilm emission spectra show all the above mentioned characteristics, and in addition this series shows the structured emission of hydrocarbon film, as seen by the maxima at circa 720, 950, 1230,1450, etc. cm^{-1}.

The MCT data in Figure 3.6 also show the absorbance of the radiant energy by

atmospheric moisture in all emission spectra as a series of bands at circa 1400-1800 cm^{-1}. The absorbance band at 670 cm^{-1} is not observed due to the MCT cut-off. However, due to the high signal intensity, the absorbance due to atmospheric CO_2 can now be seen at circa 2300-2400 cm^{-1}. All the above mentioned spectral features are embedded in the series of parafilm emission spectra. In addition this series shows the structured emission of hydrocarbon film, as seen by the maxima at circa 950, 1230, etc. cm^{-1}. However, this emission intensity appears weak since it is imbedded in the considerably larger blackbody emission. Also, the abnormally low intensities of the emission spectra at 298 K and 308 K seem to indicate a contact problem between the parafilm and heating surface.

3.5.1.2 Signal Processing and SVD

Data preconditioning, namely, filtering was first performed on each experimental emission spectrum in the parafilm series in order to eliminate the high frequency noise components.

As mentioned in the beginning of this section (3.5), the series of DTGS emission spectra was processed in two ways in order to compare the different BTEM analysis results with / without blackbody type spectra in the data sets. In the first case, only the sub-set of 6 parafilm emission spectra was subjected to singular value decomposition. In the second case the entire set of 18 emission spectra (blackbody, aluminum pellet and parafilm) was subjected to singular value decomposition.

The SVD results for consolidated data set 1 and 2 from DTGS are shown in

Figure 3.7 and 3.8, respectively.

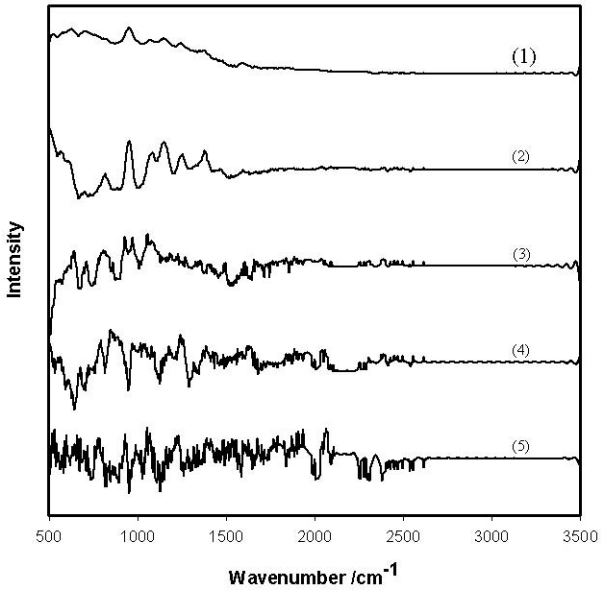

Figure 3.7. First six right singular vectors of V^T Matrix for consolidated data set 1.

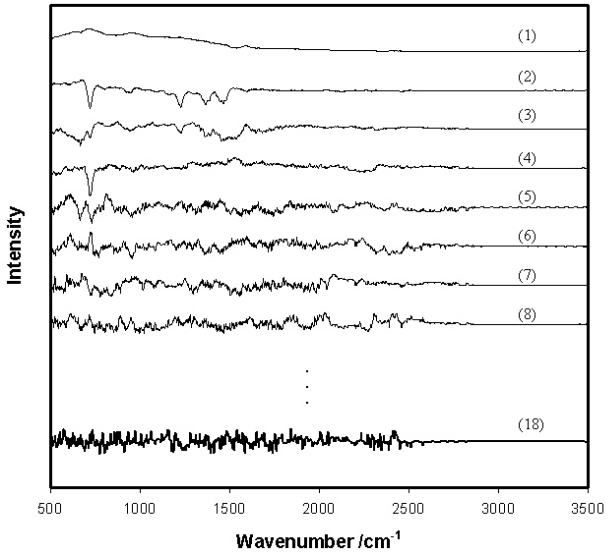

Figure 3.8. First eight and eighteenth right singular vectors of V^T Matrix for consolidated data set 2.

The first 4 right singular vectors from Figure 3.7 show discernable spectral features with physical meaning. The first 2 vectors clearly have a lot of useful information, the third vector appears to have signal primarily from the CO_2 at 670 cm^{-1} plus considerable noise and finally the fourth vector has predominantly noise but also

a clear contribution from CO_2 at 2300-2400 cm^{-1}. The remaining 2 vectors appear to be essentially noise.

In Figure 3.8 more right singular vectors from the DTGS data show good signal-to-noise ratios. Indeed, the first 4 vectors have quite good signal-to-noise ratios. In addition, the next four vectors clearly have some useful and embedded physical signals. The remaining right singular vectors were more-or-less white noise as indicated clearly by vector 18. There is a considerable difference in the noise level between the low wavenumber and high wavenumber regions

Similarly, the series of MCT emission spectra was processed in two different ways and the results for consolidated data set 3 and 4 from MCT are shown in Figures 3.9 and 3.10.

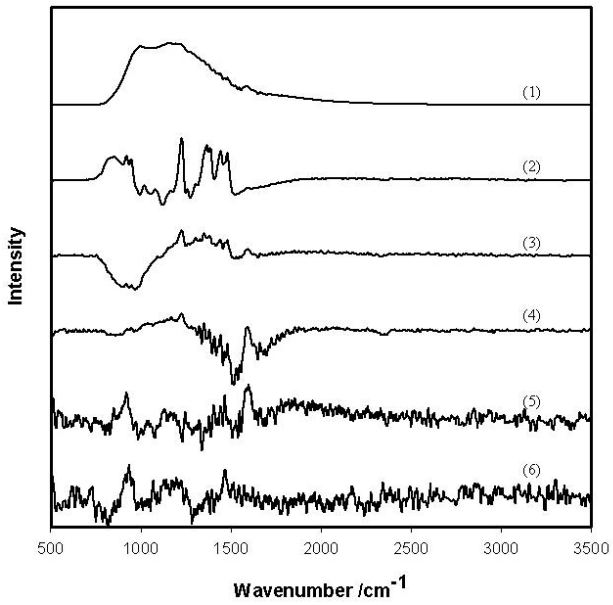

Figure 3.9. First six singular vectors of V^T Matrix for consolidated data set 3.

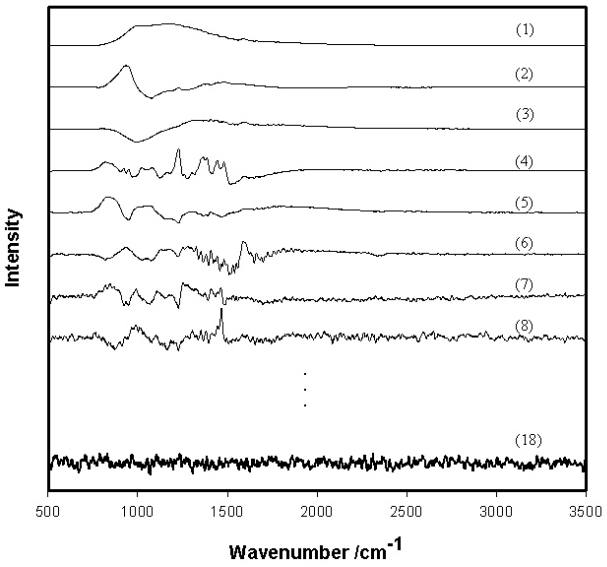

Figure 3.10. First eight and eighteenth right singular vectors of V^T Matrix for consolidated data set 4.

In contrast to the right singular vectors obtained from DTGS data sets, Figures 3.9 and 3.10 show more significant spectral features with physical meaning.

In Figure 3.9 the first 3 vectors clearly have a lot of useful information and very little noise, and the fourth vector has considerable signal from atmospheric moisture. The remaining 2 vectors appear to be essentially heteroscedastic noise. The first vector shows a very broad band corresponding to the background spectrum.

In Figure 3.10, the first 8 right singular vectors from consolidated data set 4 show quite good signal-to-noise ratios. It is clear that since the MCT series have superior signal-to-noise ratio, this will carry over to the SVD analysis also. The 18th vector is essentially white noise.

3.5.1.3 Spectral Reconstruction Using BTEM

The right singular vectors from the DTGS data were subjected to BTEM analysis. The first 4 vectors from Figure 3.7 and the first 8 vectors from Figure 3.8

were used. The results are shown in Figure 3.11.

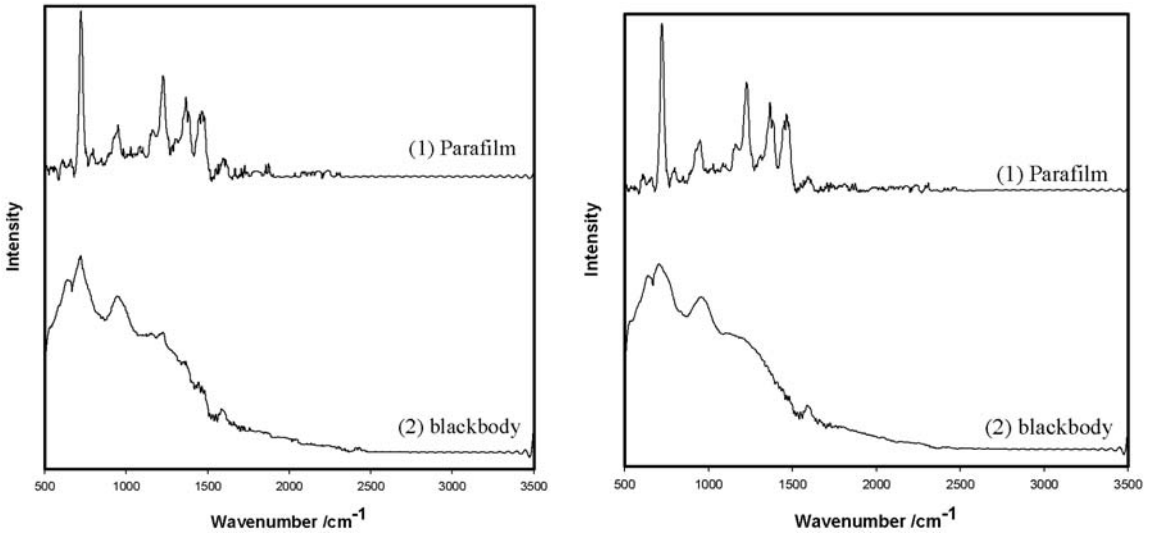

Figure 3.11. Emittance patterns reconstructed using BTEM for (a) consolidated data set 1 and (b) consolidated data set 2.

In both cases, 2 spectral patterns could be reconstructed. These were the blackbody emission and the parafilm emission. The blackbody emission spectrum has essentially all signals from the parafilm removed, but the signals from moisture and CO_2 still embedded. The parafilm emission spectrum seems to be free of most other signals. Comparison of Figures 3.11 (a) and (b) indicates that a slight improvement in spectral quality was obtained by using 8 right singular vectors where the blackbody type references were included in the raw data set.

In the same manner the right singular vectors from the MCT data were subjected to BTEM analysis. The first 4 vectors from Figure 3.9 and the first 8 vectors from Figure 3.10 were used. The results are shown in Figure 3.12.

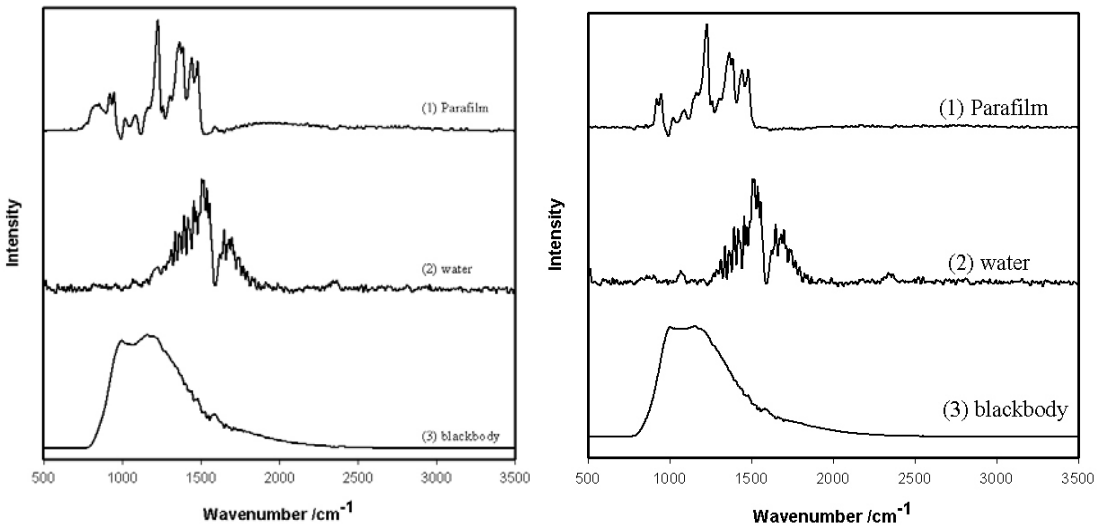

Figure 3.12. Emittance patterns reconstructed using BTEM for (a) consolidated data set 3 and (b) consolidated data set 4.

In both cases, 3 spectral patterns could be recovered. These were the blackbody emission, the moisture absorbance and the parafilm emission. The blackbody emission spectrum has essentially all signals from both CO_2 absorbance and the parafilm removed, and only a minimum amount of signal from moisture is seen. The "moisture" absorbance spectrum has only a slight amount of residual CO_2 signal still embedded. The parafilm emission spectrum seems to be free of most other signals. It is important to note that the spectral reconstruction of the parafilm for both DTGS and MCT data are consistent, since the features in the region 1000-1500 cm^{-1} are very similar (data below 750 cm^{-1} for the MCT data are not very accessible due to the optical cutoff). The signal-to-noise of the MCT data analysis is significantly better compared to the DTGS results as evidenced particularly by the reconstructed parafilm spectrum.

3.5.1.4 Comparison of Emission and Absorbance Spectra

For the purpose of comparison, the absorbance spectrum of parafilm was also measured. The parafilm absorbance spectrum is shown in Figure 3.13.

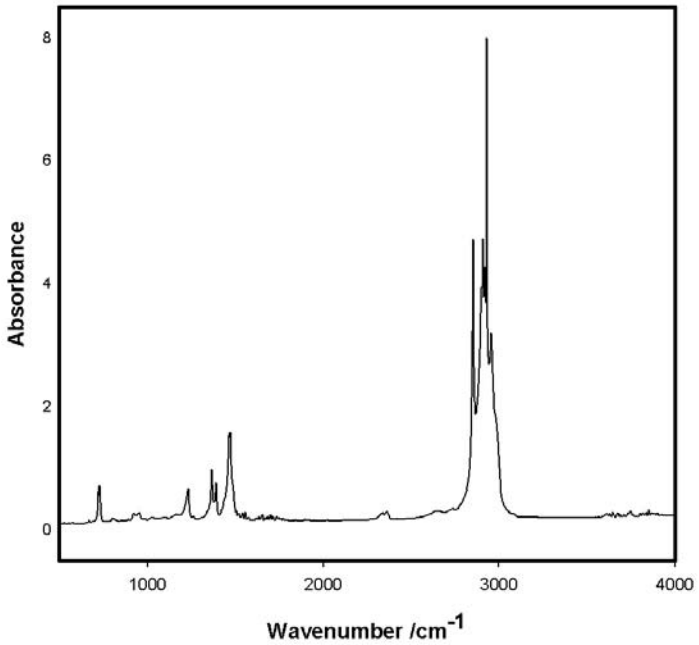

Figure 3.13. The absorbance spectra of parafilm.

Comparison of this absorbance spectrum with the emission spectra obtained from BTEM analysis shows that the prominent bands (or sets of bands) in the low wavenumber region are all present, namely 950, 1230, 1450 etc cm^{-1}. Due to the physics of the thermal emission process versus the thermal absorption process, the relative ratios of these bands differ somewhat and the apparent bandwidths are different.

3.5.2 Pure Liquid Films: Isopropanol

3.5.2.1 Experimental Data Sets

The experimental data set for the isopropanol series included the ZnSe

window, the empty cell and isopropanol, all measured at 5 different temperatures with both the DTGS and MCT detectors. The experimental spectra are shown in Figure 3.14 and Figure 3.15, respectively.

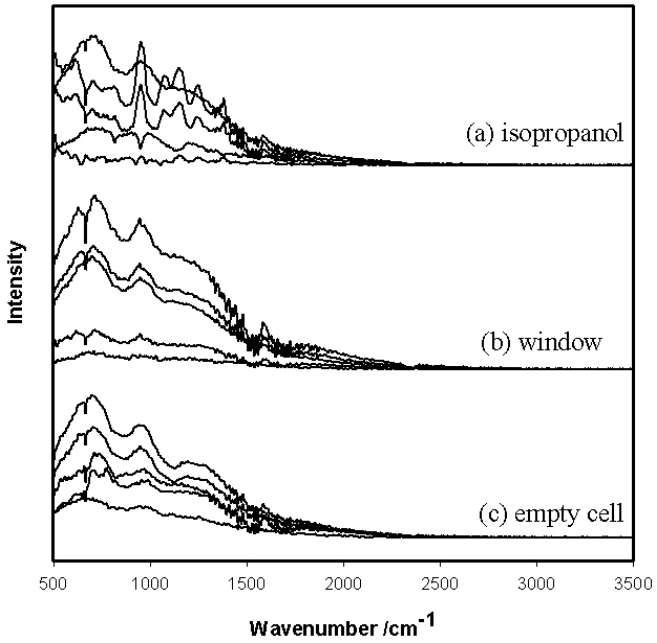

Figure 3.14. The emission spectra of (a) isopropanol; (b) the window; (c) the empty cell taken at five temperatures (338, 328, 318, 308, 298 K) using DTGS detector.

The DTGS data in Figure 3.14 show significant radiant emission down to 500 cm^{-1}. The absorbance of the radiant energy by atmospheric moisture can be seen in all emission spectra as a series of bands at circa 1400-1800 cm^{-1} and the absorbance of the radiant energy by atmospheric carbon dioxide can be seen by the band at 670 cm^{-1}. The series of spectra of the window and the empty cell show similar generic characteristics. In addition the emission intensity of these two series is quite similar at a given temperature. The series of isopropanol emission spectra show all the above mentioned characteristics, and in addition this series shows the structured emission of

isopropanol, as seen by the maxima at circa 820, 950, 1150,1380, etc. cm^{-1}. Also, interesting to note are the inverted bands at 298K and 308K which seem to be caused by the self-absorbance of isopropanol.

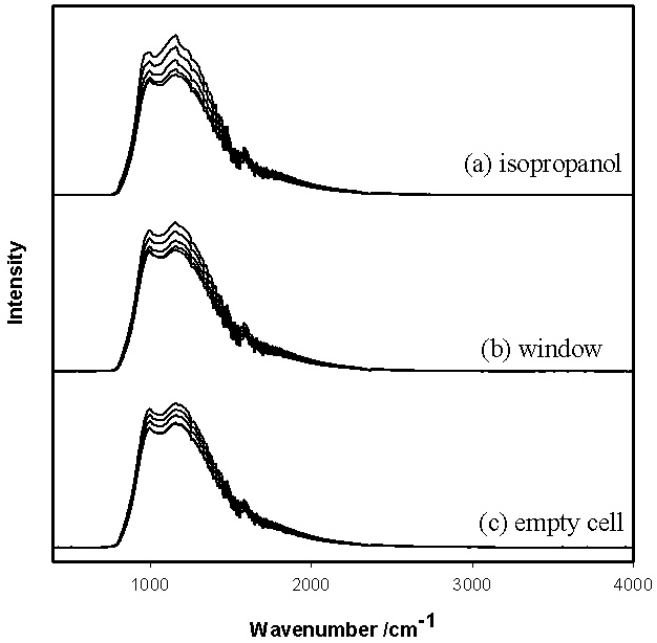

Figure 3.15. The emission spectra of (a) isopropanol; (b) the window; (c) the empty cell taken at five temperatures (338, 328, 318, 308, 298 K) using MCT detector.

The MCT data in Figure 3.15 show significant radiant emission down to 750 cm^{-1}. All the emission spectra have a significantly high signal intensity (in contrast to the DTGS data) as evidenced by the relatively smooth quality of the spectra. Again, the absorbance of the radiant energy by atmospheric moisture can be seen in all emission spectra as a series of bands at circa 1400-1800 cm^{-1}. Due to the MCT cut-off, the absorbance band at 670 cm^{-1} is not observed. However, due to the high signal intensity, the small absorbance due to atmospheric CO_2 can now be seen at circa 2300-2400 cm^{-1}. The series of window and empty cell emission spectra show similar

generic characteristics. Finally, the series of isopropanol emission spectra show all the above mentioned characteristics, and in addition this series shows the structured emission of the liquid. However, the blackbody effect is the major component of the experimental spectra and overwhelms much of the emission of the liquid.

3.5.2.2 Signal Processing and SVD

The series of DTGS emission spectra was processed in the same way as the parafilm series. In the first case, only the sub-set of 5 isopropanol emission spectra was subjected to singular value decomposition. In the second case the entire set of 15 emission spectra (window, the empty cell and isopropanol) was subjected to singular value decomposition. The results for consolidated data set 5 and 6 are shown in Figures 3.16 and 3.17.

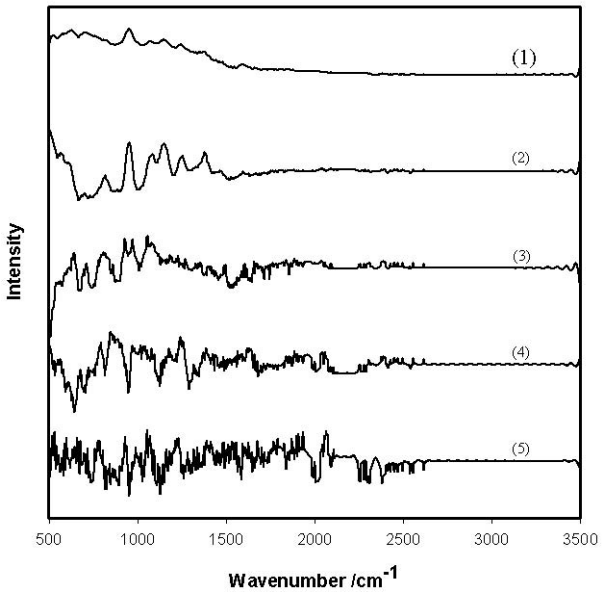

Figure 3.16. First five right singular vectors of V^T Matrix for consolidated data set 5.

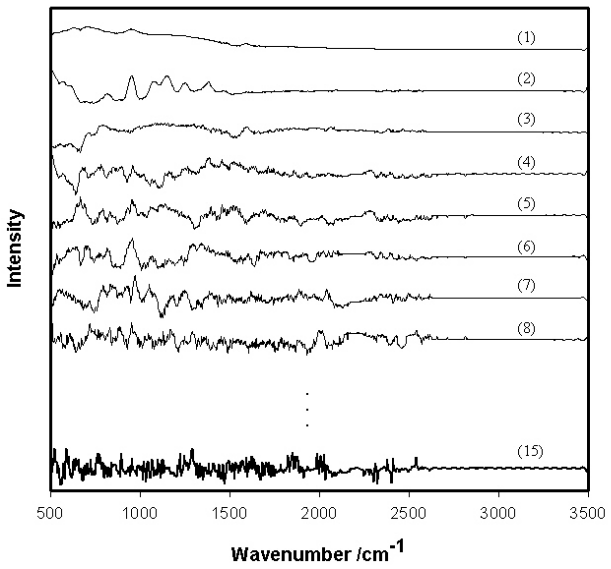

Figure 3.17. First eight and fifteenth right singular vectors of V^T Matrix for consolidated data set 6.

In Figure 3.16, the first 2 vectors show the main spectral features associated with the sample and Planck blackbody function. Vectors 3 and 4 appear to be relatively noisy but have many characteristics bands from isopropanol, the moisture and the CO_2. Finally, the fifth vector is predominantly noise and has a little contribution from CO_2 at 2300-2500 cm^{-1}. Since the first 4 right singular vectors all have discernable spectral features with physical meaning these 4 right singular vectors were used for BTEM analysis.

In Figure 3.17 more right singular vectors from the DTGS data show good signal-to-noise ratios due to large data size. Indeed, the first 2 vectors have quite good signal-to-noise ratios. In addition, the next five vectors clearly have some useful and embedded physical signals. The eighth vector appears to be predominantly noise but also has a clear contribution from CO_2 at 2300-2400 cm^{-1}. The remaining right singular vectors were essentially noise as indicated by vector 15. There is a

considerable difference in the noise level between the low wavenumber and high wavenumber regions.

For the series of MCT emission spectra SVD was performed on consolidated data set 7 and 8. The results are shown in Figure 3.18 and 3.19, respectively.

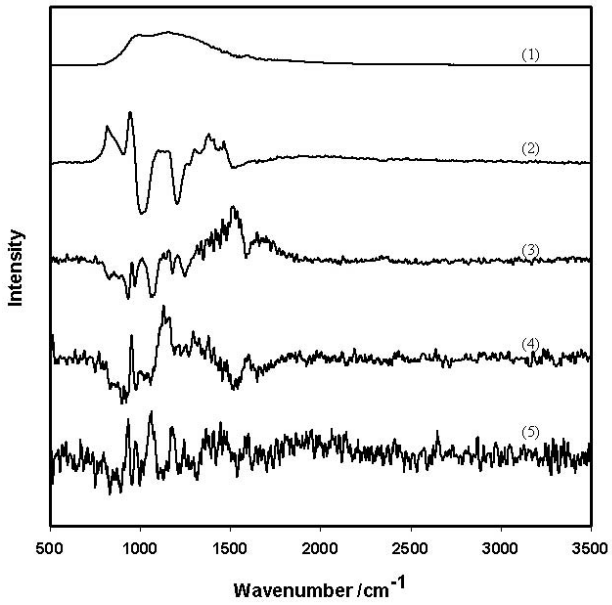

Figure 3.18. First five right singular vectors of V^T Matrix for consolidated data set 7.

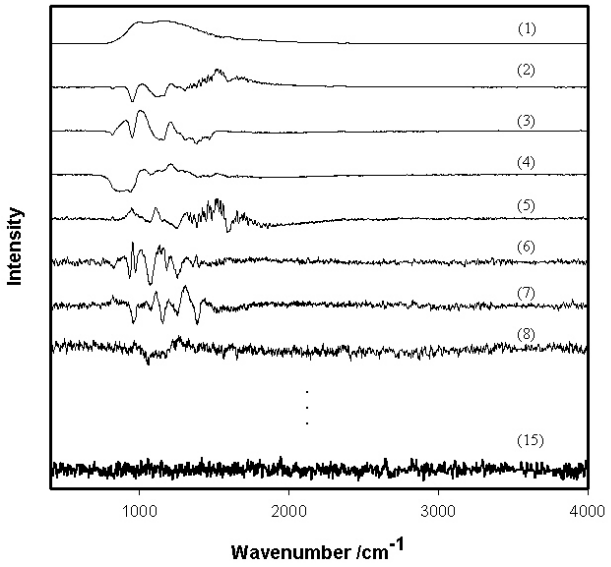

Figure 3.19. First eight and fifteenth right singular vectors of V^T Matrix for consolidated data set 8.

Most physically meaningful spectral features are localized in the first 4 right singular vectors from Figure 3.18. The first 2 vectors are very smooth and have a lot of useful information. The third and fourth vector has considerable signal from atmospheric moisture plus some noise. Finally, the fifth vector appears to have a very poor signal-to-noise ratio.

In Figure 3.19 the right singular vectors from consolidated data set 8 generally show better signal-to-noise ratios than those from consolidated data set 7 and more right singular vectors from consolidated data set 8 show good signal-to-noise ratios. The first five vectors have major essential spectral features. The sixth and seventh vectors also have a clear physical meaning plus more noticeable noise. The eighth vector is predominantly noise with few spectral features. The 15^{th} vector can be considered as essentially white noise. The first eight right singular vectors were used to reconstruct the pure component emission spectra with BTEM analysis.

3.5.2.3 Spectral Reconstruction using BTEM

The right singular vectors from the DTGS data were subjected to BTEM analysis. The first 4 vectors from Figure 3.16 and the first 8 vectors from Figure 3.17 were used. The estimated pure components spectra for consolidated data set 5 and 6 are shown in Figure 3.20. Two spectral patterns, background emission spectrum and isopropanol emission spectrum, are reconstructed for both cases. However, a weak signal from moisture and CO_2 still remains in both the background emission and the isopropanol emission spectra.

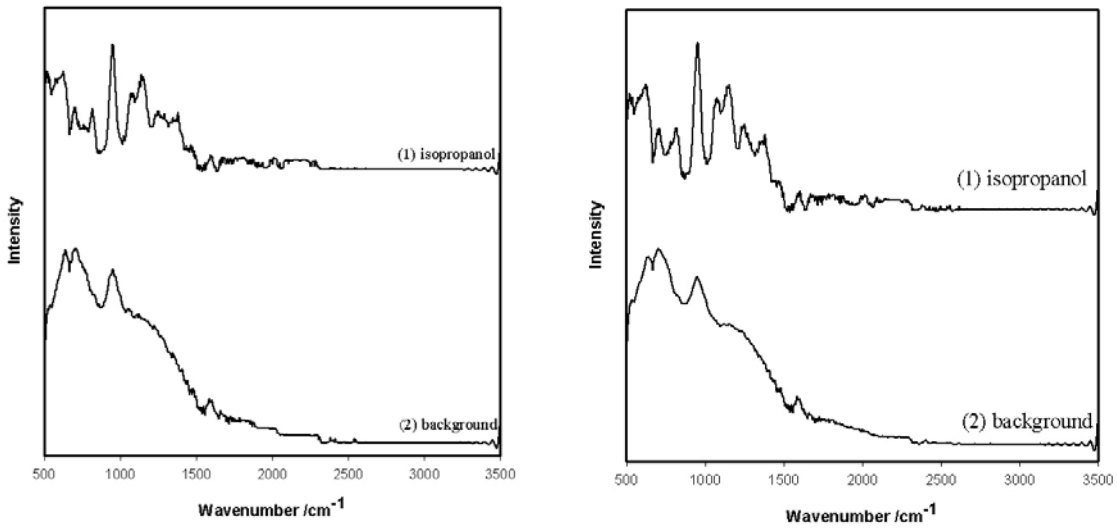

Figure 3.20. Emittance patterns reconstructed using BTEM for (a) consolidated data set 5 and (b) consolidated data set 6.

The right singular vectors from the MCT data were similarly subjected to BTEM analysis. The first 4 vectors from Figure 3.18 and the first 8 vectors from Figure 3.19 were used. The results of consolidated data set 7 and 8 are shown in Figure 3.21.

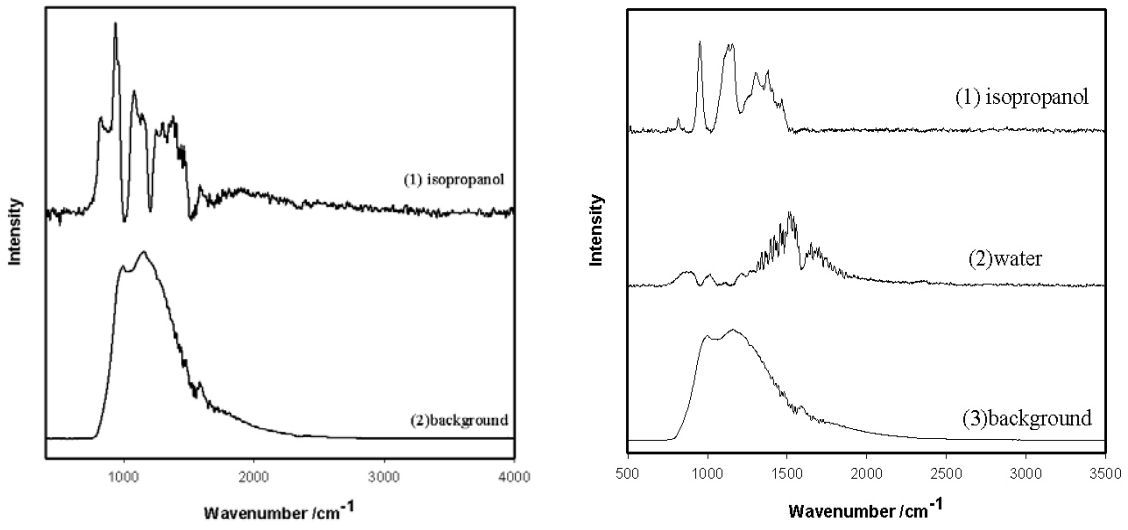

Figure 3.21. Emittance patterns reconstructed using BTEM for (a) consolidated data set 7 and (b) consolidated data set 8.

In the first case, two spectral patterns could be recovered; background emission and isopropanol emission. A weak signal from moisture and CO_2 can still be seen in both spectra as in the previous DTGS spectra. In the second case, 3 spectral patterns could be recovered; the background emission, the moisture and isopropanol emission. The background spectrum has essentially all signals from both CO_2 and isopropanol removed, but some noticeable signal from moisture is seen. The moisture absorbance spectrum has some residual signal from the background and isopropanol as evidenced by the features at circa 700-1200 cm^{-1}. It is clear by comparison of Figures 3.21 (a) and (b) that the isopropanol emission spectrum is improved significantly when 8 instead of 4 right singular vectors are used in the BTEM analysis. The emission bands become better resolved, i.e. the signals at 820cm^{-1} and 950 cm^{-1}, and the signal-to-noise is much better.

3.5.2.4 Comparison of Emission and Absorbance Spectra

Comparison of the isopropanol absorbance spectrum (see Figure 3.22) with the emission spectrum obtained from BTEM analysis shows that the prominent bands (or sets of bands) in the low wavenumber region are all present, namely 820, 950, 1150, 1380 etc cm^{-1}. Due to the physics of the thermal emission process versus the thermal absorption process, the relative ratios of these bands differ somewhat and the apparent bandwidths are different.

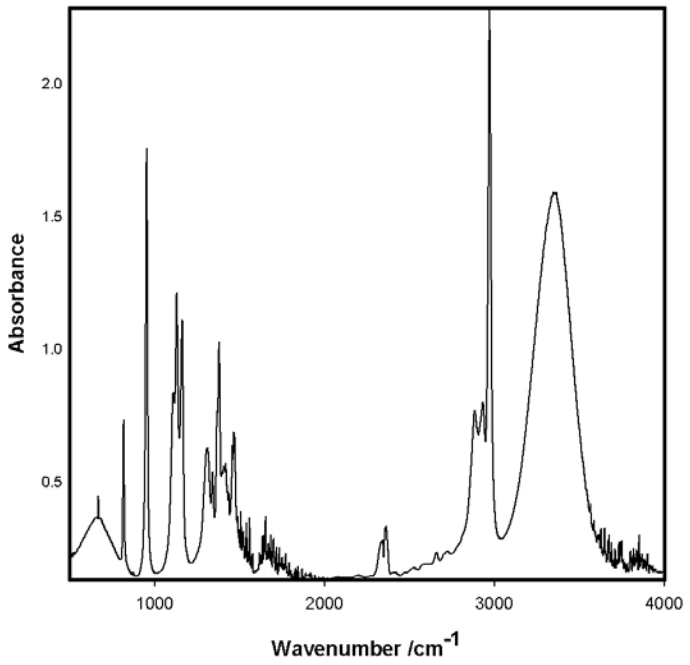

Figure 3.22. The absorbance spectra of isopropanol.

3.5.3 Large Blackbody Radiation: *Issue of Spectral Non-Linearities*

3.5.3.1 Blackbody Radiation

The laws of thermal radiation concerning the emission of a blackbody play a fundamental role in infrared emission spectroscopy. These laws define the conditions for any object to emit radiation spontaneously. An object that absorbs all the radiation that is directed to it is called a blackbody. Theoretically, the absorbance of the blackbody at all frequencies should be unity.

In 1900, Planck found the correct expression for the thermal radiation of a blackbody known as the Planck function which has integrated in itself all radiation laws established earlier. There are two forms of the analytical expression of this function, namely the wavenumber $\tilde{\nu}$ representation and wavelength, λ, representation as indicated in Eqs. 3.20 and 3.22:

$$H_{\tilde{\nu}}(T) = \frac{2hc^2\tilde{\nu}^3}{e^{\frac{hc\tilde{\nu}}{KT}} - 1} \tag{3.20}$$

$$H_{\lambda}(T) = \frac{2hc^2}{\lambda^5(e^{\frac{hc}{\lambda kT}} - 1)} \tag{3.21}$$

It should be noted that the two forms are consistent when integrated over the whole spectrum. However, caution is needed when comparing the measured blackbody emission spectra with the theoretical blackbody spectra as both representations yield curves of substantially different shapes. Modern Fourier transform spectrometers produce spectra with constant resolution in the wavenumber scale that are consistent with the above described wavenumber $\tilde{\nu}$ representation of Planck function.

Figure 3.23 shows the theoretical blackbody radiation curves in the wavenumber representation for temperature ranging from 273.15 K to 383.15 K in 10 K increments. A simple MATLAB Function is used to generate the following curves.

Figure 3.23 shows (1) the intensity of the curves at any wavenumber increases as temperature increases, and (2) the curve maximum shifts towards higher wavenumber as the temperature increases. It is noted that the emission spectra are highly depended on the temperature as well as on the wavenumber. In most cases, the measurements of emission from samples is made rather complex, due to the need of various reference measurements. The newly developed emission BTEM can easily handle this problem: it can retrieve pure component emission spectra with only the

single-beam emission spectra as demonstrated as subsection 3.5.1 and 3.5.2. More discussions on this issue will be presented below.

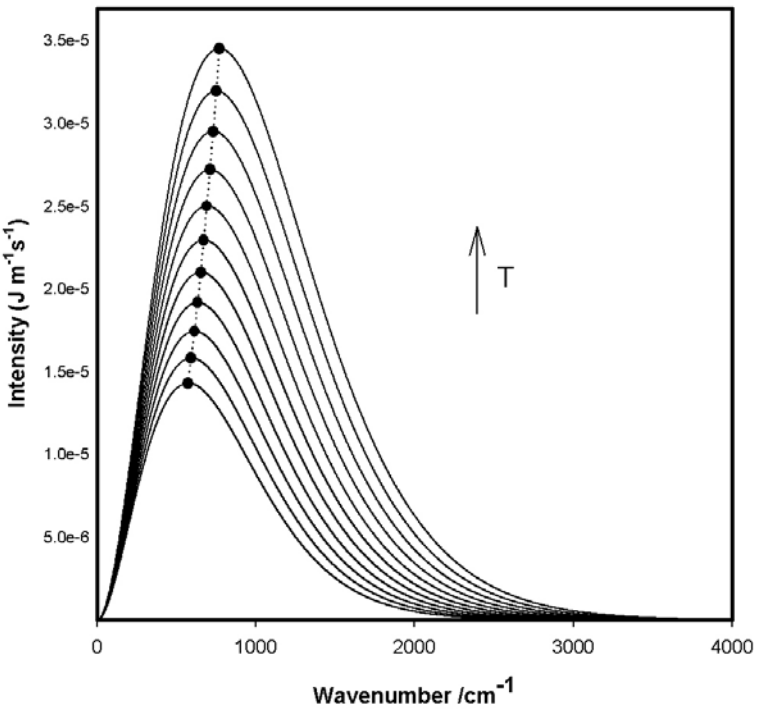

Figures 3.23 Theoretical blackbody radiation curves in the wavenumber representation for temperature ranging from 273.15 K to 383.15 K in 10 K increments.

3.5.3.2 Spectral Non-linearity

In this study six different temperatures were used for the parafilm samples, namely, 298, 308, 318, 328, 338, and 348 K. The corresponding Planck function maxima occur at circa 585, 605, 625, 644, 664, and 683 cm^{-1}. In other words, there is an extreme non-stationary quality to the background radiation. In addition, at these different temperatures, the emittance $E(\tilde{\nu})$ will also change for each component – some bands will decrease in relative intensity and some will increase. In other words, at each different temperature the "pure component emittance" will be significantly different. Indeed, it is well known that the luminance of a sample is proportional to

the luminance of the blackbody at the same temperature and hence a function of both wavenumber and temperature. Taken together, there are at least two signals which are highly non-stationary and hence two significant contributions to non-linear spectral effects in emission spectroscopy.

In order to show the effect of the non-stationary quality of the blackbody radiation, the blackbody spectra obtained with an MCT detector and shown in Figure 3.6 were used. A singular value decomposition was performed on these 6 emission spectra alone. The results are shown in Figure 3.24.

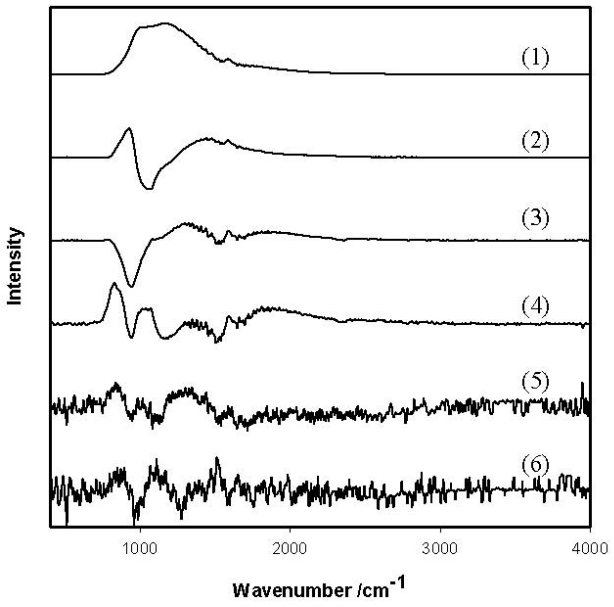

Figure 3.24. First six right singular vectors of V^T Matrix for consolidated data set of blackbody emission spectra.

As seen in Figure 3.24, at least 4 very significant right singular vectors are observed that have good to outstanding signal-to-noise. This means that at least 4 basis functions are needed to represent the signal from this “one component” system over the interval of temperatures used and hence a set of observations. In particular,

the second vector is a sigmoid band, the typical signature of a shifting signal.

3.6 Results and Discussion: *Liquid-Phase Organic Reaction*

A cyclo-addition reaction in the liquid phase is studied by IRES in this study. The reaction between cyclopentadiene (CP) and dimethyl acetylenedicarboxylate (DMAD) to generate the product* is:

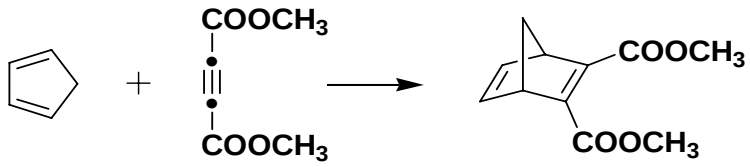

The experimental data by IRES, the deconvoluted pure component spectra by BTEM and first approximations of the concentration profiles will be discussed in the following subsections.

3.6.1 Experimental Data

Two semi-batch experiments were performed in the way mentioned in section 3.2 (see Table 3.1). A total of 55 emission spectra were obtained from the two semi-batch experiments and these are shown in Figure 3.25. The emission spectra from experiment 1 have a considerably better signal-to-noise ratio than those from experiment 2. However, the spectra from experiment 2 have higher overall signal intensity. The differences in the two data sets illustrate the sensitivity of emission experiments, particularly due to changes in film thickness, optical alignment etc.

* Name of product: dimethyl bicyclo[2.2.1]-2,5-heptadiene-2,3-dicarboxylate (DBHD)

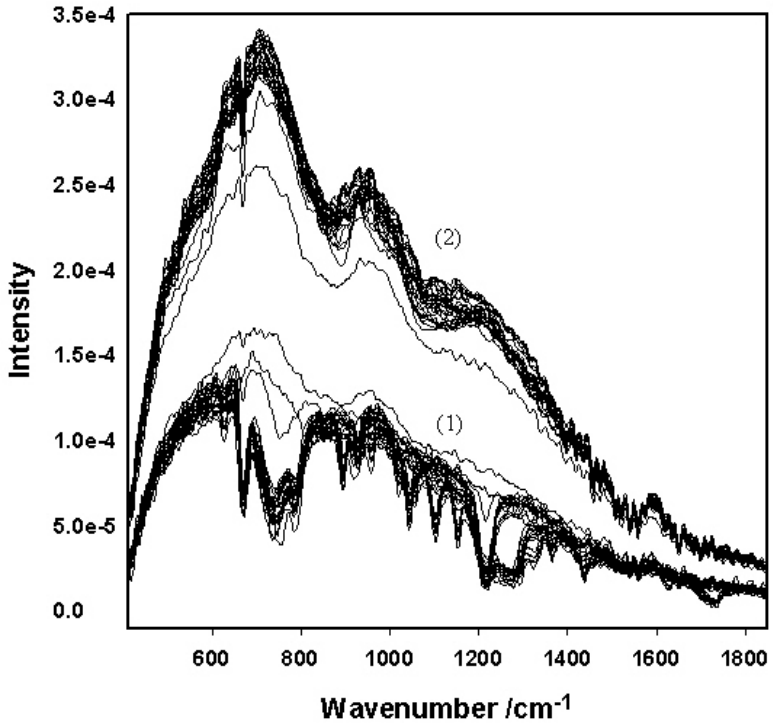

Figure 3.25 Emission spectra from two experiments: (1) experiment 1; (2) experiment 2 (see Table 3.1).

Figure 3.26 shows a sub-set of the data from experiment 1. Since the temperature of the reactive solution is just above room temperature and a room temperature detector is used, the spectra in Figure 3.26 show mixed emission-absorption phenomena. The first spectrum shows the emission of the cell which roughly resembles a smooth blackbody emission. All of the subsequent spectra show rather sharp signals due to the molecular vibrations of the species present. Thus spectra 2-8 correspond to various steps during the addition of solvent, reactants and then the emission of the reactive multi-component solution. The spectral range is limited to the region 450 cm^{-1} (instrumental cut-off) to circa 1900 cm^{-1} (where emission at 308K becomes more-or-less negligible).

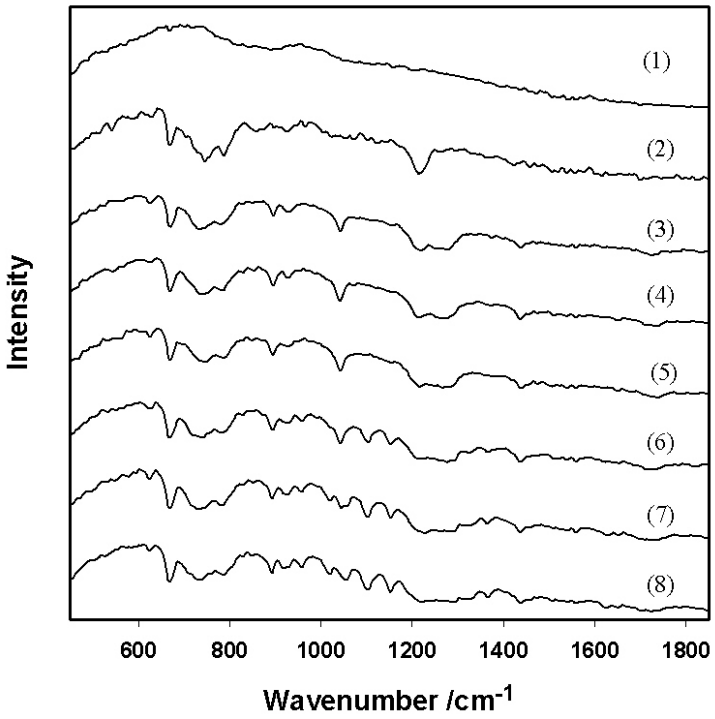

Figure 3.26. The emission spectra of (1) the empty cell; (2) chloroform; (3) ~ (5) DMAD in chloroform; (6) ~ (8) CP, DMAD and reaction in the solution.

Spectrum 2 shows bands centered at circa 670, 740, 925, 1215 etc cm^{-1}. These bands are consistent with chloroform's IR spectrum in the low wavenumber region. Spectra 3-5 show some significant new bands at circa 896, 1042, 1438, and 1726 cm^{-1} corresponding to the vibrations of DMAD. Spectra 6-8 where obtained after introduction of CP. These spectra show several new peaks appearing at 624, 960, 1020, 1102, 1152, 1366 etc. cm^{-1} indicating the presence of both CP and the organic product DBHD. Taken together, the spectra in Figure 3.26 clearly show that meaningful spectral changes can be observed during a liquid phase organic synthesis conducted in the vicinity of room temperature using an emission-type instrument configuration.

3.6.2 Singular Value Decomposition (SVD)

The two sets of experimental emission spectra involving a total of 55 emission spectra were first consolidated into a single matrix $E(\nu)$ which was then subjected to singular value decomposition. The first 6 right singular vectors as well as the 10^{th}, 20^{th}, 30^{th} and 55^{th} vectors are shown in Figure 3.27.

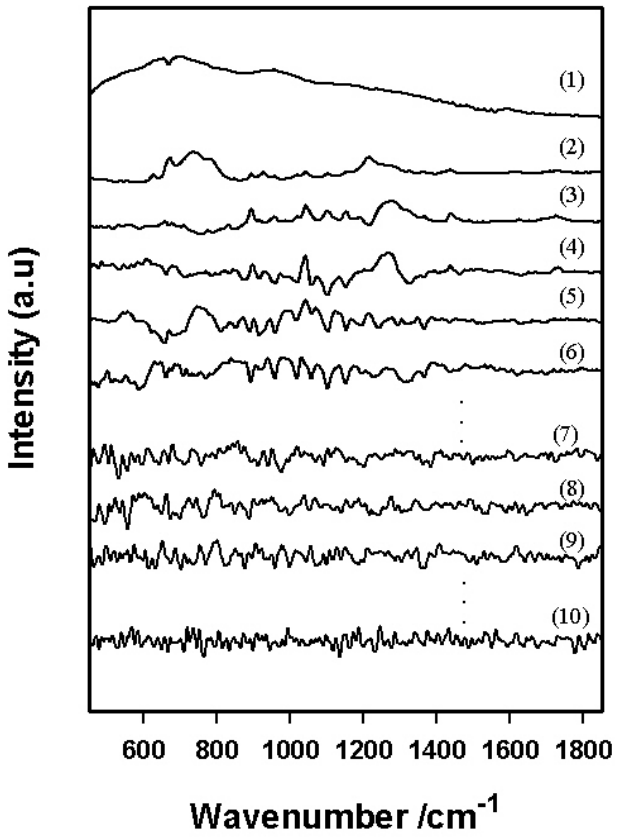

Figure 3.27. 10 right singular vectors of V^T Matrix for consolidated data set: (1)~(6) first six right singular vectors; (7) tenth right singular vector; (8) twentieth right singular vector; (9) thirtieth right singular vector; (10) fifty-fifth right singular vector.

The first 6 right singular vectors in Figure 3.27 show clearly meaningful signals corresponding to the background as well as the vibrations from the species present. These vectors have rather good signal-to-noise ratios. More specifically, it

can be observed that the 1st vector has signal due primarily from the blackbody background, the 2nd vector has a significant contribution from the solvent chloroform, the 3rd vector has a lot of spectral features from DMAD and the 4th-6th vectors also have considerable contributions from CP and the organic product. The 10th, 20th and 30th right singular vectors still show some molecular vibrations, however, there is a considerable contribution from noise. Finally the 55th vector is more-or-less white noise. Since localized and meaningful signals can still be seen in the first circa 30 right singular vectors, these will be used in the following analysis.

3.6.3 Spectral Reconstruction using BTEM

3.6.3.1 Spectral Reconstruction using BTEM – Full Spectral Range Analysis

The right singular vectors from the two emission experiments were subjected to BTEM analysis. The first 30 vectors of consolidated data set were employed. The results are shown in Figure 3.28.

Four estimated spectral patterns could be successfully reconstructed from the BTEM analysis. As shown in Figure 3.28 these spectral patterns resemble chloroform, DMAD, CP and the product. All of the estimated spectra have quite good signal-to-noise ratio. The first estimated spectrum having the major bands located at circa 672, 740, 928, 1215 etc cm^{-1} corresponds to the chloroform emittance, where the broad and intense signal at circa 740 cm^{-1} belongs to the C-Cl vibration. The second estimated spectrum having bands at circa 896, 1041, 1438, and 1727 cm^{-1} corresponds to the DMAD emittance, the signal at 1727 cm^{-1} belongs to the C=O group. The third

estimated spectrum having major bands at circa 656, 890, 912, 1090, 1366 etc cm^{-1} corresponds to the CP emittance, where the signal at 1366 cm^{-1} corresponds to the C-H bending mode. Finally, the fourth spectrum having major bands located at circa 1020, 1102, 1152, 1324, 1626 etc cm^{-1} corresponds to the product DBHD, where the signal at 1626 cm^{-1} belongs to the C=C groups and the signal at circa 1720 cm^{-1} belongs to the C=O group.

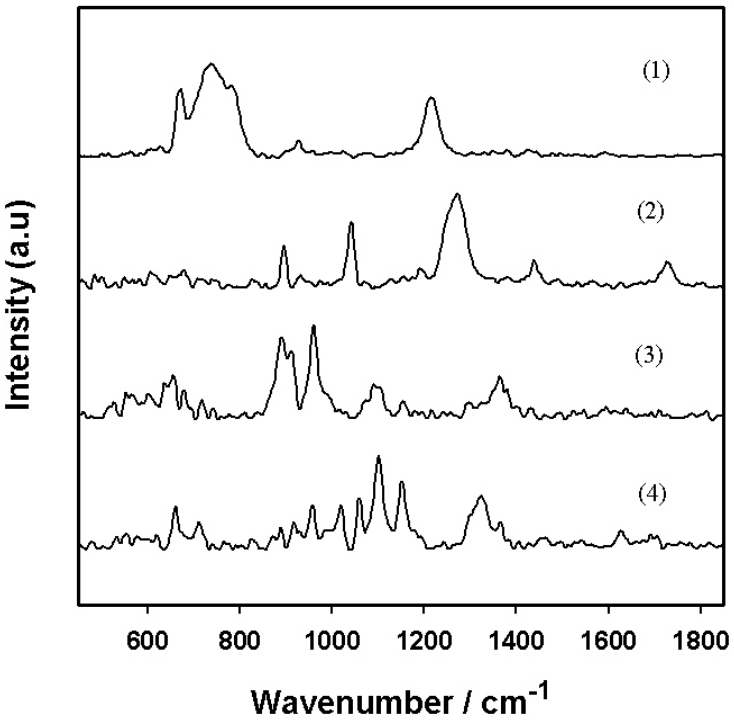

Figure 3.28. Full range emittance patterns reconstructed using BTEM: (1) Chloroform; (2) DMAD; (3) CP; (4) Product.

It should be noted that a similar analysis was performed with just the data from experiment 1 (the high signal-to-noise data set). This analysis did not provide spectral estimates as good as those obtained after the combination of both data sets. Indeed, different experimental designs and sequences of reagent additions were used in experiments 1 and 2 (resulting in different concentrations), and hence a greater

signal variance in the combined data sets. Consequently, more useful basis vectors and better spectral estimates were obtained.

3.6.3.2 Spectral Reconstruction using BTEM – Partial Spectral Range Analysis

The full range spectral reconstructions shown in Figure 3.28 resemble the four reagents present, but they could be better. For example, it is clear from Figure 3.28 that some reconstructions are sub-optimal and possess residual signal from other components. In particular, the organic product spectral estimate appears too complex in the C-C stretch region, and some of these vibrations coincide with vibrations from other reagents. It is known that spectral artifacts similar to those mentioned above can arise if there is too much noise in the experimental spectra. If a wide spectral range is used, then too much noise is incorporated into the spectral estimates, and the quality frequently deteriorates. Thus truncating the spectral range is often advantageous, since it reduces the accumulation of too much noise (and hence signal entropy) in the final estimates. Accordingly, BTEM was rerun for just the region 860-1200 cm^{-1}. In addition, the cycloaddition reaction was performed using FTIR transmission spectroscopy. The resulting absorbance spectra of this cycloaddition reaction were analyzed using BTEM and the estimated pure component spectrum of the reactants were recovered. Figure 3.29 compares the new estimated emission spectra with the estimated FTIR spectra in the region 860-1200 cm^{-1}.

The estimated spectra for each species from both IR emission and FTIR experiment are quite similar. The two major bands for DMAD at 896 and 1041 cm^{-1} present in the estimated FTIR spectra are present in the estimated emission spectra.

The three major bands for CP at 890, 960 and 1090 cm^{-1} present in the estimated FTIR spectra are present in the estimated emission spectra. Finally, the two major bands for the organic product at 1102 and 1152 cm^{-1} present in the estimated FTIR spectra are present in the estimated emission spectra. As expected, the estimated emission spectra show some line broadening. Relatively few artifacts are present in the estimated emission spectra obtained over a partial spectral range.

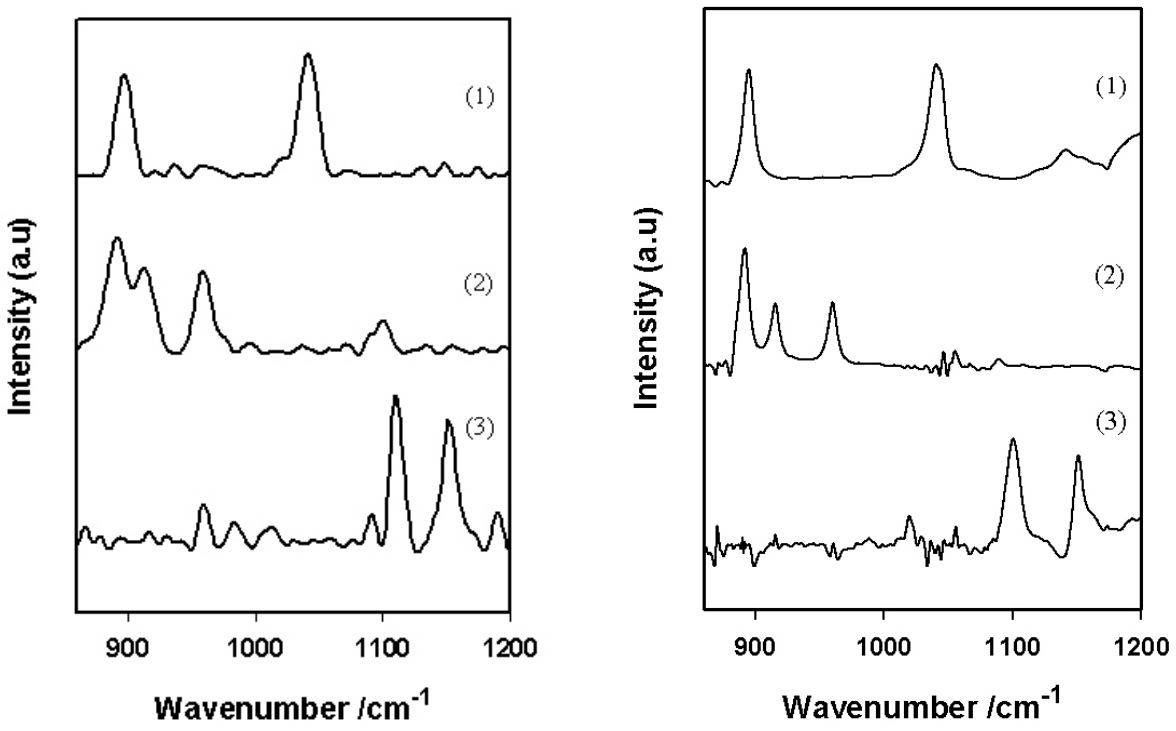

Figure 3.29. Comparison of (a) estimated emittance patterns via BTEM and (b) IR spectra: (1) DMAD; (2) CP; (3) Product.

3.6.4 Relative Concentrations of Reactants

The relative concentration profiles were calculated using the original experimental emission spectra and pure component spectral estimates of the partial range from 800-1200 cm^{-1}. This results in an estimate of the relative concentration

profiles of the reactants as shown in Figure 3.30. The addition of the DMAD and CP can clearly be seen at spectra 15 and 22 respectively in experiment 1. Furthermore, the decline in DMAD and the increase of DBHD due to reaction can also clearly be seen. The fluctuations in the relative concentration profiles are somewhat large due to high noise level in the present emission spectra. The experimental data from experiment 2 was also analyzed. However, since the signal-to-noise level was very low, the concentration profiles show considerable scatter.

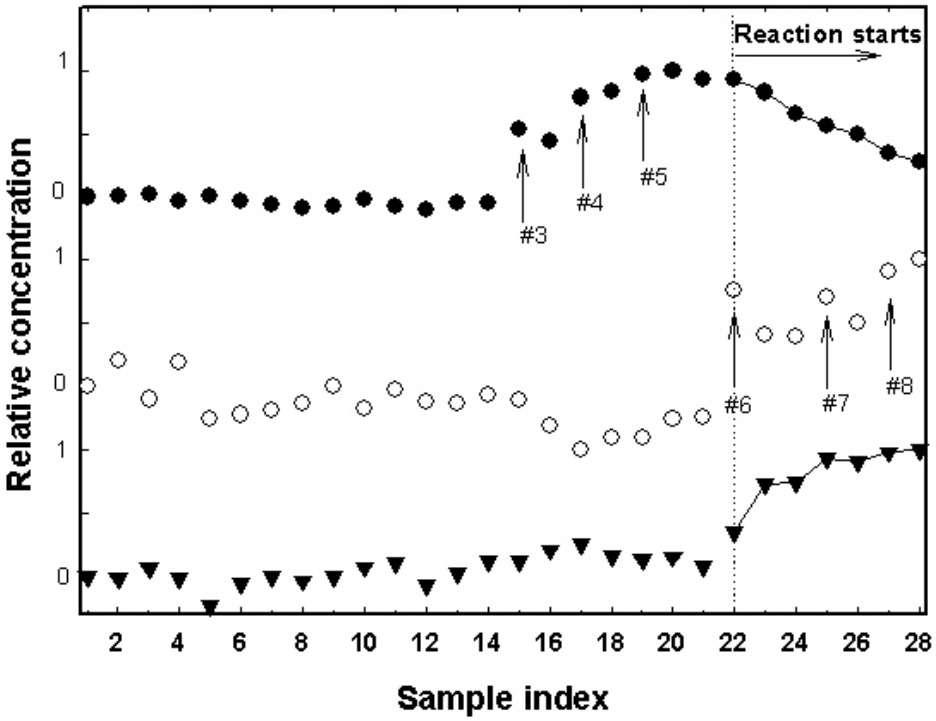

Figure 3.30. The concentration profiles of DMAD (●), CP (○), and product (▼) from Experiment 1. Perturbation numbers #3~#8 correspond to the experimental designs provided in Table 3.1.

3.7 Summary

3.7.1 The Present Results and Conclusions

(1) The IR emission spectra of both parafilm and isopropanol were

successfully recovered using the BTEM algorithm and a conventional FT-IR spectrometer. All the measurements were made without any purging of the equipment and in a small temperature interval. For both DTGS and MCT detectors, the reconstructed emission signals were in good agreement with those of corresponding IR absorbance spectra.

(2) A liquid phase cyclo-addition reaction, performed in the vicinity of ambient temperature, was successfully measured by infrared emission spectroscopy using a room temperature DTGS detector. Multiple perturbation experiments were performed in order to obtain data necessary for multivariate calibration. The BTEM algorithm was successfully applied to the data to recover the pure component emission spectra of the solvent, the organic reactants DMAD and CP, and the organic product DBHD. These recovered emission spectra were consistent with those of independent FTIR absorbance spectra. Furthermore, least squares analysis using these BTEM spectral estimates provided first approximations to the relative concentration profiles of the species during the course of the reaction.

In summary, the present chapter confirms the applicability of BTEM to emission spectroscopy, and as an efficient approach to eliminate the effects of large background radiation. In addition, this contribution appears to be the first time that a liquid-phase reaction has been studied by the combination of infrared emission spectroscopy and BTEM.

3.7.2 Implications for Future Applications

The present work indicates the possibility of studying simple solid and liquid

film samples as well as organic reactive systems by means of IRES techniques. This contribution could provide some new opportunities for various applications to organic syntheses. For example, it is well-known that many heterogeneous catalysts and many organic solvents have very strongly absorbing spectral regions in infrared transmission spectroscopy and diffuse reflectance, where nearly all the signal is absorbed, and hence these spectroscopies can not frequently be used for good qualitative and quantitative analysis. However, IR emission measurements does not have this type of signal throughput problem (the signal is from emission, not absorption), so that the whole spectra range can be utilized. In addition, it is common that complex organic syntheses are multi-phase which may have solids or bubbles in the liquid phase and hence the entire system is not good enough for transmission spectroscopy and attenuated total reflectance (ATR) spectroscopy. Again, it appears that IRES might provide various advantages in such situations.

Chapter 4

The Application of BTEM to UV-VIS and UV-VIS CD Spectroscopies: The Reaction of $Rh_4(CO)_{12}$ with Chiral and Achiral Ligands

The current chapter will focus on the application of BTEM to ultraviolet-visible (UV-Vis) absorbance spectroscopy and electric circular dichroism (ECD) spectroscopy. Although BTEM has been widely used for FTIR and Raman spectroscopy it has rarely been applied to UV type spectroscopy. In particular this is the first time that BTEM has been applied to ECD spectroscopy, a kind of chiroptical spectroscopy, for a reaction system. Two different organometallic ligand substitution reactions were investigated: (1) $Rh_4(CO)_{12}$ with an achiral ligand, PPh_3 and (2) $Rh_4(CO)_{12}$ with a chiral ligand, (S)-BINAP .

4.1 UV-Vis Absorbance and Electric Circular Dichroism Spectroscopy

4.1.1 Introduction

UV-Vis spectroscopy detects the electronic transitions of molecules as they absorb light in the UV and visible regions of the electromagnetic spectrum. The ultraviolet (UV) region is normally from 200 to 400 nm, and the visible portion is from 400 to 800 nm. Ultraviolet radiation having wavelengths less than 200 nm is difficult to handle, and is seldom used as a routine tool for structural analysis. The absorption spectroscopy carried out in the current region (200 to 800 nm) is sometimes called "electronic spectroscopy" because the energies within the region are sufficient to excite a molecular electron to a

higher energy orbital. The electronic transitions of UV or visible radiation are usually involving transitions between π, σ, and *n* orbitals. Species with conjugated double bonds will absorb UV light and species with color absorb visible light, which makes UV-Vis spectroscopy applicable to a wide range of samples.

The first commercial UV-Vis spectrophotometer, the Beckman DU UV-Vis spectrophotometer was introduced in 1941 (Cary and Beckman, 1941) and was used to determine the presence of vitamins in food. Although modern UV-Vis instruments are quite different than when the DU was introduced, UV-Vis spectroscopy is a useful technique in modern biochemistry, biology, and pharmaceutical research. In addition, the traditional role of UV-Vis spectroscopy is that of quantitative analysis of solutions of transition metal ions and highly conjugated organic compounds which often have different colors.

Electric circular dichroism (ECD) has the same origin as UV-Vis spectroscopy i.e. the process in which a molecule is prompted from its electronic ground state to an electronically excited state. Inherently asymmetric chromophores (some chiral molecules) will interact differently with left and right circularly polarized light. CD can be observed for a chiral molecule if the left and right circularly polarized light is absorbed to different extents at certain wavelengths. Consequently, CD spectra can take on either a positive or a negative signal while UV spectra are restricted to be non-negative although both UV and CD spectra are absorptive.

Circular dichroism (CD) spectroscopy is a valuable tool to detect and quantify the chirality of molecular structures (asymmetric chromophores) such as chiral organometallic complexes, particularly complexes of biological and medical importance.

It is also an ideal optical technique to provide information about the secondary and tertiary structures of proteins as well as the macromolecule conformation of nucleic acids (Greenfield and Fasman, 1969; Waterhous and Johnson, 1994; Venyaminov and Vassilenko, 1994；Sreerama *et al.*, 2001). [Chapter 6 contains the introduction to various chiroptical spectroscopic techniques of CD, VCD and ROA.]

4.1.2 Merits of UV-Vis and CD Absorption for Quantitative Work

X-ray crystallography, NMR and FT-IR spectroscopy are well-known analytic techniques which are available for studying the structure of organic molecules. In the current section, some advantages of UV and CD spectroscopy compared to these techniques will be addressed briefly.

X-ray crystallography can provide us with much valuable structure information but it requires a suitable crystal for study, consequently, only the conformation of the molecule in the crystal can be learned. In contrast, UV and CD are excellent for measuring solutions.

With regard to NMR, it typically requires high solute concentrations, on the order of many milligrams per ml. UV and CD, however, have high sensitivity and the detection limitation can be lower than ppm level in optimal cases. Consequently, UV and CD absorbance of dilute solutes is much easier to detect than NMR.

FTIR analysis can frequently be performed at much lower concentrations than NMR or even in situ during catalytic reactions (in the ppm range). Since the molar absorptivities of chromophores in the UV-Vis are typically orders of magnitude greater than fundamental vibrations in the IR, UV-Vis has the potential for characterizing chromophore-containing organometallics at much lower concentrations. Similarly, since

the phenomenon of ECD is normally many orders of magnitude greater than either vibrational circular dichroism (VCD) or Raman Optical Activity (ROA), ECD holds the potential for detecting chiral organometallics possessing chromophores at very low concentrations. In addition, UV and CD are also used in following reactions because the timescale is very fast and the sensitivity is very high. Compared to the spectra recorded in the IR region, however, UV-Vis absorption spectra in solution tend to be broad and without well-defined fine structure. Consequently, UV-Vis is seldom thought of as a detailed structural information technique.

In summary, both UV and CD are highly sensitive probes of chromophore containing solutions and are good quantitative methods to determine concentrations of an absorbing species in dilute solution.

4.1.3 Chemometric Methods for UV and CD Data Analysis

Many techniques have been proposed for UV/UV-CD spectroscopic data analysis of multi-component solutions in order to reconstruct the pure component spectra. Basically, the main idea of these methods is to first determine the basis vectors associated with the observed UV/UV-CD spectroscopic data. The most generally used decomposition techniques include principal component analysis (PCA) (Lawton and Sylvester,1971), singular value decomposition (SVD) (Konno, 1988; McPhie and Shrager, 1992; Sreerama and Woody, 1994; McMullen *et al.*, 1967) and non-linear iterative partial least-squares (NIPALS) (Antonov *et al.*, 1999). These basis vectors are then transformed to give the spectral estimates of the pure components in the mixture. Examples include; (1) a self-modelling curve resolution (SMCR) technique based on principal component analysis (PCA) and non-negativity constraints to resolve a two-component mixture

system measured using UV-Vis spectroscopy introduced by Lawton and Sylvestere . (2) A computer-assisted target factor analysis (CAT) algorithm, where SVD was applied to the abstract factor analysis and SIMPLISMA (simple-to-use interactive self-modelling mixture analysis) was applied to optimize UV-Vis spectral estimates of the components (Meinrath and Lis, 2001). (3) A singular value decomposition analysis was applied to a large set of UV-CD spectra measured from a metalloprotein (Konno, 1988).

Although, other SMCR methods have been proposed and implemented, some serious problems remain for spectral resolution of UV-Vis data. In particular, UV-Vis spectra are normally very broad with few distinct features. Moreover, there is often a very high degree of spectral overlap between the spectra of different species. In addition, prior information of some sort is often needed for spectral reconstruction, i.e. an estimate of the number of species present and / or an estimate of the concentrations of the species present. In conclusion, the literature clearly shows that the blind deconvolution of UV-Vis data has been an often investigated problem, *but only little progress has been made*.

In this chapter BTEM/Chiral-BTEM is applied to UV-Vis data from two ligand substitution reactions ($Rh_4(CO)_{12}$ reacts with triphenyl phoshine (PPh_3) and $Rh_4(CO)_{12}$ with (S)-BINAP) in order to reconstruct the pure component spectra. Chiral-BTEM is also applied to the CD data of a chiral ligand substitution reaction ($Rh_4(CO)_{12}$ with (S)-BINAP) to reconstruct the chiral component spectra. Although BTEM has been successfully applied to many spectroscopic data sets with non-negative localized signals, i.e. FTIR, Raman, NMR, this is the first time it has been applied to broad UV-Vis data. In addition, this is the first application of Chiral-BTEM to UV-CD spectra which possess both positive and negative parts.

4.2. Computational Section

4.2.1 Bilinear Model

Both multi-component UV-Vis and UV-Vis CD measurements obey the Bouguer-Lamber-Beer law in the low concentration range. Consequently, they can be modeled as follows:

$$A_{k\times\tilde{\nu}} = l_{k\times k} C_{k\times s} a_{s\times\tilde{\nu}} + e_{k\times\tilde{\nu}} \tag{4. 1}$$

$$\Delta A_{k\times\tilde{\nu}} = l_{k\times k} C_{k\times s} \Delta\varepsilon_{s\times\tilde{\nu}} + [e_{k\times\tilde{\nu}}]_{CD} \tag{4. 2}$$

$$\text{where } \Delta\varepsilon = (\varepsilon_L - \varepsilon_R) \tag{4. 3}$$

In the above equations, $A_{k\times\tilde{\nu}}$ is an absorbance matrix, $C_{k\times s}$ a concentration matrix, $a_{s\times\tilde{\nu}}$ a pure component spectral matrix, ΔA is the difference between absorbance of left circularly polarized (LCP) and right circularly polarized (RCP) light, ε_L and ε_R are the molar extinction coefficients for RCP and LCP light, l is the path length, subscript k the number of measurements (spectral patterns), subscript s is the number of the observed species, subscript $\tilde{\nu}$ is the number of data channels, subscript CD refers to polarized data and $e_{k\times\tilde{\nu}}$ is error which includes the experimental noise and model non-linearity.

In multi-component spectroscopic data analysis, there are two frequent major tasks: (1) determine the pure component spectra of the observable species i.e. $a_{s\times\tilde{\nu}}$ and $\Delta\varepsilon_{s\times\tilde{\nu}}$, and (2) determine the concentrations $C_{k\times s}$ of all observable species present. These inverse problems are typically ill posed. In order to constrain the problems and hence obtain meaningful solutions, various constraints are usually imposed. Non-negativity in concentrations and non-negativity in pure component spectra $a_{s\times\tilde{\nu}}$ are the most frequently

used. Since CD spectra possess both positive and negative parts, a non-negativity constraint can not be imposed on $\Delta\varepsilon_{s\times\tilde{\nu}}$.

4.2.2 BTEM and Chiral-BTEM

The main goal of this contribution is to investigate the application of BTEM/Chiral-BTEM to reconstruct the pure component spectra from UV and CD spectroscopic data for a reactive system. In BTEM, the entropy minimization concept is used in the objective function and optimization is performed using simulated annealing to give the simplest spectral patterns. Some frequently encountered difficulties in UV and CD signal processing, such as spectra nonlinearities arising from shifting band position and changing band shapes as well as spectra overlapping, are well accommodated by the BTEM algorithm.

As mentioned in chapter 2, the first computation step in BTEM is to perform singular value decomposition (SVD) in order to decompose the experimental UV absorbance data, $A_{k\times\nu}$, into three matrices according to Eq. 4.4, where $U_{k\times k}$ and $\mathrm{V}^{T}_{\nu\times\nu}$ are the left singular vectors and right singular vectors which form an orthonormal basis, and $\Sigma_{\mathrm{k}\times\mathrm{v}}$ is the corresponding singular value of matrix. The UV-Vis CD data $\Delta A_{k\times\nu}$ can be decomposed in a similar manner Eq. 4.5.

$$A_{k\times\tilde{\nu}} = U_{k\times k}\Sigma_{k\times\tilde{\nu}}\mathrm{V}^{T}_{\tilde{\nu}\times\tilde{\nu}} \tag{4.4}$$

$$\Delta A_{k\times\tilde{\nu}} = [U_{k\times k}\Sigma_{k\times\tilde{\nu}}\mathrm{V}^{T}_{\tilde{\nu}\times\tilde{\nu}}]_{CD} \tag{4.5}$$

The first several row vectors of $\mathrm{V}^{T}_{\tilde{\nu}\times\tilde{\nu}}$ will consist of meaningful spectral features while the rest will consist primarily of noise. The BTEM algorithm searches the subspace of *z* basis vectors for the simplest underlying patterns. This is achieved by transforming

the abstract right singular vectors in $\mathbf{V}^{\mathrm{T}}$ into pure component spectra estimates, $\hat{a}$ for UV-Vis data and $\Delta\hat{\varepsilon}$ for UV-Vis CD data, one-at-a-time using Eqs. 4.6 and 4.7.

$$\hat{a}_{1\times\tilde{\nu}} = T_{1\times z}\mathbf{V}^{\mathrm{T}}_{z\times\tilde{\nu}} \tag{4.6}$$

$$\Delta\hat{\varepsilon}_{1\times\tilde{\nu}} = [T_{1\times z}\mathbf{V}^{\mathrm{T}}_{z\times\tilde{\nu}}]_{CD} \tag{4.7}$$

The z transformation elements $T_{1\times z}$ are determined using a non-linear optimization. The objective function as shown in Eq.2.9 includes two terms: information entropy function (H) and penalty function (P) for non-negativity of the corresponding concentrations.

In turn, the information entropy function is given by Eq.2.4 where $h_{\tilde{\nu}}$ (see Eq.2.5) is a discrete probability distribution function is and the exponent m is the degree of spectrum differentiation. In the present study, both the first derivative and second derivative were used in the BTEM/Chiral-BTEM analyses. These provided good spectral reconstruction for bands having shoulders and for those with severe overlap.

4.3. Experimental Section

Rhodium complexes are frequently used as catalyst precursors for hydroformylation, hydrogenation, cyclotrimerization etc (Dickson, 2003). This group of complexes is one of the most extensively studied in organometallic chemistry . A rather large variety of achiral and chiral ligands have been used to modify the reactivity and selectivity of rhodium in catalytic reactions. In particular, mono-dentate and bi-dentate ligands are widely used to generate new mono-nuclear and poly-nuclear rhodium complexes.

The tetranuclear rhodium complex $Rh_4(CO)_{12}$ is a well known and widely used catalyst precursor. In this study, two ligand substitution reactions (see Eqs.4.8 and 4.9) were tested. It has been shown that $Rh_4(CO)_{12}$ readily reacts with 1 equivalent triphenyl phosphine at room temperature to give the corresponding mono-substituted product (Whyman, 1972). Alternately, it is known that disubstitution can occur when 2 equivalents of triphenyl phophine are used. It is also shown in Eq.4.9 that 1 equivalent of (S)-BINAP, a chiral bidentate phosphine , will be used to react with $Rh_4(CO)_{12}$ (Seyden-Penne, 2004).

$$Rh_4(CO)_{12} + PPh_3 \rightleftharpoons Rh_4(CO)_{11}PPh_3 + CO \quad (4.8)$$

$$Rh_4(CO)_{12} + \text{(S)-BINAP} \rightleftharpoons Rh_4(CO)_{10}\text{BINAP} + 2CO \quad (4.9)$$

The polynuclear metal cluster $Rh_4(CO)_{12}$ has a very strong red color and all known derivatives are also highly colored. Consequently, the above mentioned reactions can be detected by UV spectroscopy. In addition, since the second reaction involves a chiral naphthalene derivative (S)-BINAP, the corresponding chiral product cluster has both intense UV and CD spectra.

4.3.1. General Information

All solution preparations and transfers were carried out under argon (99.999%, Soxal, Singapore) atmosphere using standard Schlenk techniques (Shriver and Drezdzon, 1986). The argon was further purified before use by passing it through a deoxy and zeolite column to reduce the trace oxygen and water, respectively. The solvents n-hexane and cyclohexane (99.6%+, Fluka) were refluxed over sodium-potassium alloy under argon atmosphere. Purified nitrogen (99.999%, Saxol, Singapore) was used to purge the 2550 Shimadzu UV-visible spectrometer and Jasco-810 UV-visible spectropolarimeters.

The metal complex tetrarhodium dodecacarbonyl, $Rh_4(CO)_{12}$ (98%) and the chiral ligand (S)-(-)-2,2'-Bis(diphenylphosphino)-1,1'-binaphthyl, (S)-BINAP (97%) from Strem chemicals (Newport, MA) and the achiral ligand triphenylphosphine, PPh_3 (99%+) from Merck were used as received.

4.3.2. Equipmental Setup

A schematic diagram of the experimental setup is shown in Figure 4.1. The two semi-batch ligand substitutions (1) $Rh_4(CO)_{12}$ with PPh_3, and (2) $Rh_4(CO)_{12}$ with (S)-BINAP were performed in a Schlenk tube equipped with magnetic stirring. A rubber septum was used at the top of the Schlenk tube in order to insert transfer lines and in order to inject perturbations during the semi-batch runs. The liquid phase was circulated through a quartz cuvette with 10mm pathlength using a Teflon membrane pump (Cole Parmer) at the flow rate of 5 ml/min via Teflon tubes of 1/16" outer diameter. The quartz cuvette was fixed in a stainless steel cell holder and placed in the cell chamber of UV spectrometer. For any particular experiment, either the Shimadzu UV-2550 spectrometer or the Jasco-810 spectropolarimeter was used. Experiments were run at ambient temperature circa 298K.

The entire system was cleaned with anhydrous solvent (n-hexane/cyclohexane) prior to experiments. Furthermore, the reactions were carried out under argon in order to avoid of the degradation of $Rh_4(CO)_{12}$, PPh_3, (S)-BINAP and the resulting metal complexes.

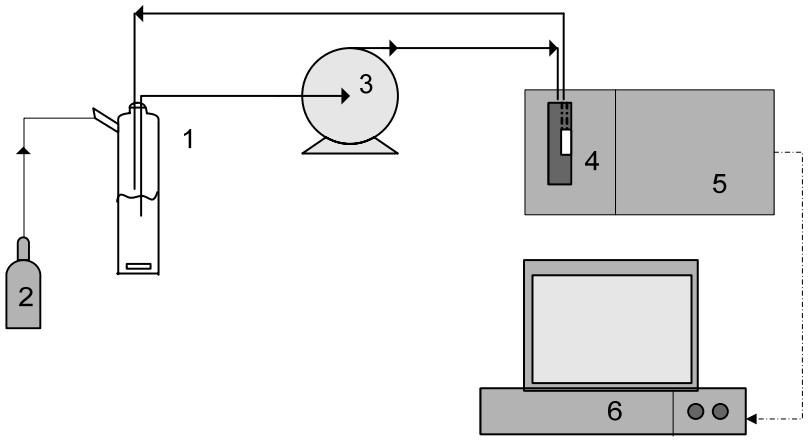

Figure.4.1. Schematic of experimental configuration: 1. Schlenk tube; 2. Argon tank; 3. Pump; 4. Quartz cell; 5. UV-Vis spectrometer; 6. Data acquisition.

4.3.3. In-situ Spectroscopic Measurements

50 ml n-hexane and 50ml cyclohexane were used as solvent for the ligand substitution reactions Eq.4.8 and Eq.4.9, respectively. Both semi-batch reactions were performed in a similar manner. For example, in the ligand substitution reaction Eq.4.8 first, 50ml of n-hexane was transferred to the Schlenk tube under argon and the stirrer was turned on. The pressure was controlled at just over 0.1013 MPa of argon. After the n-hexane solvent was circulated through the entire system, the UV-visible spectra in the quartz cuvette were collected. A stock solution of n-hexane with $Rh_4(CO)_{12}$ (*ca.* 27.5mg in 20ml) was prepared and a predetermined amount was injected into the Schlenk tube under argon. Typically, after each perturbation the solution was circulated for circa 10 minutes to achieve solution homogeneity. Then the UV-Vis spectra of the $Rh_4(CO)_{12}$ /n-hexane solution in the quartz cuvette were collected. A stock solution of n-hexane with PPh_3 (*ca.* 8.4mg in 20ml) was prepared and a predetermined amount was injected into the Schlenk tube under argon. After equilibrium, the UV-visible spectra of the reactive

system were collected. The perturbation steps in each experiment correspond to the experimental design as shown in Table 4.1.

In a similar manner, a stock solution of 13.5mg (S)-BINAP dissolved in 20ml cyclo hexane and a stock solution of 31.5mg of $Rh_4(CO)_{12}$ dissolved in 20ml cyclohexane were prepared for the ligand substitution reaction Eq.4.9. The corresponding experimental design is also shown in Table 4.1.

Table 4.1. Experimental design for ligand substitution reaction indicating the individual perturbation steps.

Index	**Experiment 1: $Rh_4(CO)_{12}$ with PPh_3**		**Experiment 2: $Rh_4(CO)_{12}$ with (S)-BINAP**	
	Perturbation	**Spectra #**	**Perturbation**	**Spectra #**
1	Solvent: n-hexane	1-2	Solvent: cyclohexane	1-2
2	Add 100 µl $Rh_4(CO)_{12}$	3-4	Add 100 µl $Rh_4(CO)_{12}$	3
3	Add 100 µl $Rh_4(CO)_{12}$	5-6	Add 200 µl $Rh_4(CO)_{12}$	4
4	Add 50 µl PPh_3	7-8	Add 200 µl $Rh_4(CO)_{12}$	5
5	Add 100 µl PPh_3	9-10	Add 50 µl (S)-BINAP	6-7
6	Add 250 µl $Rh_4(CO)_{12}$	11-12	Add 50 µl (S)-BINAP	8
7	Add 250 µl $Rh_4(CO)_{12}$	13-14	Add 50 µl (S)-BINAP	9
8	Add 200 µl PPh_3	15-17	Add 100 µl (S)-BINAP	10
9	Add 250 µl PPh_3	18-19	Add 100 µl (S)-BINAP	11-12

All the UV-visible and/or CD spectra were recorded at scanning speed of 200nm/min in the range of 800 nm to 200 nm. Since $Rh_4(CO)_{12}$ reacts with PPh_3 almost instantaneously, most of these spectra were collected under nearly full transformation of PPh_3, i.e. where the equilibrium is shifted to the far right in Eq.4.8. Similarly, $Rh_4(CO)_{12}$ reacted rapidly with (S)-BINAP, most of these spectra were collected under nearly full

transformation of (S)-BINAP, i.e. where the equilibrium is shifted to the far right in Eq.4.9.

4.4. Results and Discussions: *Ligand Substitution of $Rh_4(CO)_{12}$ with PPh_3*

4.4.1 Experimental Data

The ligand substitution of $Rh_4(CO)_{12}$ with the achiral ligand PPh_3 was carried out in n-hexane under argon atmosphere. The in-situ spectroscopic measurements were performed using the Shimadzu UV-2550 spectrometer. A total of 19 UV-Vis spectra were obtained from this experiment as shown in Figure 4.2.

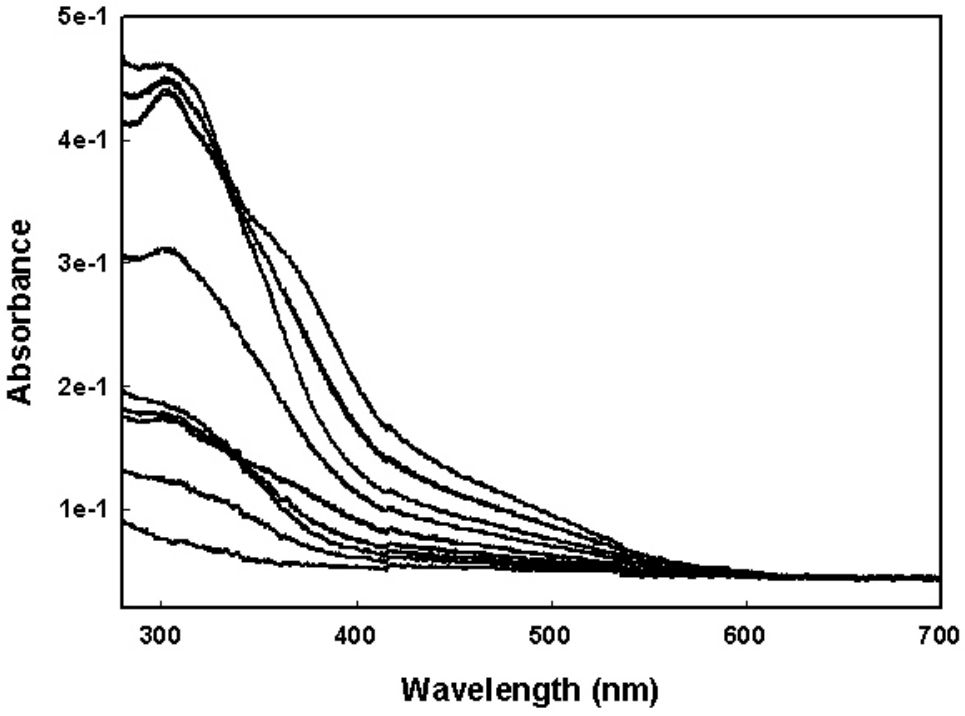

Figure.4.2. UV-Vis reaction spectra of the ligand substitution reaction of $Rh_4(CO)_{12}$ with PPh_3 (under argon) involving 9 perturbation steps (Experiment 1, see Table 4.1).

These measurements show absorbance from the solvent, $Rh_4(CO)_{12}$ and the cluster. A few spectral maxima and shoulders are seen i.e. at 305, 380 etc nm. All spectral

features are broad, as expected for UV-visible spectra. Two spectral step changes, one at 420 nm and the other at 540 nm are also observed. These are caused by the optical filter changes.

4.4.2 Singular Value Decomposition (SVD)

The 19 UV-visible spectra were first consolidated into a single matrix. The spectra preconditioning, namely background subtraction, was performed on the consolidated absorbance data matrix and then singular value decomposition (SVD) was employed to decompose this preconditioned absorbance data matrix to obtain the right singular vectors, the orthonormal matrix V^T. The first 6 right singular vectors and 19th vector are shown in Figure 4.3.

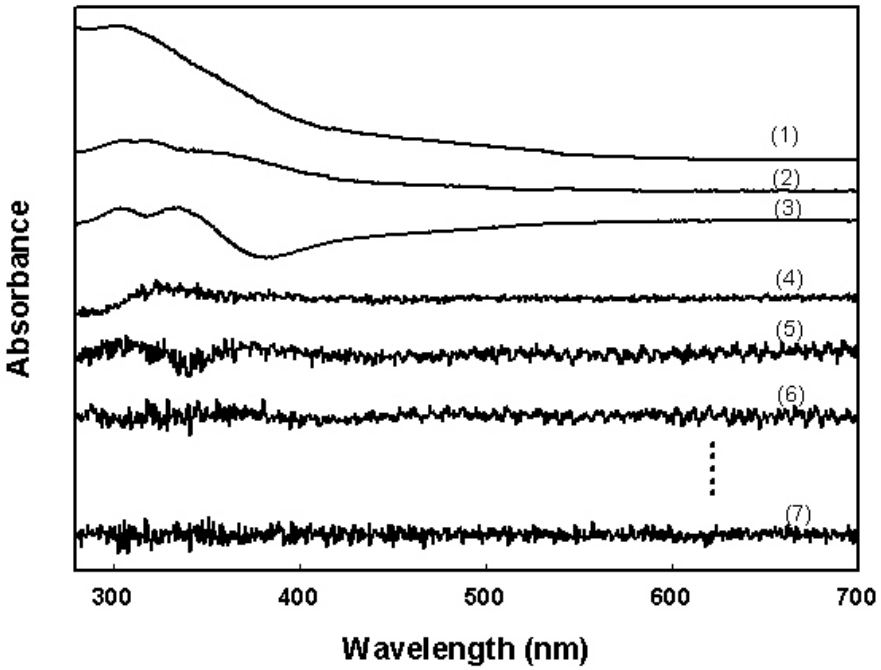

Figure 4.3. 7 right singular vectors of the V^T matrix for the consolidated data set from the ligand substitution reaction of $Rh_4(CO)_{12}$ with PPh_3 (Experiment 1, see Table 4.1): (1)~(6) first six right singular vectors; (7) nineteenth right singular vector.

The first 3 right singular vectors in Figure 4.3 show meaningful signals although the bands are quite broad. These bands are significant spectral features associated with the metal carbonyl and metal complex. The 4^{th} and 5^{th} right singular vectors still show some absorbance bands, however, there is a considerable contribution from noise. The 6^{th} to the 19^{th} right singular vector can be considered to be primarily white noise. Since all meaningful spectral features are seen in the first five right singular vectors, only vectors 1-5 were used in the following BTEM analysis.

4.4.3 Spectral Reconstruction using BTEM

The 5 right singular vectors from the experimental absorbance data were transformed to pure component spectra using BTEM analysis. Two estimated spectral patterns could be successfully reconstructed from the BTEM analysis. These are the estimated UV-visible pure component spectra of $Rh_4(CO)_{12}$ and the product $Rh_4(CO)_{11}PPh_3$. Figure 4.4 compares the estimated UV-visible spectra with the experimental reference spectra. Both estimated spectra are in quite good agreement with the experimental reference spectra.

More right singular V^T vectors (up to 19 V^T vectors) were used in other analyses, however, no additional meaningful spectra patterns were obtained. Since $Rh_4(CO)_{12}$ reacts instantaneously with PPh_3 and since Eq.4.8 is shifted to the far right, the analysis indicates that little or no free PPh_3 was present in these spectra (note that PPh_3 has a broad chromophore from 200-300 nm due to the phenyl groups).

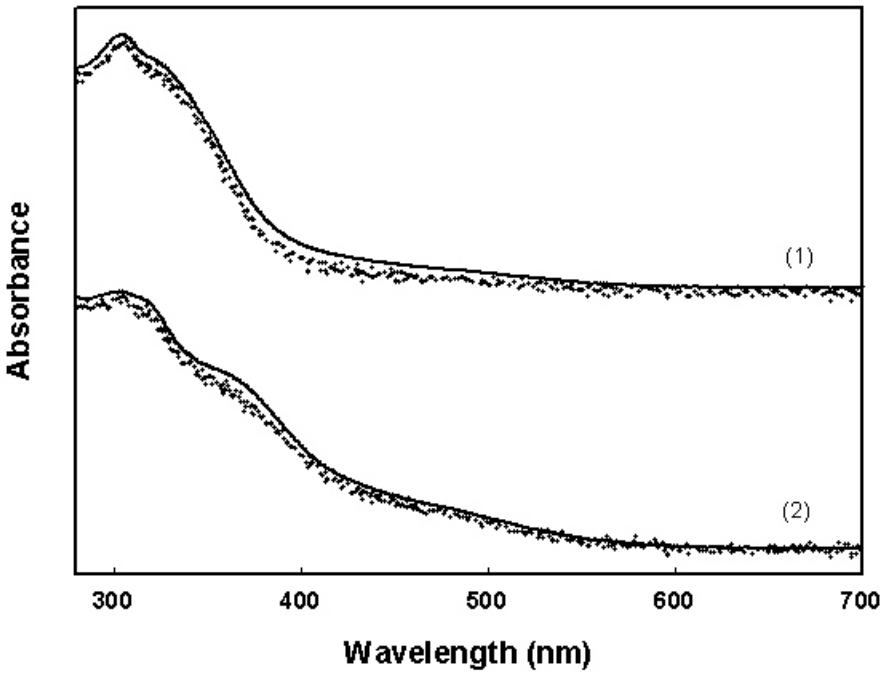

Figure 4.4. Solid lines: recovered pure component spectra obtained by BTEM: (1) $Rh_4(CO)_{12}$ and (2) $Rh_4(CO)_{11}PPh_3$; Dotted lines: UV-Vis experiment reference spectra: (1) $Rh_4(CO)_{12}$ and (2) $Rh_4(CO)_{11}PPh_3$.

4.4.4 Concentrations Profiles

The relative concentration profiles of the reactants were calculated by a least squares fit of the estimated UV-visible spectra onto the original experimental UV-Vis absorbance spectra. Since the present experiments were conducted at PPh_3 : $Rh_4(CO)_{12}$ ratios less than 0.7 the presence of the di-substituted product $Rh_4(CO)_{10}(PPh_3)_2$ can be neglected (Tjahjono *et al.*, 2006). Furthermore, the mono-substituted product was totally soluble in n-hexane in the range of concentration used in this study (less than 5ppm). Accordingly, the mass balance from the experimental design was used as a constraint in order to determine the calibrations for both $Rh_4(CO)_{12}$ and $Rh_4(CO)_{11}PPh_3$. Figure 4.5 compares the concentration profiles of $Rh_4(CO)_{12}$ and $Rh_4(CO)_{11}PPh_3$ obtained from the experimental design with those obtained from the spectroscopic measurements. It is

clearly seen that satisfactory concentration profiles for both $Rh_4(CO)_{12}$ and the product $Rh_4(CO)_{11}PPh_3$ are obtained. However, some discrepancy appears as more and more perturbations are made. This increasing discrepancy is probably due to accumulation of error during the experimental procedure, either from systematic error during injection and/or the slow loss of hexane through the septum (it is very volatile).

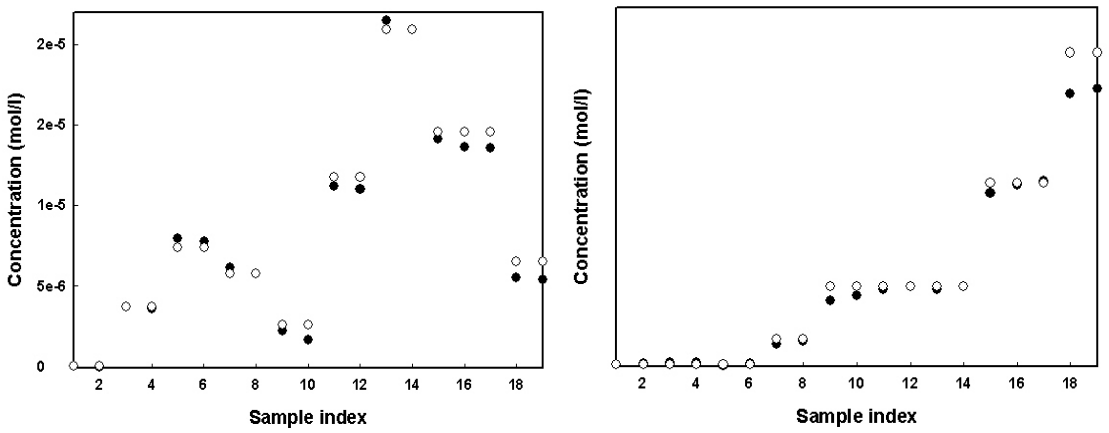

(a) (b)

Figure 4.5. Comparison of the concentration profiles from recovered UV-Vis pure component spectra (●) and experiment design (○). Profiles for (a) $Rh_4(CO)_{12}$ and (b) $Rh_4(CO)_{11}PPh_3$.

4.5 Results and Discussions: *Ligand Substitution of $Rh_4(CO)_{12}$ with (S)-BINAP*

The ligand substitution of $Rh_4(CO)_{12}$ with the chiral bidentate ligand (S)-BINAP was carried out in cyclohexane under an argon atmosphere. This reaction was carried out in a semi-batch mode by introducing perturbations of (S)-BINAP into the reactive system. The concentrations of all the reactants involved in this reaction were less than 20ppm and the concentration of the product $Rh_4(CO)_{10}$BINAP was less than 10ppm. The in-situ spectroscopic measurements were performed using the UV Jasco-810 spectropolarimeter.

A total of 12 UV-Vis spectra and 12 UV-Vis CD spectra were obtained simultaneously from the above experiment.

4.5.1. UV-visible Experimental Data Set

4.5.1.1 Experimental Data

The 12 UV-visible spectra from the above experiment in the range of 700~280 nm are shown in Figure 4.6.

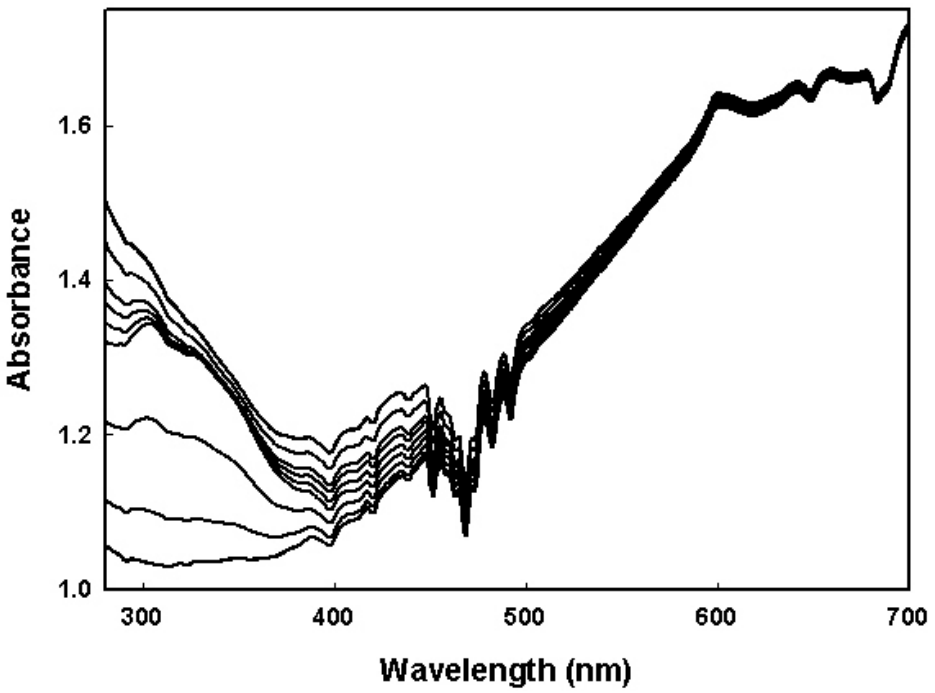

Figure 4.6. UV-Vis reaction spectra of the ligand substitution reaction of $Rh_4(CO)_{12}$ with (S)-BINAP (under argon) involving 9 perturbation steps (Experiment 2, see Table 4.1).

Since all spectra are below absorbance of 2, these spectra were taken in a more-or-less linear instrument response region. In the high nm range, the UV-Vis spectra are rather featureless and correspond primarily to the instrument function. The primary signals of interest are all below 500 nm. At the reagent concentrations used, significant changes are seen in the region of circa 280-500 nm during the semi-batch experiment.

Since none of the experimental spectra have absorbance above circa 1.5, rather strict additivity of component spectra should exist, and the bilinear form of the Bouguer-Lamber-Beer law should remain valid.

4.5.1.2 Singular Value Decomposition (SVD)

A total of 12 UV-Visible spectra were first consolidated into a single matrix. To minimize the effects of the solvent and cuvette signals on the spectral analysis, spectral preconditioning was performed. This background subtraction resulted in a new consolidated absorbance data matrix. Next, singular value decomposition (SVD) was employed to decompose this preconditioning absorbance data matrix to give the right singular vectors, the orthonormal matrix V^T. The first 6 right singular vectors and 12th vector are shown in Figure 4.7.

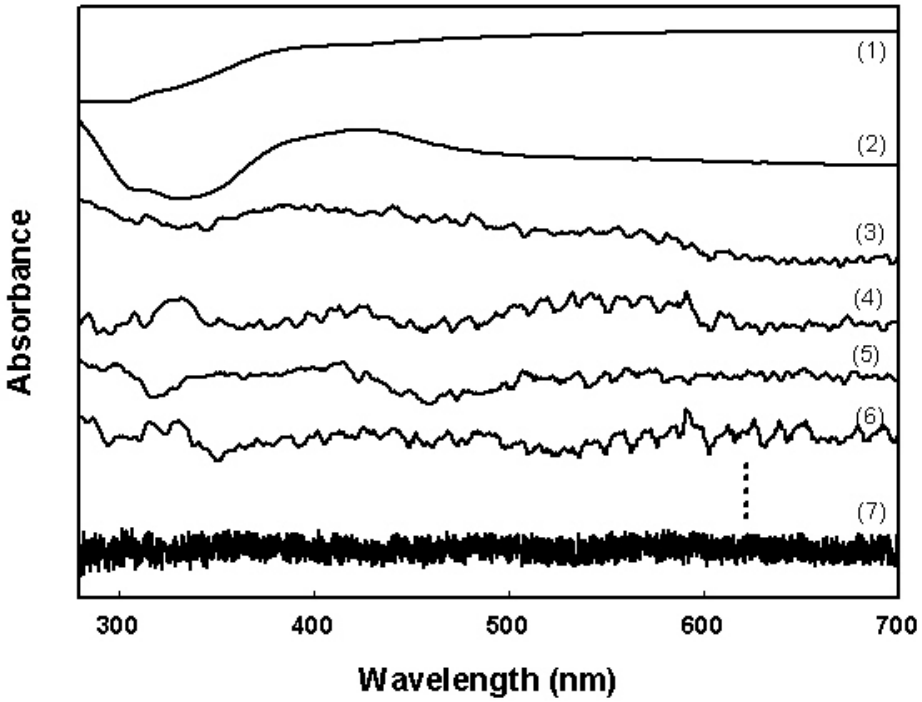

Figure 4.7. 7 right singular vectors of the V^T matrix for UV-Vis consolidated data set from the ligand substitution reaction of $Rh_4(CO)_{12}$ with (S)-BINAP (Experiment 2, see Table 4.1): (1)~(6) first six right singular vectors; (7) twelfth right singular vector.

The first 2 right singular vectors in Figure 4.7 show significant spectral features with the very broad bands associated with the metal carbonyl and metal complex. The third to 6th right singular vectors still show some absorbance bands, however, there is a considerable contribution from noise. The 12th right singular vector can be considered to be white noise. Since prominent spectra features can be observed only in the first six right singular vectors, these will be used in the following BTEM analysis.

4.5.1.3 Spectral Reconstruction using BTEM

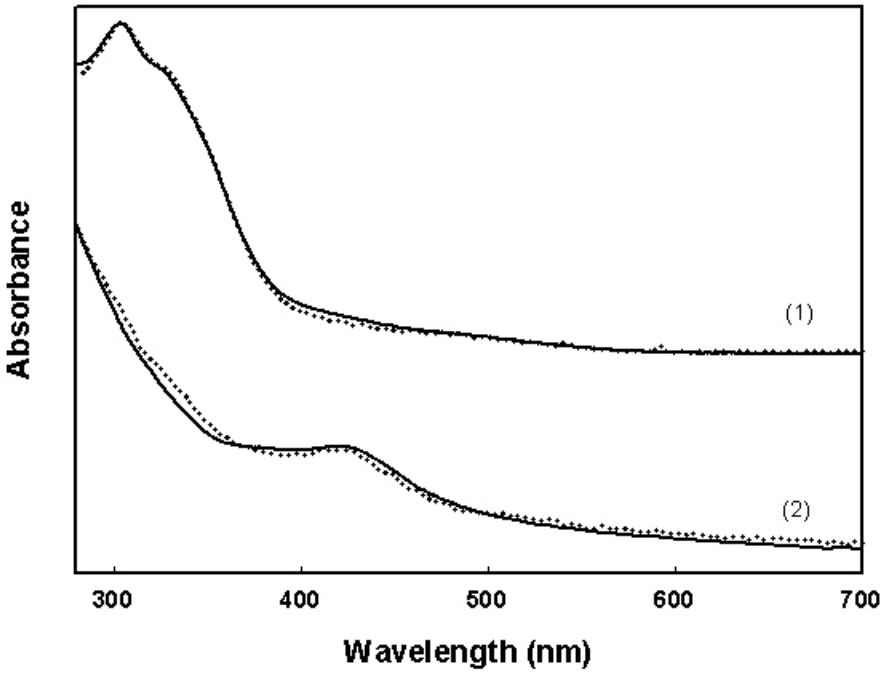

Figure 4.8. Solid lines: recovered pure component spectra obtained by BTEM: (1) $Rh_4(CO)_{12}$ and (2) $Rh_4(CO)_{10}$ BINAP; Dotted lines: UV-Vis experiment reference spectra: (1) $Rh_4(CO)_{12}$ and (2) $Rh_4(CO)_{10}$BINAP.

BTEM analysis was performed using the first 6 right singular vectors from the preconditioned UV-Vis absorbance data in order to reconstruct the pure component spectra involved in the reaction. The noticeable spectral extrema in the first 6 right singular vectors were used as targets. Two estimated UV-Vis spectral patterns, from

$Rh_4(CO)_{12}$ and the product $Rh_4(CO)_{10}BINAP$, could be successfully reconstructed from the BTEM analysis.

Figure 4.8 compares the estimated UV-Vis spectra with the experimental reference spectra. Both estimated spectra are in quite good agreement with the experimental reference spectra.

4.5.1.4 Concentrations Profiles

An estimate of the relative concentration profiles of the reactants was calculated by a least squares fit of the estimated UV-Vis spectra onto the original experimental UV-Vis absorbance spectra. Further quantitative spectroscopic analysis was performed by using the mass balances from the experimental design as a constraint and assuming that only reaction 2 occurs. The quantitative analysis resulted in two concentration profiles for $Rh_4(CO)_{12}$ and the product $Rh_4(CO)_{10}BINAP$ as shown in Figure 4.9. It is clearly seen that satisfactory concentration profiles of both $Rh_4(CO)_{12}$ and the product $Rh_4(CO)_{10}BINAP$ were obtain from the quantitative analysis, at least for the first 10 steps of the semi-batch reaction.

The 10^{th} step corresponds to a (S)-BINAP : $Rh_4(CO)_{12}$ ratio of circa 0.5. In the 11^{th} and 12^{th} step higher ratios of (S)-BINAP : $Rh_4(CO)_{12}$ up to 2:3 were used. In these last two steps, some discrepancy occurs between the estimated and experimental design concentrations. With the addition of more (S)-BINAP, some non-negligible side reactions are taking place. These side reactions perhaps involve the formation of small amounts of a di-substituted product $Rh_4(CO)_8(BINAP)_2$ and/or a dinuclear species of the stoichiometry $Rh_2(CO)_6BINAP$.

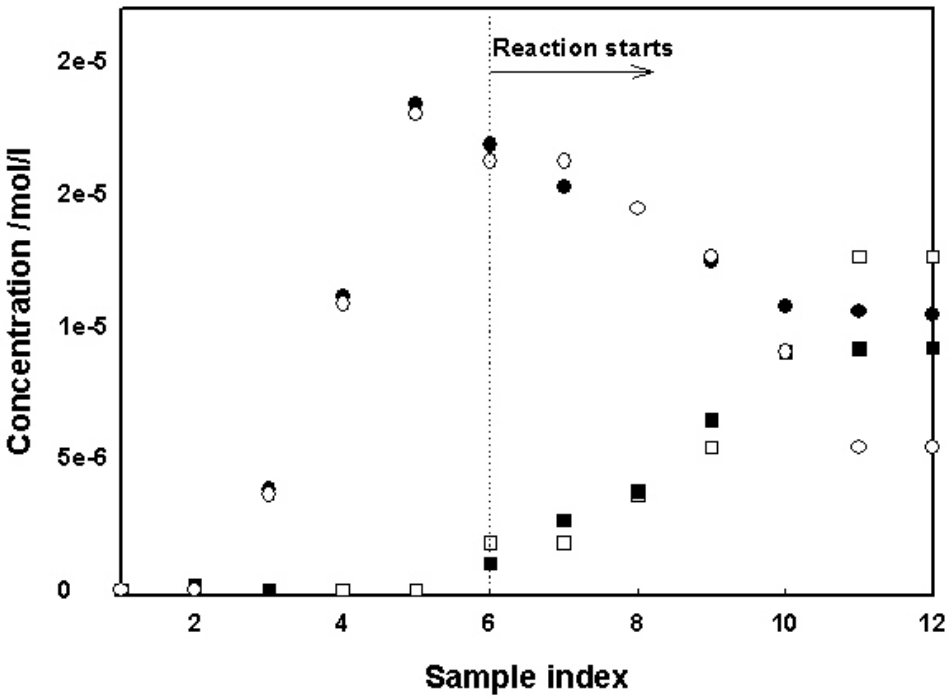

Figure 4.9. Comparison of the concentration profiles from recovered UV-Vis pure component spectra (solid symbols) and experiment design (open symbols). Profiles for: ● $Rh_4(CO)_{12}$ and ■ $Rh_4(CO)_{10}$ BINAP.

4.5.2 CD Experimental Data Set

4.5.2.1 Experimental Data

The 12 UV-visible CD spectra from the above experiment in the range of 225~425 nm are shown in Figure 4.10. These spectra show (1) a non-flat and non-zero baseline (at least in the region of <300 nm) due to the instrument function and (2) pronounced CD features at circa 235, 265 and 320 nm. In addition, these CD spectra have considerably lower S/N ratios compared to the unpolarized UV-Vis measurements.

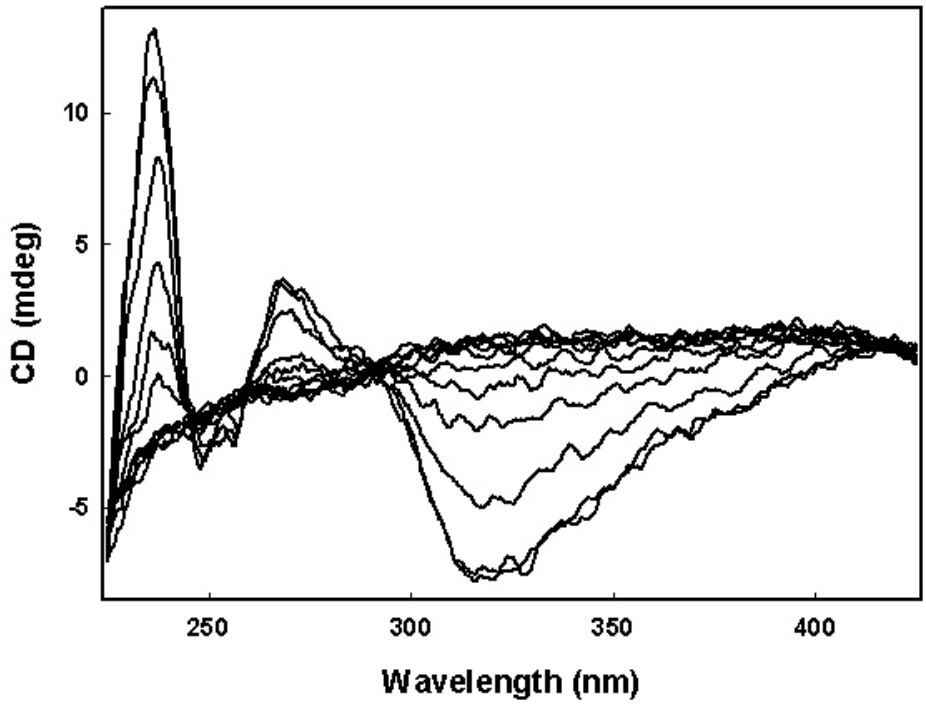

Figure 4.10. UV-Vis CD reaction spectra of the ligand substitution reaction of $Rh_4(CO)_{12}$ with (S)-BINAP (under argon) involving 9 perturbation steps (Experiment 2, see Table 4.1).

4.5.2.2 Singular Value Decomposition (SVD)

No base-line correction was performed with the 12 UV-Vis CD spectra, however, they were smoothed with the Savitzky-Golay smoothing algorithm. Subsequently, the smoothed spectra were consolidated into a single matrix. Next, singular value decomposition (SVD) was employed to decompose this CD data matrix to give the right singular vectors, the orthonormal matrix V^T. The first 6 right singular vectors and 12th vectors are shown in Figure 4.11.

The first 2 right singular vectors in Figure 4.11 show significant spectral features associated with the instrument function and the chiral metal complex. The third to 6th right singular vectors still show some features, however, there is a considerable contribution from noise. The 12th right singular vector can be considered to be more-or-

less white noise. Most of the prominent spectral features are embedded in the first six right singular vectors and these will be used in the following Chiral-BTEM analysis.

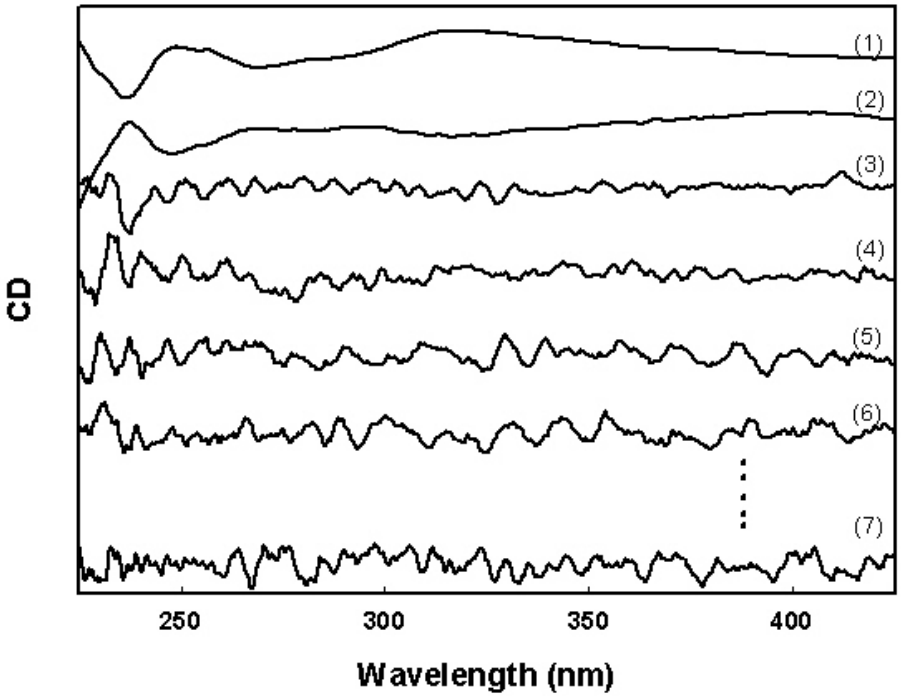

Figure 4.11. 7 right singular vectors of the V^T matrix for UV-Vis CD consolidated data set from the ligand substitution reaction of $Rh_4(CO)_{12}$ with (S)-BINAP (Experiment 2, see Table 4.1): (1)~(6) first six right singular vectors; (7) twelfth right singular vector.

4.5.2.3 Spectral Reconstruction using BTEM

The first 6 right singular vectors were used to reconstruct the pure component ECD spectrum of the chiral metal complex $Rh_4(CO)_{10}$BINAP . The noticeable spectral extrema in the first 6 right singular vectors were used as targets. Figure 4.12 compares the estimated UV-Vis CD spectrum with the experimental reference spectrum. This result indicates that the BTEM algorithm can be used to obtain accurate CD pure component spectra i.e. spectra with both positive and negative parts.

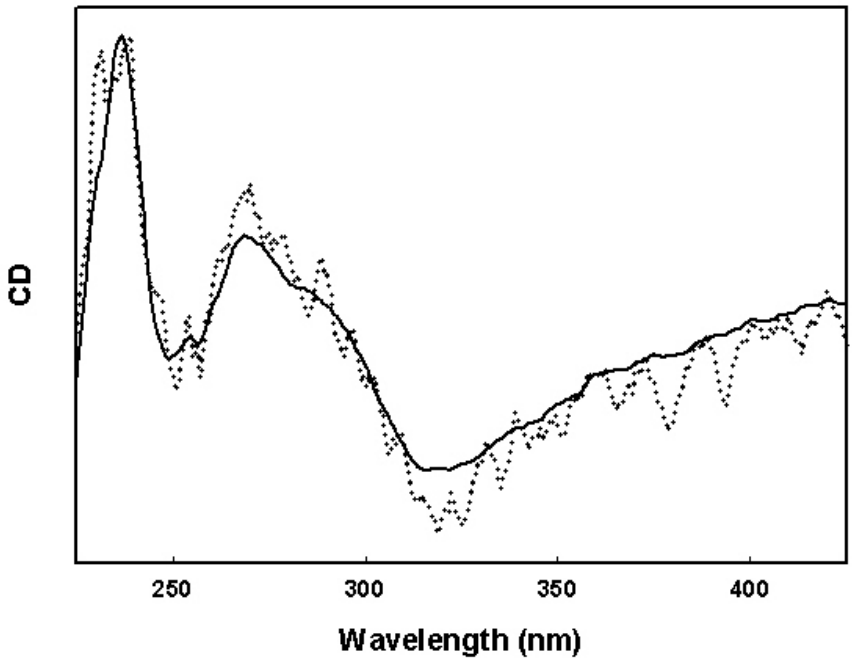

Figure 4.12. Recovered pure component spectra obtained by BTEM: $Rh_4(CO)_{10}$ BINAP, solid line and UV-Vis CD experiment reference spectra: $Rh_4(CO)_{10}$ BINAP, dotted line.

4.5.2.4 Concentration Profiles

The estimated relative concentration profiles of the reactants were computed by least squares fit of the estimated UV-Vis CD spectra onto the original experimental UV-visible CD spectra. Further quantitative spectroscopic analysis was performed using the mass balances to constrain the numerical solution, assuming that only reaction 2 occurs. The quantitative analysis resulted in the concentration profile for the product $Rh_4(CO)_{10}$ BINAP. Figure 4.13 compares the estimated concentration profile of the product $Rh_4(CO)_{10}$ BINAP obtained from (1) the UV-Vis CD experimental data set with (2) the UV-Vis experimental data set and (3) the experimental design 'real' concentration profile. The 3 concentration profiles of the product $Rh_4(CO)_{10}$ BINAP are in very good agreement. With the exception of the last 2 steps, 11 and 12 appear to indicate that some non-negligible side reactions are occurring. Again side reactions might be associated with

the formation of small amounts of a disubstituted product $Rh_4(CO)_8(BINAP)_2$ and/or a dinuclear species of the stoichiometry $Rh_2(CO)_6BINAP$.

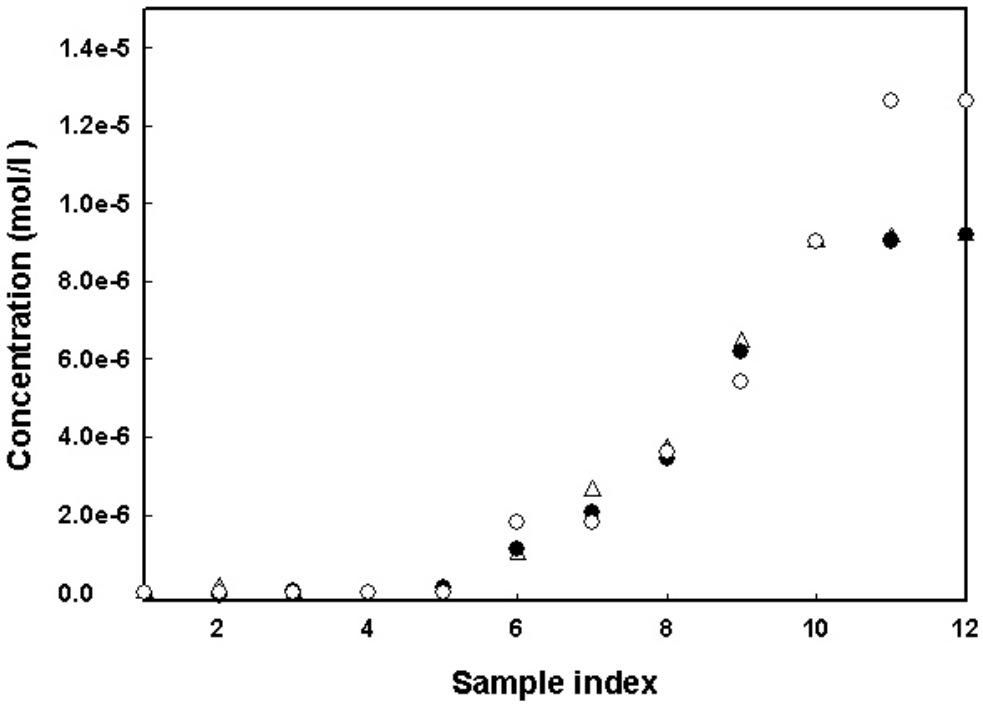

Figure.4.13. Comparison of $Rh_4(CO)_{10}$ BINAP concentration profile determined from recovered UV-Vis CD pure component spectra (●) ,UV-Vis pure component spectra (Δ) and experiment design (○).

4.6. Summary

4.6.1 The Present Results and Conclusions

The present results demonstrate that spectral reconstruction for organometallic reactive systems can be achieved by the application of UV-Vis /UV-Vis CD spectroscopy combined with reliable and effective chemometric techniques, namely, the BTEM and Chiral-BTEM algorithms. Moreover, the present results suggest that much more complex systems can be studied. Since the BTEM algorithm has been previously shown to be effective with systems containing 10 or more species (using FTIR, Raman etc), analysis

of complex reactive systems using UV-Vis / UV-Vis CD spectroscopy appears possible in the near future.

In a broader context, and as noted in section 4.1.3, general and satisfactory solutions for the deconvolution of UV-Vis data have until now, not been available. The present chapter demonstrates that BTEM and Chiral-BTEM provide a good solution to this frequently encountered problem. Therefore, many new opportunities are opened.

4.6.2 Systems for Future Study

For achiral systems these opportunities include (1) the detection and better quantification of frequently used biomarkers (fluorophores etc) where the complex organic matrix itself should also contain some residual signals (Nida *et al.*, 2005; El-Sayed *et al.*, 2007), (2) many homogeneous organometallic catalyzed reaction solutions are highly colored due to the metal complex and the deconvolution of all these signals could assist further in the identification of intermediates (especially if this is combined with first principal calculations of the associated UV-VIS spectrum), and (3) chemo-luminescent assay analysis where multiple signals are often present and deconvolution could assist in better quantitative analysis.

With respect to chiral systems, the development of Chiral-BTEM should open new possibilities for rapid purity determination without the requirement of a stereo-pure standard as calibration in many enantio-selective syntheses of pharmaceutical products and other biological active substances. Moreover, in addition to UV CD and ROA already mentioned, Chiral-BTEM should be applicable to vibrational circular dichroism (VCD), fluorescence CD, x-ray CD, luminescence CD and magnetic circular dichroism (MCD).

Chapter 5

Studies of the Far-Infrared and Far-Raman spectra of Neutral Metal Carbonyl Complexes: the Combination of IR, Raman Spectroscopies and Density Functional Theory

In the previous chapter organometallic ligand substitution reactions were investigated using UV-Vis/UV-Vis CD spectroscopy combined with the BTEM/Chiral-BTEM algorithms. In this chapter, the vibrational properties of the metal carbonyl clusters $Mn_2(CO)_{10}$, $Mo(CO)_6$ and $Re_2(CO)_{10}$ at low wavenumbers were measured by both IR and Raman spectroscopy and these results were compared to density functional theory (DFT) calculations.

Transition metal carbonyl complexes have played a crucial role in the development and understanding of modern transition metal chemistry. The nature of the bonds between transition metals and carbon monoxide has been extensively investigated by both experimental and theoretical calculations. Most of these studies have focused on the mid-infrared where information on the C=O bond can be studied. However the reports on the vibrational modes in the low wavenumber range such as the bonds between metal and metal and some of bonds between transition metals and carbon are rather limited, especially for experimental measurements of organometallic complexes in the solution.

The current chapter will focus on these low wavenumber range vibrational modes. It will use density function theory methods with various basis sets to carry out prediction of vibrational spectra for metal carbonyl complexes and compare them with the experimental measurements. It is demonstrated that the spectra predictions

obtained with DFT are usually sufficiently accurate. *It is important to note that low-wavenumber vibrational studies are quite uncommon* since (1) there are numerous experimental problems (for example, most researchers do not have access to a FIR spectrometer, and especially not one equipped with good transparency diamond windows) and (2) DFT calculations in the low-wavenumber regions are frequently ignored because the complimentary experimental data is not available for comparison.

5.1 Introduction

The following section will first address a brief introduction to density functional theory and then focus on the application of DFT in transition metal chemistry. The use of density function theory (DFT) for predicting vibrational spectra will be discussed and the recent developments in the field especially the use of DFT to study metal complex will be highlighted.

5.1.1 Short Introduction to Density Functional Theory

Density functional theory is an extremely successful approach for the description of ground state properties of a system without dealing directly and explicitly with a many-electron description. Consequently, the main idea of DFT is to describe an interacting system of fermions via its density and not via its many-body wave function. In 1930, Fermi first suggested that the total energy of an electronic system can be determined in the terms of electron density. This notion is the basis of DFT and later it was further developed by Kohn (1964) who won the Nobel Prize for chemistry in 1998 as the founder of density functional theory (DFT).

DFT in general gives a good description of ground state properties although practical applications of DFT are based on approximations for the so-called exchange-correlation potential. Therefore it is necessary to carefully choose the density

functionals with the basis sets, especially for large size molecules or molecules possessing heavy atoms such as metal complexes.

5.1.2 The Performances of DFT in Transition Metal Chemistry

Recently development in density functional theory has shown that DFT may become a reliable and effective computational tool for a variety of chemical systems including transition metal systems. Since DFT calculation is much faster than Hartree-Fock etc it has the potential of handling large transition metal systems with more computational efficiency. Indeed, DFT performs very well in the calculations of molecular structure, bond energies and spectroscopy properties of transition metal systems in non-reaction and reaction cases (Fan and Zeigler, 1991,1992; Jacobsen *et al.*, 1992; Pollak *et al*., 1997; Szilagyi and Frenking, 1997; Decker *et al*., 1997; Cotton and Feng, 1997, 1998; Mineva *et al*., 2001; Cedeno *et al.*, 2001; Jacobsen, 2005; Fielicke *et al*., 2005; Szabo *et al*., 2005). Geometry optimizations performed by the pure DFT methods and the hybrid methods are in general in good agreement with experiment values. In addition, bond distances are usually calculated with an accuracy of 0.02 angstrom or better with the hybrid methods (Fan and Zeigler, 1991). Consequently, DFT calculations can provide relatively accurate molecular structures and energies of species involved in chemical reactions, in other words, starting from the reactant(s) to the transition state to the product(s).

On the other hand, molecules in transition metal chemistry are characterized extensively by spectroscopic methods such as IR and Raman spectroscopy. With both pure and hybrid DFT functionals it is possible to calculate the vibrational frequencies of the normal modes of transition metal complexes with high accuracy (Berces and Ziegler, 1994, 1996; Xie *et al*., 2005). C-O bond vibrational frequencies of metal

carbonyl have been intensively studied and the shifts in frequency are generally circa 10 to 100 cm^{-1} (Berces, 1996; Xie *et al.*, 2005; Allian *et al.*, 2006). M-C and M-M bonds has been much less investigated. One DFT study on Tungsten hexacarbonyl showed that the calculated vibrational frequency of W-C stretch bond agree well with the experimental reference and the differences are up to70 cm^{-1}. In addition, in the very low wavenumber (below 100 cm^{-1}) the calculated vibrational frequencies are essentially equal to the experimental reference and the differences are often less than 10 cm^{-1} (Berces, 1996). Comparison of vibrational frequencies obtained from experiment and DFT calculations can be used to identify the structural modes of transition metal complexes (such as intermediates). This approach has particular merits in treating large molecules to generate highly reliable optimized geometries and vibrational frequencies.

5.2 Experimental Section

The following section will briefly describe the general components of the in-situ IR and Raman experimental setups used. In addition, various aspects of the procedure and the handling of chemicals will be described.

5.2.1 General Experiment Configuration

The general experimental configuration of in-situ spectroscopy for both Far-IR and Far-Raman measurements is similar to the experimental scheme used in chapter 4 for UV measurements (see Figure 4.1) except for the different spectroscopy used. It consists of three major parts: (1) a Schlenk tube with gas supply (argon and/ carbon monoxide), (2) a pump to circulate the fluid through the entire system (from Schlenk tube to spectroscopic cell and back to Schlenk tube), and (3) a spectroscopy (in this chapter using Far-IR or Far-Raman) with a suitable cell.

5.2.2 Preparation of Chemicals

Since the system of interest in this chapter is very close to that in chapter 4 the preparation procedure is also similar. Again, in order to minimize transition metal carbonyl exposure to oxygen, moisture and light, all solution preparations and transfers were carried out under purified Argon (99.9995%, Saxol, Singapore) atmosphere using standard Schlenk techniques (Shriver and Drezdzon, 1986). The argon was further purified before use by passing it through a deoxy and zeolite column.

The transition metal carbonyls $Mo(CO)_6$, $Mn_2(CO)_{10,}$ and $Re_2(CO)_{10}$ (98%) purchased from Strem Chemicals (Newburyport, MA, USA) were used as obtained. The Puriss quality toluene (99.6%) from Fluka was further distilled over sodium-potassium under argon to remove the trace water and oxygen. The anhydrous solvents, after distillation, were kept under Argon in a two necks 2L round bottom flask. Glass pipettes, 5 ml, 10 mL and 50 mL (Ace-glass), were used to transfer the required volumes of the solvent from flask to the Schlenk tube.

Purified carbon monoxide (Research grade, 99.97%, linde, Singapore) was also further purified through de-oxy and zeolite columns and was used in the experiments to minimize oxidation during measurements.

For Far-Raman measurements, all stock solutions of metal carbonyl were prepared under argon using 5ml anhydrous toluene as solvent. The mass of solid crystals were determined by using a balance (Analytical *Plus,* Ohaus, New Jersey) with a precision of $\pm\ 10^{-5}$ g. 14.4 mg $Mo(CO)_6$, 33.2 mg $Mn_2(CO)_{10}$, and 37.1 mg $Re_2(CO)_{10}$ were used for each stock solution.

For Far-IR measurements, all stock solutions of metal carbonyl were prepared under argon using 5.3685g anhydrous toluene as solvent. The mass of solid crystals

were determined by using a balance (Analytical *Plus*, Ohaus, New Jersey) with a precision of $\pm 10^{-5}$ g. 52.0 mg $Mo(CO)_6$, 60.7 mg $Mn_2(CO)_{10}$, and 65.3mg $Re_2(CO)_{10}$ were used for each stock solution.

5.2.3 Equipments

All the measurements were conducted at the Institute of Chemical Engineering and Sciences (ICES), Singapore. A Bruker, Vertex 70, spectrometer (Far-IR) and Chiral*RAMAN*^{TM} spectrometer (this instrument can be used for the measurements of both Raman and ROA spectra) from BioTools (there are only a few ROA instruments in the world) were used.

The Far-IR spectrometer has a room temperature detector (DTGS) and dry air was used to purge the spectrometer system in order to remove the moisture. The far infrared cell was equipped with diamond windows (from ElementSix) with dimensions of 20mm diameter by 1.25mm thickness. A quartz cuvette with dimensions of $40 \times 10 \times 10$ mm was used as Far-Raman cell.

5.2.4 In-Situ Spectroscopic Measurements

All the Far-IR and Far-Raman spectra of $Mo(CO)_6$, $Mn_2(CO)_{10,}$ and $Re_2(CO)_{10}$ were measured in a similar manner. For example, for the Far-Raman experiment of $Mn_2(CO)_{10}$, first, in order to avoid of the decomposition of metal complexes, the entire system was cleaned with anhydrous toluene prior to experiments. Then 10ml of anhydrous toluene was transferred to the Schlenk tube under argon and the stirrer was turned on. After the toluene solvent was circulated through the entire system, the Far-Raman spectra of toluene in the quartz cuvette were measurements. Next a predetermined amount of a stock solution of $Mn_2(CO)_{10}$ was injected into the Schlenk tube under argon. This volumetric perturbation was made using gas-tight Hamilton

2.0 ml syringe. Typically, after each perturbation the solution was circulated for circa 10 minutes to achieve solution homogeneity. Then the measurements of Far-Raman spectra of the $Mn_2(CO)_{10}$ /toluene solution in the quartz cuvette were undertaken. Several perturbation steps were conducted in the each experiment in order to generate a set of data set which is suitable to BTEM analysis for the reconstruction of pure metal carbonyl Raman spectra. The corresponding experimental designs of Far-Raman and Far-IR measurements are shown in Tables 5.1~5.6.

Table 5.1. Experimental design for $Mo(CO)_6$ measurements using Far-Raman indicating the individual perturbation steps.

Index	**Experiment: $Mo(CO)_6$**	
	Perturbation	**Spectra #**
1	Solvent: toluene	1-4
2	Add 2ml $Mo(CO)_6$ solution	5-8
3	Add 1ml $Mo(CO)_6$ solution	9-12
4	Add 1ml $Mo(CO)_6$ solution	13-16
5	Add 1ml $Mo(CO)_6$ solution	17-20
6	Add 2ml toluene	21-24
7	Add 3ml toluene	25-28

Table 5.2. Experimental design for $Mn_2(CO)_{10}$ measurements using Far-Raman indicating the individual perturbation steps.

Index	**Experiment:$Mn_2(CO)_{10}$**	
	Perturbation	**Spectra #**
1	Solvent: toluene	1-4
2	Add 1.5ml $Mn_2(CO)_{10}$ solution	5-8
3	Add 1ml $Mn_2(CO)_{10}$ solution	9-12
4	Add 1ml toluene	13-16
5	Add 2ml toluene	17-20
6	Add 0.5ml $Mn_2(CO)_{10}$ solution	21-24
7	Add 2ml toluene	25-28

In regard to Far-Raman experiments, spectra from the region 35-900 cm^{-1} are presented. 256 scans were accumulated for one spectrum. In addition, 260 mW laser power was used. On the other hand, for Far-IR experiments, spectra collection was from 50-680 cm^{-1} and 10 scans were accumulated for each spectrum with resolution of 2 cm^{-1}.

Table 5.3. Experimental design for $Re_2(CO)_{10}$ measurements using Far-Raman indicating the individual perturbation steps.

Index	**Experiment: $Re_2(CO)_{10}$**	
	Perturbation	**Spectra #**
1	Solvent: toluene	1-4
2	Add 1.5ml $Re_2(CO)_{10}$ solution	5-8
3	Add 1ml $Re_2(CO)_{10}$ solution	9-12
4	Add 1ml $Re_2(CO)_{10}$ solution	13-16
5	Add 1ml $Re_2(CO)_{10}$ solution	17-20
6	Add 2ml toluene	21-24
7	Add 3ml toluene	25-28

Table 5.4. Experimental design for $Mo(CO)_6$ measurements using Far-IR indicating the individual perturbation steps.

Index	**Experiment:$Mo(CO)_6$**	
	Perturbation	**Spectra #**
1	Solvent: 18.52g toluene	1-9
2	Add 0.45g $Mo(CO)_6$ solution	10-21
3	Add 0.45g $Mo(CO)_6$ solution	22-33
4	Add 0.45g $Mo(CO)_6$ solution	34-44
5	Add 0.44g $Mo(CO)_6$ solution	45-59
6	Add 0.45g $Mo(CO)_6$ solution	60-69
7	Add 0.45g $Mo(CO)_6$ solution	70-99
8	Add 0.46g $Mo(CO)_6$ solution	100-145

Table 5.5. Experimental design for $Mn_2(CO)_{10}$ measurements using Far-IR indicating the individual perturbation steps.

Index	**Experiment:$Mn_2(CO)_{10}$**	
	Perturbation	**Spectra #**
1	Solvent: 18.45g toluene	1-29
2	Add 0.44g $Mn_2(CO)_{10}$ solution	30-48
3	Add 0.44g $Mn_2(CO)_{10}$ solution	49-67
4	Add 0.44g $Mn_2(CO)_{10}$ solution	68-82
5	Add 0.44g $Mn_2(CO)_{10}$ solution	83-114
6	Add 0.66g $Mn_2(CO)_{10}$ solution	115-134

Table 5.6. Experimental design for $Re_2(CO)_{10}$ measurements using Far-IR indicating the individual perturbation steps.

Index	**Experiment: $Re_2(CO)_{10}$**	
	Perturbation	**Spectra #**
1	Solvent: 18.56g toluene	1-42
2	Add 0.44g $Re_2(CO)_{10}$ solution	43-56
3	Add 0.44g $Re_2(CO)_{10}$ solution	57-69
4	Add 0.44g $Re_2(CO)_{10}$ solution	70-81
5	Add 0.65g $Re_2(CO)_{10}$ solution	82-93
6	Add 0.65g $Re_2(CO)_{10}$ solution	94-107
7	Add 0.65g $Re_2(CO)_{10}$ solution	108-133

5.2.5 Data Analysis: The Application of BTEM to IR and Raman Spectroscopic Data

All Far-IR and Far-Raman spectra in this study were subjected to BTEM analysis. The primary objective of BTEM analysis is to extract the pure metal carbonyl spectra from the mixture spectra without any priori information. Although the typical system in this study simply involved two species, i.e. solvent and metal carbonyl, each collected spectrum is an overlap of the signals of metal carbonyl and

the solvent. Nevertheless, the process of deconvoluting the pure component spectra of each metal complex is not a simply task. In particular, difficulties can be encountered with the Raman deconvolution when dealing with highly overlapping bands such as a narrow M-M vibration bands and the broad instrumental response feature (*ca.* at 50-110 cm^{-1}).

Band Target Entropy Minimization (BTEM) has been successfully applied to in-situ mid-FTIR and mid-FT-Raman spectra from a variety of non-catalytic as well as catalytic homogenous organometallic systems (Chew *et al*., 2002; Li *et al*., 2002, 2003, 2004; Widjaja *et al*., 2002; 2003) and it has been shown capable of reconstructing the pure component spectra of numerous species in solution. It has been demonstrated that BTEM has the capability to extract the spectrum of intermediates that existed at ppm levels such as the rhodium carbonyl hydride (Li *et al*., 2002). Although rhodium carbonyl hydride constitutes less than 0.01% of the overall signal intensity, its spectra was deconvoluted with good signal to noise ratio using BTEM.

The problems in this study are analogous to the above situations, i.e. the goal of analyzing the in-situ IR and Raman spectra collected from the transition metal carbonyl system is to obtain the pure component IR and Raman spectra for each transition metal carbonyl complex. Similarly, the procedure of performing a BTEM analysis consists of two major steps (the details can be found in chapter 2): (1) performing singular value decomposition (SVD) to decompose the IR and Raman spectroscopic data in order to obtain the right singular vectors $\mathbf{V}^T$ which consist of the localized and meaningful spectral features; (2) transforming these right singular vectors $\mathbf{V}^T$ into a pure component spectrum one-at-a-time, where the transformation is achieved by a constrained non-linear optimization by simulated annealing.

5.3 Results: The Experimental Far-IR and Far-Raman Spectra

5.3.1 Experimental Data Sets

The series of spectra for $Mo(CO)_6$, $Mn_2(CO)_{10,}$ and $Re_2(CO)_{10}$ with both Far-IR and Far-Raman spectroscopy are shown in Figures 5.1, 5.2 and 5.3, respectively.

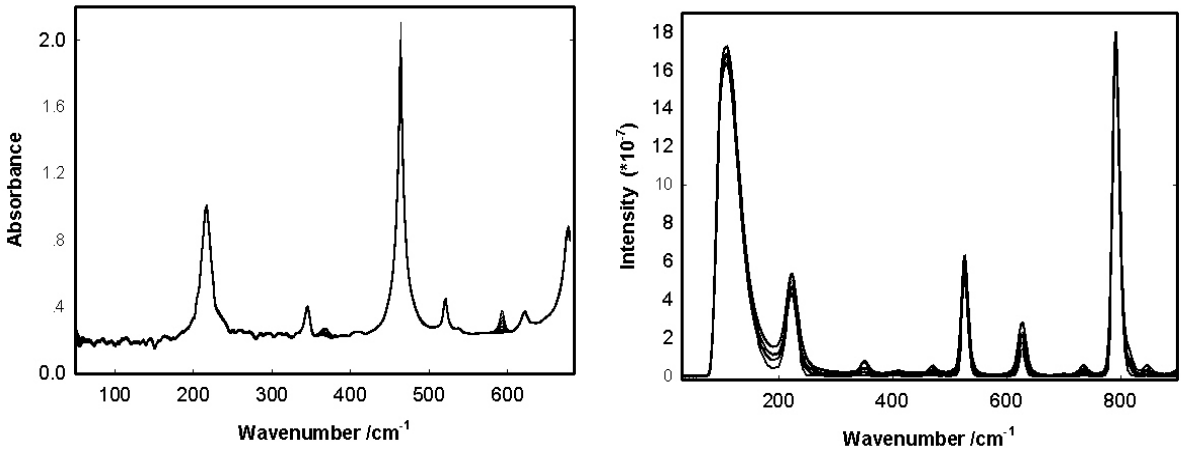

(a) (b)

Figure 5.1. (a) experimental Far-IR spectra of Mo $(CO)_6$ and (b) experimental Far-Raman spectra of Mo $(CO)_6$.

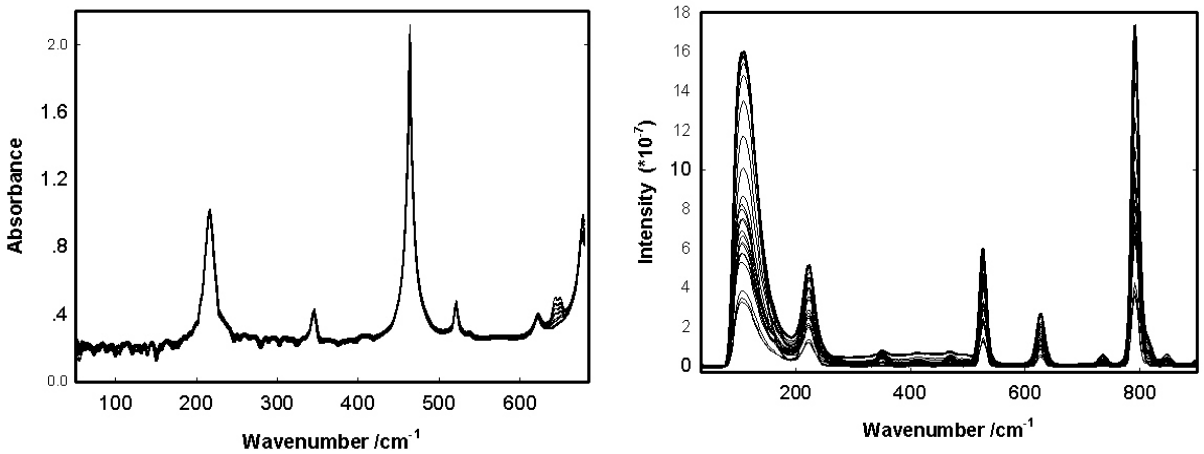

(a) (b)

Figure 5.2. (a) experimental Far-IR spectra of $Mn_2(CO)_{10}$ and (b) experimental Far-Raman spectra of $Mn_2(CO)_{10}$.

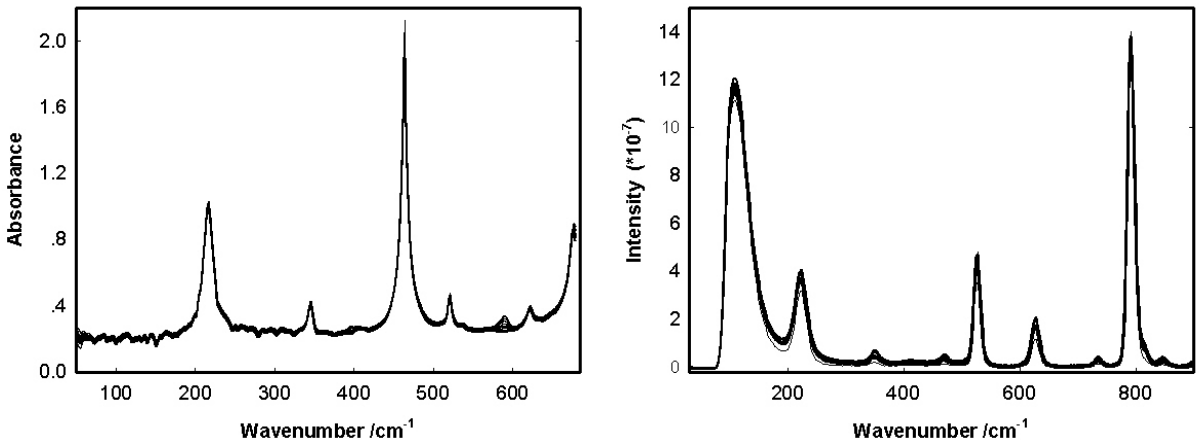

Figure 5.3. (a) experimental Far-IR spectra of $Re_2(CO)_{10}$ and (b) experimental Far-Raman spectra of $Re_2(CO)_{10}$.

In each of the three figures, part (a) shows the far infrared spectra and part (b) shows the far Raman spectra. Both far infrared and far Raman experimental spectra have a good signal-to-noise ratio. For the different metal carbonyl complexes, the distinguishing spectral features from far infrared experimental spectra can be seen in Figures 5.1 (a), 5.2 (a), and 5.3 (a). For instance, each metal carbonyl complex processes its own characteristic far infrared spectral bands such as the bands at circa 594 and 368 cm^{-1} appearing in Figure 5.1 (a), the band at circa 650 cm^{-1} appearing in Figure 5.2 (a) and the bands at circa 592 and 396 cm^{-1} appearing in Figure 5.3 (a).

It is noted that all these IR bands belong to M-C vibrations and appear above 300cm^{-1}. It is reasonable that the bands due to M-M vibrational stretches are not presented in far infrared range. The structures of $Mn_2(CO)_{10}$ and $Re_2(CO)_{10}$ are symmetric in terms of the metal atoms. Although IR and Raman spectroscopy both measure the vibrational energies difference of molecules they rely on different selection rules. Briefly, for a vibrational mode to be IR active, there be must a change in the dipole moment of the molecule and for a vibrational mode to be Raman active,

there must be a change in the polarizability of the molecule. Therefore, the symmetric stretch of an M-M vibrational motion is not IR active but is Raman active.

One of the most important spectral issues associated with the far Raman spectra of the different metal carbonyls, however, can not be easily seen from the raw experimental data. Broad bands with high intensity at circa 50-150 cm^{-1} exist in the far Raman spectra of each metal carbonyl solution. These bands are caused by the Raman scattering of the quartz cell. Since the M-M stretching frequencies are generally sharp and appear in the range below 200 cm^{-1} these peaks were, in large part, masked by the broad band from the quartz cell.

5.3.2 Spectral Reconstruction using BTEM

Both far infrared and far Raman experimental data sets of the three metal carbonyl complexes were subjected to BTEM analysis. Since there are no IR active very low wavenumber vibrations, only the results of the far Raman analysis below 300 cm^{-1} are shown in Figure 5.4.

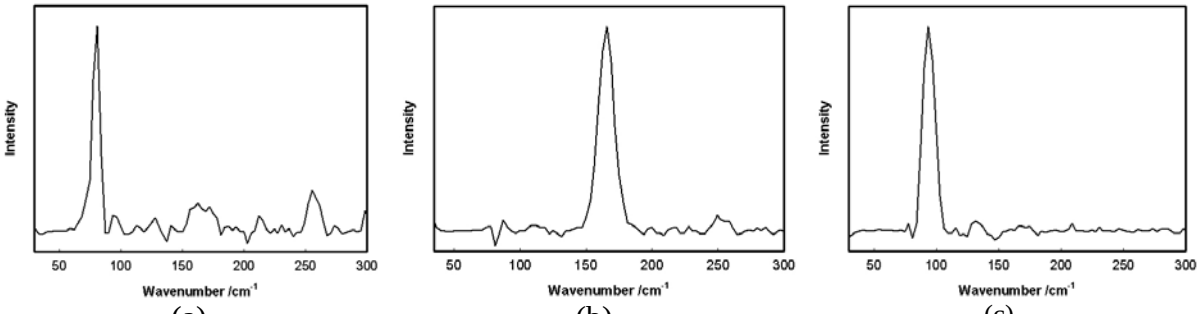

Figure 5.4. Reconstruction far Raman spectra of (a) $Mo(CO)_6$, (b) $Mn_2(CO)_{10}$ and (c) $Re_2(CO)_{10}$ in the range of 35-300 cm^{-1}.

In all cases, the far Raman spectrum of $Mo(CO)_6$, $Mn_2(CO)_{10}$ and $Re_2(CO)_{10}$ in the low wavenumber range of 35-300 cm^{-1} could be reconstructed. The large background effect from the quartz cell was successfully removed. It is worth mentioning that the band at circa 81 cm^{-1} in the Figure 5.4 (a) of $Mo(CO)_6$ is not due

to M-M vibrational motion but due to the symmetric vibrational stretches of M-C. The band at circa 166 cm^{-1} in the Figure 5.4 (b) of $Mn_2(CO)_{10}$ and the band at circa 94 cm^{-1} in the Figure 5.4 (c) of $Re_2(CO)_{10}$ arise from M-M vibrational transitions (See section 5.4 for DFT comparison).

In the M-C vibrational frequency range, both far IR and far Raman spectra of $Mo(CO)_6$, $Mn_2(CO)_{10}$ and $Re_2(CO)_{10}$ could be reconstructed. In Figures 5.5 to 5.7, the signal-to-noise of the far IR data (part a) analysis is significantly better than the far Raman (part b) results. This is due in large part to the good IR sensitivity versus the poor Raman scatter of the carbonyl complexes. In addition, the quality of the reconstructed far IR spectrum of $Mn_2(CO)_{10}$ is slightly worse than the IR spectra of $Mo(CO)_6$ and $Re_2(CO)_{10}$. This is due to spectral overlap with the intense solvent band. The far infrared spectral band of $Mn_2(CO)_{10}$ at circa 650 cm^{-1} (Figure 5.6 (a)) is in roughly the same position as the intense band of the solvent toluene (see Figure 5.2).

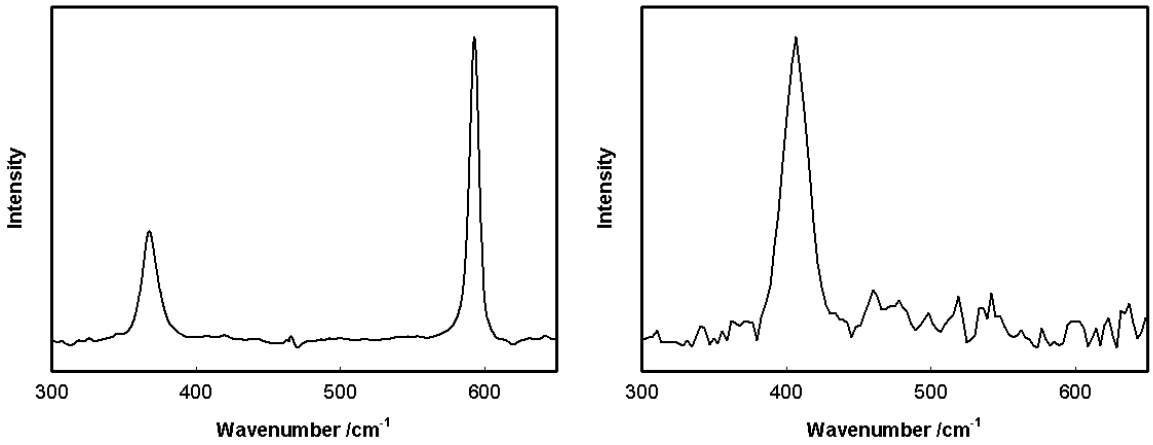

Figure 5.5. Reconstruction (a) far infrared spectrum and (b) far Raman spectrum of $Mo(CO)_6$.

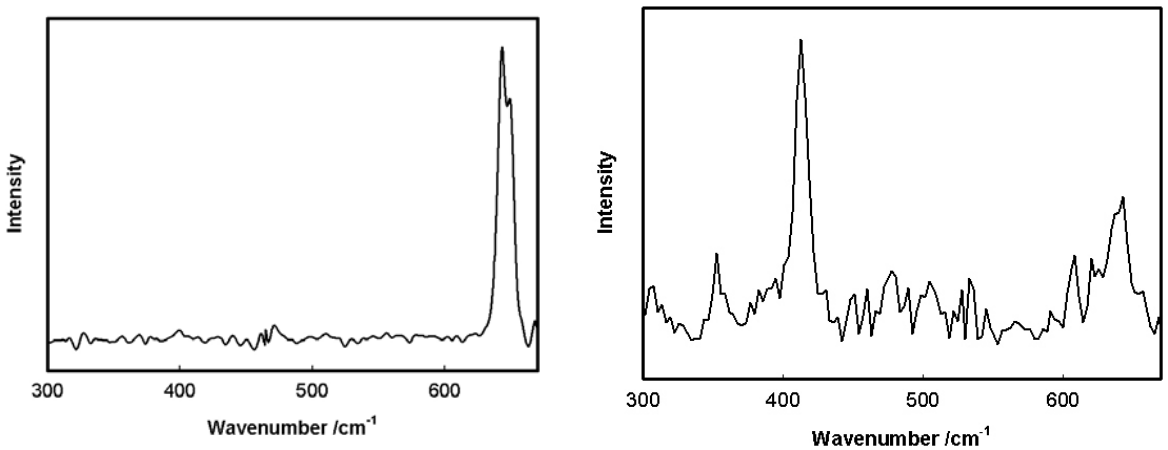

Figure 5.6. Reconstruction (a) far infrared spectrum and (b) far Raman spectrum of $Mn_2(CO)_{10}$.

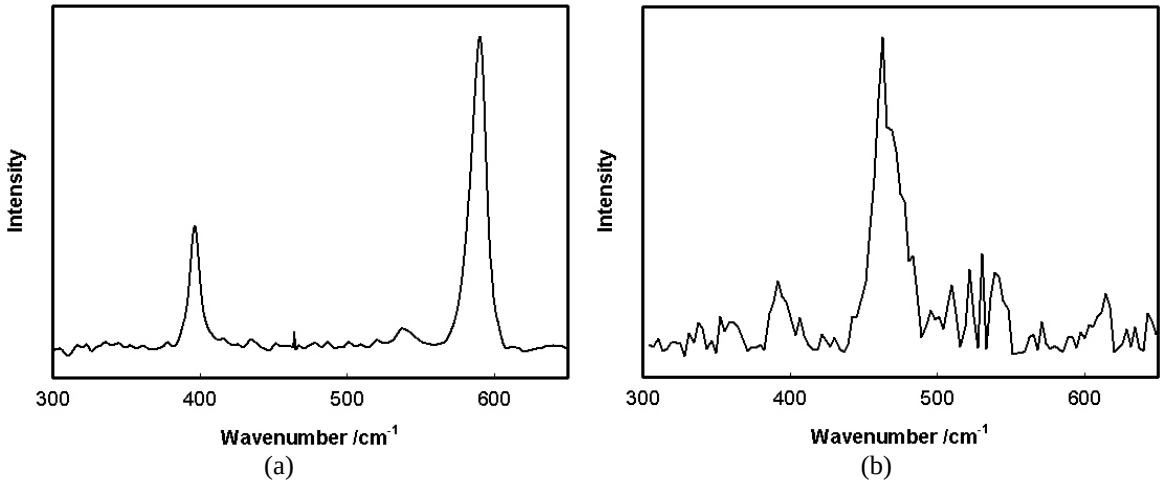

Figure 5.7. Reconstruction (a) far infrared spectrum and (b) far Raman spectrum of $Re_2(CO)_{10}$.

For each metal carbonyl complex, the far infrared and far Raman spectra are different due to the different vibrational motions involved. For example, $Mo(CO)_6$ has far infrared spectral bands at circa 594 and 368 cm^{-1} as well as far Raman spectral band at circa 407 cm^{-1}. Similarly, $Mn_2(CO)_{10}$ has far infrared spectral band at circa 650 cm^{-1} and far Raman spectral band at circa 413 cm^{-1}. Finally, $Re_2(CO)_{10}$ has far infrared spectral bands at circa 397 and 590 cm^{-1} and far Raman spectral band at circa 463 cm^{-1}.

5.4 Vibrational Frequencies Predictions by DFT

All the spectra obtained from BTEM analysis were used to examine the accuracy of the various combinations of density functionals and basis sets in predicting the far infrared and far Raman spectra of $Mo(CO)_6$,$Mn_2(CO)_{10}$and $Re_2(CO)_{10}$.

5.4.1 Computational Procedures

The DFT calculations were first performed to obtain molecular structures through geometry optimization. The prediction of IR and Raman spectra (vibrational frequencies) were carried out by employing the fully optimized molecular structure with further DFT frequency calculations. Four types of basis functions were selected for these calculations of molecular geometry and vibrational frequencies predictions. The first functional is the hybrid B3LYP method, which incorporates Becke's three-parameter exchange functional with the Lee, Yang, and Parr correlation functional (Lee *et al*., 1988; Becke,1993).The second method is the hybrid B3PW91, which combine Becke's three-parameter exchange functional with the Perdew-Wang's 1991 correlation functional (Perdew and Wang, 1992; Becke, 1993). These two hybrid functionals are often thought to be reliable and effective computational methods, especially for molecules containing transition metals. The third approach is PBE, an orthodox DFT functional, which has been shown to afford the better results than hybrids methods for neutral or mildly charged binuclear transition metal complexes (Petrie and Stranger, 2004; Allian *et al.*, 2006). The last approach used in this research is the LSDA (Local Spin Density Approximation), using the Slater (S) exchange functional and the Vosko-Wilk-Nusair (VWN) correlation functional for the DFT calculation (Vosko *et al.*, 1980). It is equivalent to SVWN. It should be noted that LSDA as implemented in the Gaussian 03 program may differ from other

implementations. For example, some other software packages with DFT use different correlation functionals such as Perdew's correlation functional.

With respect to the basis sets used, since Mo, Mn and Re are in different rows of the periodic table, the available basis sets are also different. (1) For $Mn_2(CO)_{10}$, three types of basis sets were used in both the geometry optimization and the frequencies calculations. In the first case the 6-311G basis sets were used for all the elements (metal and other atoms). In the second case, the LanL2DZ (Los Alamos effective core potential plus double-zeta) basis sets (Hay and Wadt, 1985; Nicklass *et al.*, 1995) were used. Thirdly, the polarized double zeta DGDZVP basis sets were used for the calculations. (2) For $Mo(CO)_6$, two types of basis sets, namely LanL2DZ and DGDZVP were used. (3) For $Re_2(CO)_{10}$, only LanL2DZ basis sets were selected since the other two are not applicable for heavy metal atom rhenium.

All of the computations were carried out with the Gaussian 03 program.

5.4.2 Results

5.4.2.1 $Mo(CO)_6$

Geometric optimizations and frequency calculations were carried out at DFT level of theory using the above mentioned four types of functionals, namely B3LYP, B3PW91, PBE and LSDA. Each of the density functionals were combined with the two basis sets described earlier namely the LanL2DZ and DGDZVP for both geometric optimizations and frequency predictions. The theoretically calculated vibrational bands for both IR and Raman frequencies are shown in Table 5.7.

As shown by Table 5.7, the DFT predictions of both IR and Raman frequencies were good while the predictions for lower wavenumber were slightly better than the higher wavenumber.

Table 5.7 Experimental and calculated vibrational wavenumbers (cm^{-1}) for $Mo(CO)_6$ and the corresponding deviation (%) in bracket.

		Raman		**IR**	
		M-C	M-C	M-C	M-C
B3LYP	LanL2DZ	86	415	390	612
		(6.17)	*(1.97)*	*(5.99)*	*(3.03)*
	DGDZVP	82	394	363	600
		(1.23)	*(-3.19)*	*(-1.36)*	*(1.01)*
B3PW91	LanL2DZ	87	430	409	623
		(7.41)	*(5.65)*	*(11.14)*	*(4.88)*
	DGDZVP	82	408	378	613
		(1.23)	*(0.25)*	*(2.72)*	*(3.20)*
PBE	LanL2DZ	82	426	405	603
		(1.23)	*(4.69)*	*(10.05)*	*(1.52)*
	DGDZVP	77	407	380	595
		(-4.94)	*(0)*	*(3.26)*	*(0.17)*
LSDA	LanL2DZ	82	454	439	622
		(1.23)	*(11.55)*	*(19.29)*	*(4.71)*
	DGDZVP	76	435	413	615
		(-6.17)	*(6.88)*	*(12.23)*	*(3.54)*
Expt.		81	407	368	594

It is clear that the hybrid functionals B3LYP and B3PW91with DGDZVP as the basis set generated better predictions than the other approaches for both IR and Raman of the carbonyl vibrational frequencies (comparison with experimentally obtained spectra shows a mean error less than 3.2%). It has been previously shown that the hybrid Hartree-Fock/DFT methods such as B3LYP and B3PW91 are the most reliable approaches for the theoretical calculation of organometallic compounds (Lee *et al.*, 1988; Li, *et al.*, 2006). In contrast, the predictions through the combination of LSDA method with either LanL2DZ or DGDZVP show quite large deviations from

the reference values. It is also noted that the largest deviations for both Raman and IR spectra occur in the range of 350~400 cm^{-1}, i.e. M-C bands at 407 cm^{-1} for Raman spectrum and 368 cm^{-1} for IR spectrum.

The relative intensities of the vibrations are an equally important piece of information. In Figures 5.8 and 5.9, the best spectral estimate for $Mo(CO)_6$ (using B3PW91 functional with DGDGVP basis set) is compared to the experimental spectrum of $Mo(CO)_6$. In Figure 5.8, it is clearly seen that the predicted and experimental IR spectra have similar relative band intensities.

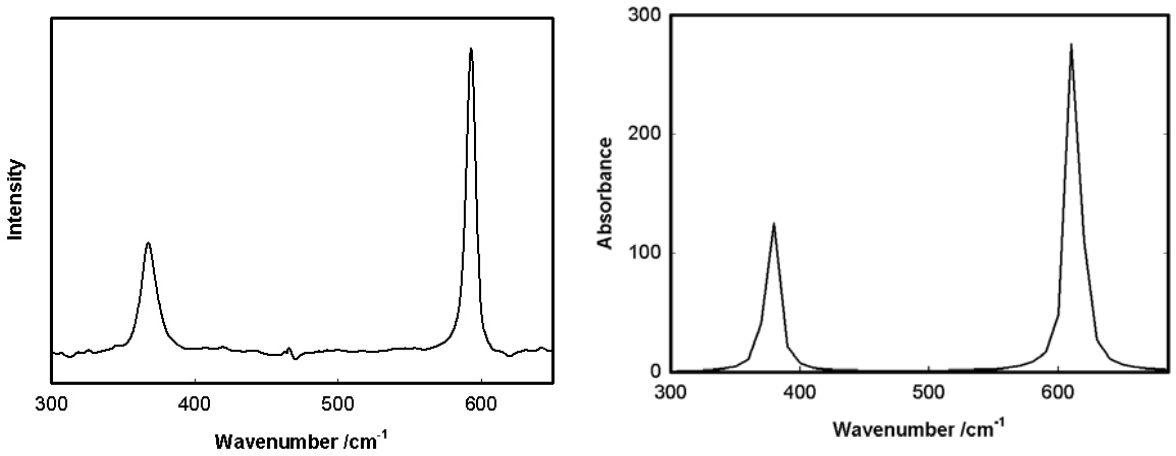

(a) (b)

Figure 5.8. Comparison of (a) the reconstruction IR spectrum of $Mo(CO)_6$ from the experiment and (b) the predicted IR spectrum of $Mo(CO)_6$ using DFT.

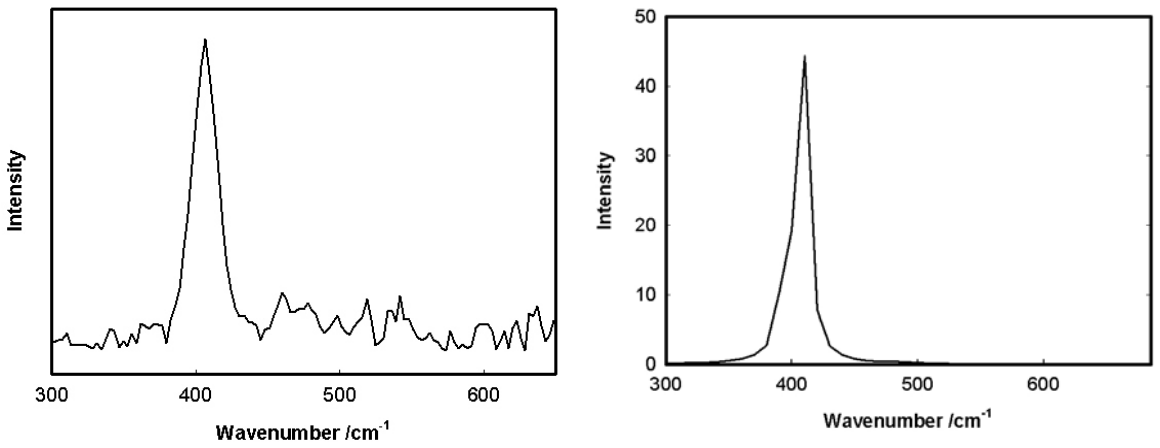

(a) (b)

Figure 5.9. Comparison of (a) the reconstruction Raman spectrum of $Mo(CO)_6$ from the experiment and (b) the predicted Raman spectrum of $Mo(CO)_6$ using DFT.

5.4.2.2 $Mn_2(CO)_{10}$

Four types of proposed functionals, namely B3LYP, B3PW91, PBE and LSDA with three types of basis sets (6-311G, LanL2DZ and DGDZVP) were employed in the calculations of molecular structure optimizations and frequency calculations of $Mn_2(CO)_{10}$. The theoretically calculated vibrational frequencies for both IR and Raman spectra are shown in Table 5.8.

From Table 5.8, it is clear that the DFT predictions of both IR and Raman frequencies were good although the predictions of Raman vibrational frequencies using LSDA functionals were not as good as the other methods, especially for the M-M band calculations of Raman frequencies (the biggest deviation is 68 cm^{-1} from the experimental values – compare the predicted value of 481 cm^{-1} with experimental 413 cm^{-1}). In addition, it is noted that the predictions for both IR and Raman frequencies using the LanL2DZ basis set are always higher than those using other basis sets. Furthermore, the two hybrid functionals B3LYP and B3PW91 and the PBE functional with DGDZVP and 6-311G as the basis sets generated quite good predictions for both IR and Raman of the carbonyl vibrational frequencies when compared to experimentally obtained spectrum (the differences from experimental values were less than 45 cm^{-1}). Compared to the results of mononuclear metal carbonyl $Mo(CO)_6$ using the PBE method, the results shown in Table 5.8 indicated that a pure DFT functional like PBE affords reliable predictions when it is applied to neutral binuclear transition metal complexes (Petrie and Stranger, 2004). In addition, the results also show that with DGDZVP as the basis set, the calculations of vibrational frequencies usually provide better estimates than other basis sets used in this study.

Table 5.8. Experimental and calculated vibrational wavenumbers (cm^{-1}) for $Mn_2(CO)_{10}$ and the corresponding deviation (%) in bracket.

		Raman		IR
		M-M	M-C	M-C
B3LYP	LanL2DZ	152 *(-8.43)*	418 *(1.21)*	669 *(2.92)*
	DGDZVP	153 *(-7.83)*	404 *(-2.18)*	660 *(1.54)*
	6-311G	143 *(-13.86)*	409 *(-0.97)*	653 *(0.46)*
B3PW91	LanL2DZ	161 *(-3.01)*	439 *(6.23)*	692 *(6.46)*
	DGDZVP	162 *(-2.41)*	421 *(1.94)*	679 *(4.46)*
	6-311G	153 *(-7.83)*	427 *(3.39)*	672 *(3.38)*
PBE	LanL2DZ	155 *(-6.63)*	441 *(6.78)*	677 *(4.15)*
	DGDZVP	155 *(-6.63)*	429 *(3.88)*	668 *(2.77)*
	6-311G	147 *(--11.45)*	430 *(4.12)*	660 *(1.54)*
LSDA	LanL2DZ	180 *(8.43)*	481 *(16.46)*	713 *(9.69)*
	DGDZVP	178 *(7.23)*	464 *(*12.35)	698 *(7.38)*
	6-311G	171 (3.01)	468 *(13.32)*	690 *(6.15)*
Expt.		166	413	650

Figures 5.10 and 5.11 show that the comparison of the experimental spectrum and the predicted spectrum of both IR and Raman spectra. The predicted spectrum of

both IR and Raman spectra shown in Figures 5.10 and 5.11 were one of best predicted spectra for $Mn_2(CO)_{10}$, and this used the B3PW91 functional with DGDGVP basis set. As seen in Figure 5.10, that the relative intensities of predicted and experimental IR spectra are in good agreement. The most intense bands are located at circa 650 cm^{-1} and the other two small peaks at circa 400 and 480 cm^{-1}. In comparison, the quality of the reconstructed Raman spectrum from the experiment is a bit poor. It can be seen in Figure 5.11 that the bands at circa 410 and 490 cm^{-1} of both the predicted and experimental Raman spectra have similar relative intensities.

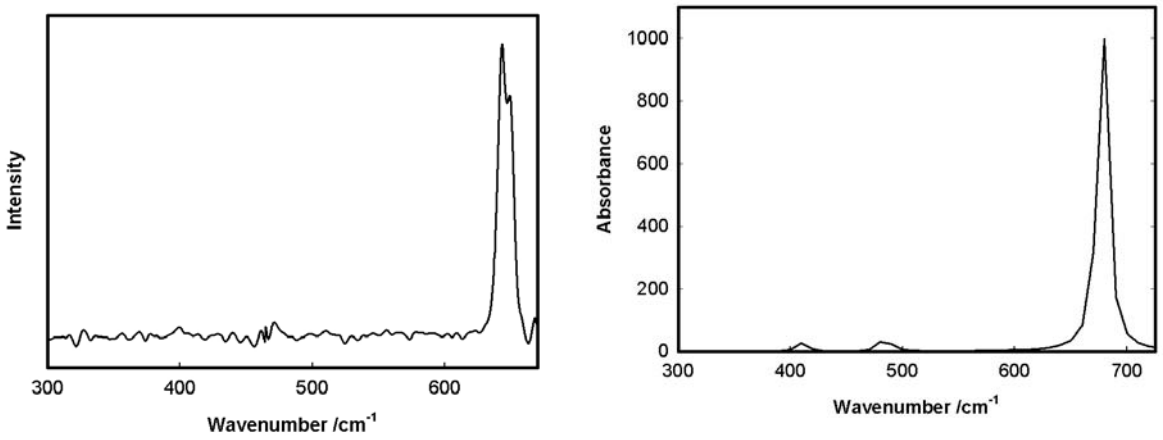

(a) (b)

Figure 5.10. Comparison of (a) the reconstruction IR spectrum of $Mn_2(CO)_{10}$ from the experiment and (b) the predicted IR spectrum of $Mn_2(CO)_{10}$ using DFT.

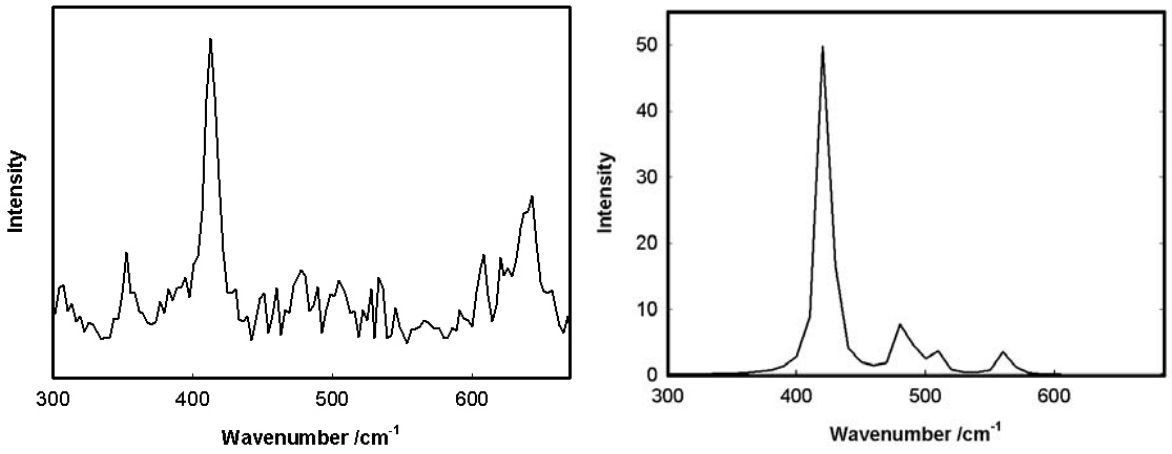

(a) (b)

Figure 5.11. Comparison of (a) the reconstruction Raman spectrum of $Mn_2(CO)_{10}$ from the experiment and (b) the predicted Raman spectrum of $Mn_2(CO)_{10}$ using DFT.

5.4.2.3 $Re_2(CO)_{10}$

The same four types of proposed functionals, namely B3LYP, B3PW91, PBE and LSDA with LanL2DZ basis sets (basis sets 6-311G and DGDZVP can not be used for the atom rhenium) were combined to carry out the calculations of molecular structure optimizations and frequency calculations of $Re_2(CO)_{10}$. The theoretically calculated vibrational frequencies for both IR and Raman spectra are shown in Table 5.9.

Table 5.9. Experimental and calculated vibrational wavenumbers (cm^{-1}) for $Re_2(CO)_{10}$ and the corresponding deviation (%) in bracket.

		Raman		IR	
		M-M	M-C	M-C	M-C
B3LYP	LanL2DZ	104 *(10.64)*	470 *(1.51)*	420 *(5.80)*	605 *(2.54)*
B3PW91	LanL2DZ	101 *(7.45)*	483 *(4.32)*	443 *(11.59)*	614 *(4.07)*
PBE	LanL2DZ	99 *(5.32)*	476 *(2.81)*	433 *(9.07)*	592 *(0.34)*
LSDA	LanL2DZ	98 *(4.26)*	503 *(8.64)*	461 *(16.12)*	602 *(2.03)*
Expt.		94	463	397	590

It is shown that the DFT calculations of both IR and Raman frequencies were good. It is also shown that the density functional PBE with LanL2DZ as the basis set generated the best predictions for both IR and Raman carbonyl vibrational bands when compared to experimentally obtained spectrum. All the predicted frequency values for $Re_2(CO)_{10}$ obtained using LanL2DZ as basis sets have higher wavenumbers than the experimental values. This result is consistent with the previous results for $Mo(CO)_6$ and $Mn_2(CO)_{10}$ in this study.

A comparison of the experimental and predicted IR and Raman spectra are shown in Figures 5.12 and 5.13. The predicted spectra for IR and Raman shown in Figures 5.12 and 5.13 were the best predicted spectra for $Re_2(CO)_{10}$, and this used the PBE functional with LanL2DZ basis set. It is clear that both the predicted and experimental spectra of IR and Raman have similar band positions and similar relative intensities.

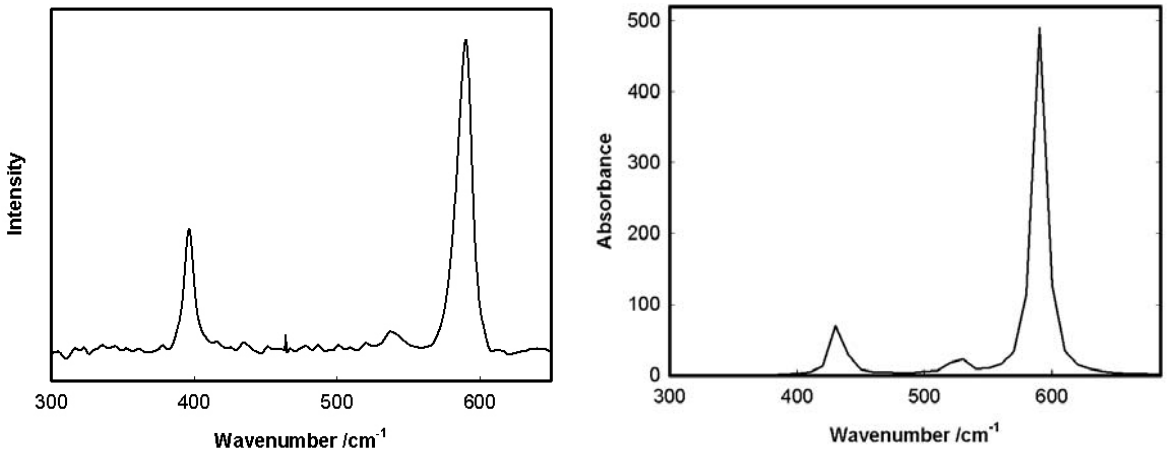

(a) (b)

Figure 5.12. Comparison of (a) the reconstruction IR spectrum of $Re_2(CO)_{10}$ from the experiment and (b) the predicted IR spectrum of $Re_2(CO)_{10}$ using DFT.

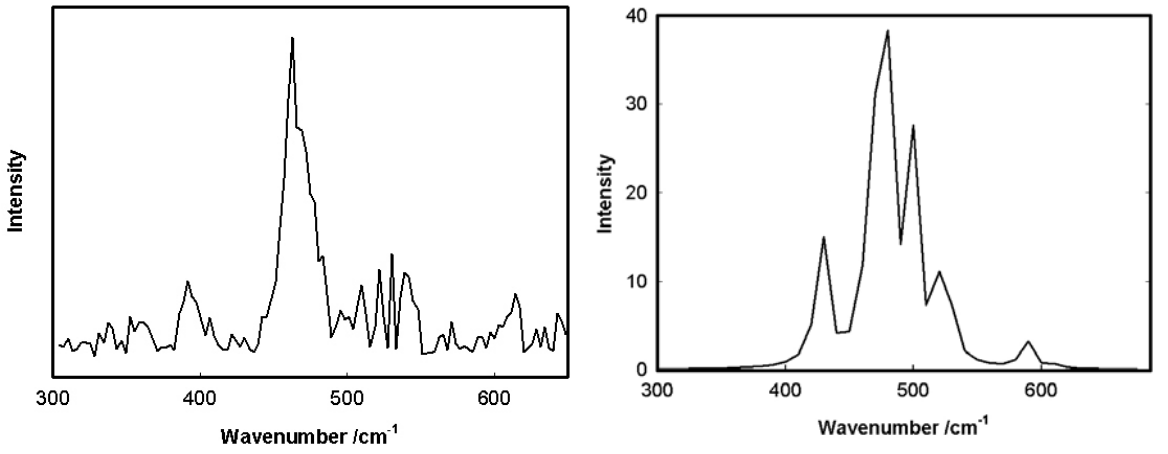

(a) (b)

Figure 5.13. Comparison of (a) the reconstruction Raman spectrum of $Re_2(CO)_{10}$ from the experiment and (b) the predicted Raman spectrum of $Re_2(CO)_{10}$ using DFT.

In summary, the results from three different natural metal carbonyls, i.e. $Mo(CO)_6$, $Mn_2(CO)_{10}$ and $Re_2(CO)_{10}$ indicated that:

(1) The hybrid functionals B3LYP and B3PW91 performed better than the other two functionals (PBE and LSDA) in the calculations of frequency predictions for the mononuclear metal carbonyl $Mo(CO)_6$. Additionally, the basis set DGDZVP produced better predictions than basis set LanL2DZ when using the hybrid functionals.

(2) For binuclear metal carbonyl $Mn_2(CO)_{10}$ and $Re_2(CO)_{10}$, the pure DFT functional PBE and the two hybrid DFT functionals B3LYP and B3PW91 generally gave satisfactory predictions for both the IR and Raman vibrational frequencies.

(3) DFT calculations can provide quite reliable vibrational frequency predictions for neutral metal carbonyls. The predicted band positions and relative intensity are very consistent with the experimental spectra.

(4) DGDZVP is a reliable basis set for the calculations of geometric optimization and vibrational frequencies predictions for both mononuclear and binuclear metal carbonyls. Note that DGDZVP is not applicable to rhenium.

(5) With basis set LanL2DZ, the frequency predictions are in general overestimated compared to experimental values.

(6) The calculations of vibrational frequencies using LASD functional were normally not as good as those using the other three DFT functionals.

5.5 Summary

5.5.1 The Present Results and Conclusions

The BTEM algorithm was successfully applied to these far-IR and far-Raman spectroscopic data to reconstruct pure component spectra. The predicted far-IR and far-Raman vibrational frequencies of $Mo(CO)_6$, $Mn_2(CO)_{10}$ and $Re_2(CO)_{10}$ are in

good agreement with the reconstructed IR and Raman spectra from experiments. In particular, the M-C vibrations in the IR and Raman could be assigned as well as the M-M vibrations in the Raman.

The present results indicate that theoretical calculations combining with the experimental spectroscopies is a valuable tool to assign the vibrations of metal-metal, metal-carbon bonds of metal carbonyls at low wavenumber. Such a combined approach seems be applicable to a wide range of structural identification problems in reactive organometallic systems, such as homogeneously catalyzed systems, in order to identify new species in solution.

5.5.2 Systems for Future Study

A combined approach of far-vibrational spectroscopy, BTEM and DFT should be a useful tool for a wide range of structural identification problems. These include, but are not restricted to: (1) reactive organometallic systems, such as homogeneously catalyzed systems, in order to directly identify the presence of metal-metal bonds, new species and intermediates in solution etc, (2) Since regio-isomers show profound difference in the low-wavenumber regions (they usually appear almost identical in mid-wavenumber vibrational region), on-line and in-situ monitoring of regio-selectivities should become possible, (3) Since conformers also show pronounced differences in low-wavenumber regions, it should be possible to readily determine their relative concentrations and hence their free energy differences, and (4) The slow motions of lattice vibrations in solids are in the Terahertz range (far-IR and Far-Raman) and the application of BTEM should allow their deconvolution.

Chapter 6

Raman Optical Activity of Organic Chiral Molecules and the Development of General Chemometric Methods for the Signal Processing of ROA Spectroscopic Data

In this chapter, the two primary problems are (1) to experimentally obtain good Raman optical activity (ROA) spectra for chiral solutions and (2) to successfully develop Chiral-BTEM so that the broader system identification problem (for example, the determination of the absolute configurations of chiral compounds and the determination of the concentration or the enantiomeric excess) in pharmaceutical and fine chemical reactive systems can be solved. The critical issue is the presence of stereo-isomers and the need for vibrational optical activity in order to measure them.

The development of exploratory chemometric methods to resolve pure component spectra from chiroptical data has many challenges. In this work, the determination of all the concentrations of all species or enantiomeric excess (ee) of all chiral species is also involved. One of the biggest issues in stereochemistry is the determination of enantio-excess (the stereochemist's version of selectivity). Many methods for analysis of ee take a long time i.e. chiral chromatography measurements which take up to circa 1 hour to perform, and can thus only be used for stable compounds. In addition, it is well known that it is not easy to completely separate one enantiomer from one another through a chromatographic column (enantiomers have identical physico-chemical properties like free energy, boiling point, etc). Moreover, all existing methods of determination of ee

require some sort of a prior knowledge in order to calibrate the analysis. A method that could determine enantiomeric excess without any prior information would represent a very significant contribution to the science of stereochemistry.

6.1 A Brief Introduction to Chirality

Chirality is widespread in nature and is fundamental to life. The understanding of this peculiar property can be traced back to Louis Pasteur, who discovered that two crystalline forms of the sodium-ammonium double salt of para-tartaric acid existed as two asymmetric hemihedral forms that were mirror images of one another in 1848 (Debre and Forster, 1998). The term 'chiral', meaning 'hand', was first introduced into science by Lord Kelvin in 1904, in his Baltimore Lectures he stated ...*"I call any geometrical figure, or group of points, chiral, and say that it has chirality, if its image in a plane mirror, ideally realized, cannot be brought to coincide with itself."* (Barron, 2007).

Generally speaking, chirality in organic chemistry is a property of carbon compounds which have four different components, or substituents, attached to one carbon. This central carbon atom is known as a chiral center or center of chirality. Enantiomers represent the simplest molecular examples of chirality (Figure 6.1) and more complex examples are represented by multiple chiral centers, such as those arising in diasteriomers. Enantiomers have the same constitution /connectivity but the arrangement in 3D space is a mirror image. Figure 6.1 uses the conventional Fischer representation for illustrating the arrangement.

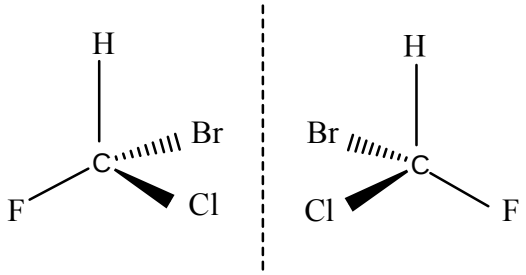

Figure 6.1 Illustration of a pair of enantiomers as the Fischer projection.

The inherent chirality of living systems dictates extraordinary specificity in the recognition of chiral molecules since a chiral molecule and its mirror image (such as found for many pharmaceuticals and fragrances) will almost always have different biological effects. A simple example is provided by carvone. The enantiomer S-(+)-carvone has the smell and taste of caraway seeds, whereas, the enantiomer R-(−)-carvone has the smell and taste of spearmint. This requires that the chiral purity must be controlled during the synthesis of these compounds so that only the required enantiomer is produced.

6.2 Raman Optical Activity (ROA)

Although this chapter will focus on just one type of chiroptical data for purpose of illustration, namely ROA spectroscopic data, the ultimate aim of this chapter is to provide a general solution for all chiroptical spectroscopies. In the following section, a brief introduction of the available chiral spectroscopies is given.

6.2.1 A Survey of Chiral Spectroscopies

The difference in the response of a chiral molecule to left and right circularly polarized light is the basis of all chiral optical spectroscopic techniques. Circularly polarized radiation exists across the electromagnetic spectrum. A survey of known chiral spectroscopies are: (1) X-ray CD. It has a very high energy, but the merit is that one can easily obtain the spectral response from a chiral molecule. The main disadvantage is that normal molecules are usually destroyed by the measurement (Alagna *et al.*, 1998; Stewart *et al.*, 1999); (2) UV-Vis CD. It is the circular dichroism in the electronic transitions in the chiral molecules. Since it also has relatively high energy, its application has been extensively studied for a long time. However, it can only provide information on molecules having electronic chromophores. (3) Vibrational optical activity (VOA). This includes both vibrational circular dichroism (VCD) and the differential Raman optical activity (ROA). Since the difference in the response of a chiral molecules to left and right circularly polarized light is proportion to the frequency of the light (Buckingham, 1994), low frequency VOA has only been rapidly developed in the last thirty years with the major advances in the development of instrumental techniques. These two different techniques, VCD and ROA, can provide complementary information (like the relationship between IR and Raman) on the vibrational optical activity. They have been proven to be the most incisive tools for the studies of biological molecules and organic chiral species.

6.2.2 Raman Optical Activity

Raman Optical Activity (ROA) measures a small difference in the Raman-

scattered intensity of right and left circularly polarized incident light. ROA combines the structural specificity of vibrational spectroscopy with stereo-sensitivity of chiral detection.

ROA is a form of VOA and is complementary to VCD in the same way that Raman spectroscopy is complementary to IR spectroscopy. In the earlier years, the technique of VCD had more applications in the studies of stereochemistry and biologically important molecules such as proteins and nucleic acids (Nafie *et al.*, 1998; Freedman *et al.*, 1995, 1996, 2005; Baumruk and Keiderling, 1993; Keiderling *et al.*, 1994; Lassen *et al.*, 2006; Schweitzer-Stenner, 2004, 2006; Lamparska *et al.*, 2006). In ROA "the scattered intensity is slightly different in the right and left-circularly polarized incident light" (Zhu *et al.*, 2005). Since the Raman effect is already a rather rare phenomenon, the even more difficult measurement of ROA has generally been restricted to neat liquid samples.

Water is an excellent medium for studies of biomolecules and it is not excluded as solvent for ROA but not applicable for VCD. Recently, the major advances achieved in ROA instrumentation have provided the necessary increase in sensitivity so that the ROA spectra of biological molecules in the aqueous solutions and chiral molecules in solutions can be recorded (Yu *et al.*, 1995; Nafie *et al.*, 1995; Barron *et al.*, 2000, 2003, 2004, 2006; McCool *et al.*, 2003, 2004; Bell *et al*., 1999; Smyth *et al.*, 2001; Schweitzer-Stenner *et al.*, 2002; Blanch *et al.*, 2002, 2003, 2004; Zhu *et al.*, 2005). have made great contributions to the ROA studies in biological science and good ROA spectra of many types of biomolecules such as protein, nucleic acids, viruses and biopolymers have been recorded to provide detailed information on the molecular structure and the functions of these biomolecules.

ROA is also a promising technique for determining optical purity, especially in the pharmaceutical situations. Nafie and co-workers designed and built the first commercial ROA spectrometer. It provides us with a chance to take measures of both Raman and ROA simultaneously. ROA combines the structural specificity of Raman spectroscopy with the stereo-sensitivity of chiral detection. This gives access to multiple, well-defined bands that can provide chemical quantitative information. This information will enhance our determination of optical purity since there is no need for separation or tedious method development. The analysis of chiral purity using ROA has been reported by Spencer *et al.* (1996). They demonstrated that ROA can be used to identify the enantiomeric mixtures with quite high enantiomeric excess (higher than 98%). The related chemometric methods for ee determination using ROA are less studied. Our aim here is to apply a new chemometric method, Chiral-BTEM, to retrieve the pure ROA spectra from mixtures and to determine ee or the concentrations.

6.2.3 Stereochemistry and ROA

For a ROA spectrometer, Raman and ROA spectra (in this thesis, only one of the forms of ROA, namely scattered circular polarization will be addressed) are taken simultaneously during the period of measurements. The spectroscopies associated with the spectra have an optical path length l, wavenumber $\tilde{\nu}$ and four principal types of scattered Raman intensity (I):

(1) I_L : the intensity of the left circularly polarized components of the scatter light (subscript L);

(2) I_R : the intensity of the right circularly polarized components of the scatter light (subscript *R*);

(3) $I_{Raman} = (I_R + I_L)$ for unpolarized Raman scattering intensity (subscript *Raman*);

(4) $I_{ROA} = (I_R - I_L)$ for ROA intensity (subscript *ROA*).

The last two quantities I_{Raman} and I_{ROA} are directly given by ROA measurements.

6.2.3.1 Achiral Molecules

For achiral molecules, the scattered Raman intensity of left and right circularly polarized are identical over the entire frequency range, so the difference is identically zero and there is no signal in the ROA spectra. With the Eqs.6.1 ~6.3, we can explain the absorbance of an achiral molecule (superscript ac) clearly and easily.

$$I^{ac}_{Raman}(\tilde{\nu}) = (I^{ac}_R(\tilde{\nu}) + I^{ac}_L(\tilde{\nu})) \qquad I^{ac}_L(\tilde{\nu}) \geq 0, \;\; I^{ac}_R(\tilde{\nu}) \geq 0, \tag{6.1}$$

$$I^{ac}_R(\tilde{\nu}) = I^{ac}_L(\tilde{\nu}) \tag{6.2}$$

$$I^{ac}_{ROA}(\tilde{\nu}) = (I^{ac}_R(\tilde{\nu}) - I^{ac}_L(\tilde{\nu})) = 0 \qquad I^{ac}_R(\tilde{\nu}) \geq 0, \;\; I^{ac}_L(\tilde{\nu}) \geq 0 \tag{6.3}$$

6.2.3.2 Diasteriomers

Briefly, it can be noted that a diasteriomer is a chiral molecule with more than one chiral center and each of the chiral centers has a non-zero ROA spectrum. Eq. 6.4 is valid for any diasteriomer.

$$I^{di}_{ROA}(\tilde{\nu}) = (I^{di}_R(\tilde{\nu}) - I^{di}_L(\tilde{\nu})) \neq 0 \tag{6.4}$$

6.2.3.3 Enantiomers

In chemistry, two stereoisomers are said to be enantiomers if they can be superimposed on the mirror images of one another. A simple analogy would be the relationship between left and right human hands. Let (+)-enantiomer and (−)-enantiomer denote a pair of enantiomers. When one pure enantiomer, for example (+)-enantiomer, interacts with the right and left circularly polarized incident light, I_R^+ and I_L^+ are non-negative and unequal (see Eq.6.5). In addition, the ROA spectra for a pair of enantiomer are mirror images of each another. The set of basic relationships for I_R^+ and I_L^- as well as I_L^+ and I_R^- are given by a group of equations (see Eq.6.5). In addition, as illustrated by Figure 6.1.1 previously, the special relationships for the observable spectra are given by a group of equations (see Eq.6.6.).

$$\begin{cases} I^+_{Raman}(\tilde{\nu}) = (I^+_R(\tilde{\nu}) + I^+_L(\tilde{\nu})), \quad I^+_R(\tilde{\nu}) \neq I^+_L(\tilde{\nu}) \qquad I^+_R(\tilde{\nu}) \geq 0, \;\; I^+_L(\tilde{\nu}) \geq 0 \\ I^-_{Raman}(\tilde{\nu}) = (I^-_R(\tilde{\nu}) + I^-_L(\tilde{\nu})), \quad I^-_R(\nu) \neq I^-_L(\tilde{\nu}) \qquad I^-_R(\tilde{\nu}) \geq 0, \;\; I^-_L(\tilde{\nu}) \geq 0 \\ I^+_R(\tilde{\nu}) = I^-_L(\tilde{\nu}), \qquad I^+_L(\tilde{\nu}) = I^-_R(\tilde{\nu}) \\ I^+_{ROA}(\tilde{\nu}) = (I^+_R(\tilde{\nu}) - I^+_L(\tilde{\nu})), \qquad I^-_{ROA}(\tilde{\nu}) = (I^-_R(\tilde{\nu}) - I^-_L(\tilde{\nu})) \end{cases} \tag{6.5}$$

$$\Rightarrow \quad \begin{cases} I^+_{Raman}(\tilde{\nu}) = \; I^-_{Raman}(\tilde{\nu}) \\ I^+_{ROA}(\tilde{\nu}) = - \; I^-_{ROA}(\tilde{\nu}) \end{cases} \tag{6.6}$$

It is easy to deduce that a racemic solution, a solution of equal parts of an optically active isomer and its enantiomer, has a zero ROA spectrum and positive Raman spectrum along the whole range.

In summary, achiral molecules have positive Raman spectra but zero ROA spectra. The pure chiral molecules have positive Raman spectra and non-zero ROA spectra. For a pair of enantiomers, their Raman spectra are identical but the ROA spectra are mirror images.

6.3 Enantiomeric Excess

Enantiomeric excess (ee) determination of complex mixtures is a challenge for the analytical chemist. Many methods for analysis of ee involve separation and purification steps. Therefore they can be time consuming and very costly. However, the combination of vibrational optical activity techniques (experimentally, both ROA and VCD have made considerable progresses in the last few decades) and chemometric methods of multivariate calibration can be a very promising tool for ee determination of complex mixtures. Some preliminary work in the filed of the analytical capabilities of the VCD and ROA techniques on the ee determination were carried out by several groups (Spencer *et al.*, 1996; Hecht *et al.*, 1995; Guo *et al.*, 2004, 2005). Nafie and his co-worker (2004) successfully applied the chemometric method of partial least squares (PLS) to VCD quantitative analysis for multi-component chemical system. Previous chemometric methods for the analysis of ROA mixture spectra, however, have been limited. Some preliminary analytical work for ROA spectra using Chiral-BTEM will be carried out in the current chapter.

Chiral-BTEM/BTEM can be used to retrieve pure component spectra (Raman or ROA) from the measurements of multi-component systems. Further calibrations using the retrieved pure component spectra can provide concentration information for each species present and thus EE can be determined. For concentrations C^+ and C^- of the (+) and (−) enantiomers of chiral molecules in a solution, the %EE of the chiral sample is $(C^+\text{-}C^-)$ / $(C^+ + C^-)$ ×100% where, the (+)-enantiomer is selected as the reference. The total concentration $(C^+ + C^-)$ can be determined by the Raman measurement and the difference

in concentrations (C^+-C^-) can be then determined from the ROA measurement (see Eqs.6.7 and 6.8).

$$I_{Raman} = (C^+ + C^-) \cdot l \cdot i_{Raman} \tag{6.7}$$

$$I_{ROA} = (C^+ - C^-) \cdot l \cdot i^+_{ROA} \tag{6.8}$$

Where, I_{Raman} and I_{ROA} are the intensity of Raman and ROA measurements obtained from experiments and i_{Raman} and i^+_{ROA} are analogous to the molar absorptivity of IR spectroscopy but they are the molar properties for Raman and ROA.

A sample that contains only a single enantiomer is enantiomeric pure, and is said to have an enantiomeric excess of 100% (or -100%). A mixture of equal amounts of the two enantiomers of a chiral compound has an ee identically 0 and is called a racemic mixture or simply racemate. Choosing (+)-enantiomer as ee reference, the ROA has its maximum value for a sample of 100% EE in (+)-enantiomer, the ROA spectra is zero across the entire spectrum for the racemic mixture, and the ROA has its minimum value for a sample with -100% ee in the (−)-enantiomer.

6.4. Computational Section

The application of BTEM/Chiral-BTEM to UV and CD spectroscopic data (a type of chiroptical data) has been studied in the Chapter 4. The main goal of this chapter is to investigate the application of BTEM/Chiral-BTEM to reconstruct the pure component Raman and ROA spectra from spectroscopic data for a chiral system.

In BTEM, the entropy minimization concept is used in the objective function and optimization is performed using Simulated Annealing so that the simplest spectral patterns can be achieved. ROA spectra, especially if the sample is not a neat liquid chiral

compound, usually have low signal-to-noise ratios. Moreover, the other problem with ROA spectra is that the shape, relative intensity and sign of a few vibrational bands are not entirely reproducible. BTEM is good at processing low signal-to-noise ratio data. In addition, the second problem is analogous to the difficulties like spectra nonlinearities, band position shifting and band shapes changing. BTEM has demonstrated that it can accommodate these problems quite well when applied to the FTIR spectra.

In multi-component chiroptical data analysis, there are two frequent major tasks: (1) determine the pure component Raman and ROA spectra of the observable species and (2) determine concentrations of all observable species present and/or determine the enantiomeric excess if there are enantiomers present.

The first task will be tested using the Chiral-BTEM method. In order to retrieve physically meaningful spectra, based on the spectral features of ROA (see section 6.2.3), three constraints are imposed on the optimization process in Chiral-BTEM: (1) non-negativity in estimated Raman spectra for all the species, (2) the estimated ROA spectra can have both positive and negative parts, and (3) non-negativity in concentrations (predicted using estimated Raman spectra) for all the species.

The first step in Chiral-BTEM/BTEM is to perform singular value decomposition (SVD) in order to decompose the experimental data, I^{Raman} or I^{ROA}, into three matrices according to Eqs.6.9 and 6.10, where $U_{k\times k}$ and $\mathrm{V}^{T}_{\nu\times\nu}$ are the left singular vectors and right singular vectors which form an orthonormal basis, and $\Sigma_{\mathrm{k}\times\mathrm{v}}$ is the corresponding singular value matrix.

$$I^{Raman}_{k\times\nu} = [U_{k\times k}\Sigma_{k\times\nu}\mathrm{V}^{T}_{\nu\times\nu}]_{Raman} \tag{6.9}$$

$$I^{ROA}_{k\times\nu} = [U_{k\times k}\Sigma_{k\times\nu}\mathrm{V}^{T}_{\nu\times\nu}]_{ROA} \tag{6.10}$$

It is noted that $U_{k\times k}$, $\Sigma_{k\times\tilde{\nu}}$ and $\mathrm{V}^{T}_{\tilde{\nu}\times\tilde{\nu}}$ are different according to the decomposed matrix (I^{Raman} or I^{ROA}), where subscript k is the number of measurements and subscript ν is the number of data channels. The first several row vectors of $\mathrm{V}^{T}_{\tilde{\nu}\times\tilde{\nu}}$ will consist of meaningful spectral features while the rest will consist primarily of noise. The BTEM algorithm searches the subspace of $z<k$ chosen basis vectors for the simplest underlying patterns. This is achieved by transforming the abstract right singular vectors in $\mathbf{V}^{\mathrm{T}}$ into pure component spectra estimates, $\hat{i}^{Raman}_{1\times\tilde{\nu}}$ and $\hat{i}^{ROA}_{1\times\tilde{\nu}}$, one-at-a-time using Eqs.6.11 and 6.12. The z transformation elements $T_{1\times z}$ are determined using a non-linear optimization.

$$\hat{i}^{Raman}_{1\times\tilde{\nu}} = [T_{1\times z}\mathbf{V}^{\mathrm{T}}_{z\times\tilde{\nu}}]_{Raman} \tag{6.11}$$

$$\hat{i}^{ROA}_{1\times\tilde{\nu}} = [T_{1\times z}\mathbf{V}^{\mathrm{T}}_{z\times\tilde{\nu}}]_{ROA} \tag{6.12}$$

The objective function (Eq.2.9) includes two terms: information entropy function (H) and penalty function (P) which includes the constraints mentioned above.

With the pure component Raman and ROA spectra estimated by BTEM, the second task, i.e. the determination of the concentrations or enantiomeric excess can be further performed. If the mixture is not an enantiomeric mixture, either Raman or ROA spectra is able to predict the concentration profiles for all the species. If enantiomers are present, the combination of Raman and ROA spectra can predict the ee for each enantiomer. An important quantity for intermediate calculations of enantiomeric excess will be the quantity (I^{+}-I^{-}) which is obtained from the ROA measurement.

6.5 Experimental Section

Four types of ROA experiments were carried out in this work: (1) ROA spectroscopic measurements of pure chiral molecules ((+)-α-pinene, (−)-α-pinene, (+)-camphor and (−)-camphor; (2) a semi-batch experiment for the measurement of one chiral component ((−)-α-pinene) at different concentrations in solution; (3) two semi-batch experiments for the measurements of two chiral components ((−)-α-pinene and (+)-carvone) in solution and (4) the measurements of a pair of enantiomers ((+)-α-pinene and (−)-α-pinene) in solution.

6.5.1. General Information

Micro pipettes, 10~100 μL and 100~1000 μL, were used to accurately measure the volume of the chiral liquids and solvent in order to prepare solutions with different concentrations or different enantiomeric excess. On the other hand, volumetric perturbations were made using gas-tight Hamilton, 1.0 mL and 2.5 mL syringes during the semi-batch experiments.

The chiral molecules (+)-α-pinene (99+%, Aldrich), (-)-α-pinene (≥99.0%, Fluka), (+)-camphor (≥97%, Fluka), (-)-camphor (≥99.0%, Aldrich), (+)-carvone (≥98.5%, Fluka) and (-)-carvone (≥99.0%, Fluka) were stored in the refrigerator and used as received. The solvent n-hexane and chloroform (99.6%+, Fluka) was used as received.

6.5.2. Equipmental Setup

The above experiments (1) and (4) were performed in the similar manner. All the samples were filled into a miniature quartz cuvette with the 2mm pathlength (from

BioTools). The cuvette was fixed into a special cell holder and the samples were measured with the ROA instrument. The quartz cuvette was cleaned three times with acetone and then it was dried by vacuum prior to each sample measurement.

The experiments (2) and (3) were run in flow-through mode. The schematic diagram of the experimental setup of these experiments is shown in Figure 6.2.

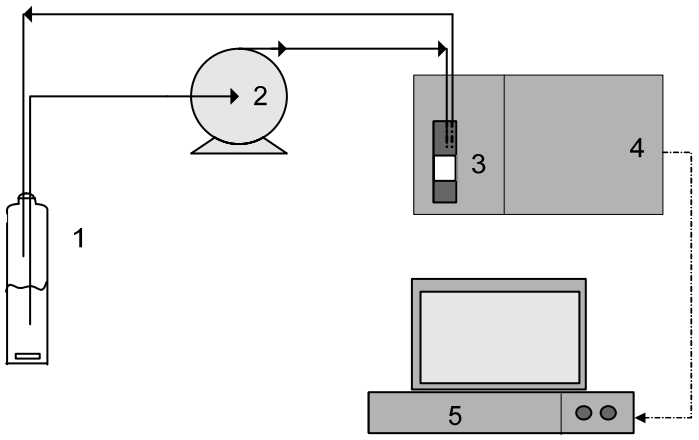

Figure.6.2. Schematic of experimental configuration: 1. Schlenk tube; 2. Pump; 3. Quartz cell; 4. ROA (Chiral*RAMAN*^{TM}); 5. Data acquisition.

First, solutions were transferred to the Schlenk tube equipped with magnetic stirring. A rubber septum was used at the top of the Schlenk tube in order to insert transfer lines and in order to make perturbations during the semi-batch experiments. Inside the ROA instrument, a quartz flow-through cuvette with dimensions of $40\times10\times10$ mm (Hellma, Germany) was placed in an in-house designed cell holder before the lens. The liquid phases were circulated through the Schlenk tube to the quartz cuvette using a Teflon membrane pump (Cole Parmer) at the flow rate of 5 ml/min. At this point, the position of the cell was adjusted to maximize signal quality. All the measurements were carried out at ambient temperature circa 298K.

In order to clean the system, 20 ml solvent (n-hexane) was used to purge the whole system prior to each semi-batch experiment. In the flow through mode, the period of sample interacted with the laser is quite short so any photo-induced degradation that might occur is greatly reduced, especially for long time measurements. (Note that such a situation would be very important for the study of sensitive chiral metal complexes and associated reactive systems.)

6.5.3. Spectroscopic Measurements

The measurements of Raman and ROA spectra were conducted with the Chiral*RAMAN*^{TM} SCP-ROA spectrometer from BioTools. This spectrometer is one of the very few ROA instruments in the world.

For the experiments (1) and (4), each sample was injected into the quartz cuvette and the spectra were collected. The details of each sample in experiment (4) are given in Table 6.1. For each measurement, Raman and ROA spectra were obtained simultaneously. The experimentally obtained Raman and ROA spectra were the result of 10 minutes co-added scans.

Table 6.1. Experimental design for experiment (4) indicating the individual sample details. ((+)-α-pinene is selected as the reference for EE)

Sample	**Experiments for 7 different Concentration (V/V %)**						
Index	100	80	70	60	50	40	30
1-3	EE: -90%	-90%	-90%	-90%	-90%	-90%	-90%
4-6	EE: -80%	-80%	-80%	-80%	-80%	-80%	-80%
7-9	EE: -70%	-70%	-70%	-70%	-70%	-70%	-70%
10-12	EE: -60%	-60%	-60%	-60%	-60%	-60%	-60%
13-15	EE: -50%	-50%	-50%	-50%	-50%	-50%	-50%

For the experiments (2) and (3), the semi-batch experiments with volumetric perturbations were carried out. Circa 13 ml of solvent n-hexane was used in each semi-batch experiment, and then various quantities of the chiral compounds were added according to the experimental design given in Tables 6.2 and 6.3. The experimentally obtained Raman and ROA spectra were the result of 512 co-added scans.

Table 6.2. Experimental design for experiment (2) indicating the individual perturbation steps.

Index	Perturbation	Spectra #
1	Solvent: n-hexane	1-2
2	Add 0.2 ml (−)-α-pinene	2
3	Add 0.4 ml (−)-α-pinene	4-5
4	Add 0.7 ml (−)-α-pinene	6-7
5	Add 1.0 ml (−)-α-pinene	8-10
6	Add 1.3 ml (−)-α-pinene	11-12

Table 6.3. Experimental design for experiment (3) indicating the individual perturbation steps.

Index	Semi-batch Experiment 1		Semi-batch Experiment 2	
	Perturbation	Spectra #	Perturbation	Spectra #
1	Solvent: n-hexane	1-2	Solvent: n-hexane	1
2	Add 0.3 ml (-)-α-pinene	3-4	Add 0.2 ml (+)-carvone	2-3
3	Add 0.3 ml (-)-α-pinene	5-6	Add 0.2 ml (+)-carvone	4-5
4	Add 0.4 ml (+)-carvone	7-8	Add 0.2 ml (-)-α-pinene	6
5	Add 0.4 ml (-)-α-pinene	9-10	Add 0.5 ml (+)-carvone	7-8
6	Add 0.4 ml (-)-α-pinene	11-12	Add 0.3 ml (-)-α-pinene	9-10
7	Add 0.4 ml (+)-carvone	13-14	Add 0.4 ml (+)-carvone	11-12
8	-	-	Add 0.3 ml (-)-α-pinene	13-14

6.6 Results: ROA Measurements and Density Functional Theory (DFT) Calculations of Chiral Molecules

6.6.1 Neat (+)-α-pinene and (−)-α-pinene

6.6.1.1 Experiment Data

The Raman and ROA measurements were performed using the BioTools Chiral*RAMAN*^{TM} spectrometer which can collect the Raman and SCP-ROA spectra at the same time. The experimentally obtained Raman and ROA spectra were the result of 10 minutes co-added scans at 210mW laser power. The series of spectra for neat (+)-α-pinene and (−)-α-pinene samples are shown in Figure 6.3.

Both Figure 6.3 (a) and (b) show very good spectral quality with high signal-to-noise ratio. Basically, the Raman spectra of (+)-α-pinene and (−)-α-pinene in Figure 6.3 (a) are identical except of a slight discrepancy in the intensities. Additionally, the ROA spectra of (+)-α-pinene and (−)-α-pinene in Figure 6.3 (b) are mirror images although there are two artifact bands in the range between 1500 cm^{-1} to 1700 cm^{-1} for (−)-α-pinene. Both α-pinene ROA have positive bands at circa 660 cm^{-1}. It is probably due to the error instrumental responses. It is noted that the magnitude of Raman intensity is approximately 10^4 higher that that of ROA intensity. Moreover, the vibrational bands in the Raman spectra must not necessarily correspond to the positions of the vibrational bands in ROA. It is clear that some significant bands appearing in Raman spectra do not appear or have much less intensity in the ROA spectra. For example, the most intensity bands at circa 1660 cm^{-1} in Raman spectrum of (−)-α-pinene are quite flat in the ROA spectrum.

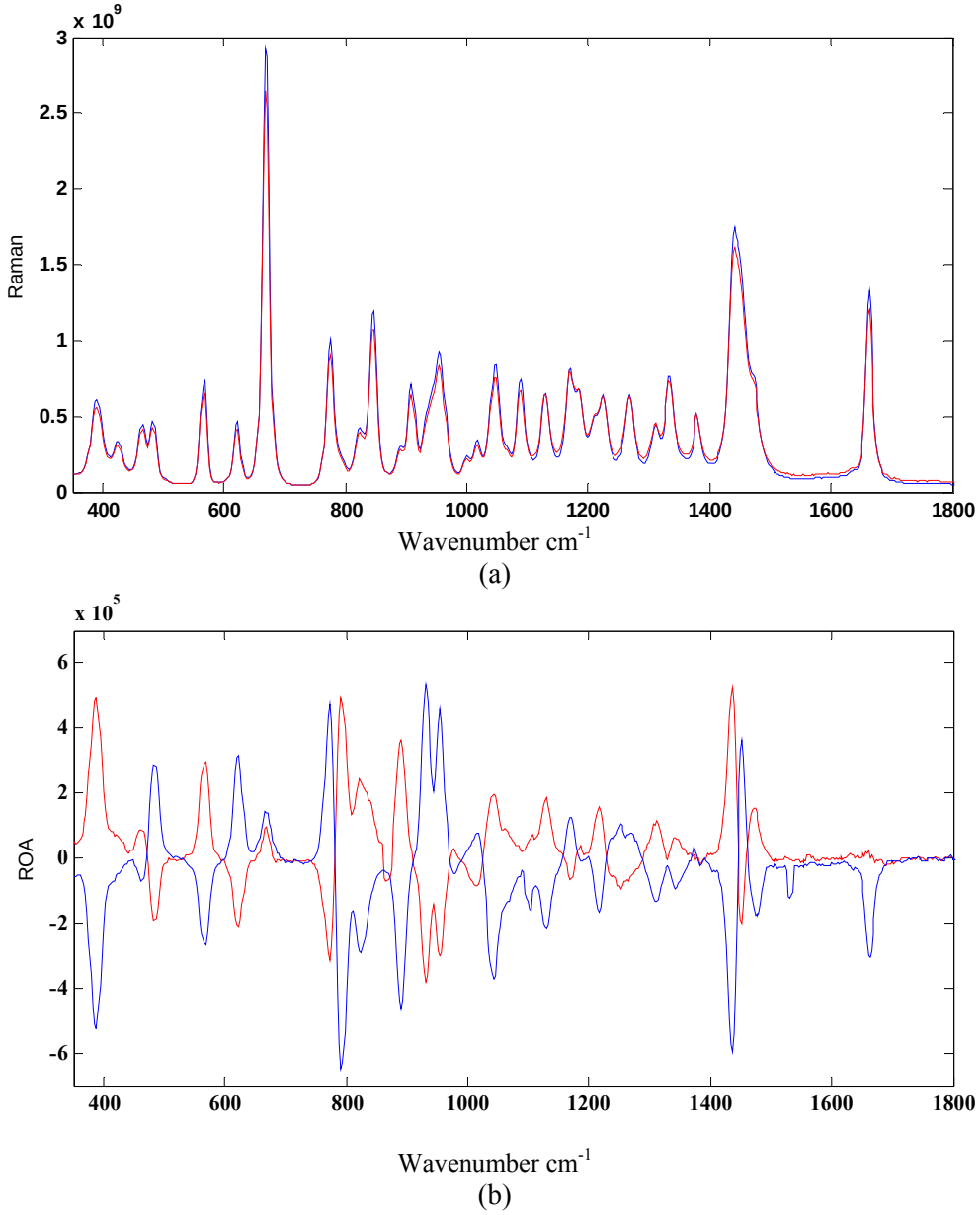

Figure 6.3. The experimental (a) Raman spectra and (b) ROA spectra of neat (+)-α-pinene and (−)-α-pinene. Red lines for: (+)-α-pinene and blue lines for (−)-α-pinene.

6.6.1.2 DFT Studies

DFT is a promising approach for the electronic wave function calculations of the ground state and it can generally produce sufficiently accurate calculations for structure determinations and vibrational frequency predictions. The primary aim in this section is

to report on the DFT calculations with the Becke- Lee-Yang-Parr (B3LYP) (Becke, 1993; Lee *et al*., 1988) functional and 6-311G* basis set applied to the geometric optimizations, and Raman and ROA spectra predictions. These DFT calculations are able to assist in the determination of the absolute configurations of the chiral molecules present.

The DFT calculations were first performed to obtain molecular structures through geometric optimization. The prediction of Raman and ROA spectra were carried out by employing the fully optimized molecular structure with further DFT frequency calculations. All of the computations were carried out with the Gaussian 03 program.

The optimized geometries of (+)-α-pinene and (−)-α-pinene are show in Figure 6.4. It is obvious that the geometries of (+)-α-pinene and (−)-α-pinene are mirror images as well as neither (+)-α-pinene nor (−)-α-pinene can be superimposed on its mirror image. With the two optimized structures, further DFT vibrational frequency calculations generated quite good Raman and ROA spectra corresponding to experimental spectra of (+)-α-pinene and (−)-α-pinene.

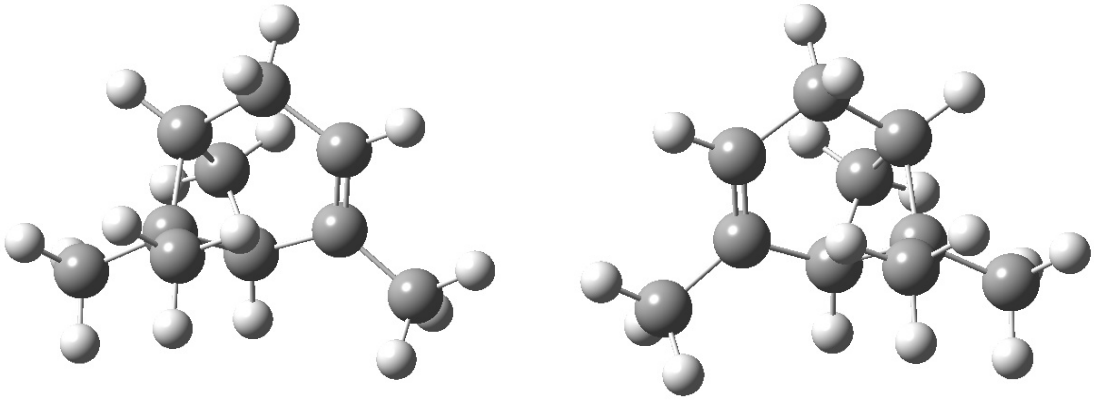

Figure 6.4. Optimized geometries of (+)-α-pinene and (−)-α-pinene using DFT with B3LYP/6-311G*. Right side: (+)-α-pinene and left side: (−)-α-pinene.

The predicted Raman spectrum of both (+)-α-pinene and (−)-α-pinene from the DFT calculations were the same. It is well understood that the Raman spectra of a pair of enantiomers are identical. The ROA spectra of a pair of enantiomers, however, are mirror images of each another and can be used to determine the absolute configuration. The predicted Raman spectra and the ROA intensity are shown in Figures 6.5 and 6.6. Figure 6.5 shows that the predicted Raman spectrum in terms of both band positions and relative intensities is in good agreement with the experimental spectrum, especially in the range below 1000 cm^{-1}. The two biggest deviations for the frequency predictions appear at the two most intensity bands of the predicted Raman spectrum at circa 1480 cm^{-1} and 1720 cm^{-1} and the deviation is less than 3%. It is also seen that the predicted and experimental Raman spectra have similar relative intensities over much of the spectral range (with notable exception of the band at 1480 cm^{-1}). Figure 6.6 shows the predicted ROA spectra of (+)-α-pinene and (−)-α-pinene. These two spectra have the same band positions and opposite intensities.

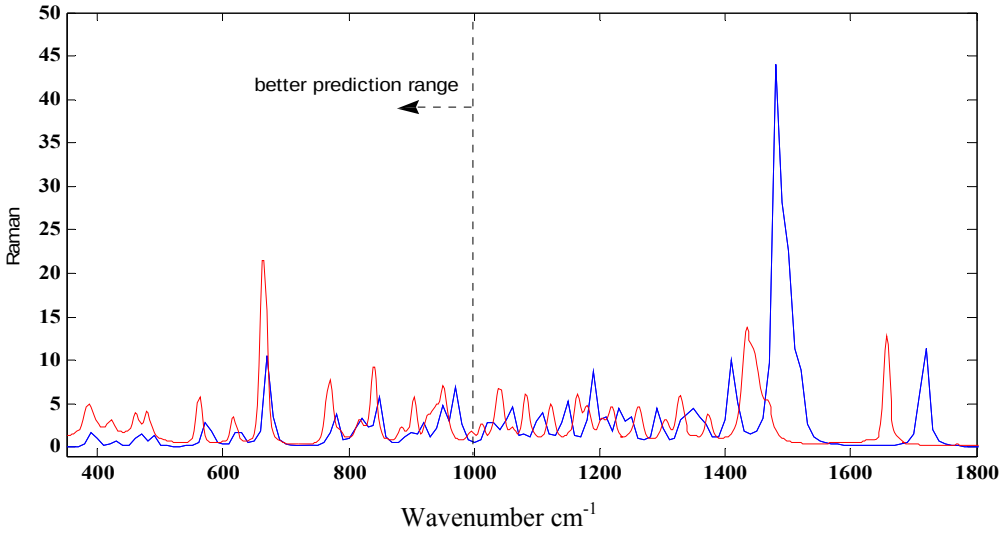

Figure 6.5. The comparison of DFT predicted Raman spectrum (blue line) and the experimental spectrum (red line) of (+)-α-pinene.

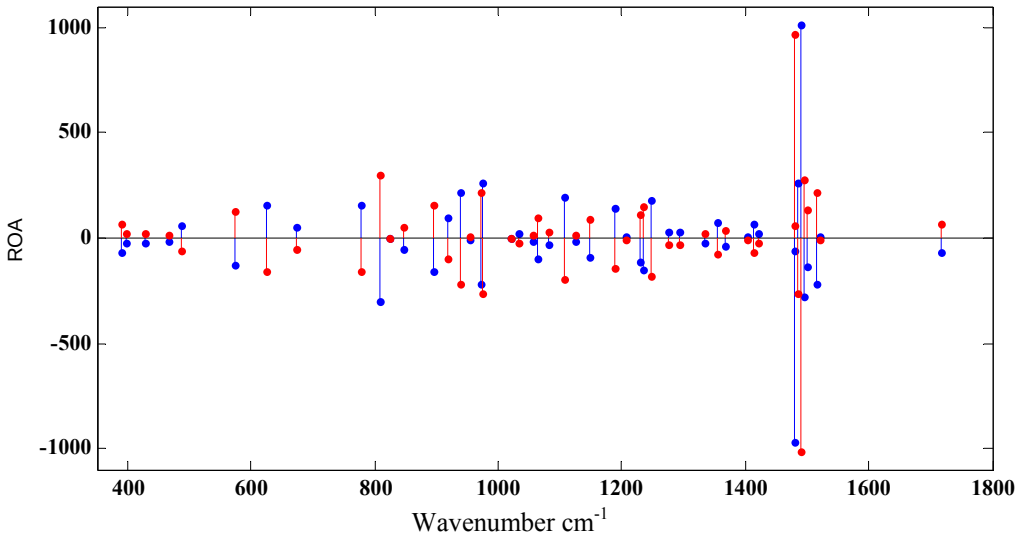

Figure 6.6. The predicted ROA intensities of (+)-α-pinene (red lines) and (−)-α-pinene (blue lines).

The comparison of (+)-α-pinene and (−)-α-pinene is shown in Figure 6.7. In both cases, the predictions of the signs are mostly consistent with the experimental values in the range below 1000 cm^{-1} (note that the bands marked by '*' show good agreement between the predicted ROA spectra and experimental spectra). The 2 strong bands located at circa 1400 to 1500 cm^{-1} (marked by '×') in the experimental ROA spectra are circa 50 cm^{-1} lower than their DFT predicted positions. Between the range of 1000 cm^{-1} and 1400 cm^{-1}, the predictions are rather inconsistent with the experimental values at many band positions. Therefore it is difficult to use the DFT predicted spectra in this range to assign the absolute configuration. In summary, the predictions for both the Raman spectra and the ROA spectra are in good agreement with the experimental spectra below 1000 cm^{-1} and the biggest deviation between predicted and experimental spectra occurred at the same wavenumber range, i.e. between the range of 1400 cm^{-1} and 1500 cm^{-1}.

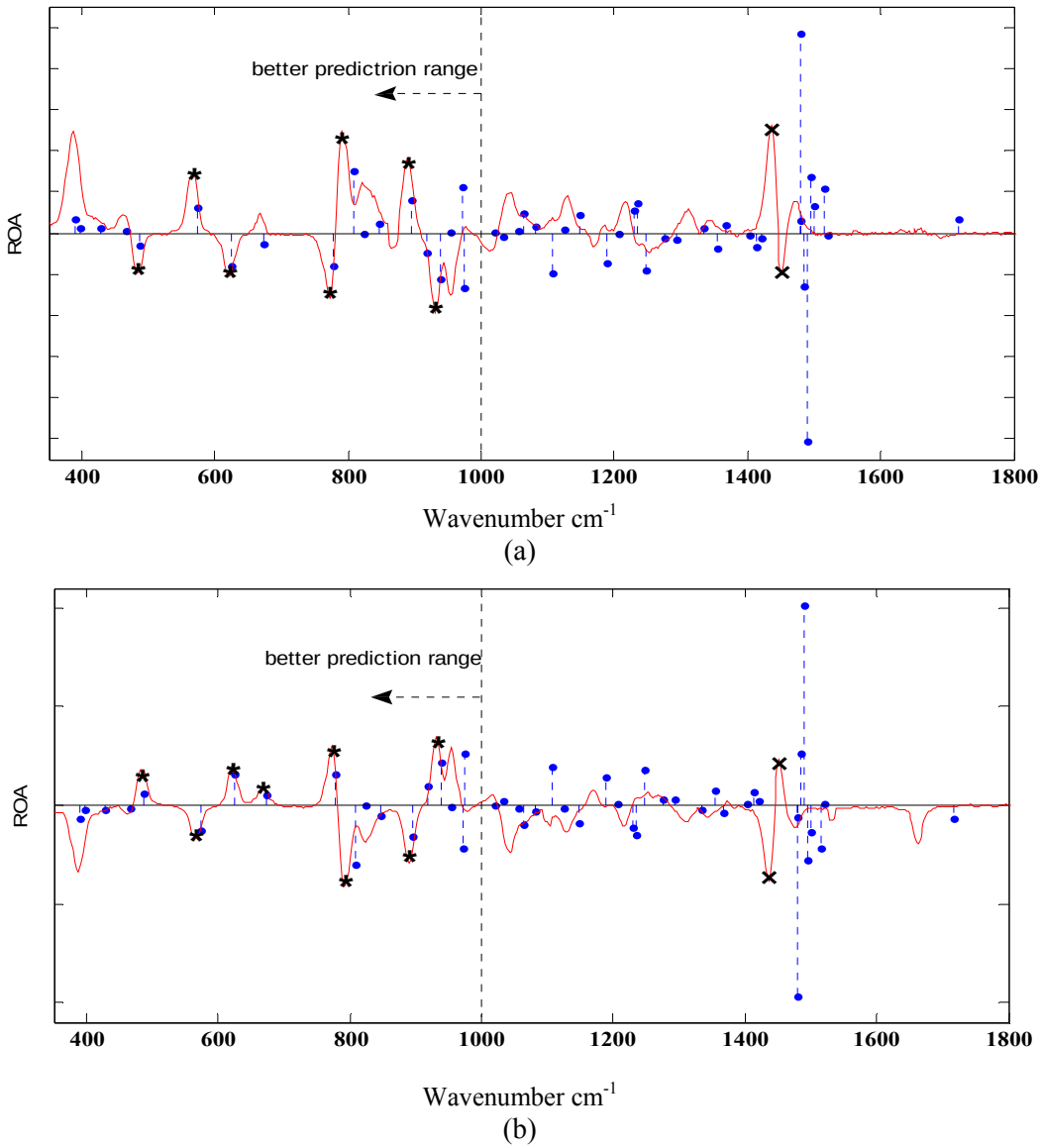

Figure 6.7. The comparison of the predicted ROA intensities (blue lines) and the experimental spectrum (red line). (a): (+)-α-pinene and (b): (−)-α-pinene.

6.6.2 (+)-Camphor and (−)-Camphor in Solvent Chloroform

6.6.2.1 Experiment Data

Solutions of (1) 110.0mg (+)-camphor in 400µl chloroform and (2) 104.5mg (−) camphor in 400µl chloroform were prepared. The Raman and ROA spectra were

collected using the BioTools Chiral*RAMAN*™ spectrometer. Each spectrum was the result of co-added scans for 30 minutes at 210 mw laser power. The Raman spectra of solutions (1) and (2) were measured. The Raman spectra of the (+)-camphor and (−)-camphor solutions are essentially the same although the intensities are slightly different. In order to retrieve the pure (+)-camphor and (−)-camphor Raman spectra, preconditioning, namely background subtraction, was performed. On the other hand, the solvent chloroform is an achiral molecular and it should have zero signal in the ROA measurement. Consequently, the pure ROA spectra of (+)-camphor or (−)-camphor can be obtained directly from the experiments although the samples were (+)-camphor and (−)-camphor solutions. The experimental spectra and the preconditioned spectrum are shown in Figure 6.8.

Figure 6.8 indicates that both the experimental and preconditioned Raman spectra of camphor have as good spectral quality as the experimental Raman spectra of neat α-pinene (see Figure 6.3). The ROA spectra of (+)-camphor and (−)-camphor, however, show worse signal-to-noise ratios than those of (+)-α-pinene and (−)-α-pinene. Clearly, it is easier to get better S/N from neat samples. Despite the spectral quality, the mirror images for the ROA spectra of enantiomers can be clearly observed in the ROA spectra of (+)-camphor and (−)-camphor. Therefore, the absolute configuration of non-neat chiral samples such as (+)-camphor and (−)-camphor solutions can be determined using the technique of ROA.

In addition, comparison of Figure 6.8 (a) and (b) indicates that the preconditioned Raman spectrum of camphor has essentially all signals from chloroform removed. It indicates that the peak positions of the Raman and ROA spectra for a chiral molecular are not necessarily the same. However, most vibrational bands in the ROA spectra could be

observed in the Raman spectra although some peaks in the Raman spectra do not appear in the ROA spectra.

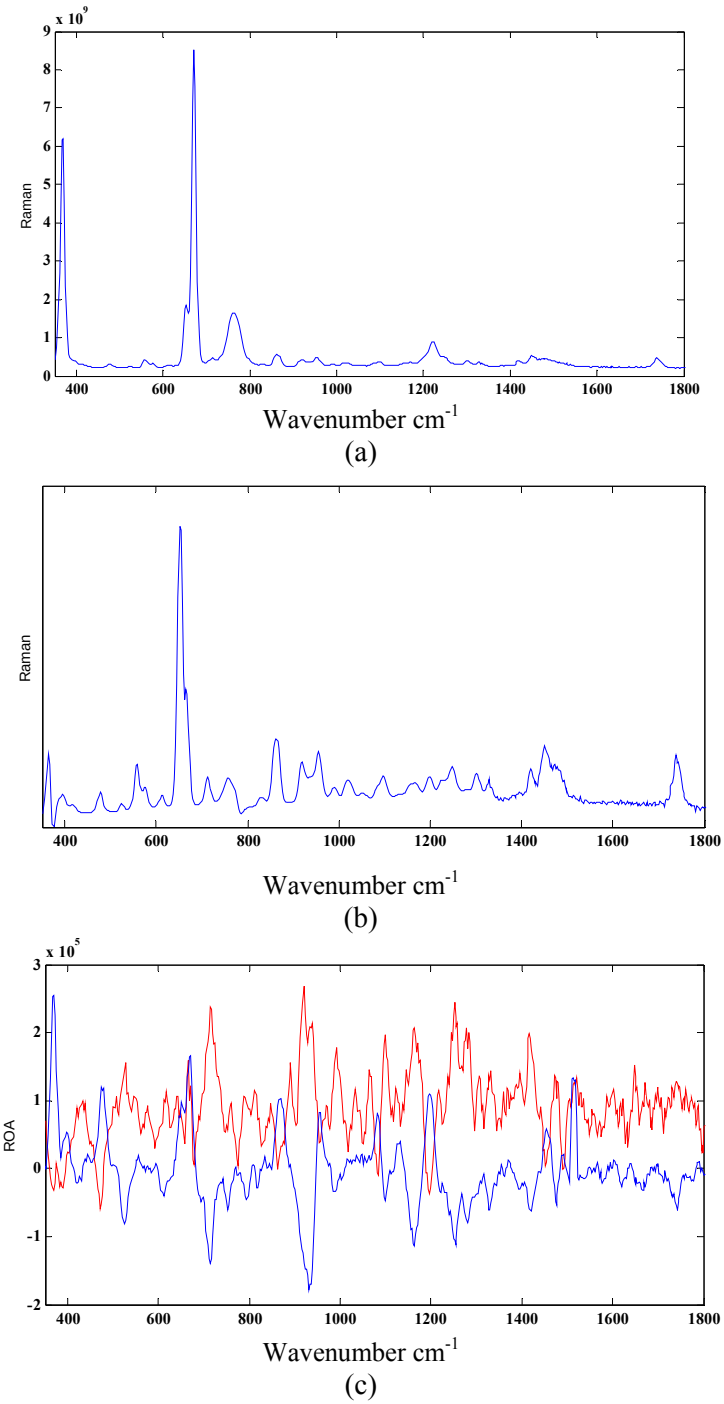

Figure 6.8. The experiment spectra: (a) Raman spectrum of (+)-camphor solution (b) preconditioned Raman spectrum of pure (+)-camphor (c) ROA spectra of (+)-camphor (blue line) and (−)-camphor (red line) solutions.

6.6.2.2 DFT Studies

The DFT calculations with the B3LYP functional and 6-311G* basis set were applied to the geometric optimization, as well as Raman and ROA spectra predictions of (+)-camphor and (−)-camphor. All of the computations were carried out with the Gaussian 03 program.

The DFT calculations were first performed to obtain molecular structures through geometry optimization. The prediction of Raman and ROA spectra were carried out by employing the fully optimized molecular structure with further DFT frequency calculations.

The optimized geometries of (+)-camphor and (−)-camphor are show in Figure 6.9. Figure 6.9 shows that the molecular structure of (+)-camphor and (−)-camphor are mirror images.

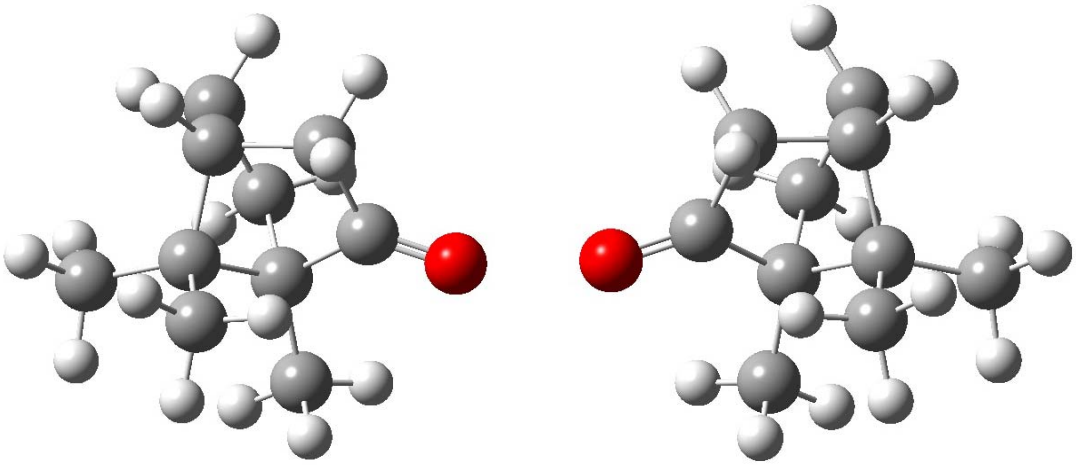

Figure 6.9. Optimized geometries of (+)-camphor and (−)-camphor using DFT with B3LYP/6-311G*. Right side: (−)-camphor and left side: (+)-camphor.

The DFT vibrational frequency calculations generated identical Raman spectra and mirror image ROA spectra for (+)-camphor and (−)-camphor. The predicted and

experimental Raman spectra, the predicted ROA spectra, and predicted and experimental ROA spectra are shown in Figures 6.10, 6.11 and 6.12, respectively.

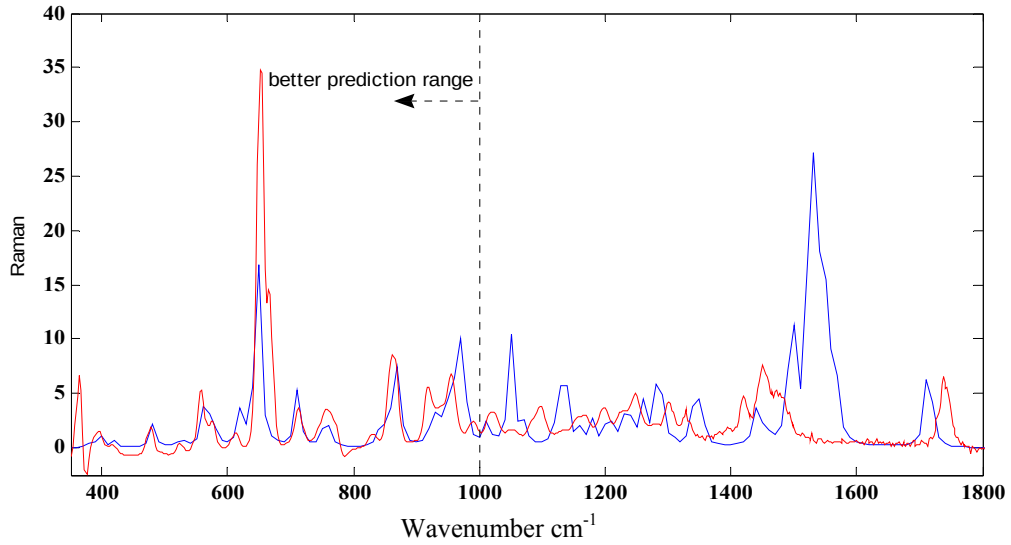

Figure 6.10. The comparison of DFT predicted Raman spectrum (blue line) and the experimental spectrum (red line) of (−)-camphor.

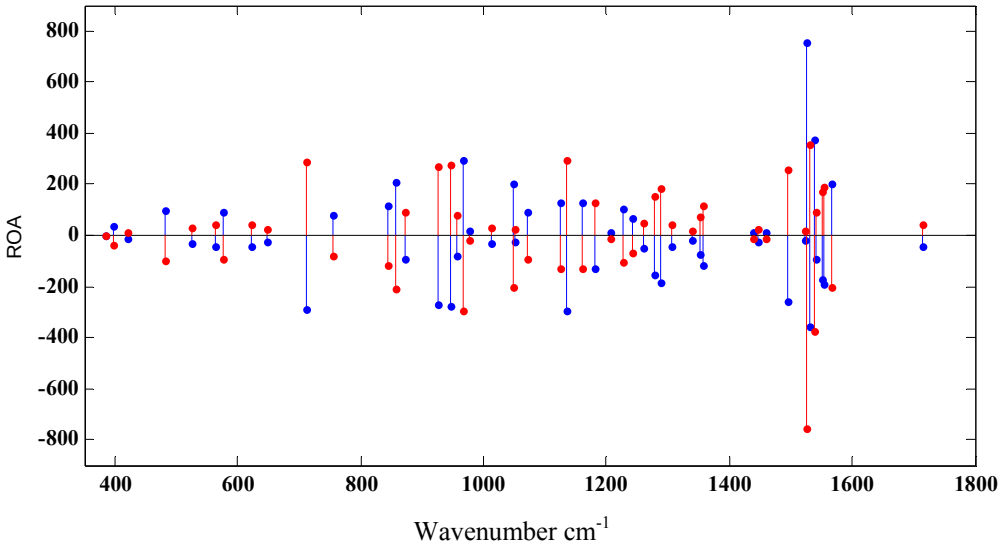

Figure 6.11. The predicted ROA intensities of (−)-camphor (red lines) and (+)-camphor (blue lines).

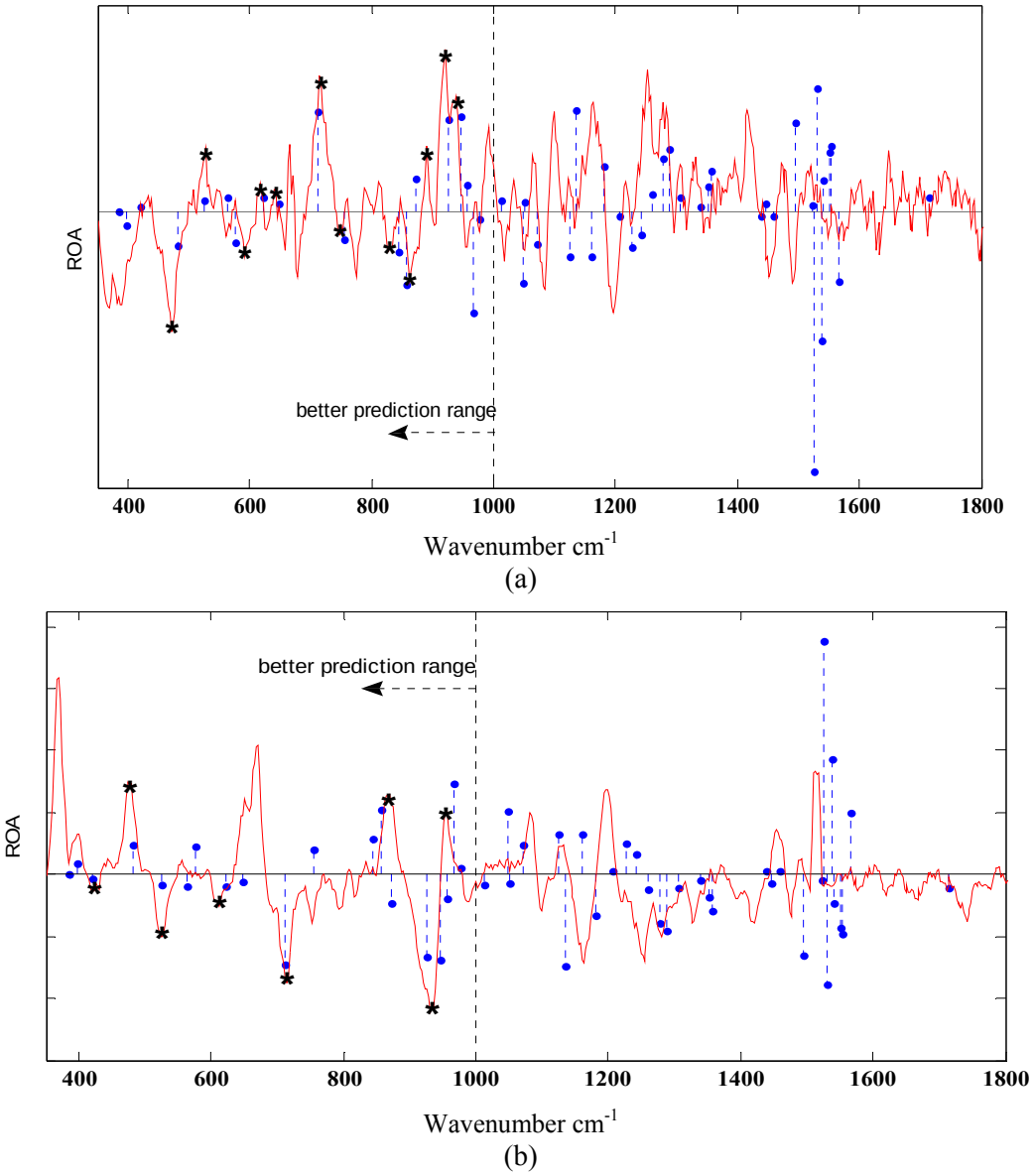

Figure 6.12. The comparison of the predicted ROA intensities (blue lines) and the experimental spectrum (red line). (a): (−)-camphor and (b): (+)-camphor.

Figures 6.10 and 6.12 show that the predicted Raman and ROA spectra in terms of both band positions and relative intensities are in good agreement with the experimental spectra, especially in the range below 1000 cm^{-1}. The biggest deviation for the frequency predictions appear at the most intensity band of the predicted spectrum at circa 1520 cm^{-1} and the deviation is less than 3%.

Compared to the DFT calculations of (+)-α-pinene and (−)-α-pinene, the present results indicates that (1) in the range below circa 1000 cm^{-1}, DFT calculations generated good predictions for both Raman and ROA spectra of α-pinene and camphor enantiomers; (2) the overestimated frequencies always appear at circa 1400 to 1600 cm^{-1}; and (3) the sign predictions for the ROA spectra of α-pinene and camphor enantiomers in the range between 1000 to 1400 cm^{-1} are not as good as other ranges. Since there are overtones in this range, it is probably not easy to perform accurate frequency predictions using DFT.

In general, the DFT calculations with B3LYP functional and 6-311G* basis set were successfully applied to the geometric optimization, and Raman and ROA spectra predictions of both α-pinene and camphor enantiomers. The DFT calculations are sufficiently accurate and able to facilitate the determination of the absolute configurations of the chiral molecules.

6.7 Results: Chiral Solution

In this section, the tested systems are binary and ternary mixtures but they are not enantiomeric mixtures. Our aim is to apply Chiral-BTEM to the mixture spectra to retrieve the pure Raman and ROA spectra of each species.

6.7.1 Binary System: (−)-α-pinene in the Solvent (n)-hexane

6.7.1.1 Experimental Data

A semi-batch experiment was performed in the way mentioned in Table 6.2. A total of 12 pairs of Raman and ROA spectra for the (−)-α-pinene solutions were obtained

from the experiment. The experimentally obtained Raman and ROA spectra were the result of 512 co-added scans at 270mw laser power.

Two typical Raman spectra and two typical ROA spectra are shown in Figure 6.13 and 6.14, respectively. The two sets of the Raman and ROA spectra indicate that the magnitude of Raman intensity is normally 10^4 times more than ROA intensity. The Raman spectra have a considerably better signal-to-noise ratio than the ROA spectra. The neat liquid chiral molecule can normally give a good ROA spectrum while it is difficult to obtain a high quality ROA spectrum for the chiral solution or it might take a very long time to obtain good spectrum. In Figure 6.13, the lower spectrum shows the Raman spectrum of (n)-hexane and the top one shows the Raman spectrum of (−)-α-pinene with the solvent (n)-hexane. However, both the ROA spectra show signals only due to the molecular vibrations of the (−)-α-pinene.

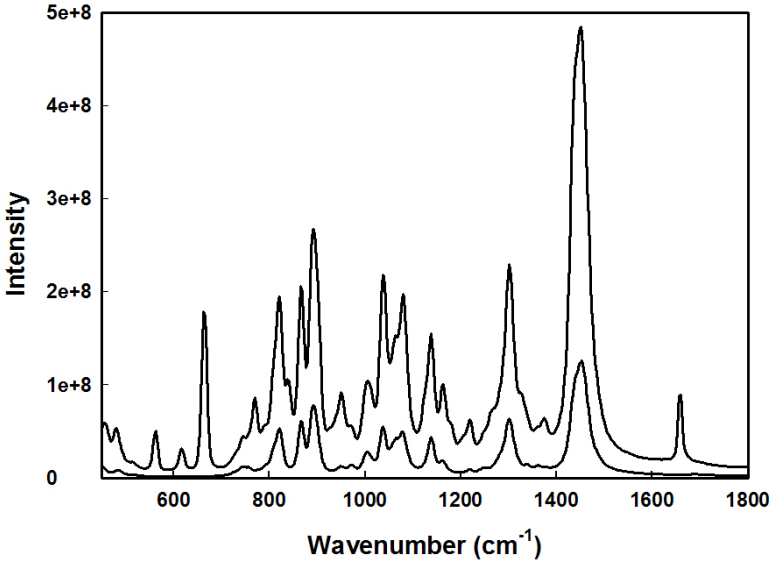

Figure 6.13. Two typical experimental Raman spectra: the bottom one is the Raman spectrum of pure hexane solution and the top one is the Raman spectrum of (−)-α-pinene in hexane.

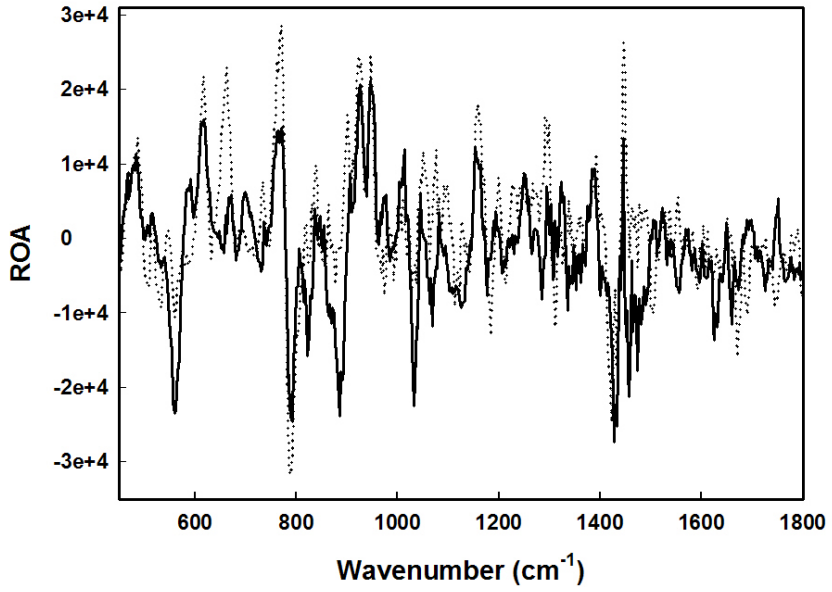

Figure 6.14. Two typical experimental ROA spectra of (−)-α-pinene in hexane with different concentrations.

6.7.1.2 Spectral Reconstruction using BTEM

The procedure of performing a BTEM/Chiral-BTEM analysis consists of two major steps: (1) performing singular value decomposition (SVD) to decompose the Raman or ROA spectroscopic data in order to obtain the right singular vectors $\mathbf{V}^T$ which consist of the localized and meaningful spectral features; and (2) transforming these right singular vectors $\mathbf{V}^T$ into a pure component spectrum one-at-a-time.

The recovered Raman and ROA spectra are shown in Figures 6.15 and 6.16. The recovered Raman spectra of both (−)-α-pinene and (n)-hexane are quite consistent with the pure reference experimental spectra. The estimated ROA spectrum of (−)-α-pinene is good enough for system identification. The relative intensities of the bands at circa 890, 1100 and 1440 cm^{-1} are different between the recovered ROA spectra and the reference.

It might be due to the problem mentioned previously, i.e. the shape, relative intensity and sign of a few vibrational bands are not reproducible in the ROA spectra.

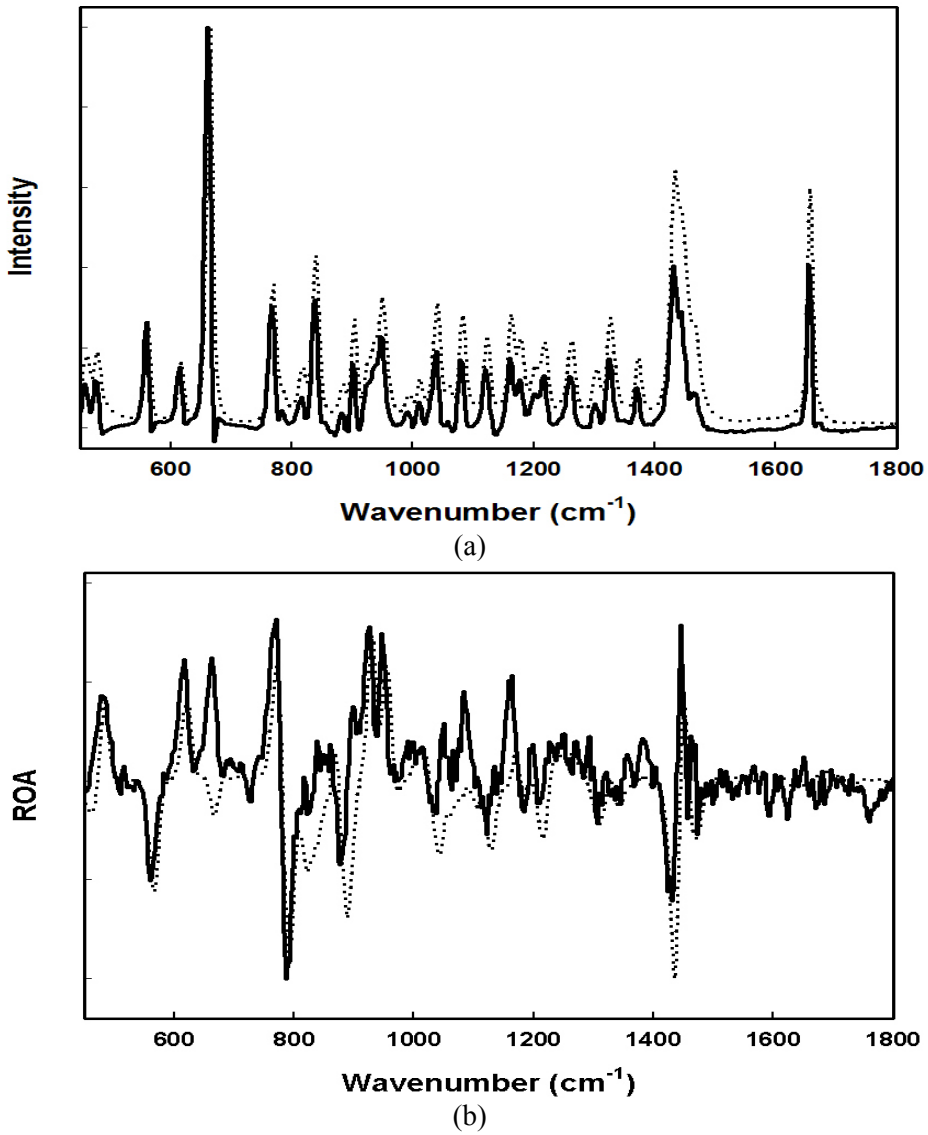

Figure 6.15. Recovered pure component spectra by BTEM (solid lines) and experiment reference spectra (dotted line): (a) Raman spectra of (−)-α-pinene and (b) ROA spectra of (−)-α-pinene.

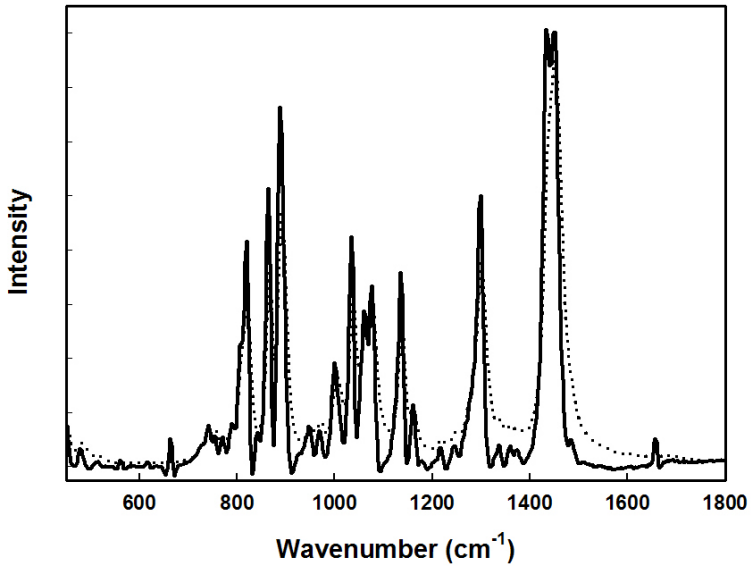

Figure 6.16. Solid lines: recovered pure component Raman spectra of hexane obtained by BTEM and Dotted lines: experiment reference Raman spectra.

6.7.1.3 Concentrations Profiles

The relative concentration profiles of (−)-α-pinene were calculated using both the estimated Raman and ROA spectra. The concentration was the average of each repeated measurement for the same sample. Figure 6.17 compares the concentration profiles of (+)-α-pinene predicted from estimated Raman and ROA spectra and obtained from the experimental design. It is clearly seen that satisfactory concentration profiles for both Raman and ROA spectra are obtained. In addition, the predicted concentrations are better for solutions with higher concentrations. Furthermore, two concentration profiles are quite similar. It indicates that ROA can provide good quantitative results, just like Raman spectroscopy. However, some discrepancy appears as more and more perturbations are made. This is probably due to accumulation of error at each step.

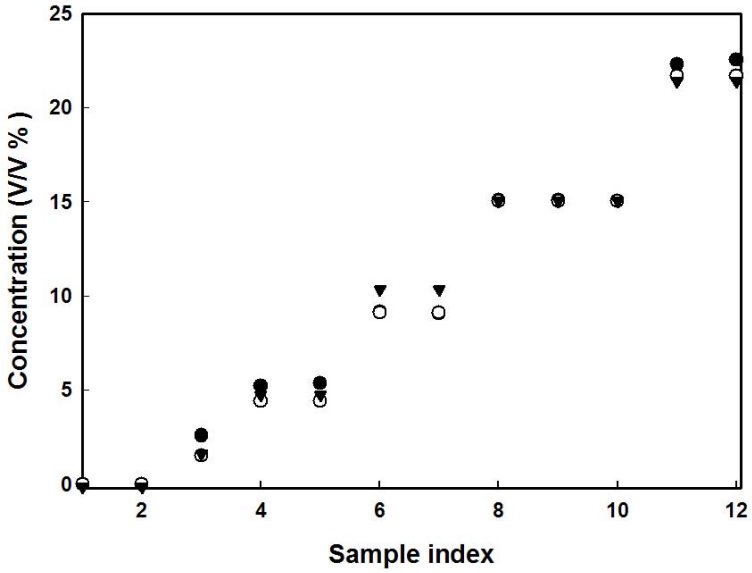

Figure 6.17. Comparison of (−)-α-pinene concentration profile determined from recovered Raman pure component spectra (●), ROA pure component spectrum (▼) and experiment design (○).

6.7.2 Two Chiral Component Solution

6.7.2.1 Experimental Data

Two semi-batch experiments were performed as the experimental design (see Table 6.3). A total of 28 sets of Raman and ROA spectra for the chiral solutions were obtained from the experiments. The experimentally obtained Raman and ROA spectra were the result of 512 co-added scans at 270 mw laser power.

Three typical Raman spectra and two typical ROA spectra are shown in Figure 6.18 and 6.19, respectively. The Raman spectra again have a considerably better signal-to-noise ratio than the ROA spectra. It is due to the quite low concentrations (less than 8 % volumetric concentration) for the ROA measurements. Three spectra in Figure 6.18 clearly show that meaningful spectral changes can be observed during the different perturbation steps. The top, middle and bottom spectra correspond to the solution of pure (n)-hexane, and (−)-α-pinene and (+)-carvone with (n)-hexane. The spectral changes can

also be found in the experimental ROA spectra in Figure 6.19 but it is not as obvious as in the Raman spectra. In order to retrieve the pure Raman and ROA spectra, BTEM/Chiral-BTEM were performed on all the 28 sets of spectra.

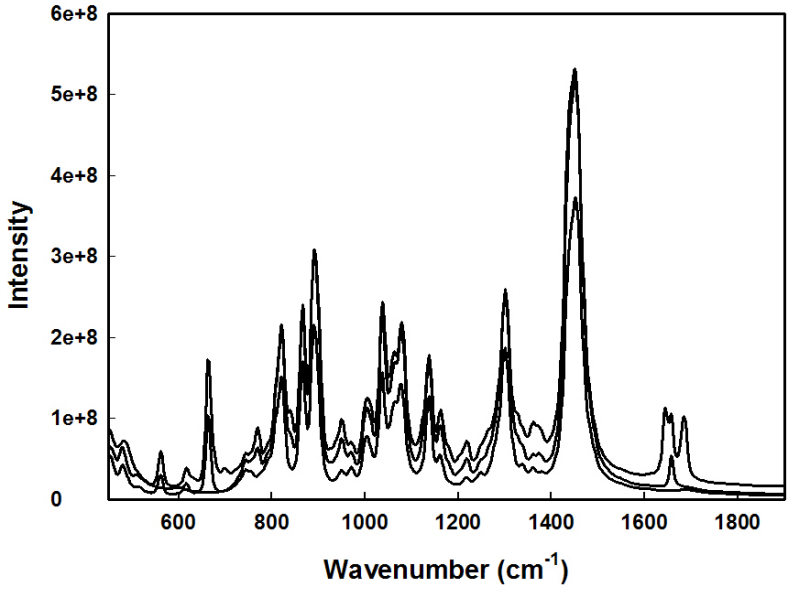

Figure 6.18. Three experimental Raman spectra. Spectra # 1, 5 and 10 from the semi-batch experiment 1. (see Table 6.3)

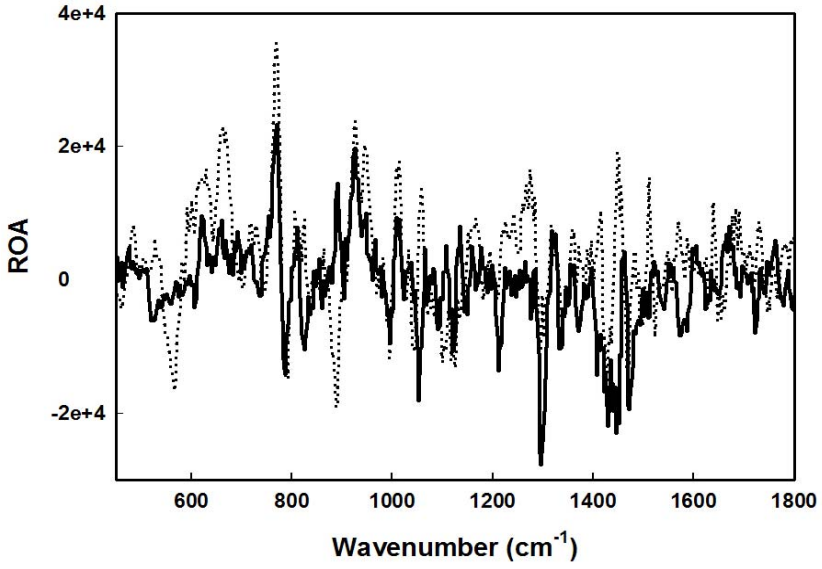

Figure 6.19. Two experimental ROA spectra. Spectra # 5 and 10 from the semi-batch experiment 1. (see Table 6.3)

6.7.2.2 Spectral Reconstruction using BTEM

A total of 28 Raman spectra and 28 ROA spectra were subjected to BTEM separately. The recovered Raman and/or ROA spectra of hexane, (−)-α-pinene and (+)-carvone are shown in Figures 6.20, 6.21and 6.22, respectively.

The recovered Raman spectrum of (n)-hexane is in good agreement with the reference although there are some (−)-α-pinene and/or (+)-carvone signals embedded in the hexane Raman spectrum at some points where the reference spectrum show a flat line. Similarly, the recovered Raman spectrum of (−)-α-pinene in Figure 6.21 (a) has some signals from hexane at circa 900 cm^{-1} (two inverted peaks) but all the main signals from (+)-carvone are removed. The recovered Raman spectrum of (+)-carvone is in good agreement with the reference and only a few signals from hexane are embedded (see Figure 6.22 (a)).

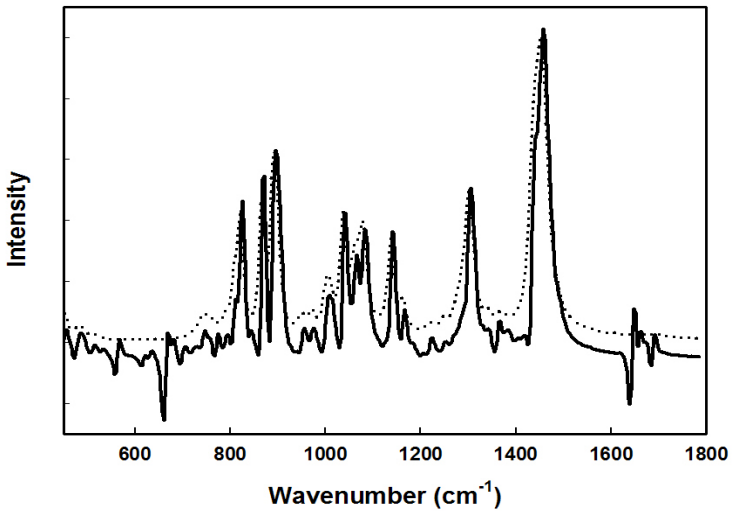

Figure 6.20. Solid lines: recovered pure component Raman spectra of hexane obtained by BTEM and Dotted lines: experiment reference Raman spectra.

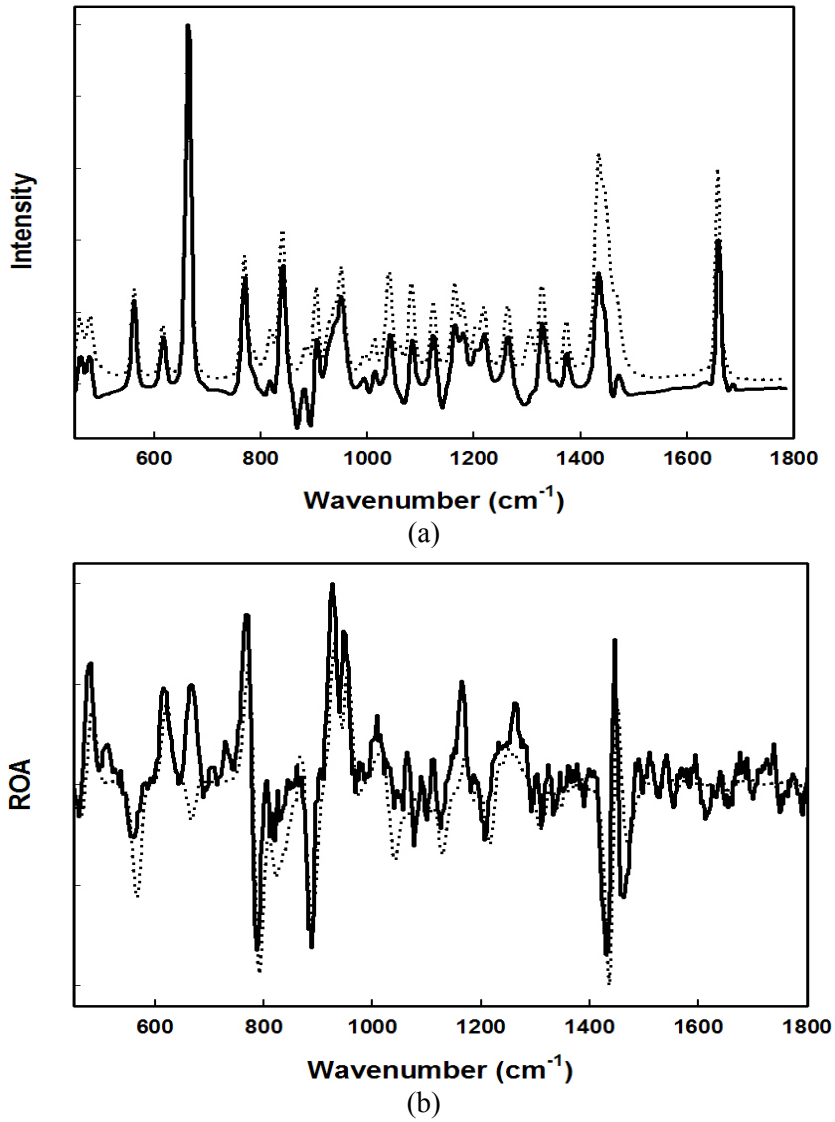

Figure 6.21. Recovered pure component spectra by BTEM (solid lines) and experiment reference spectra (dotted lines): (a) Raman spectra of (−)-α-pinene; (b) ROA spectra of (−)-α-pinene.

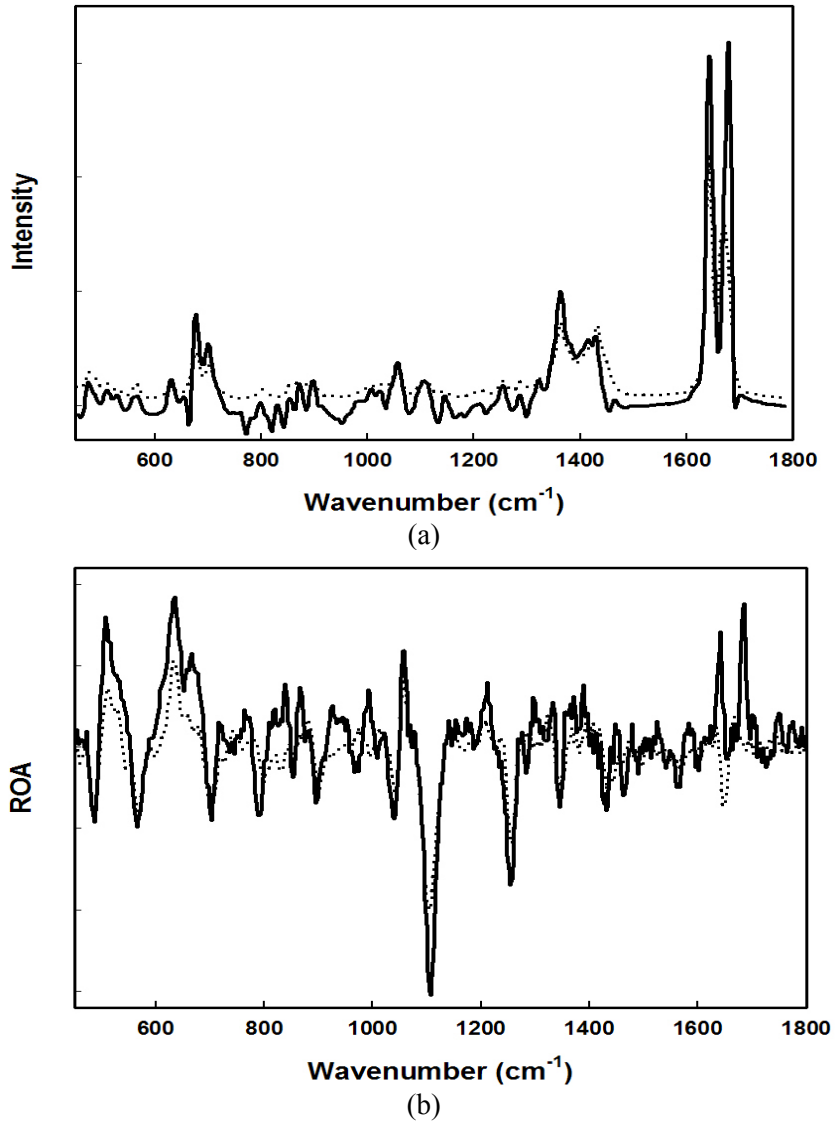

Figure 6.22. Recovered pure component spectra by BTEM (solid lines) and experiment reference spectra (dotted lines): (a) Raman spectra of (+)-carvone and (b) ROA spectra of (+)-carvone.

It is promising that the recovered ROA spectra of both (−)-α-pinene and (+)-carvone in Figures 6.21 (b) and 6.22 (b) are in good agreement with the reference spectra considering the poor quality of the raw experimental ROA data. This indicates that spectral reconstruction from *dilute* chiral systems can be achieved by the application of ROA spectroscopy combined with a reliable and effective chemometric technique, the Chiral-BTEM algorithm.

6.7.2.3 Concentrations Profiles

The relative concentration profiles of (−)-α-pinene and (+)-carvone were further calculated using the recovered pure component Raman and ROA spectra. For the sample with repeated measurements, the concentration was the average of each repeated measurement. Figure 6.23 compares the concentration profiles of (−)-α-pinene and (+)-carvone predicted from estimated Raman and ROA spectra and obtained from the experimental design.

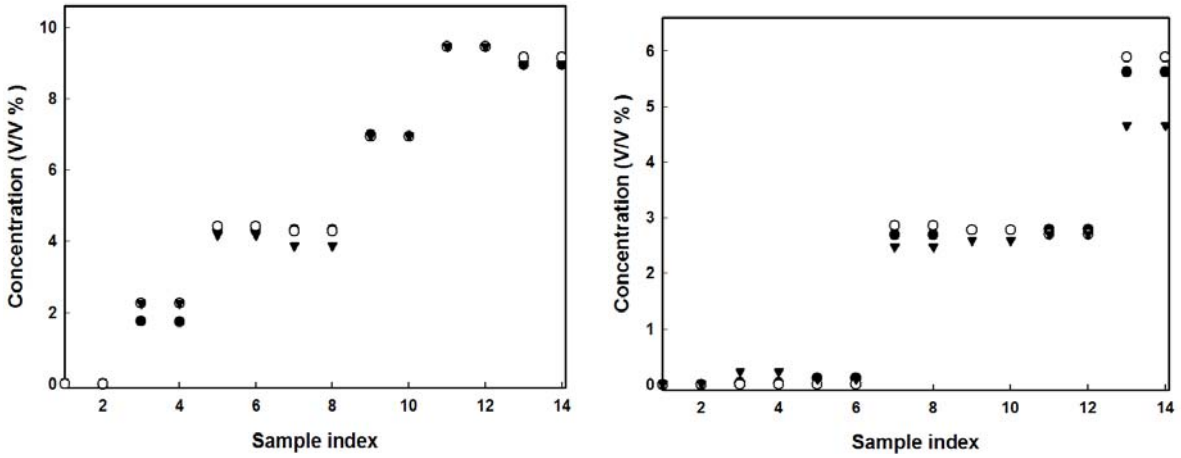

(a) (b)

Figure 6.23. Comparison of concentration profile determined from recovered Raman pure component spectra (●), ROA pure component spectrum (▼) and experiment design (○). Profiles for (a) (−)-α-pinene and (b) (+)-carvone.

In Figure 6.23 (a), satisfactory concentration profiles of (−)-α-pinene using both the recovered Raman and ROA spectra are obtained. The deviations between the calculated concentration profiles and the experiment design are very small. In Figure 6.23 (b), the concentration profiles of (+)-carvone calculated from both the recovered Raman and ROA spectra are consistent with the experiment design except that some discrepancy appears at the last two points as more and more perturbations are made. In addition, the predicted concentrations for (−)-α-pinene are generally better than (+)-carvone and this is

probably due to the higher (−)-α-pinene concentrations present. *It is very important to note that, since a multivariate approach is taken, quite good concentration estimates can be obtained even though the spectra or spectral estimates are noisy / slightly in error.*

The current results indicate that (1) the experimentally obtained Raman and ROA spectra of the chiral mixtures using the Chiral*Raman*^{TM} instrument combined with the application of BTEM/Chiral-BTEM method can successfully obtain the individual spectra of each species (chiral or achiral compounds) present; (2) with the Raman and ROA spectra recovered using BTEM/Chiral-BTEM, satisfactory qualitative and quantitative information can be achieved; (3) the recovered ROA spectra from the dilute chiral mixtures have good spectral quality and accuracy compared to the experiment references; and (4) ROA is an attractive quantitative tool for organic chiral mixtures.

6.8 Determination of Enantiomeric Excess

The goal of this study is to develop the technology for fast enantiomeric excess (optical purity) determination without separation of products. This includes ROA analysis of enantiomeric solutions.

6.8.1 Experimental Data

The enantiomeric solutions of (+)-α-pinene and (−)-α-pinene in (n)-hexane with different ee at several different concentrations were measured using ROA instrument. Five different enantio-excesses (-90%, -80%, -70%, -60% and -50%) were used, where the (+)-α-pinene is selected as the reference. The concentrations used were from the high concentration (100%) to relative low concentration (30%) regime. The details of each

sample can be found in Table 6.1. A total of 105 pairs of Raman and ROA spectra for the enantiomeric solutions were obtained from the experiment. The experimentally obtained Raman and ROA spectra were the result of 512 co-added scans at 270mW laser power.

Two typical experimental Raman spectra and two typical ROA spectra are shown in Figure 6.24 and 6.25, respectively. Both the Raman and ROA spectra have considerably good signal-to-noise ratio. Moreover, the ratio of the magnitude of Raman intensity and ROA intensity is circa 10^4. The observed intensity changes occur due to the different concentrations present in both Raman and ROA spectra.

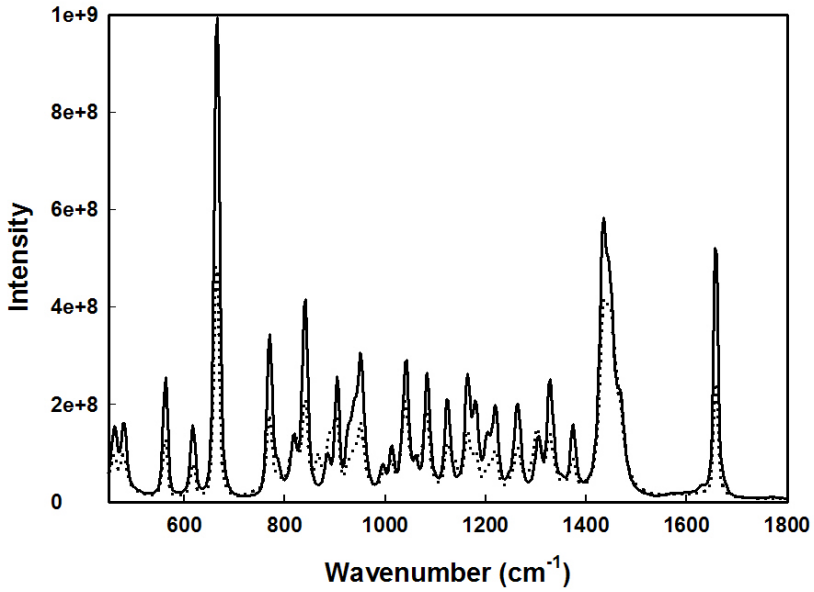

Figure 6.24. Two typical experimental Raman spectra from the samples of -90% ee in the volumetric concentration of 100% and 50% (see Table 6.1).

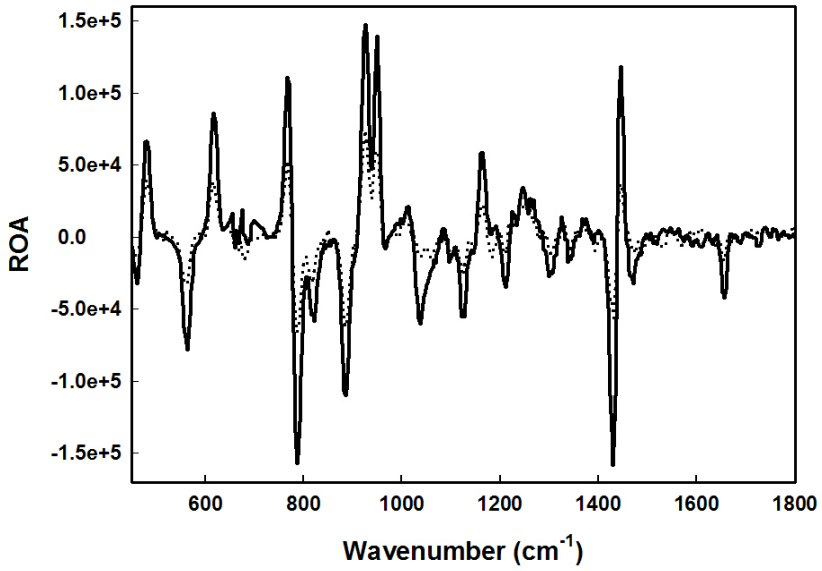

Figure 6.25. Two typical experimental ROA spectra from the samples of -90% ee in the volumetric concentration of 100% and 50% (see Table 6.1).

6.8.2 Spectral Reconstruction using BTEM

A total of 105 Raman spectra and 105 ROA spectra were subjected to BTEM/Chiral-BTEM to retrieve the pure component spectra. The recovered Raman spectrum of (n)-hexane is shown in Figure 6.26. The recovered Raman spectrum of (n)-hexane has most signals from both (+)-α-pinene and (−)-α-pinene removed, and only a minimum amount of signal is seen in the region where the reference spectrum are quite flat. Figure 6.27 show the recovered Raman and ROA spectra of both (+)-α-pinene and (−)-α-pinene. All of these recovered spectra are in good agreement with the reference spectra. The only discrepancy for the relative intensity of the recovered Raman spectrum in Figure 6.27 (a) appears for the band at circa 1670 cm^{-1}.

The results demonstrate that the spectral reconstruction method BTEM/Chiral-BTEM can be successfully applied to the ROA spectroscopy for enantiomeric solutions.

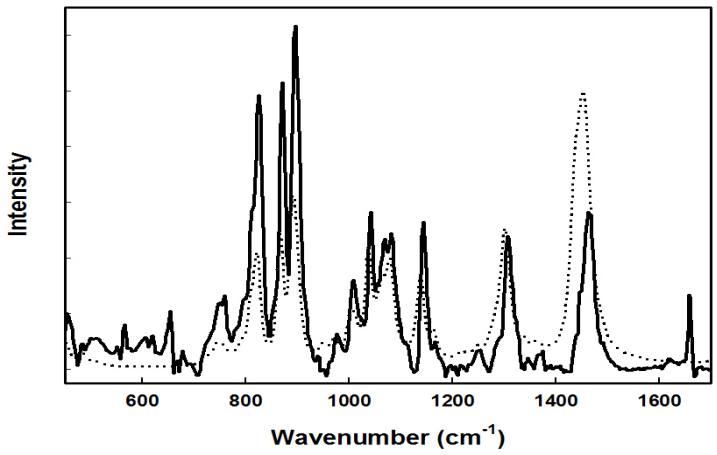

Figure 6.26. Solid line: recovered pure component Raman spectra of hexane obtained by BTEM and Dotted line: experiment reference Raman spectra.

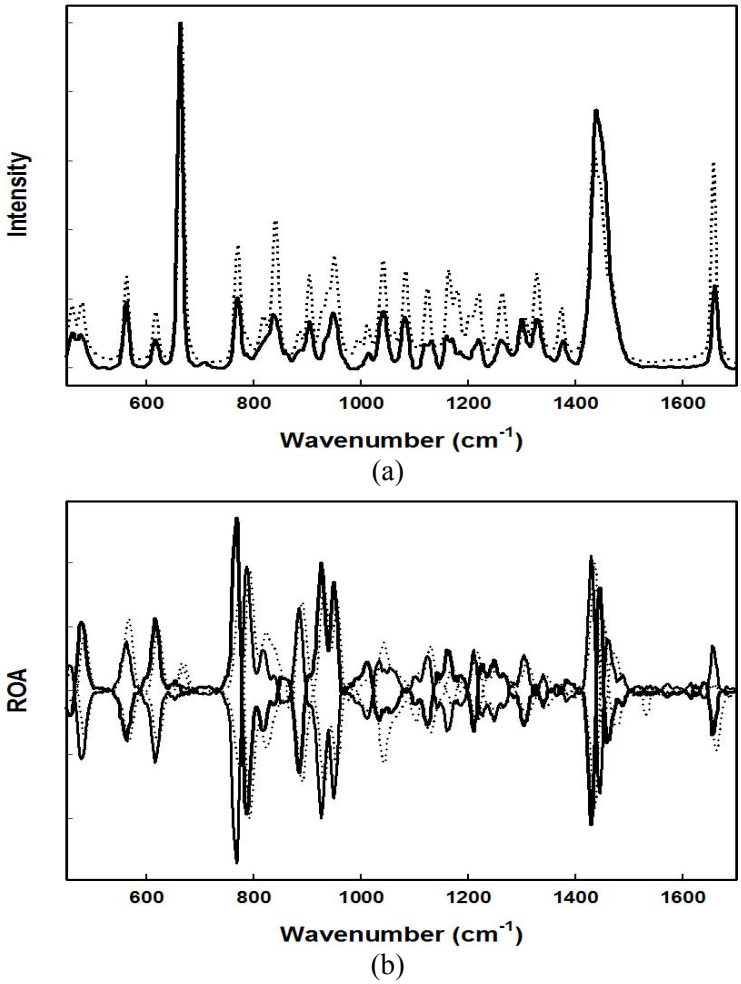

Figure 6.27. Recovered pure component spectra by BTEM (solid lines) and experiment reference spectra (dotted lines): (a) Raman spectra of α-pinene and (b) ROA spectra of (+)-α-pinene and (−)-α-pinene.

6.8.3 Concentrations Profiles

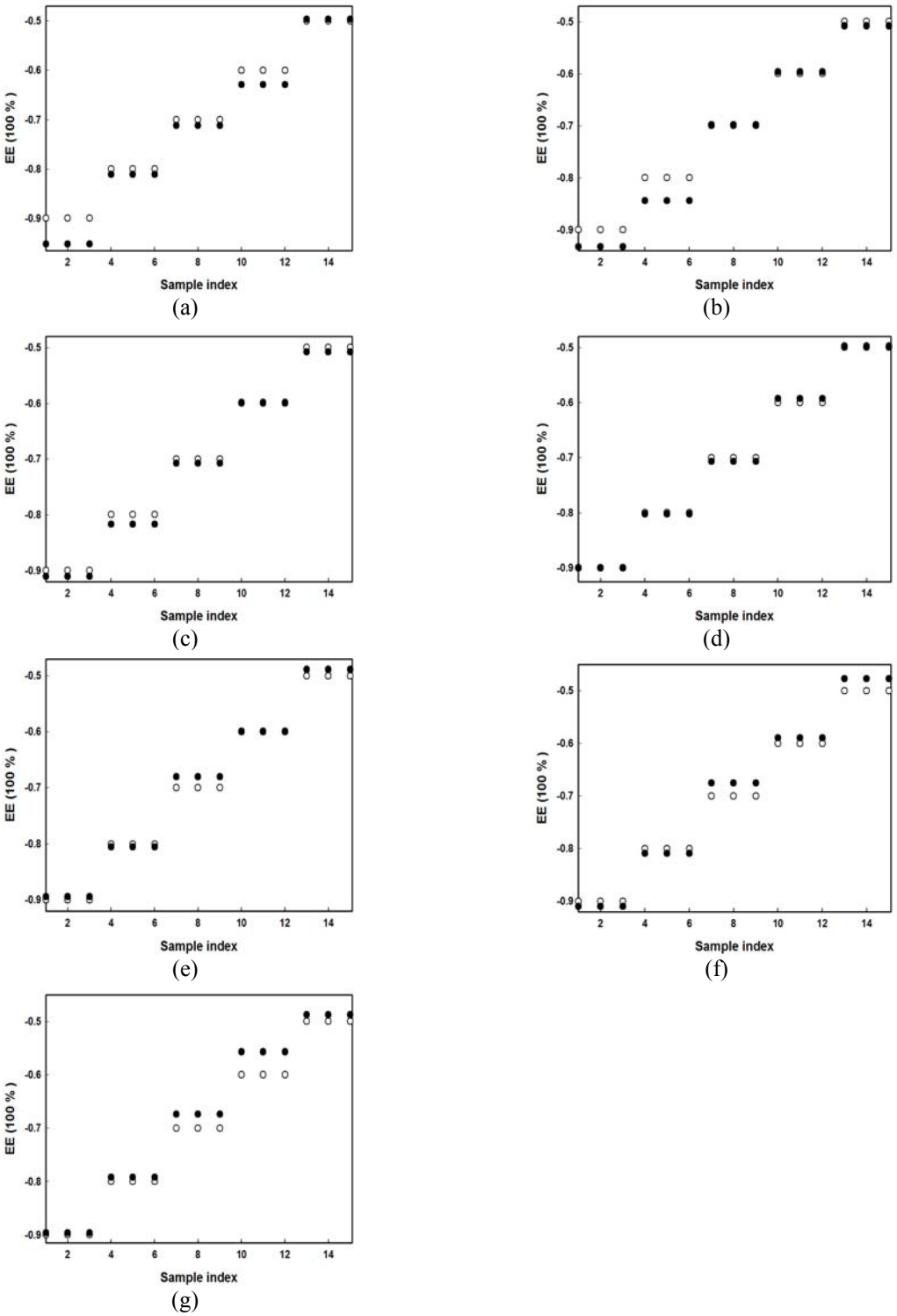

Figure 6.28. Comparison of enantiomeric excess determined for α-pinene from recovered Raman and ROA pure component spectra (●) and experiment design (○). Profiles for different concentration experiments as experiment designs (see Table 6.1): (a) 100%, (b) 80%, (c) 70%, (d) 60%, (e) 50%, (f) 40%, (g) 30%.

The enantiomeric excess profiles of α-pinene were further calculated using the combination of the recovered pure component Raman and ROA spectra. For the sample with repeated measurements, the concentration was the average of each repeated measurement.

Figures 6.28 (a)~(g) compare the predicted enantiomeric excess profiles of α-pinene enantiomer and those obtained from the experimental design for seven different concentration experiments (see Table 6.1). In Figure 6.28, for all 7 experiments with ee from -90% to -50%, satisfactory enantiomeric excess profiles are obtained while the best enantiomeric excess profile predictions were given by the intermediate concentration experiments. Thus the 70%, 60% and 50% concentration experiments present the best enantiomeric excess predictions.

Figure 6.29 shows all the predicted enantiomeric excess in a different manner.

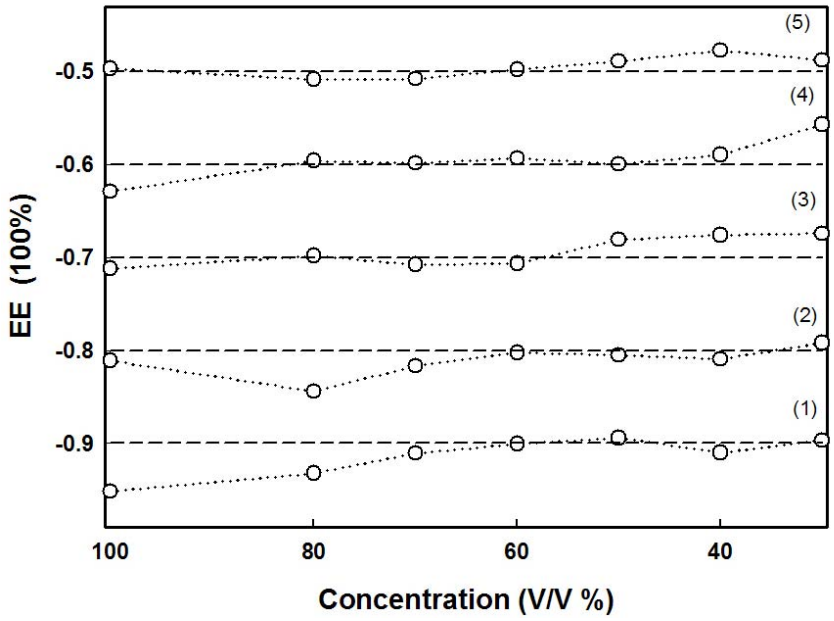

Figure 6.29. The prediction of ee for α-pinene determined from recovered Raman pure component spectra and ROA pure component spectra.

The X axis stands for the volumetric concentration and the Y axis stands for enantiomeric excess. In this way, it is clearly seen that the experiments performed at the intermediate concentrations and moderate ee provide the most accurate results. This might be due to the nonlinear dependency of the Raman and ROA response for enantiomeric solutions.

6.9 Summary

In the current chapter, the ROA spectra of neat chiral liquid, chiral solutions and enantiomeric solutions were experimentally obtained using the Chiral*RAMAN*^{TM} instrument from BioTools which can carry out Raman and SCP-ROA measurements at the same time. The experimentally obtained ROA spectra of neat chiral liquid (+)-α-pinene and (−)-α-pinene have good quality (10 minutes measurement period) and they are almost mirror images of each another. Good agreement was found between the theoretical DFT calculations with B3LYP functional with 6-311G∗ basis set for the ROA spectra of (+)-α-pinene and (−)-α-pinene and the experimental spectra although the calculated ROA signs and positions of some bands did not correspond to the experiments. The ROA spectra of the chiral compounds of (+)-camphor and (−)-camphor in chloroform were also recorded (10 minutes measurement period) and quite good ROA spectra were achieved. Again good agreement between the theoretical DFT calculations for the ROA spectra of (+)-camphor and (−)-camphor and the experimental spectra were obtained. This demonstrates that experimental ROA spectra combined with Chiral-BTEM and DFT calculations can be a promising tool for the determination of the absolute configuration of chiral molecules.

In addition, the Chiral-BTEM algorithm was successfully applied to spectral reconstruction of ROA spectra from chiral solutions and enantiomeric solutions. The recovered ROA spectra for the pure chiral components have good quality and are in good agreement with the experimental spectra. Moreover, quantitative analysis such as the determination of concentrations for the chiral species in the solution and the determination of the enantiomeric excess for enantiomers in solution were performed and good agreement was found between the calculated concentrations or ee and the experiment design. The enantiomeric excess for enantiomers in solution was achieved without any sample separations. This new development for fast enantiomeric excess (optical purity) determination without separation of products can provide useful information for pharmaceutical and fine chemical reactive systems.

Chapter 7

Conclusions and Future Work

7.1 Conclusions

The main contribution of this thesis is to develop multivariate curve resolution (MCR) methods based on minimum-entropy to solve important system identification problems associated with the resolution of pure component spectra and their associated concentration profiles in four different type spectroscopies, namely, IR emission spectroscopy (IRES), Ultra-violet circular dichroism (UV CD), Raman Optical Activity (ROA) and Far-IR/ Far-Raman spectroscopies. In addition, the combination of such MCR methods and theoretical calculations on Density Functional Theory level have proven to be a valuable tool for the vibration assignments and the determination of absolute configurations.

7.1.1 IRES Aspects

The present work systematically studied the non-reactive solid and liquid phase samples as well as reactive systems, for instance, a cyclo-addition organic synthesis in the liquid phase using IRES in terms of the experimental and MCR tools.

As for experiments, a stainless steel thermostated emission cell used in the present study was newly designed and constructed in-house. This cell is suitable for both solid samples and liquid film samples. Good experimental IRES spectra were

obtained with the new experimental configuration.

Emission mode BTEM (Band-Target Entropy Minimization) was developed and successfully applied to resolve the pure component emission spectra from the mixture data for both the non-reactive as well as reactive systems. An approximate Lambert-Beer law for emission spectroscopy, similar to the Lambert-Beer law for absorbance IR spectroscopy, was formulated. This new equation is simpler and more applicable than the Beer-Lambert law of the emission spectroscopy. It provides the essential bilinear model for emission mode BTEM algorithm. The present work confirmed that emission mode BTEM is an efficient approach to eliminate the effects of large background radiation. In addition, the present work demonstrated that it is possible to remotely monitor a liquid phase organic synthesis near ambient temperature by infrared emission spectroscopy, thus obtaining the pure component spectral estimates of the species and first approximations to the relative concentration profiles. This contribution appears to be the first time that a liquid-phase reaction has been studied by the combination of infrared emission spectroscopy and BTEM. However, the present work also indicated that some experimental and numerical improvements are needed in order to obtain better signal-to-noise IRES spectra and apply the method to more general reactive systems. For example, (1) using a dedicated infrared emission spectrometer instead of the current multi-purpose spectrometer modified for emission experiments would greatly increase signal throughput, (2) a new design for the cell which has a special thermostated window will help to reduce thermal gradients in the fluid and hence reduce re-absorption

phenomenon, and (3) optimize the film thickness in order to obtain sharper and more resolved spectral features.

7.1.2 UV CD Aspects

This work mainly focused on the development of Chiral-BTEM and its application to UV CD spectroscopy for reactive systems containing chiral compounds. The current work also focused on the application of BTEM to Ultraviolet-visible (UV-Vis) absorbance spectroscopy for achiral systems (BTEM has until now been focused on other spectroscopies). Consequently, two different organometallic ligand substitution reactions were investigated: (1) $Rh_4(CO)_{12}$ with an achiral ligand, PPh_3 and (2) $Rh_4(CO)_{12}$ with a chiral ligand, (S)-BINAP. These two reactions were carried out at ultra high dilution, i.e. the concentrations of all the solutes were less than 40ppm and many solute concentrations were just 1~10ppm. The reconstructed UV-Vis pure component spectra of $Rh_4(CO)_{12}$, $Rh_4(CO)_{11}PPh_3$ and $Rh_4(CO)_{10}$BINAP as well as the reconstructed UV-Vis CD pure component spectra of $Rh_4(CO)_{10}$BINAP were successfully obtained from the Chiral-BTEM analyses. All these reconstructed pure component spectra are in good agreement with the experimental references. The quantitative analysis for these two substitutions was also performed.

The present results demonstrated that Chiral-BTEM can successfully resolve UV CD spectral data, a type of spectra with negative signals due to chiral chromophores, for reactive systems at high dilutions. This result may suggest that much more complex systems can be studied by means of a combination of UV CD and Chiral-BTEM.

7.1.3 ROA Aspects

In present thesis, experimental measurements, numerical work (application of Chiral-BTEM) and DFT calculations were all integrated for ROA studies. ROA spectra of neat chiral liquid, chiral solutions and enantiomeric solutions were experimentally obtained with good quality using the Chiral*RAMAN*^{TM} instrument from BioTools within reasonable measurement time. An appropriate DFT method B3LYP/6-311G∗ was found to be successful in predicting the molecular structure and the ROA spectra of various chiral molecules. DFT combined with the ROA experimental spectra and Chiral-BTEM results played a vital role in the determination of absolute configurations in the current dissertation. In addition, Chiral-BTEM was used to determine the concentration or the enantiomeric excess. The present results indicated that this new Chiral-BTEM development is a useful tool for the accurate determination of enantiomeric excess without separation of products. Thus it can provide meaningful information for studying stereo-selective syntheses for many industrial products such as pharmaceuticals, fragrances, pesticides and biological substances.

7.1.4 Far-IR and Far-Raman Aspects

In this work, an integration of BTEM, DFT and experimental methodology (Far-IR and Far-Raman spectroscopy) was used to assign the vibrational properties of the metal carbonyl clusters $Mn_2(CO)_{10}$, $Mo(CO)_6$ and $Re_2(CO)_{10}$ at low wavenumbers. DFT calculations were performed using different functionals (B3LYP, B3PW91, PBE

and LSDA involved) and basis sets (6-311G, LanL2DZ and DGDZVP involved) The comparison of such DFT predicted spectrum and the one experimentally observed was the basis for carrying out the vibrational assignment. Preliminary results showed that the chosen basis sets generated satisfactory vibrational frequencies predictions for both mononuclear and binuclear metal carbonyls. Additionally, B3LYP, B3PW91 and PBE often performed better than LSDA in the frequency predictions. It is worth mentioning that the basis set DGDZVP was applied on the entire cluster which includes the metal center and the other elements. In the future research, however, more than one basis wherein a certain basis set is used for the metal while another appropriate basis set is used for the coordinated organic ligands might be used to obtain better DFT predictions when studying organometallics.

7.2 Future Work

In the current studies, it has been shown that many system identification problems associated with IR emission spectroscopy (IRES), chiroptical spectroscopy including Ultra-violet circular dichroism (UV CD) and Raman Optical Activity (ROA), and Far-IR and Far-Raman spectroscopy can be solved using a combination of in-situ spectroscopies, emission BTEM/Chiral-BTEM, and/or DFT calculations method. In this section, some related future research and improvements will be recommended.

1. The use of infrared emission spectroscopy and emission mode BTEM to the investigation of liquid phase organic syntheses could be further used to study much

more complex organic syntheses. For example, it would be a good alternative to IR transmission or ATR spectroscopy for studying multi-phase complex organic syntheses involving floating solids or bubbles in the liquid phase (i.e. salt forming reactions, Gringard reactions, heterogeneous catalytic reactions and hydrogenations). Due to the suspended solids or with bubbles, the entire reaction system has low transparency and hence it is difficult to obtain good spectra IR transmission or ATR spectroscopy. Future work can further investigate heterogeneous catalytic syntheses wherein the catalysts may have strongly absorbing bands in IR transmission spectroscopy or diffuse reflectance. In addition, IRES would be an appropriate tool for remote monitoring of combustion and other extreme processes.

2. Research related to DTF calculations can be extended to other analytical technique such UV-Vis spectroscopy. Recent work with time-dependent DFT has shown that reasonably good spectral estimates can be made for many mononuclear and dinuclear complexes. Since UV-Vis absorptivities are generally very large, it may be possible in the future to use UV-Vis spectroscopy with BTEM and DFT to identify organometallic intermediates at very low concentrations during homogeneous catalytic reactions.

3. Chiral-BTEM proved to be an efficient method to resolve pure spectra from UV CD and ROA spectroscopies as well as to obtain qualitative analysis such as concentration and ee. Continuing in this direction, further studies will be extended to develop chemometric methods for additional chiroptical spectroscopies such as vibrational circular dichroism (VCD), fluorescence CD, x-ray CD, luminescence CD

and magnetic circular dichroism (MCD). In addition, it could provide a promising tool with which to investigate enantio-selective organic reactions, i.e. transition metal homogeneous catalysis for fine chemicals and pharmaceutical syntheses. Further work could also focus on determining the enantio-excess of metal complexes present as intermediates using Chiral-BTEM.

References

Alagna, L., T. Prosperi, S. Turchini, J. Goulon, A. Rogalev, C. Goulon-Ginet, C.R. Natoli, R.D. Peacock and B. Stewart. X-ray Natural Circular Dichroism. Phys. Rev. Lett. *80* (21), pp. 4799-4802. 1998.

Allian, A.D., E. Widjaja and M.Garland. Experimental Raman Spectra of Dilute and Laser-Light-Sensitive $[Rh_4(CO)_9(mu\text{-}CO)_3]$ and [(mu(4)-eta(2)-3-hexyne)$Rh_4(CO)_8(mu\text{-}CO)_2$]. Comparison with Theoretically Predicted Spectra. Dalton Trans. *35*, pp. 4211-4217. 2006.

Andrew, J.J. and T.M. Hancewicz. Rapid Analysis of Raman Image Data Using Two-Way Multivariate Curve Resolution. Appl. Spectrosc. *52*, pp. 797-807. 1998.

Antonov, L., G. Gergov, V. Petrov, M. Kubista and J. Nygren. UV-Vis Spectroscopic and Chemometric Study on the Aggregation of Ionic Dyes in Water. Talanta *49* (1), pp. 99-106. 1999.

Barron, L.D. Chemistry - Compliments from Lord Kelvin. Nature. *446* (7135), pp. 505-506. 2007. (Lord Kelvin Baltimore Lectures (Clay, London, 1904)).

Barron, L.D., L. Hecht, E.W. Blanch and A.F. Bell. Solution Structure and Dynamics of Biomolecules from Raman Optical Activity. Prog. Biophys. Mol. Biol. *73*, pp. 1-49. 2000.

Barron, L.D., E.W. Blanch, I.H. McColl, C.D. Syme, L. Hecht and K. Nielsen. Structure and Behaviour of Proteins, Nucleic Acids and Viruses from Vibrational Raman Optical Activity. Spectroscopy- An International Journal *17*, pp. 101-126. 2003.

Barron, L.D., L. Hecht, I.H. McColl and E.W. Blanch. Raman Optical Activity Comes of Age. Mol. Phys. *102* (8), pp. 731-744. 2004.

Barron, L.D., F.J. Zhu and L. Hecht. Raman Optical Activity: An Incisive Probe of Chirality, and of Biomolecular Structure and Behaviour. Vib. Spectrosc. *42*, pp. 15-24. 2006.

Baumruk, V. and T.A. Keiderling. Vibrational Circular-Dichroism of Proteins in H_2O. J. Amer. Chem. Soc. *115* (15), pp. 6939-6942. 1993.

Becke, A.D. A New Mixing of Hartree-Fock and Local Density-Functional Theories. J. Chem. Phys. *98*, pp. 1372-1377. 1993.

Becke, A.D. Density-Functional Thermochemistry. 3. The Role of Exact Exchange. J. Chem. Phys. *98*, pp. 5648-5652. 1993.

Bell, A.F., L. Hecht and L.D. Barron. Evidence for a New Transition in Polyribonucleotides from Raman Optical Activity. J. Raman Spectrosc. *30* (8), pp. 651-656. 1999.

Berces, A. Harmonic Vibrational Frequencies and Force Constants of $M(CO)_5CX$ (M=Cr, MO, W: X=O, S, Se). The Performance of Density Functional Theory and the Influence of Relativistic Effects. J. Phys. Chem. *100*, pp. 16538-16544, 1996.

Berces, A. and T. Ziegler. Harmonic Force-Fields and Vibrational Frequencies of Benzene, Dibenzene-Chromium, Benzene-Chromium Tricarbonyl, and Chromium-Hexacarbonyl – A Density-Functional Study. J. Phys. Chem. *98* (50), pp. 13233-13242. 1994.

Berces, A. and T. Ziegler. Application of Density Functional Theory to the Calculation of Force Fields and Vibrational Frequencies of Transition Metal Complexes. Density Functional Theory III Topics in Current Chemistry *182*, pp. 41-85. 1996.

Blanch, E.W., D.D. Kasarda, L. Hecht, K. Nielsen and L.D. Barron. New Insight into the Solution Structures of Wheat Gluten Proteins from Raman Optical Activity. Biochemistry. *42*, pp. 5665-5673. 2003.

Blanch, E.W., L. Hecht and L.D. Barron. Vibrational Raman Optical Activity of Proteins, Nucleic Acids, and Viruses. Methods *29*, pp. 196-209. 2003.

Blanch, E.W., A.C. Gill, A. Rhie, J. Hope, L. Hecht, K. Nielsen and L.D. Barron. Raman Optical Activity Demonstrates Poly(L-proline) II Helix in the N-terminal Region of the Ovine Prion Protein: Implications for Function and Misfunction. J. Mol. Biol. *343*, pp. 467-476. 2004.

Blanch, E.W., I.H. McColl, L. Hecht, K. Nielsen and L.D. Barron. Structural Characterization of Proteins and Viruses using Raman Optical Activity. Vib. Spectrosc. *35*, pp. 87-92. 2004.

Bu, D.S. and C.W. Brown. Self-Modeling Mixture Analysis by Interactive Principal Component Analysis. Appl. Spectrosc. *54*, pp. 1214-1221. 2000.

Buckingham, A.D. The Theoretical ackground to Vibrational Optical-Activity – Introductory Lecture. Faraday Discuss. *99*, pp. 1-12. 1994.

Braekeleer, K.D. and Massart, D.L. Evaluation of the Orthogonal Projection Approach (OPA) and the Simplisma Approach on the Windig Standard Spectral Data Sets. Chemom. Intell. Lab. Syst. *39*, pp. 127-141. 1997.

Brown, S.D., T. Barke and R. Larivee. Chemometrics. Anal. Chem. *60*, pp. 252R-273R. 1988.

Brown, S.D. Chemometrics. Anal. Chem. *62*, pp. 84R-101R. 1990.

Brown, S.D., R. S. Bear, and T.B. Blank. Chemometrics. Anal. Chem. *64*, pp. 22R-49R. 1992.

Brown, S.D., T.B. Blank, S.T. Sum and Lois G. Weyer. Chemometrics. Anal. Chem. *66*, pp. 315R-359R. 1994.

Brown, S.D., S.T. Sum, F.Despagne and B.K. Lavine. Chemometrics. Anal. Chem. *68*, pp. 21R-61R. 1996.

Brown, S.D. Information and data handling in chemistry and chemical engineering: the state of the field from the perspective of chemometrics. Comput. Chem. Eng. *23* (2), pp. 203-216. 1998.

Bu, D.S. and C.W. Brown. Self-Modeling Mixture Analysis by Interactive Principal Component Analysis. Appl. Spectrosc. *54*, pp. 1214- 1221. 2000.

Carvalho, A., G. Hancock and M. Saunders. The Reaction Products of the 193 nm Photolysis of Vinyl Bromide and Vinyl Chloride Studied by Time-Resolved Fourier Transform Infrared Emission Spectroscopy. Phys. Chem. Chem. Phys. *8*(37), pp. 4337-4346. 2006.

Cary, H.H. and A.O. Jr. Beckman. "A Quartz Photoelectric Spectrophotometer." J. Opt. Soc. Am. *31*, pp. 682-689. 1941.

Decker, S.A., O. Donini and M. Klobukowski. A Contribution to the Understanding of Carbonyl Migration in Mn2(CO)10 via the Pairwise Exchange Mechanism. J. Phys. Chem. A *101*(46), pp. 8734-8740. 1997.

Cedeno, D.L., E. Weitz and A. Berces. Bonding Interactions in Olefin (C2X4, X = H, F, Cl, Br, I, CN) Iron Tetracarbonyl Complexes: Role of the Deformation Energy in Bonding and Reactivity. J. Phys. Chem. A *105* (34), pp. 8077-8085. 2001.

Chase, D.B. The Sensitivity and Limitations of Condensed Phase Infrared-Emission Spectroscopy. Appl. Spectrosc. *35*, pp. 77-81. 1981.

Chalmers, J. M. and P. R. Griffiths. Handbook of Vibrational Spectroscopy Volume 1& 2, John Wiley & Sons, Chichester, 2002.

Chen, L. and M. Garland The Use of Entropy Minimization for the Preconditioning of Large Spectroscopic Data Arrays. Application to In-Situ FTIR Studies from the Unmodified Homogeneous Rhodium Catalyzed Hydroformylation Reaction. In Press. Applied Spectroscopy. 2002.

Chen, L., W. Chew and M. Garland. Spectral Pattern Recognition of *in Situ* FT-IR Spectroscopic Reaction Data Using Minimization of Entropy and Spectral Similarity (MESS): Application to the Homogeneous Rhodium Catalyzed Hydroformylation of Isoprene. Appl. Spectrosc., *57*, pp. 491-498. 2003.

Chew, W., E. Widjaja and M. Garland. Band-Target Entropy Minimization (BTEM): An Advanced Method for Recovering Unknown Pure Component Spectra. Application to the FTIR Spectra of Unstable Organometallic Mixtures. Organometallics *21*(9), pp. 1982-1990. 2002.

Chiang, S., R.G. Tobin and P.L. Richards. Vibrational Spectroscopy of Chemisorbed Molecules by Infrared-Emission. *J. Vac. Sci. Technol. A. 2* (2), pp. 1069-1074. 1984.

Chiang, S., R.G. Tobin, P.L. Richards and P.A. Thiel. Molecule-Substrate Vibration of CO on Ni(100) Studied by Infrared-Emission Spectroscopy. Phys. Rev. Lett. 52 (8), pp. 648-651. 1984.

Coblentz, W.A. Supplementary Investigations of Infrared Spectra, Part 7. The Carnegie Institute, Washington, D.C., 1908.

Corana, A., M. Marchesi, C. Martini, and S. Ridella. Minimizing Multimodal Functions of Continuous Variables with the "Simulated Annealing" Algorithm, ACM Trans. Math. Softw. *13*, pp. 262-280. 1987.

Cotton, F. A. and X. Feng. Density Functional Theory Study of Transition-Metal Compounds Containing Metal-Metal Bonds. 1. Molecular Structures of Dinuclear Compounds by Complete Geometry Optimization. J. Amer. Chem. Soc. *119*(32), pp. 7514-7520. 1997.

Cotton, F. A. and X. Feng. Density Functional Theory Study of Transition-Metal Compounds Containing Metal-Metal Bonds. 2. Molecular Structures and Vibrational Spectra of Dinuclear Tetracarboxylate Compounds of Molybdenum and Rhodium. J. Amer. Chem. Soc. *120*(14), pp. 3387-3397. 1998.

DeBlase, F.J. and S. Compton. Infrared-Emission Spectroscopy – A Theoretical and Experimental Review. Appl. Spectrosc. *45* (4), pp. 611-618. 1991.

Debre, P. and E. Forster. Louis Pasteur. Baltimore, MD: Johns Hopkins University Press. 1998

Deming, D., D. Charbonneau and J. Harrington. Spectroscopy of Molecular Hydrogen Emission from KH 15D, Astrophys. J. *601* (1), pp. 87-90. 2004.

Dickson, R. Homogeneous Catalysis with Compounds of Rhodium and Iridium (Catalysis by Metal Complexes), Springer, 2003.

Du, Y.P., J.H. Jiang, Y.Z. Liang and Y. Ozaki. Chemometric Resolution of ATR-IR Spectra Data for Polycondensation Reaction of Bis(hydroxyethylterephthalate) with a Combination of Self-Modeling Curve Resolution (SMCR) and Local Rank Analysis. Analyst *128* (11), pp. 1320-1325. 2003.

Durana, J.F. Infra-red Emission Studies of Thin Polymer Films. Polymer. *20* (11), pp. 1306-1307. 1979.

El-Sayed, I., X. Huang, F. Macheret, J.O. Humstoe, R. Kramer and M. El-Sayed. Effect of Plasmonic Gold Nanoparticles on Benign and Malignant Cellular Autofluorescence: A Novel Probe for Fluorescence Based Detection of Cancer. Technology in Cancer Research & Treatment. *6* (5), pp. 403-412. 2007.

Esteban, M., C. Arino, J.M. Diaz-Cruz, M.S. Diaz-Cruz and R. Tauler. Multivariate Curve Resolution with Alternating Least Squares Optimisation: A Soft-Modelling Approach to Metal Complexation Studies by Voltammetric Techniques. TrAC, Trends Anal. Chem. *19* (1), pp. 49-61. 2000.

Faber, K. and B.R. Kowalski. Modification of Malinowski's F-test for Abstract Factor Analysis Applied to the Quail Roost II Data Sets. J. Chemom.. *11*, pp. 53-72. 1997.

Fan, L.Y. and T. Ziegler. Optimization of Molecular-Structures by Self-Consistent and Density-Functional Theory. J. Chem. Phys. *95*(10), pp. 7401-7408. 1991.

Fan, L. and T. Ziegler. Application of Density Functional Theory to Infrared Absorption Iintensity Calculations on Transition-Metal Carbonyls. J. Phys. Chem., 96(17), pp. 6937-6941. 1992.

Fielicke, A., C. Ratsch, G. Von Helden and G. Meijer. Isomer Selective Infrared Spectroscopy of Neutral Metal Clusters. J. Chem. Phys. *122*(9), pp. 1-4. 2005.

Fielicke, A., G. von Helden and G. Meije. Far-Infrared Spectroscopy of Isolated Transition Metal Clusters. Eur. Phys. J. D *34*(1-3), pp. 83-88. 2005.

Freedman, T.B., S. Liu, F. Lee and L.A. Nafie. Infrared Vibrational Circular Dichroism of Cyclosporin A and Several Analogs. Biophys. J. *70* (2), pp. TU435-TU435. 1996.

Freedman, T.B., L.A. Nafie and T.A. Keiderling. Vibrational Optical-Activity of Oligopeptides. Biopolymers. *37* (4), pp. 265-279. 1995.

Freedman, T.B., X.L. Cao, L.A. Nafie, M. Kalbermatter, A. Linden and A.J. Rippert. Determination of the Atropisomeric Stability and Solution Conformation of Asymmetrically Substituted Biphenyls by Means of Vibrational Circular Dichroism (VCD). HeIv. Chim. Acta *88* (8), pp. 2302-2314. 2005.

Frenich, A.G., M.M. Galera, J.L.M. Vidal, D.L. Massart, J.R. Torres-Lapasio, K. De Braekeleer, J.H. Wang, and P.K. Hopke. Resolution of Multicomponent Peaks by Orthogonal Projection Approach, Positive Matrix Factorization and Alternating Least Squares. Anal. Chim. Acta. *411*, pp. 145-155. 2000.

Frost, R.L. and A.M. Vassallo. The Dehydroxylation of the Kaolinite Clay Minerals using Infrared Emission Spectroscopy, Clays Clay Miner. *44*(5), pp. 635-651. 1996.

Gemperline, P.J. A Prior Estimate of the Elution Profiles of the Pure Component in Overlapped Liquid Chromatography Peaks Using Target Factor Analysis. J. Chem. Inf. Comput. Sci., *24*, pp. 206-212, 1984.

Gemperline, P.J. Target Transformation Factor Analysis with Linear Inequality Constraints Applied to Spectroscopic-Chromatographic Data, Anal. Chem. *58*, pp. 2656-2663, 1986.

Gemperline, P.J., S.E. Boyette and K. Tyndall. Background Correction in Multicomponent Spectroscopic Analysis Using Target Transformation Factor Analysis. Appl. Spectrosc. *41* (3): 454-459. 1987.

Golub, G.H. and W. Kahan. Calculating the Singular Values and Pseudo-Inverse of a Matrix, J. SIAM, Numer. Anal. Ser. B, *2*, pp. 205-224. 1965.

Golub, G.H. and C.F. van Loan. Matrix Computations. Baltimore: The John Hopkins University Press. 1996.

Gourvenec, S., D.L. Massart and D.N. Rutledge. Determination of the Number of Components During Mixture Analysis Using the Durbin-Watson Criterion in the Orthogonal Projection Approach and in the Simple-to-Use Interactive Self-Modelling Mixture Analysis Approach. Chemom. Intell. Lab. Syst. *61*, pp. 51-61. 2002.

Greenfield, N. and G.D.Fasman. Computed Circular Dichroism Spectra for the Evaluation of Protein Conformation. Biochemistry *8* (10), pp. 4108. 1969.

Griffiths, P.R. Infrared Emission Spectroscopy. I. Basic Considerations**.** Appl. Spectrosc. *26*, pp. 73-76. 1972.

Guo, C..N., R.D. Shah, R.K. Dukor, X.L. Cao, T.B. Freedman and L.A. Nafie. Determination of Enantiomeric Excess in Samples of Chiral Molecules using Fourier Transform Vibrational Circular Dichroism Spectroscopy: Simulation of Real-Time Reaction Monitoring. Anal. Chem. *76* (23), pp. 6956-6966. 2004.

Guo, C..N., R.D. Shah, R.K. Dukor, X.L. Cao, T.B. Freedman and L.A. Nafie. Enantiomeric Excess Determination by Fourier Transform Near-Infrared Vibrational Circular Dichroism Spectroscopy: Simulation of Real-Time Process Monitoring. Appl. Spectrosc. *59* (9), pp. 1114-1124. 2005.

Guo, L.F. and M. Garland. Application of Two-Dimensional Band-Target Entropy Minimization to Fluorescence data: Implications for the Recovery of Patterns Arising from Only Bilinear and not Trilinear Structures. Appl. Spectrosc. *61* (2), pp. 148-156. 2007.

Guo, L.F, F. Kooli and M. Garland. A General Method for the Recovery of Pure Powder XRD Patterns from Complex Mixtures Using No *a priori* Information. Application of Band-Target Entropy Minimization (BTEM) to Materials Characterization of Inorganic Mixtures, Anal. Chim. Acta, *517*(1-2), pp.229-236. 2004.

Guo, L.F., A. Wiesmath, P. Sprenger and M. Garland. Development of 2D Band-Target Entropy Minimization and Application to the Deconvolution of Multicomponent 2D Nuclear Magnetic Resonance Spectra, Anal. Chem., *77*, pp. 1655-1662. 2005.

Hamilton, V.E. Thermal Infrared Emission Spectroscopy of the Pyroxene Mineral Series, J. Geophysical Res. *105*, pp. 9701-9716. 2000.

Handke, M. and N.J. Harrick. A New Accessory for Infrared-Emission Spectroscopy Measurements. Appl. Spectrosc. *40* (3), pp. 401-405. 1986.

Hay, P. J. and W. R. Wadt. Ab initio Effective Core Potentials for Molecular Calculations. Potentials for the Transition Metal Atoms Scandium to Mercury. J. Chem. Phys. *82*(1), pp. 270-83. 1985.

Hay, P. J. and W. R. Wadt. Ab initio Effective Core Potentials for Molecular calculations. Potentials for Potassium to Gold Including the Outermost Core Orbitals. J. Chem. Phys. *82*(1), pp. 299-310. 1985.

Nicklass, A., M. Dolg, H. Stoll and H. Preuss. Ab-initio Energy-Adjusted Pseudopotentials for the Noble-Gases Ne Through Xe – Calculation of Atomic Dipole and Quadrupole Polarizabilities. J. Chem. Phys. *102* (22), pp. 8942-8952. 1995.

Hecht, L., A.L. Phillips and L.D. Barron. Determination of Enatiomeric Excess using Raman Optical-Activity. J. Raman Spectrosc. *26*, pp. 727-732. 1995.

Heard, D. E., R. A. Brownsword, D. G. Weston and G. Hancock, Time-Resolved Pulsed FT-IR Emission Studies of Photochemical-Reactions. Appl. Spectrosc. 47(9), pp. 1438-1445. 1993.

Hohenberg, P. and W. Kohn. Inhomogeneous Electron Gas. Phys. Rev. *136*, pp. B864 - B871. 1964.

Hou,Y.C., S.J. Jenkins and D. A. King. Surface Infra-Red Emission during Alkaki-Metal Incorporation at an Oxide Surface. Surface Science, *550*, pp. L27-L32. 2004.

Hvistendahl, J., E. Rytter and H.A. Oye. IR Emission Spectroscopy of Molten-Salts and Liquids using Thick Samples as Reference. Appl. Spectrosc. *37*(2), pp. 182-187. 1983.

Jacobsen, H., H.B. Kraatz, T. Ziegler and P.M. Boorman. A New Look at an Old Ligand – Surprises with Thioethers – A Density Functional-Study. J. Am. Chem. Soc. *114* (20), pp. 7851-7860. 1992.
Jacobsen, H. Bonding Aspects of P-heterocyclic Carbene Transition Metal Complexes. A Computational Assessment. J. Organomet. Chem. *690,* pp. 6068-6078. 2005.

Jaumot, J., N. Escaja, R. Gargallo, C. Gonzalez, E. Pedroso and R. Tauler. Multivariate Curve Resolution: A Powerful Tool for the Analysis of Conformational Transitions in Nucleic Acids. Nucleic Acids Res. *30* (17), Art. e92. 2002.

Jaumot, J., R. Gargallo, A. de Juan and R. Tauler. A Graphical User-Friendly Interface for MCR-ALS: A New Tool for Multivariate Curve Resolution in MATLAB. Chemom. Intell. Lab. Syst.*76* (1), pp. 101-110. 2005.

Jiang, J.H., Y.Z. Liang and Y. Ozaki. On Simplex-Based Method for Self-Modeling Curve Resolution of Two-way Data. Chemom. Intell. Lab. Syst. *65* (1), pp. 51-65. 2003.

Keiderling, T.A., P. Pancoska, V.M.. Urbanova, V.P. Gupta, R.K. Dukor and D.F. Huo. Determination of Secondary Structures of Proteins using Vibrational Circular-Dichroism. Molecular Modeling ACS Symposium Series. *576*, pp. 61-70. 1994.

Keller, H.R. and D.L. Massart. Peak Purity Control in Liquid-Chromatography with Photodiode-Array Detection by a Fixed Size Moving Window Evolving Factor Analysis. Anal. Chim. Acta *246* (2), pp. 379-390. 1991.

Keller, H. R. and D.L. Massart. Evolving Factor Analysis**.** Chemom. Intell. Lab. Syst. *12*, pp. 209-224. 1992.

Keller, H.R., D.L. Massart, Y.Z. Liang and O.M. Kvalheim. A Comparison of the Heuristic Evolving Latent Projections and Evolving Factor-Analysis Methords for Peak Purity Control in Liquid-Chromatography with Photodiode Array Detection. Anal. Chim. Acta *267* (1), pp. 63-71. 1992.

Kember, D. and N. Sheppard. The Use of Ratio-recording Interferometry for the Measurement of Infrared Emission Spectra: Applications to Oxide Films on Copper Surfaces, Appl. Specstrosc. 29 (6), 496-500 (1975).

Keresztury, G. and J. Mink. Significance of Correction for Detector Temoerature in Infrared-Emission Spectroscopy. Appl. Specstrosc. *46* (11), pp. 1747-1749. 1992.

Keresztury, G., J. Mink and J. Kristof. Quantitative Aspects of FT-IR Emission-Spectroscopy and Simulation of Emission-Absorption Spectra. ,Anal. Chem. *67* (20), pp. 3782-3787. 1995.

Kirkpatrick, S., C.D. Gelatt and M.P. Vecchi. Optimization by Simulated Anealing. Science *220* (4598), pp. 671-680. 1983.

Kohn, W. and L. J. Sham. Self-Consistent Equations Including Exchange and Correlation Effects. Phys. Rev. *140*, pp. A1133 - A1138. 1965.

Konno, T. Conformational Diversity of Acid-Denatured Cytochrome C Studied by a Matrix Analysis of Far-UV CD Spectra. Protein Sci. *7*, pp. 975 -982. 1988.

Kvalheim, O. M. and Y.Z. Liang, Heuristic Evolving Latent Projections: Resolving Two-Way Multicomponent Data: 1. Selectivity, Latent-Projective Graph, Datascope, Local Rank and Unique Resolution. Anal.Chem. *64*, pp. 936–946. 1992.

Lamparska, E., V. Liegeois, O. Quinet and B. Champagne. Theoretical Determination of the Vibrational Raman Optical Activity Signatures of Helical Polypropylene Chains. Chemphyschem *7* (11), pp. 2366-2376. 2006.

Lane, M.D. and P.R. Christensen, Thermal Infrared Emission Spectroscopy of Salt Minerals Ppredicted for Mars, ICARUS. *135* (2), pp. 528-536. 1998.

Lassen, P.R., L. Guy, I. Karame, T. Roisnel, N. Vanthuyne, C. Roussel, X.L. Cao., R. Lombardi, J. Crassous, F.B. Freedman and L.A. Nafie. Synthesis and Vibrational Circular Dichroism of Enantiopure Chiral Oxorhenium(V) Complexes Containing the Hydrotris(1-pyrazolyl)Borate Ligand. Inorg. Chem. *45* (25), pp. 10230-10239. 2006.

Lauer, J.L. and P. Vogei. Emission FTIR Analyses of Thin Microscopic Patches of Jet Fuel Residues Deposited on Heated Metal-Surfaces. Appl. Surface Sci. *18*, pp. 182-206. 1984.

Lauer, J.L., L.E. Keller and W.R. Jones. Infrared-Emission Spectrophotometric Study of the Changes Produced by Tin Coating of Metal-Surfaces in an Operating EHD Contact. *ASLE Transactions 26* (4), pp.437-444. 1983.

Lavine, B.K. Chemometrics. Anal.Chem. *70*, pp. 209R-228R. 1998.

Lavine, B.K.Chemometrics. Anal.Chem. *72*, pp. 91R-97R. 2000.

Lavine, B.K. and J. Workman.Chemometrics. Anal.Chem. *74*, pp. 2763-2770. 2002.

Lavine, B.K. and J. Workman.Chemometrics. Anal.Chem. 76 (12): 3365-3371.2004

Lavine, B.K. and J. Workman.Chemometrics. Anal.Chem. 78 (12): 4137-4145.2006

Lawton, W.H. and E.A. Sylvestre. Self Modeling Curve Resolution. Technometrics. *13*, pp. 617-633, 1971.

Lee, C.T., W.T. Yang and R.G. Parr. Development of the Colle-Salvetti Correction-Energy Formula into a functional of the Electron-Density. Phys. Rev. B *37* (2), pp. 785-789. 1988.

Letendre, L., D.K. Liu, C. D. Pibel, J. B. Halpern and H.L. Dai. Vibrational Spectroscopy of a Transient Species Through Time-Resolved Fourier Transform Infrared Emission Spectroscopy: The Vinyl Radical. J. Chem. Phys. *112* (21), pp. 9209-9212. 2000.

Leung, A.K.M, F. Gong, Y.Z. Liang and F.T. Chau. Analysis of the Water Soluble Constituents of Cordyceps Sinensis with Heuristic Evolving Latent Projections. Anal. Lett. *33* (15), pp. 3195-3211. 2000.

Li, C., Q. Xin, K.L. Wang and X.X. Guo, FT-IR Emission-Spectroscopy Studies of Molybdenum Oxide and Supported Molybdena on Alumina, Silica, Zirconia, and Titania. Appl. Specstrosc. *45*(5), pp. 874-882. 1991.

Li, C., E. Widjaja, W. Chew, M. Garland. Rhodium Tetracarbonyl Hydride: the Elusive Metal Carbonyl Hydride. Angew. Chem. Int. Eng. *41*(20), pp. 3786-3789. 2002.

Li, C., E. Widjaja and M. Garland. Spectral Reconstruction of In Situ FTIR Spectroscopic Reaction Data using Band-Target Entropy Minimization (BTEM): Application to the Homogeneous Rhodium Catalyzed Hydroformylation of 3,3-dimethylbut-1-ene using $Rh_4(CO)_{12}$. J. Catal. *213*(2), pp. 126-134. 2003.

Li, C., E. Widjaja and M. Garland. The $Rh_4(CO)_{12}$-Catalyzed Hydroformylation of 3,3-Dimethylbut-1-ene Promoted with $HMn(CO)_5$. Bimetallic Catalytic Binuclear Elimination as an Origin for Synergism in Homogeneous Catalysis. J. Amer. Chem. Soc. *125*(18), pp. 5540-5548. 2003.

Li, C., L. Guo and M. Garland. Homogeneous Hydroformylation of Ethylene Catalyzed by $Rh_4(CO)_{12}$. The Application of BTEM to Identify a New Class of Rhodium Carbonyl Spectra: $RCORh(CO)_3(C_2H_4)$. Organometallics *23*(9), pp. 2201-2204. 2004.

Li, C., E. Widjaja and M. Garland. $Rh_4(CO)_{12}$-Catalyzed Hydroformylation of Cyclopentene Promoted with $HMn(CO)_5$. Another Example of $Rh_4(CO)_{12}/HMn(CO)_5$ Bimetallic Catalytic Binuclear Elimination. Organometallics *23*(17), pp. 4131-4138. 2004.

Li, X.B., X.Y. Wang, X.L. Yu, J.W. Gao and W.G. Zhu. TD-DFT Study on Electronic Spectrum Properties of Zinc Complex with 8-Thiolquinoline Anion and its Derivatives. Acta Chim. Sinica *64* (3), pp. 208-212. 2006.

Liang, Y.Z., O.M. Kvalheim, H.R. Keller, D.L. Massart and P. Kiechle. Heuristic Evolving Latent Projections-Resoving 2-Way Multicomponent Data. 2. Detection and Resolution of Minor Constituents. Anal. Chem. *64* (8), pp. 946-953. 1992.

Liang, Y.Z. and O.M. Kvalheim. Diagnosis and Resolution of multiwavelength Chromatograms by Rank Map, Orthogonal Projections and Sequential Rank Analysis. Anal. Chim. Acta *292*, pp. 5-15. 1994 .

Liang, Y.Z and O.M. Kvalheim. Resolution of Two-way Data: Theoretical Background and Practical Problem-Solving - Part 1: Theoretical Background and Methodology. Fresenius J. Anal. Chem. *370* (6), pp. 694-704. 2001.

Low, M.J.D. and I. Coleman, Spectrochim. Acta. *22*, pp. 369. 1966.
Maeder, M. Evolving Factor Analysis for the Resolution of Overlapping Chromatographic Peaks. Anal. Chem. *59*, pp. 527-530, 1987.

Malinowski, E.R. Determination of the Number of Factors and the Experimental Error in a Data Matrix. Anal. Chem. *49*, pp. 612-617. 1977.

Malinowski, E.R. Factor Analysis in Chemistry. New York: John Wiley & Sons, Inc. 1991.

Malinowski, E.R. Window Factor-Analysis-Theoretical Derivation and Application to Flow-Injection Analysis Data. J. Chemom. *6* (1), pp. 29-40. 1992.

Malinowski, E.R. Automatic Window Factor Analysis - A More Efficient Method for Determining Concentration Profiles from Evolutionary Spectra. J. Chemom.*10* (4), pp. 273-279. 1996.

Malinowski, E.R. Abstract Factor Analysis of Data with Multiple Sources of Error and a Modified Faber-Kowalski F-test. J. Chemom. *13*, pp. 69-81, 1999.

Manne, R. On the Resolution Problem in Hyphenated Chromatography. Chemom. Intell. Lab. Syst. *27*, pp. 89-94. 1995.

Manne R, H.L. Shen and Y.Z. Liang. Subwindow factor analysis. Chemom. Intell. Lab. Syst. *45*, pp. 171-176. 1999.

McColl, I.H., E.W. Blanch, L. Hecht and L.D. Barron. A Study of Alpha-Helix Hydration in Polypeptides, Proteins, and Viruses using Vibrational Raman Optical Activity. J. Am. Chem. Soc. *126* (26), pp. 8181-8188. 2004.

McMullen, D.W., S.R. Jaskunas and I. Jr. Tinoco. Application of Matrix Rank Analysis to the Optical Rotatory Dispersion of TMV RNA. Biopolymers, *5*, pp. 589- 613. 1967.

McPhie, P. and R.I. Shrager, An Investigation of the Thermal Unfolding of Swine Pepsinogen using Circular Dichroism. Arch. Biochem. Biophys. *293*, pp. 46-53. 1992.

Meinrath G. and S. Lis. Quantitative Resolution of Spectroscopic Systems using Computer Assisted Target Factor Analysis (CAT). Fresenius J. Anal. Chem. *369*, pp. 124-133. 2001.

Metropolis, N., M. Rosenbluth, A. Teller and E. Teller. Equation-of-State Calculations by Fast Computing Machines, J. Chem. Phys., *21*, pp. 1087-1092. 1953.
Mineva, T., N. Russo and H. Freund. CO Interaction with Small Rhodium Clusters from Density Functional Theory: Spectroscopic Properties and Bonding Analysis. J. Phys. Chem. A *105*(47), pp. 10723-10730. 2001.

Mink, J. and G. Keresztury. FT-IR Emission – Spectroscopy and Its Applications. Appl. Spectrosc. 47 (9), pp. 1446-1451. 1993.

Mink, J. Sampling Techniques for Vibrational Spectroscopy in Handbook of Vibrational Spectroscopy: Vol. 2, pp.1195. J. Chalmers and P. Griffiths. J. Wiley, New York, 2002,

Morrell, C., C. Breheny, V.Haverd, A. Cawley and G. Hancock. The 248 nm Photolysis of NO_2/N_2O_4: Time-Resolved Fourier Transform Infrared Emission from NO and NO_2, and Quenching of NO (v=5-8). J. Chem. Phys. *117* (24), pp. 11121-11130. 2002.

Nafie, L.A., Yu, G.S. and T.B. Freedman. Raman Optical-Activity of Biological Molecules. Vib. Spectrosc. *8*, pp. 231-239. 1995.

Nafie, L.A. and T.B. Freedman. Vibrational Circular Dichroism: An Incisive Tool for Stereochemical Applications. Enantiomer. *3*, pp. 283-297. 1998.

Nafie, L.A., T.B. Freedman, F.J. Long and E. Lee. Applications of Vibrational Optical Activity to Biological and Pharmaceutical. Biophys. J. *74* (2), pp. A29-A29. 1998.

Nida, D.L., M.S. Rahman, K.D. Carlson, R. Richards-Kortum and M. Follen. Fluorescent Nanocrystals for Use in Early Cervical Cancer Detection. Gynecologic Oncology. *99*, pp. S89-S94. 2005.

Pan, Y.Y., L. Susithra, and M. Garland. Pure Component Reconstructions Using Entropy Minimizations and Variance-Weighted Piecewise-Continuous Spectral Regions. Application to the Unstable Experimental System. J. Chemom. *14*, pp. 63-77. 2000.

Parr, R.G. and W. Yang. Density-Functional Theory of Atoms and Molecules. Oxford University Press, New York, 1989.

Perdew, J. P. and Y. Wang. Accurate and Simple Analytic Representation of the Electron-Gas Correlation Energy. Phys. Rev. B *46*, pp. 947. 1992.

Perdew, J. P., K. Burke and M. Ernzerhof. Generalized Gradient Approximation Made Simple. Phys. Rev. Lett. *77*(18), pp. 3865-3868. 1996.

Petrie, S. and R. Stranger. DFT and Metal-Metal Bonding: A Dys-Functional Treatment for Multiply Charged Complexes? Inorg. Chem. *43*(8), pp. 2597-2610. 2004.

Pollak, C., A. Rosa and E. J. Baerends. Cr-CO Photodissociation in $Cr(CO)_6$: Reassessment of the Role of Ligand-Field Excited States in the Photochemical Dissociation of Metal-Ligand Bonds. J. Amer. Chem. Soc. *119*(31), pp. 7324-7329. 1997.

Rogers, S.A. and S.R. Leone, Pulsed-Laser Photolysis Time-Resolved FT-IR Emission Studies of Molecular- Dynamics. Appl. Spectrosc. 47(9), pp. 1430-1437. 1993.

Sanchez, F.C., B. van den Bogaert, S.C. Rutan and D.L. Massart. Multivariate Peak Purity Approaches. Chemom. Intell. Lab. Syst. *34*, pp. 139-171. 1996.

Sanchez, F.C., J. Toft, B. van den Bogaert and D.L. Massart. Orthogonal Projection Approach Applied to Peak Purity Assessment. Anal. Chem. *68*, pp. 79-85. 1996.

Sanchez, F.C., S.C. Rutan, M. Garcia and D.L. Massart. Resolution of Multicomponent Overlapped Peaks by the Orthogonal Projection Approach, Evolving Factor Analysis and Window Factor Analysis. Chemom. Intell. Lab. Syst. *36*, pp. 153-164. 1997.

Sasaki, K., S. Kawata and S. Minami. Constrained Nonlinear Method for Estimating Component Spectra from Multicomponent Mixture. Appl. Optics. *22*, pp. 3599-3603. 1983.

Sasaki, K., S. Kawata and S. Minami. Estimation of Component Spectral Curves from Unkown Mixture Spectra. Appl. Optics. *23*, pp. 1955-1959. 1984.

Sasic, S., Y.Ozaki, M. Kleimann, and H.W. Siesler. On the Ambiguity of Self-Modeling Curve Resolution: Orthogonal Projection Approach Analysis of the On-Line Fourier Transform-Raman Spectra of Styrene/1,3-Butadiene Block-Copolymerization. Anal. Chim. Acta. *460*, pp. 73-83. 2002.

Schweitzer-Stenner, R., F. Eker, Q. Huang, K. Griebenow, P.A. Mroz and P.M. Kozlowski. Structure Analysis of Dipeptides in Water by Exploring and Utilizing the Structural Sensitivity of Amide III by Polarized Visible Raman, FTIR-Spectroscopy and DFT Based Normal Coordinate Analysis. J. Phys. Chem. B *106*, pp. 4294-4304. 2002.

Schweitzer-Stenner, R. Secondary Structure Analysis of Polypeptides Based on an Excitonic Coupling Model to Describe the Band Profile of Amide I ' of IR, Raman, and Vibrational Circular Dichroism Spectra. J. Phys. Chem. B *108* (43), pp. 16965-16975. 2004.

Schweitzer-Stenner, R. Advances in Vibrational Spectroscopy as a Sensitive Probe of Peptide and Protein Structure - A Critical Review. Vib. Spectrosc. *42*, pp. 98-117. 2006.

Seyden-Penne, J. Chiral Auxiliaries and Ligands in Asymmetric Synthesis, Wiley-Interscience, 1 edition, 2004

Shen, H.L., R. Manne, Q.S. Xu and Y.Z. Liang. Local Resolution of Hyphenated Chromatographic Data. Chemom. Intell. Lab. Syst. 45 (1-2): 323-328. 1999

Shriver, D. F. and M. A. Drezdzon. The Manipulation of Air-Sensitive Compounds. Wiley, New York, 1986.

Sin, S.Y., E. Widjaja, L.E. Yu and M. Garland. Application of FT-Raman and FTIR Measurements using a Novel Spectral Reconstruction Algorithm. J. Raman Spectrosc., 34(10), pp. 795-805. 2003.

Smyth, E., E.W. Blanch, L. Hecht, M. Vasak and L.D. Barron. Solution Structure of Native Proteins with Irregular Folds from Raman Optical Activity. Biopolymers *58* (2), pp. 138-151. 2001.

Spencer, K.M., R.B. Edmonds and R.D. Rauh. Analytical Chiral Purity Verification using Raman Optical Activity . Appl. Spectrosc. *50* (5), pp. 681-685. 1996.

Sreerama, N., and R.W. Woody. Protein Secondary Structure from Circular Dichroism Spectroscopy. Combining Variable Selection Principle and Cluster Analysis With Neural Network, Ridge Regression and Self-Consistent Methods. J. Mol. Biol. *242*, pp. 497–507. 1994.

Sreerama, N., S.Y. Venyaminov and R.W. Woody. Analysis of Protein Circular Dichroism Spectra Based on the Tertiary Structure Classification. Anal. Biochem. *299*, pp. 271-274. 2001.

Stewart, B., R.D. Peacock, L. Alagna, T. Prosperi, S, Turchini, J. Goulon, A. Rogalev and C. Goulon-Ginet. Circular Dichroism at the Edge: Large X-ray Natural CD in the 1s -> 3d Pre-Edge Feature of 2[Co(en)$_3$Cl-3] Center Dot NaCl Center Dot 6H$_2$O. J. Am. Chem. Soc. *121* (43), pp. 10233-10234. 1999.

Szabo, M.J., N.M. Galea, A. Michalak, S.Y. Yang, L.F. Groux, W.E. Piers and T. Ziegler. Copolymerization of Ethylene with Polar Monomers: Chain Propagation and Side Reactions. A DFT Theoretical Study using Zwitterionic Ni(II) and Pd(II) Catalysts. J. Am. Chem. Soc. *127* (42), pp. 14692-14703. 2005.

Szilagyi, R.K. and G. Frenking. Structure and Bonding of the Isoelectronic Hexacarbonyls $[Hf(CO)_6]^{2-}$, $[Ta(CO)_6]^{-}$, $W(CO)_6$, $[Re(CO)_6]^{+}$, $[Os(CO)_6]^{2+}$, and $[Ir(CO)_6]^{3+}$: A Theoretical Study. Organometallics *16*(22), pp. 4807-4815. 1997.

Tauler, R. and E.Casassas. Application of Principal Component Analysis to the Study of Multiequilibria Systems: Study of Cu(II)-Salicylate-mono-, di- and triethanolamine Systems. Anal. Chim. Acta. *223*, pp. 257-268. 1989.

Tauler, R., E.Casassas and A. Izquierdo-Ridorsa. Self-Modeling Curve Resolution Applied to Spectroscopic Titration Data using Factor Analysis. Anal. Chim. Acta. *248*, pp. 447-458. 1991.

Tauler, R., B.R.Kowalski, and S.Flemming. Multivariate Curve Resolution Applied to Spectral Data from Multiple Runs of an Industrial Process. Anal.Chem. *65*, pp. 2040-2047. 1993.

Tauler, R. and D. Barceló. Multivariate Curve Resolution and Calibration Applied to Liquid Chromatography Diode Array Detection. Trends in Anal. Chem. *12*, pp. 319-327. 1993.

Tauler, R., A. Izquierdo-Ridorsa and E. Casassas. Simultaneous Analysis of Several Spectroscopic Titrations with Self-Modelling Curve Resolution. Chemom. Intell. Lab. Syst. *18* (3), pp. 293-300. 1993.

Tauler, R., A.K. Smilde, J.M. Henshaw, L.W. Burgess, and B.R. Kowalski. Multicomponent Determination of Chlorinated Hydrocarbons Using a Reaction-Based Chemical Sensor. Part II Chemical Speciation Using Multivariate Curve Resolution. Anal. Chem. *66*, pp. 3337-3344. 1994.

Tauler, R., A. Smilde and B.R. Kowalski. Selectivity, Local Rank, Three-Way Data Analysis and Ambiguity in Multivariate Curve Resolution. J. Chemom. *9*, pp. 31-58. 1995.

Tauler, R. Multivariate Curve Resolution Applied to Second Order Data. Chemom. Intell. Lab. Syst. *30*, pp. 133-146. 1995.

Tauler, R., A. Izquierdo-Ridorsa, and E. Casassas. Simultaneous Analysis of Several Spectroscopic Titrations with Self-Modeling Curve Resolution. Chemom. Intell. Lab. Syst. *18*, pp. 293-300. 1998.

Tauler, R., I. Marqués and E. Casassas. Multivariate Curve Resolution Applied to Three-way Trilinear Data: Study of a Spectrofluorimetric Acid-base Titration of Salicylic Acid at Three Excitation Wavelengths. J. Chemom, *12*, pp. 55-75. 1998.

Tauler, R. and E. Casassas. Principal Component Analysis Applied to the Study of Successive Complex Formation Data in the Cu(II) Ethanolamine Systems. J. Chemom. *3*, pp. 151-161. 1998.

Tauler, R., R. Gargallo, M. Vives and A. Izquierdo-Ridorsa. Resolution of Temperature Dependent Conformational Multiequilibria Processes. Chemom. Intell. Lab. Syst. *46* (2), pp. 275-295. 1999.

Tjahjono, M., A.D. Allian and M. Garland. The Direct Determination of Partial Molar Volumes and Reaction Volumes in Ultra-dilute Non-Reactive and Reactive Multi-

Component Systems using a Combined Spectroscopic and Modified Response Surface. Dalton Trans. *12*, pp. 1505-1516. 2006.

Tochigi, K., H. Momose, Y. Misawa, and Y. Suzuki. Polarization-Modulation Emission FT-IR Measurement of Thin Organic Films on Metal-Surfaces. Appl. Spectrosc. *46*(1): 156-158. 1992.

Toft, J. Evolutionary Rank Analysis Applied to Multidetectional Chromatographic Structures. Chemom. Intell. Lab. Syst. *29* (2), pp. 189-212. 1995.

Vandeginste, B.G.M., W. Derks, and G. Kateman. Multicomponent Sel-Modelling Curve Resolution in High-Performance Liquid Chromatography by Iterative Target Tranformation Factor Analysis. Anal. Chim. Acta. *173*, pp. 253-264. 1985.

Venyaminov, S.Y. and K.S. Vassilenko. Determination of Protein Tertiary Structure Class from Circular Dichroism Spectra. Anal. Biochem. *222*, pp. 176–184. 1994.

Vives, M., R. Tauler, V. Moreno and R. Gargallo. Study of the Interaction of a Cis-Dichloroaminopyrrolidine Pt(II) Complex and the Polynucleotide Poly(I)-Poly(C) Acid by Means of H-1-NMR and Multivariate Curve Resolution. Anal. Chim. Acta *446,* pp. 439-450. 2001.

Vives, M., R. Tauler and R. Gargallo. Study of the Influence of Metal Ions on tRNA(Phe) Thermal Unfolding Equilibria by UV Spectroscopy and Multivariate Curve Resolution. J. Inorg. Biochem. *89*, pp. 115-122. 2002.

Vosko, S.H., L. Wilk and M. Nusair. Accurate Spin-Dependent Electron Liquid Correction Energies for Local Spin-Density Calculations – A Critical Analysis. Can. J. Phys. *58* (8), pp. 1200-1211. 1980.

Vosko, S.H. and L. Wilk. Influence of an Improved Local-Spin-Density Correlation-Energy Functional on the Cohesive Energy of Alkali-Metals. Phys. Rev. B *22* (8), pp. 3812-3815. 1980.

Wallace, R.M. Analysis of Absorption Spectra of Multicomponent System. J. Phys. Chem. *64*, pp. 899-901. 1960

Waterhous, D.V. and W.C. Jr. Johnson. Importance of Environment in Determining Secondary Structure in Proteins. Biochemistry *33*, pp. 2121-2128. 1994.

Whyman, R. Tetranuclear and dinuclear phosphine- and arsine-substituted rhodium carbonyls. J. Chem. Soc., Dalton Trans. *13*, pp 1375-81. 1972.

Widjaja, E. Development of Band-Target Entropy Minimization (BTEM) and Associated Software Tools. Ph.D Thesis, National University of Singapore. 2002

Widjaja, E. and M. Garland. Pure Component Spectral Reconstruction from Mixture Data using SVD, Global Entropy Minimization and Simulated Annealing. Numerical Investigations of Admissible Objective Functions Using a Synthetic 7-Species Data Set. J. Comput. Chem. *23*, pp. 911-919. 2002.

Widjaja, E., C.Z. Li, and M. Garland. Semi-Batch Homogeneous Catalytic In-Situ Spectroscopic Data. FTIR Spectral Reconstructions Using Band-Target Entropy Minimizations (BTEM) without Spectral Preconditioning. Organometallics. *21*, pp. 1991-1997. 2002.

Widjaja, E., C. Li, W. Chew and M. Garland. Band-target Entropy Minimization. A Robust Algorithm for Pure Component Spectral Recovery. Application to Complex Randomized Mixtures of Six Components. Anal. Chem. *75*(17), pp. 4499-4507. 2003.

Widjaja, E., N. Crane, T. Chen, M. D. Morris, M. A. Ignelzi and B. R. McCreadie. Band-Target Entropy Minimization (BTEM) Applied to Hyperspectral Raman Image Data. Appl. Spectrosc. *57*(11), pp. 1353-1362. 2003.

Widjaja E. and M. Garland. Entropy Minimization and Spectral Dissimilarity Curve Resolution Technique Applied to Nuclear Magnetic Resonance Data Sets, J. Magn. Reson., *173* (1), pp.175-182. 2005.

Windig, W. and J. Guilment. Interactive Self-Modeling Mixture Analysis. Anal. Chem. *63*, pp. 1425-1432. 1991.

Windig, W. and D.A. Stephenson. Self-Modeling Mixture Analysis of Second-Derivative Near-Infrared Spectral Data Using the Simplisma Approach. Anal. Chem. *64*, pp. 2735-2742. 1992.

Windig, W. and S. Markel. Simple-to-Use Interactive Self-Modeling Mixture Analysis of FTIR Microscopy Data. J. Mol. Struct. *292*, pp. 161-170, 1993.

Windig, W. The Use of Second-derivative Spectra for Pure-Variable based Self-Modeling Mixture Analysis Techniques. Chemom. Intell. Lab. Syst. *23*, pp. 71-86. 1994.

Windig, W. Spectral Data Files for Self-Modeling Curve Resolution with Examples Using the Simplisma Approach. Chemom. Intell. Lab. Syst. *36*, pp. 3-16. 1997.

Windig, W. and B. Antalek. Direct Exponential Curve Resolution Algorithm (DECRA): A Novel Application of the Generalized Rank Annihilation Method for a Single Spectral Mixture Data Set with Exponentially Decaying Contribution Profiles. Chemom. Intell. Lab. Syst. *37*, pp. 241 –254. 1997.

Windig, W., B. Antalek, L.J. Sorriero, S. Bijlsma, D.J. Louwerse, and A.K. Smilde. Applications and New Developments of the Direct Exponential Curve Resolution

Algorithm (DECRA). Examples of Spectra and Magnetic Resonance Images. J. Chemom. *13*, pp. 95-110. 1999.

Windig, W., B. Antalek, M.J. Robbins, N. Zumbulyadis, and C.E. Heckler. Applications of the Direct Exponential Curve Resolution Algorithm (DECRA) to Solid State Nuclear Magnetic Resonance and Mid-Infrared Spectra. J.Chemom. *14*, pp. 213-227. 2000.

Windig, W., B. Antalek, J.L. Lippert, Y. Batonneau, and C. Bremard. Combined Use of Conventional and Second-Derivative Data in the Simplisma Self-Modeling Mixture Analysis Approach. Anal. Chem. *74*, pp. 1371-1379. 2002.

Winter, D.J. Matrix Algebra. Ed. By Robert W. Pirtle. New York: Macmillan Publishing Company. 1992.

Wold ,S. Chemometrics; What Do We Mean with it, and What Do We Want from it? Chemom. Intell. Lab. Syst. *30* (1), pp. 109-115. 1995.

Xie, Y. R. B. King and H. F. Schaefer. Vibrational frequencies of the homoleptic cobalt carbonyls: $Co_4(CO)_{12}$ and $Co_6(CO)_{16}$. Acta, Part A, *61*A(7), pp. 1693-1699. 2005.

Yu, G.S., D.P. Che, T.B. Freedman and L.A. Nafie. Raman Optical-Activity of Simple Alanyl Peptides – Backscattering In-Phase Dual Circular-Polarization Measurements in Aqueous-Solution. Biospectroscopy. *1* (2), pp. 113-123. 1995.

Zachariassen, C.B., J. Larsen, F. van den Berg, R. Bro, A. de Juan and R. Tauler. Comparison of PARAFAC2 and MCR-ALS for Resolution of an Analytical Liquid Dilution System. Chemom. Intell. Lab. Syst. *83* (1), pp. 13-25. 2006.

Zeng, Y.Z. and Garland, M. An Improved Algorithm for Estimating Pure Component Spectra in Exploratory Chemometric Studies Based on Entropy Minimization. Anal. Chim. Acta. *359*, pp.303-310, 1998.

Zhao, Z.M. and E.R. Malinowski . Window Factor Analysis of Methylene Blue in Water. J. Chemom. *13* (2), pp. 83-94. 1999.

Zhao, Z.M and E.R. Malinowski . Detection and Identification of a Methanol-Water Complex by Factor Analysis of Infrared Spectra. Anal. Chem. *71* (3), pp. 602-608. 1999.

Zhang, H.J., M. Garland, Y.Z. Zeng and P.Wu. Weighted two-Band Target Entropy Minimization for the Reconstruction of Pure Component Mass Spectra: Simulation Studies and the Application to Real Systems, J. Am. Soc. Mass. Spectrom., *14* (11), pp. 1295-1305. 2003.

Zhu, F.J., N. Isaacs, L. Hecht and L.D. Barron. Raman Optical Activity: A Tool for Protein Structure Analysis. Structure *13*, pp. 1409-1419. 2005.

List of Publications

Cheng, S.Y., D. Rajarathnam, M. Tan, and M. Garland. Application of Band-Target Entropy Minimization (BTEM) to Infrared Emission Spectroscopy and the Reconstruction of Pure Component Emittance Spectra from Thin Films and Liquid Samples. Applied Spectroscopy 60 (5): 521-528, 2006

Cheng, S.Y., M. Tjahjono, D. Rajarathnam, C.Z. Li, I. Lyapkalo, D.Chen and M. Garland. Remote monitoring of a multi-component liquid-phase organic synthesis by infrared emission spectroscopy: The recovery of pure component emissivities by band-target entropy minimization. Applied Spectroscopy 61 (10): 1057-1062, 2007

Cheng, S.Y., F. Gao, K.I. Krummel and M. Garland. The application of BTEM to UV–vis and UV–vis CD spectroscopies: The reaction of $Rh_4(CO)_{12}$ with chiral and achiral ligands. Talanta, In Press, Corrected Proof, Available online 23 August 2007

Gao, F., A.D. Allian, H. Zhang, S.Y. Cheng and M. Garland. Chemical and kinetic study of acetophenone hydrogenation over Pt/Al2O3: Application of BTEM and other multivariate techniques to quantitative on-line FTIR measurements. Journal of Catalysis 241, 189, (2006)

Application of Band-Target Entropy Minimization to Infrared Emission Spectroscopy and the Reconstruction of Pure Component Emissivities from Thin Films and Liquid Samples

SHUYING CHENG, D. RAJARATHNAM, TAN MEILING, and MARC GARLAND*

Department of Chemical and Biomolecular Engineering, National University of Singapore, 4 Engineering Drive 4, Singapore 117576

Thermal emission spectral data sets were collected for a thin solid film (parafilm) and a thin liquid film (isopropanol) on the interval of 298–348 K. The measurements were performed using a conventional Fourier transform infrared (FT-IR) spectrometer with external optical bench and in-house-designed emission cell. Both DTGS and MCT detectors were used. The data sets were analyzed with band-target entropy minimization (BTEM), which is a pure component spectral reconstruction program. Pure component emissivities of the parafilm, isopropanol, and thermal background were all recovered without any *a priori* information. Furthermore, the emissivities were obtained with increased signal-to-noise ratios, and the signals due to absorbance of thermal radiation by gas-phase moisture and CO_2 were significantly reduced. As expected, the MCT results displayed better signal-to-noise ratios than the DTGS results, but the latter results were still rather impressive given the low temperatures used in this study. Comparison is made with spectral reconstruction using the orthogonal projection approach–alternating least squares (OPA-ALS) technique. This contribution introduces the primary equation for emission spectral reconstruction using BTEM and discusses some of the unusual characteristics of thermal emission and their impact on the analysis.

Index Headings: **Infrared emission spectroscopy; Emittance; Emissivity; Band-target entropy minimization; BTEM; Thin films; Liquid samples.**

INDRODUCTION

Infrared (IR) emission spectroscopy is a well-established analytical technique and is often considered as an alternative to IR absorption/transmittance spectroscopy.[1] Significant use of emission spectroscopy has been found in astrophysics to assess the chemical constituents in distant space, in remote monitoring of effluent industrial gases, and in studying photochemical initiated reactions, as well as in regular laboratory analysis of thin layer/metal oxide deposits and polymers.[2–4] Further, the development of time-resolved Fourier transform emission spectroscopy offers an excellent tool for the kinetic study of radical–radical reactions with high-resolution emission spectra.[5,6] However, obtaining a well-defined IR emission spectrum is still a major challenge. The main difficulties are the large background radiation, the self-absorption of the sample, and the internal reflection within the sample surface. All of these complications lead to low signal-to-noise ratios for the sample studied.

A number of investigations have been conducted in order to address the issue of signal-to-noise ratio, using either variations on experimental design or instrumental considerations. Many of these studies have approached the problem by taking measurements of the sample, blackbody reference, and background, and then using a modified ratio method.[7–10] Other studies have focused on the use of a thick, opaque sample as a reference instead of a blackbody to obtain a better emission signal.[11,12] A recent study implemented a polarization-modulation technique to eliminate the large background radiation in order to obtain a better emission spectrum of organic thin films.[13]

Various chemometric techniques have been used with emission data. Digital filtering, pattern recognition techniques, and multivariate calibration have been used to monitor airborne pollutants and to control industrial stack emissions.[14,15] However, one major drawback of these methods is the requirement of *a priori* information on the correct background signal and the correct spectral patterns of the compounds of interest. In other words, application to unknown systems for which reference spectra cannot be obtained presents a difficult challenge.

In this work an advanced spectral reconstruction algorithm, band-target entropy minimization (BTEM), has been employed to reconstruct the emission signal of the sample of interest from the raw emission data, without the need for any *a priori* information whatsoever. This includes information on the emissivities of the background as well as references. Furthermore, no *a priori* estimate of the number of patterns present is needed. BTEM achieves spectral prediction using a constrained optimization with simulated annealing in which a Shannon type entropy function plays a crucial role. Previous work indicates the validity of this methodology in spectral reconstruction and qualitative and quantitative analysis of pure component spectra from mixture absorbance spectra taken with Fourier transform infrared (FT-IR) spectroscopy and two-dimensional nuclear magnetic resonance (2D NMR), as well as mixture intensity data taken with FT-Raman, powder X-ray diffraction (PXRD), and mass spectroscopy.[16–20] One of the most important aspects of BTEM is its ability to deal with non-stationary signal characteristics.

In the present contribution a series of IR emission spectra was collected from an organic polymer film and a liquid sample at various temperatures with an air-cooled DTGS detector and a liquid nitrogen cooled MCT detector. The primary equation in the BTEM algorithm for emission spectroscopy is given by Eq. 1, where $\hat{\varepsilon}'_{1\times v}$ is the estimated pure component emissivity, $\mathbf{T}_{1\times z}$ is the transformation matrix of optimized coefficients, and $\mathbf{V}^{T}_{z\times v}$ is the matrix of physically meaningful right singular vectors from the emission data. It is important to note that in the present application to thermal emission spectroscopy, serious and unusual nonlinearities exist. At different temperatures the Planck function will be slightly different and the emissivity of each component will be slightly different.

$$\hat{\varepsilon}'_{1\times v} = \mathbf{T}_{1\times z}\mathbf{V}^{T}_{z\times v} \quad (1)$$

All the experimental data in this contribution were processed

Received 31 October 2005; accepted 3 March 2006.

* Author to whom correspondence should be sent. E-mail: chemvg@nus.edu.sg.

0003-7028/06/6005-0521$2.00/0

using Eq. 1. This is the first time that BTEM has been applied to thermal emission data. In the present case, the utility of BTEM is demonstrated by the relatively accurate reconstruction of the emission signals of both parafilm and isopropanol without any prior information. Moreover, BTEM significantly reduces the effects of the ambient moisture and carbon dioxide interference. BTEM significantly improves the signal-to-noise ratio of the predicted signals.

EXPERIMENTAL AND COMPUTATIONAL ASPECTS

Measurements. The emission spectra were measured on a conventional FT-IR spectrometer (Bruker Equinox-55) equipped with an external emission bench to hold the heated sample holder and parabolic mirror. With the instrument infrared source turned off, the sample serves as the radiation source, and the infrared emission is collected by the parabolic mirror and focused on the detector. The parabolic mirror was gold plated for maximum reflection (focal length, 7.5 cm). A schematic diagram of the emission attachment and the optical path is provided in the supplementary material.†

The stainless steel thermostated emission cell was designed and constructed in-house. The cell had provisions for holding a thin solid film on one side and a liquid film sample on the other side. The temperature of the cell was maintained by an external circulating water bath with ±0.1 °C accuracy. With the exception of the exposed sample area, the entire surface of the cell was masked with black paper to avoid the thermal signature from the steel body during the measurements. For thin solid films, the sample was placed in the sample well and simply fixed by a stainless steel plate screwed on top. For liquid samples, a ZnSe window was used and the sample was injected between the cell and the window. The thickness of the ZnSe window was 4 mm. The entire sample holder was tilted at an angle of approximately 15° facing towards the parabolic mirror in order to achieve maximum throughput. Photographs of the emission bench with the cell and parabolic mirror and close-ups of the solid sample holder and the liquid sample holder are shown in Fig. 1.

The samples used in this study were solid parafilm and liquid isopropanol. Both have good vibrational bands in the lower wavenumber range. An aluminum pellet with one side painted black was employed as a blackbody reference. The parafilm, with a thickness 0.05 mm, was wrapped on an aluminum pellet and fixed into the cell holder. Emission spectra were recorded for the blackbody, aluminum pellet, and the film on the aluminum pellet at temperatures from 298 K to 348 K in 10 K increments.

Similarly, the emission spectra for isopropanol were recorded with the empty cell, ZnSe window, and with the injected liquid sample at temperatures from 298 K to 338 K in 10 K increments (the boiling point of isopropanol is 355.7 K).

Emission spectra were recorded using two different detectors, namely an air-cooled DTGS detector (450 cm^{-1} cut-off) and a liquid nitrogen cooled MCT detector (750 cm^{-1} cut-off). The experimentally obtained emission spectra were the result of 400 coadded scans, at a resolution of 6 cm^{-1}. All the measurements were performed without purging the emission bench.

† All supplementary material is available on The Society for Applied Spectroscopy webpage: www.s-a-s.org.

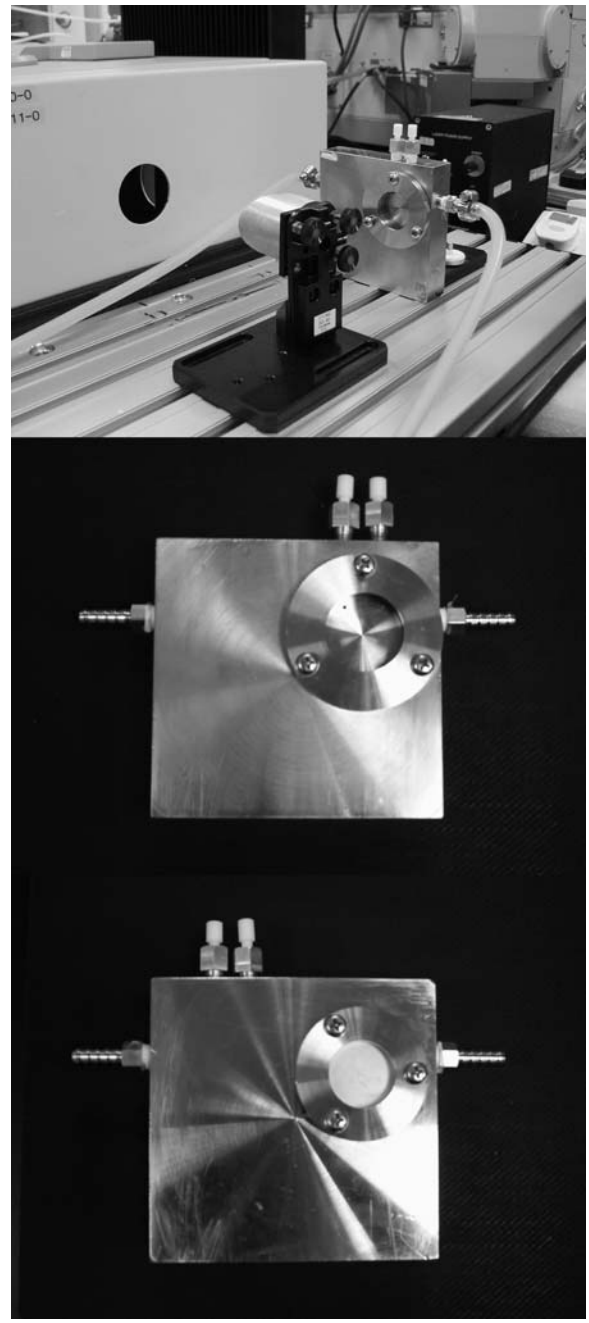

FIG. 1. The experimental setup of the custom-designed emission cell: the top picture is of the emission bench with the cell and the parabolic mirror; the middle one is a close-up of the liquid sample holder; and the bottom one is a close-up of the solid sample holder.

For the purpose of comparison, absorbance spectra for both parafilm and isopropanol were also measured; these absorbance spectra are provided in the supplementary material.

Emission Model and Singular Value Decomposition. The individual experimental emission spectra $\varepsilon_{1\times\nu}$ were first consolidated to a single matrix of dimension $\varepsilon_{k\times\nu}$, where k is the number of spectra measured and ν is the number of data channels. In the present study, the number of spectra collected for each analysis was between 5 and 18. The number of data channels was 1557 in the case of DTGS data and 1868 in the case of MCT data.

Each measured emission spectrum $\varepsilon_{1\times\nu}(T, P, l)$ at temperature T, pressure P, and path length l, can be represented as a weighted contribution of the individual emissivities $\varepsilon'_{1\times\nu}(T,P,l)$, where ω represents the weighting and $E_{1\times\nu}$ represents the associated instrumental and experimental error:

$$\varepsilon_{1\times\nu}(T,P,l) = \omega_{1\times s}\varepsilon'_{s\times\nu}(T,P,l) + E_{1\times\nu} \quad (2)$$

Then, in matrix notation, each set of measured emission spectra are related to the mean value of the emissivities $\varepsilon'_{s\times\nu}$ $(\overline{T},\overline{P},\overline{l})$ and the error by Eq. 3. In this equation, the error $E'_{1\times\nu}$ contains (1) instrumental and experimental error, as well as (2) model error due to variations in the emissivities at slightly different temperatures, pressures, and small variations in path length (which will influence re-adsorption).

$$\varepsilon_{k\times\nu}(T,P,l) = \omega_{k\times s}\varepsilon'_{s\times\nu}(\overline{T},\overline{P},\overline{l}) + E'_{k\times\nu} \quad (3)$$

The set of experimental emission spectra $\varepsilon_{1\times\nu}$ can be decomposed by singular value decomposition (SVD) as shown in Eq. 4. In this equation, $\mathbf{U}_{k\times k}$ and $\mathbf{V}^{\mathrm{T}}_{\nu\times\nu}$ are the left singular vectors and right singular vectors respectively, and $\mathbf{\Sigma}_{k\times\nu}$ is the corresponding matrix of singular values. The right singular vectors, in particular, the physically meaningful subset $\mathbf{V}^{\mathrm{T}}_{k\times\nu}$ contain the relevant abstract information on the emissivities.

$$\varepsilon_{k\times\nu} = \mathbf{U}_{k\times k}\mathbf{\Sigma}_{k\times\nu}\mathbf{V}^{\mathrm{T}}_{\nu\times\nu} \quad (4)$$

Band-Target Entropy Minimization. As mentioned in the introduction, BTEM is a self-modeling curve resolution (SMCR) program that uses a Shannon entropy type function.[16–20] BTEM analysis is performed after taking the SVD of the full data set. Once the right singular vectors are obtained, model-free deconvolution of the spectra was performed one spectrum at a time. This deconvolution is achieved by optimizing the transformation of the right singular vectors used and is guided by the user's choice of spectral features to target. In contrast to other SMCR techniques, BTEM does not rely on statistical tests. Instead, enough latent vectors $z < k$ are chosen so that practically all physically useful data are used and only vectors consisting more or less of noise are discarded. Until now, BTEM has been defined for absorbance spectroscopies such as infrared and NMR, and for intensities such as mass spectroscopy, X-ray diffraction, and Raman.

Formulation of Band-Target Entropy Minimization for Emission. The right singular vectors $\mathbf{V}^{\mathrm{T}}_{z\times\nu}$ obtained by decomposition of the experimental emission spectra $\varepsilon_{k\times\nu}$ contain all the necessary information on individual emissivities as well as the thermal background (blackbody effects, etc). Reconstruction is performed by the projection of z right singular vectors onto one single estimate of emissivity $\hat{\varepsilon}'_{1\times\nu}$, as was indicated in Eq. 1.

The most important practical issue is the determination of the transformation matrix $\mathbf{T}_{1\times z}$. This is achieved by a constrained nonlinear optimization. The nonlinear optimization has as its objective function, a term for information entropy function (H) and a penalty function (P):

$$F_{\mathrm{obj}} = H + P \quad (5)$$

The entropy function H is defined by Eq. 6, where the entropy is evaluated as the spectral derivative (smoothness) at each wavenumber:

$$H = -\sum_{\nu} h_\nu \ln(h_\nu) \quad (6)$$

where

$$h_\nu = \frac{\left|\frac{d^m\hat{\varepsilon}'_\nu}{d\nu^m}\right|}{\sum_{\nu}\left|\frac{d^m\hat{\varepsilon}'_\nu}{d\nu^m}\right|} \quad (7)$$

The corresponding penalty function takes the form of Eq. 8. The purpose of adding a penalty to the objective function is to prevent reconstruction of physically non-meaningful emissivities, in particular, non-positive values for the emissivities.

$$P(\hat{\varepsilon}'_{1\times\nu}, \hat{\varepsilon}'^{\max}_{1\times\nu}) = \gamma_{\mathrm{a}}F_1(\hat{\varepsilon}') + \gamma_{\max} \quad (8)$$

where

$$F_1(\hat{\varepsilon}') = \sum_{\nu}(\hat{\varepsilon}')^2 \quad \forall\hat{\varepsilon}' < 0 \quad (9)$$

Together with the penalty function there are three sets of associated scalar parameters: (1) γ_{a} and $\gamma_{\max}$ are penalty coefficients, (2) α is set to be the maximum emissivity of the resolved pure spectrum, in relation to the target band peak emissivity, and (3) λ_1 and λ_2 are the bounds for the emissivity constraint.

$$\gamma_{\mathrm{a}} = \begin{cases} 0 & F_1(\hat{\varepsilon}') < \lambda_1 \\ 10 & \lambda_{1\le}F_1(\hat{\varepsilon}') < \lambda_2 \\ 10^4 & F_1(\hat{\varepsilon}') \ge \lambda_2 \end{cases} \quad (10)$$

$$\gamma_{\max} = \begin{cases} 10^4 & \hat{\varepsilon}'^{\max}_{1\times\nu} < \alpha \\ 0 & \hat{\varepsilon}'^{\max}_{1\times\nu} \ge \alpha \end{cases} \quad (11)$$

Strategy for Data Set Analysis. Eight sets of BTEM analyses were performed in order to assess the importance of inclusion/exclusion of blackbody type spectra in the data sets, as well as other issues. Table I lists each set of consolidated spectra, the total number of spectra taken (k), the primary sample measured, any auxiliary measurements, the detector used, and the number of right singular vectors z used in analysis.

RESULTS AND DISCUSSION

As indicated by the experimental designs in Table I, a large number of data sets were measured and these data sets were

TABLE I. The different combinations of consolidated data sets and the number of right singular vectors used in BTEM for each of them.

Consolidated data set, No.	Total number of spectra taken, k	Primary sample measurements	Auxiliary measurements	Detector	Number of right singular vectors used, z
1	6	Parafilm		DTGS	4
2	18	Parafilm	Blackbody, aluminum pellet	DTGS	8
3	6	Parafilm		MCT	4
4	18	Parafilm	Blackbody, aluminum pellet	MCT	8
5	5	Isopropanol		DTGS	4
6	15	Isopropanol	Empty cell, window	DTGS	8
7	5	Isopropanol		MCT	4
8	15	Isopropanol	Empty cell, window	MCT	8

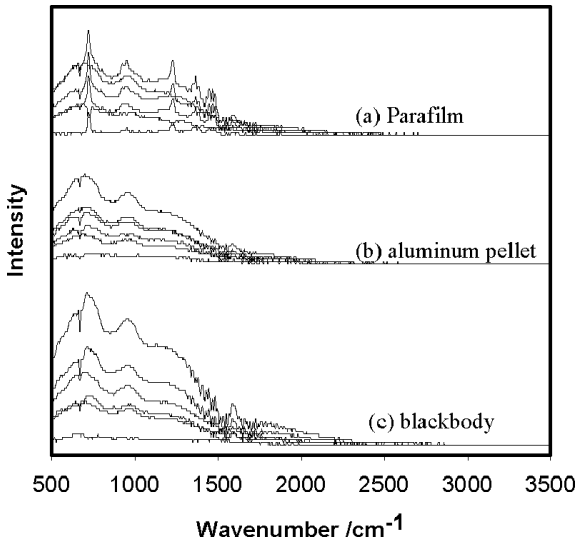

FIG. 2. The emission spectra of (*a*) parafilm, (*b*) the aluminum pellet, and (*c*) the blackbody taken at six temperatures (348, 338, 328, 318, 308, and 298 K) by the DTGS detector.

analyzed in more than one manner. Therefore, in this section, the main results are highlighted, and intermediate and secondary results will be provided in the supplementary material. In particular, all sets of right singular vectors $\mathbf{V}^{\mathrm{T}}_{k\times \mathrm{v}}$ associated with the eight experimental designs are included in the supplementary material only.

Parafilm. ***Experimental Data Sets.*** The series of experimental spectra for parafilm with both the DTGS and MCT detectors are shown in Fig. 2 and Fig. 3, respectively.

Data in both Figs. 2 and 3 show physically significant signals in the characteristic fingerprint region at low wavenumbers, while at the high wavenumber region (above 2500 cm^{-1}) little signal is observed. This is consistent with the Planck function that blackbody radiation will show a maximum in the range of 600 cm^{-1} at approximately 300 K.

The DTGS data in Fig. 2 show significant radiant emission down to 500 cm^{-1}. All the emission spectra have low signal intensity as evidenced by the choppy quality of the spectra. The absorbance of the radiant energy by atmospheric moisture can be seen in all emission spectra as a series of bands at approximately 1400–1800 cm^{-1}, and the absorbance of the radiant energy by atmospheric carbon dioxide can be seen as a band at 670 cm^{-1}. The series of blackbody emission spectra do not follow a perfect Planck function due to (1) the above-mentioned absorbance, (2) the fact that the blackbody used is not perfect, and (3) the absorbance/transmission characteristics of the optical components in the spectrometer. The series of aluminum pellet emission spectra show the same generic characteristics as the blackbody series, and in addition the emission intensity of this series is less than the blackbody at any given temperature. Finally, the series of parafilm emission spectra show all of the above-mentioned characteristics, and in addition this series shows the structured emission of hydrocarbon film, as seen by the maxima at approximately 720, 950, 1230, 1450 cm^{-1}, etc.

The MCT data in Fig. 3 show significant radiant emission down to 750 cm^{-1}, which is the optical cut-off for the MCT detector. All the emission spectra have a significantly high signal intensity (in contrast to the DTGS data), as evidenced by the relatively smooth quality of the spectra. Again, the absorbance of the radiant energy by atmospheric moisture can be seen in all emission spectra as a series of bands at approximately 1400–1800 cm^{-1}. The absorbance band at 670 cm^{-1} is not observed due to the MCT cut-off. However, due to the high signal intensity, the absorbance due to atmospheric CO_2 can now be seen at approximately 2300–2400 cm^{-1}. The series of aluminum pellet emission spectra show the same generic characteristics as the blackbody series, and in addition the emission intensity of this series is less than the blackbody at any given temperature. Finally, the series of parafilm emission spectra show all the above-mentioned characteristics, and in addition this series shows the structured emission of hydrocarbon film, as seen by the maxima at approximately 950, 1230 cm^{-1}, etc. However, this emission intensity appears weak because it is imbedded in the considerably larger blackbody emission. Also, the abnormally low intensities of the emission spectra at 298 K and 308 K seem to indicate a contact problem between the parafilm and the heating surface.

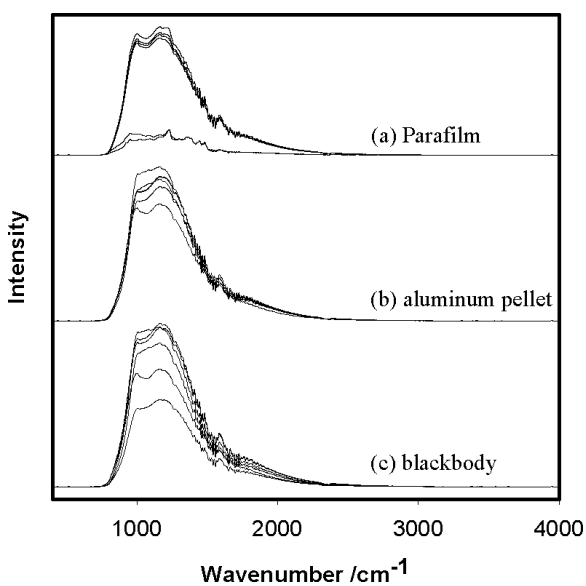

FIG. 3. The emission spectra of (*a*) parafilm, (*b*) the aluminum pellet, and (*c*) the blackbody taken at six temperatures (348, 338, 328, 318, 308, and 298 K) by the MCT detector.

Spectral Reconstruction Using Band-Target Entropy Minimization. The right singular vectors from the DTGS data were subjected to BTEM analysis. The first four vectors of consolidated data set 1 and the first eight vectors of consolidated data set 2 from the SVD were used. The results are shown in Figs. 4 and 5.

In both cases, two spectral patterns could be recovered. These were the blackbody emission and the parafilm emission. The blackbody emission spectrum has essentially all signals from the parafilm removed, but the signals from moisture and CO_2 are still embedded. The parafilm emission spectrum seems to be free of most other signals. Comparison of Figs. 4 and 5 indicates that a slight improvement in spectral quality was obtained by using eight right singular vectors.

Similarly, the right singular vectors from the MCT data were subjected to BTEM analysis. The first four vectors of consolidated data set 3 and the first eight vectors of

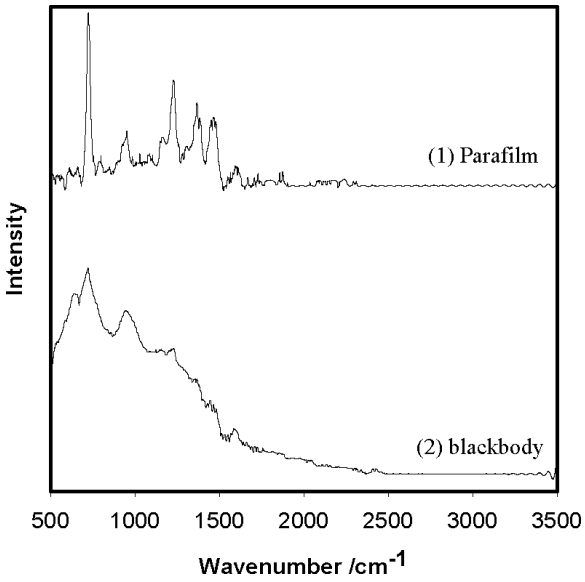

FIG. 4. Emissivities reconstructed using BTEM for consolidated data set 1.

consolidated data set 4 were used. The results obtained using eight right singular vectors are shown in Fig. 6.

In both cases, three spectral patterns could be recovered. These were the blackbody emission, the moisture absorbance, and the parafilm emission. The blackbody emission spectrum has essentially all signals from both CO_2 absorbance and the parafilm removed, and only a minimum amount of signal from moisture is seen. The "moisture" absorbance spectrum has only a slight amount of residual CO_2 signal still embedded. The parafilm emission spectrum seems to be free of most other signals. It is important to note that the spectral reconstruction of the parafilm for both DTGS and MCT data are consistent, since the features in the region 1000–1500 cm^{-1} are very similar (data below 1000 cm^{-1} for the MCT data are not very accessible due to the optical cut-off). The signal-to-noise ratio of the MCT data analysis is significantly better compared to the DTGS results as evidenced particularly by the reconstructed parafilm spectrum.

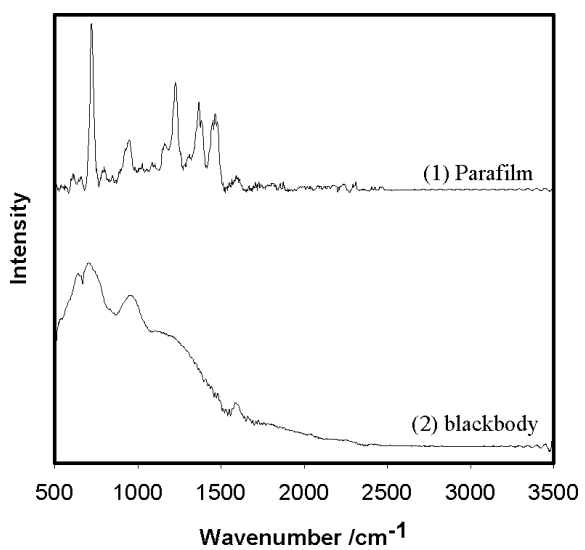

FIG. 5. Emissivities reconstructed using BTEM for consolidated data set 2.

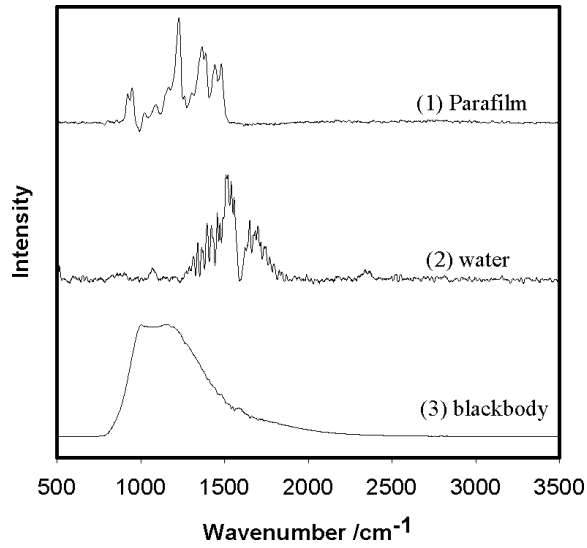

FIG. 6. Emissivities reconstructed using BTEM for consolidated data set 4.

Comparison of Emission and Absorbance Spectra. The emission spectra obtained from BTEM analysis shows that the prominent bands (or sets of bands) in the low wavenumber region are all present, namely 950, 1230, 1450 cm^{-1}, etc. Due to the physics of the thermal emission process versus the thermal absorption process, the relative ratios of these bands differ somewhat and the apparent bandwidths are different. (See supplementary material for absorbance spectra.)

Isopropanol. ***Experimental Data Sets.*** The experimental data set for the isopropanol series included the ZnSe window, the empty cell, and isopropanol, all measured at five different temperatures with both the DTGS and MCT detectors. The experiment spectra are shown in Figs. 7 and 8, respectively.

The DTGS data in Fig. 7 show significant radiant emission down to 500 cm^{-1}. All the emission spectra have low signal intensity as evidenced by the choppy quality of the spectra. The

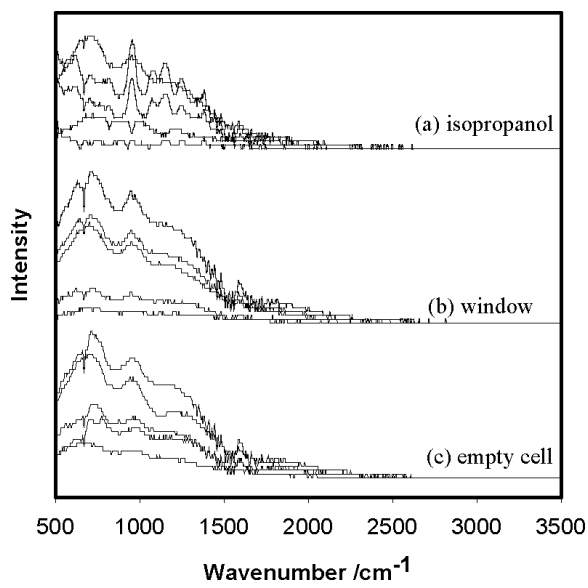

FIG. 7. The emission spectra of (***a***) isopropanol, (***b***) the window, and (***c***) the empty cell taken at five temperatures (338, 328, 318, 308, and 298 K) by the DTGS detector.

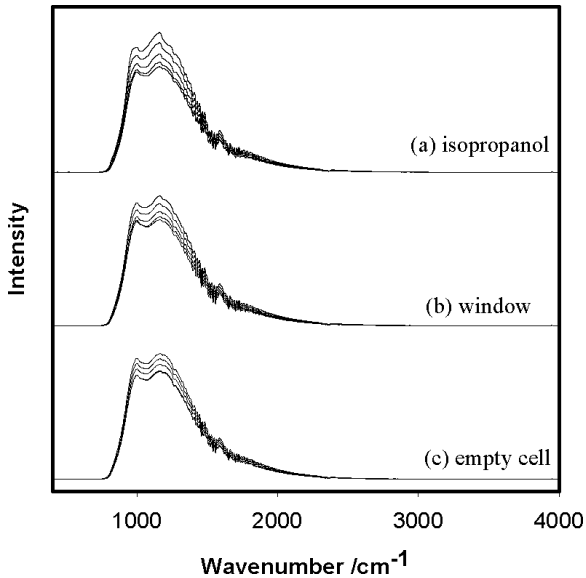

FIG. 8. The emission spectra of (*a*) isopropanol, (*b*) the window, and (*c*) the empty cell taken at five temperatures (338, 328, 318, 308, and 298 K) by the MCT detector.

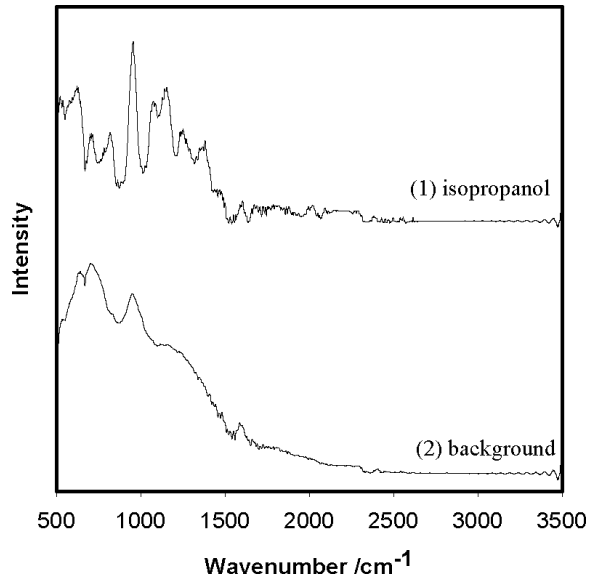

FIG. 9. Emissivities reconstructed using BTEM for consolidated data set 6.

absorbance of the radiant energy by atmospheric moisture can be seen in all emission spectra as a series of bands at approximately 1400–1800 cm^{-1} and the absorbance of the radiant energy by atmospheric carbon dioxide can be seen as the band at 670 cm^{-1}. The series of window and empty cell emission spectra show similar generic characteristics. In addition, the emission intensity of these two series is quite similar at any given temperature. The series of isopropanol emission spectra show all of the above-mentioned characteristics, and in addition this series shows the structured emission of isopropanol, as seen by the maxima at approximately 820, 950, 1150, 1380 cm^{-1}, etc. Also interesting to note are the inverted bands at 298 K and 308 K, which seem to be caused by the self-absorbance of isopropanol.

The MCT data in Fig. 8 show significant radiant emission down to 750 cm^{-1}. All the emission spectra have a high signal intensity (in contrast to the DTGS data) as evidenced by the relatively smooth quality of the spectra. Again, the absorbance of the radiant energy by atmospheric moisture can be seen in all emission spectra as a series of bands at approximately 1400–1800 cm^{-1}. The absorbance band at 670 cm^{-1} is not observed due to the MCT cut-off. However, due to the high signal intensity, the small absorbance due to atmospheric CO_2 can now be seen at approximately 2300–2400 cm^{-1}. The series of window and empty cell emission spectra show similar generic characteristics. Finally, the series of isopropanol emission spectra show all of the above-mentioned characteristics, and in addition this series shows the structured emission of the liquid. However, the blackbody effect is the major component of the experimental spectra and overwhelms much of the emission of the liquid.

Spectral Reconstruction Using Band-Target Entropy Minimization. The right singular vectors from the DTGS data were subjected to BTEM analysis. The first four vectors of consolidated data set 5 and the first eight vectors of consolidated data set 6 were used. The results for both analyses were very similar, and the latter is reported in Fig. 9.

In both cases, two spectral patterns could be recovered: background emission and isopropanol emission. A weak signal from moisture and CO_2 can still be seen in both spectra.

The right singular vectors from the MCT data were similarly subjected to BTEM analysis. The first four vectors of consolidated data set 7 and the first eight vectors of consolidated data set 8 from SVD were used. The results for the latter are shown in Fig. 10.

When only four vectors are taken for analysis, only two spectral patterns could be recovered: background emission and isopropanol emission. When eight vectors are taken for analysis, three spectral patterns could be recovered: the background emission, the moisture, and the isopropanol emission. The background spectrum has essentially all signals from both CO_2 and isopropanol removed, but some noticeable signal from moisture is seen. The moisture absorbance spectrum has some residual signal from the background and isopropanol as evidenced by the features at approximately 700-1200 cm^{-1}.

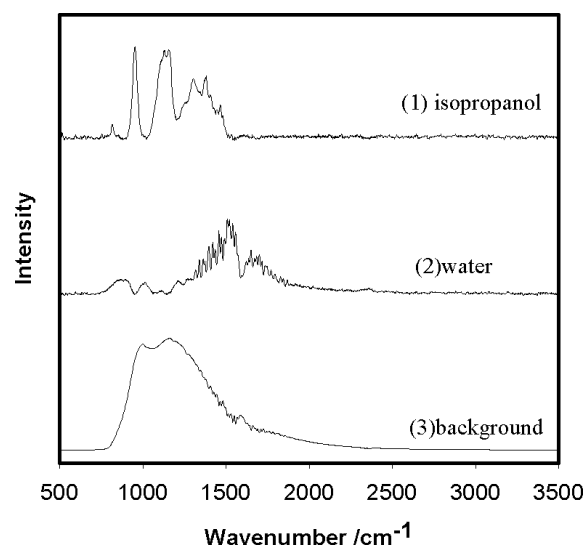

FIG. 10. Emissivities reconstructed using BTEM for consolidated data set 8.

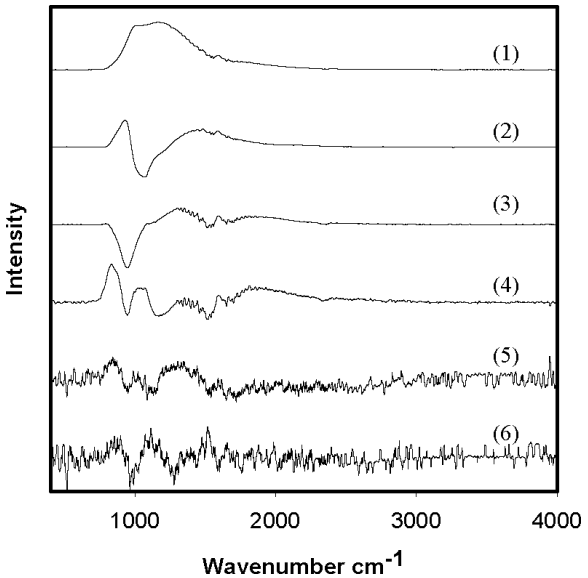

FIG. 11. First six right singular vectors of the $\mathbf{V}^T$ matrix for consolidated data set of blackbody emission spectra.

Comparison of Emission and Absorbance Spectra. The emissivity for isopropanol obtained from BTEM analysis shows that the prominent bands (or sets of bands) in the low wavenumber region are all present, namely 820, 950, 1150, 1380 cm^{-1}, etc. Due to the physics of the thermal emission process versus the thermal absorption process, the relative ratios of these bands differ somewhat and the apparent bandwidths are different (see supplementary data).

Issue of Spectral Nonlinearities. Six different temperatures were used for the samples in this study, namely, 298, 308, 318, 328, 338, and 348 K. The corresponding Planck function maxima occur at 585, 605, 625, 644, 664, and 683 cm^{-1}. In other words, there is an extreme non-stationary quality to the background radiation. In addition, at these different temperatures, the emissivity $\varepsilon'(\nu)$ will also change for each component: some bands will decrease in relative intensity and some will increase. In other words, at each different temperature the "pure component emissivity" will be significantly different. Indeed, it is well known that the luminance of a sample is proportional to the luminance of the blackbody at the same temperature and hence a function of both wavenumber and temperature.[1] Taken together, there are at least two signals (blackbody and emissivity) that are highly non-stationary and hence two significant contributions to nonlinear spectral effects in these emission measurements.

It is not possible with the present data sets to show the latter effect separately, but the former, i.e., the non-stationary quality of the blackbody luminance, can be dramatically demonstrated. For this purpose, the blackbody spectra obtained with an MCT detector and shown in Fig. 3 were used. A singular value decomposition was performed on these six blackbody emission spectra alone. The results are shown in Fig. 11. As seen in this figure, at least four very significant right singular vectors are observed that have good to outstanding signal-to-noise ratios. This means that at least four basis functions are needed to represent the signal from this "one-component" system over the interval of temperatures used and hence a set of observations. In particular, the second vector is a sigmoid band, the typical signature of a shifting signal.

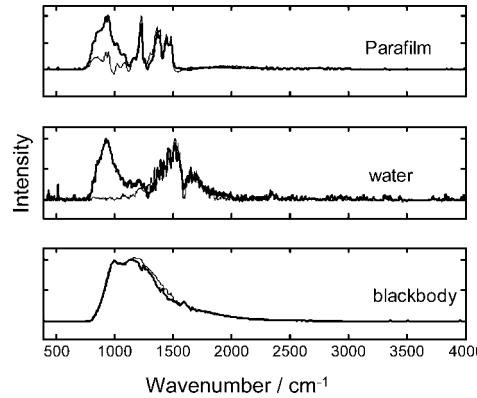

FIG. 12. The reconstructed emissivity by SIMPLISMA–ALS (dotted line) and BTEM (solid line) for consolidated data set 3.

The results of this contribution thus clearly show that BTEM overcame these very serious complications to pure component pattern reconstruction. Further, it was able to negate the non-stationary quality of the Planck function background and to produce an emissivity of each component. Technically, these emissivities are in fact a smoothest mean representation of the signals in the data set (see Eq. 3). Finally, BTEM was able to eliminate, to a good extent, the signals produced by the re-absorbance of background radiation by the gas-phase species H_2O and CO_2.

Comparison to other Self-Modeling Curve Resolution Techniques. Simple to use interactive self-modeling mixture analysis (SIMPLISMA) and orthogonal projection–alternating least squares (OPA-ALS)[21–22] are two well-known and popular self-modeling curve resolution techniques. SIMPLISMA is often used to obtain a first approximation for the spectral estimates to be inputted into OPA-ALS. The parafilm set of data measured with the MCT detector was analyzed. In the first case, only the six parafilm measurements were used, and in the second analysis all 18 parafilm, cell, and blackbody measurements were used.

The data sets were first analyzed using the assumption of three principal components. These results were quite poor. The data sets were then analyzed using the assumption of six principal components. In the latter case, spectral estimates were obtained that included estimates for parafilm, moisture, and blackbody. These results are shown in Figs. 12 and 13. The remaining estimates were super-positions of the emissivities

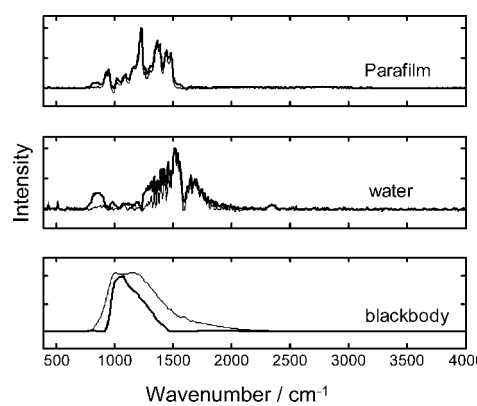

FIG. 13. The reconstructed emissivity by SIMPLISMA–ALS (dotted line) and BTEM (solid line) for consolidated data set 4.

present. As seen in these two figures, the BTEM estimates are considerably smoother for parafilm and water, and spurious signals appear to remain imbedded in the OPA-ALS estimates, particularly the large and broad signal centered at approximately 900 cm^{-1} (seen in Fig. 12) and the mismatch for moisture in Fig. 13.

Future Work, Data Array Size, Detectors, and Limitations to Spectral Recovery. The Results section demonstrated that larger experimental sets improve the quality of the BTEM spectral reconstructions somewhat, as does the use of an MCT detector. Neither of these results is particularly surprising, but both are necessary to demonstrate, particularly before more complex problems are addressed in the future.

The only noticeable shortcoming of the present analyses was the inability to reliably reconstruct the pure component absorbance of the gas-phase species H_2O and CO_2, in spite of the fact that bands for these species can be identified in the raw spectral data as well as in the right singular vectors. This is due to a small, but not negligible, sensitivity of BTEM to noisy input matrices $\mathbf{V}^{T}_{z\times v}$. Presently, the easiest way to overcome this difficulty is to take larger sets of experimental spectral data and hence decrease the noise in the first z vectors used. This approach has been repeatedly taken in some of our other work, where pure component spectra constituting only 0.01% of the total signal can be reconstructed when hundreds or thousands of spectra are measured.[23] There is every reason to believe that the same benefits can occur with emission spectra as well.

CONCLUSION

The IR emission spectra of both parafilm and isopropanol were successfully recovered using the BTEM algorithm and a conventional FT-IR spectrometer. All the measurements were made without any purging of the equipment and in a small temperature interval. For both DTGS and MCT detectors, the reconstructed emission signals were in good agreement with those of the corresponding IR absorbance spectra. This confirms the applicability of BTEM to emission spectroscopy and as an efficient approach to eliminate the effects of background radiation and other interfering signals.

1. J. Mink, "Sampling Techniques for Vibrational Spectroscopy", in *Handbook of Vibrational Spectroscopy*, J. Chalmers and P. Griffiths, Eds. (John Wiley and Sons, New York, 2002), vol. 2, p. 1195.
2. S. A. Rogers and S. R. Leone, Appl. Spectrosc. **47,** 1430 (1993).
3. J. Mink and G. Keresztury, Appl. Spectrosc. **47,** 1446 (1993).
4. D. Drake, D. Charbonneau, and J. Harrington, Astrophys. J. **601,** 87 (2004).
5. G. Hancock, V. Haverd, and M. Morrison, Phys. Chem. Chem. Phys. **5,** 2981 (2003).
6. D. E. Heard, R. A. Brownsword, D. G. Weston, and G. Hancock, Appl. Spectrosc. **47,** 1438 (1993).
7. D. Kember and N. Sheppard, Appl. Specstrosc. **29,** 496 (1975).
8. D. Kember, D. H. Chenery, N. Sheppard, and J. Fell, Spectrochim. Acta, Part A **35,** 455 (1978).
9. S. V. Compton, D. A. C. Compton, and R. G. Messerschmidt, Spectroscopy **6(6),** 35 (1991).
10. D. B. Chase, Appl. Spectrosc. **35,** 77 (1981).
11. F. J. DaBlase and S. Compton, Appl. Spectrosc. **45,** 611 (1991).
12. J. Hvistendahl, E. Rytter, and H. A. Oye, Appl. Spectrosc. **37,** 182 (1983).
13. K. Tochigi, H. Momose, Y. Misawa, and Y. Suzuki, Appl. Spectrosc. **46,** 156 (1992).
14. F. W. Koehler, G. W. Small, R. J. Combs, R. B. Knapp, and R. B. Kroutil, Vib. Spectrosc. **27,** 97 (2001).
15. M. J. Mattu, G. W. Small, R. J. Combs, R. B. Knapp, and R. T. Kroutil, Appl. Spectrosc. **54,** 341 (2000).
16. W. Chew, E. Widjaja, and M. Garland, Organometallics **21,** 1982 (2002).
17. C. Z. Li, E. Wadjaja, and M. Garland, J. Am. Chem. Soc. **125,** 5540 (2003).
18. L. F. Guo, F. Kooli, and M. Garland, Anal. Chim. Acta **517,** 229 (2004).
19. S. Y. Sin, E. Widjaja, L. E. Yu, and M. Garland, J. Raman Spectrosc. **34,** 795 (2003).
20. H. J. Zhang, M. Garland, Y. Zeng, and P. Wu, J. Am. Soc. Mass Spectrom. **14,** 1295 (2003).
21. E. Widjaja, C. Z. Li, W. Chew, and M. Garland, Anal. Chem. **75,** 4499 (2003).
22. A. G. Frenich, M. Martínez Galera, J. L. Martínez Vidal, D. L. Massart, J. R. Torres-Lapasió, K. D. Braekeleer, J. H. Wang, and P. K. Hopke, Anal. Chim. Acta **411,** 145 (2000).
23. C. Z. Li, E. Widjaja, W. Chew, and M. Garland, Angew. Chem. Int. Ed. Engl. **41,** 3758 (2002).

Remote Monitoring of a Multi-Component Liquid-Phase Organic Synthesis by Infrared Emission Spectroscopy: The Recovery of Pure Component Emissivities by Band-Target Entropy Minimization

SHUYING CHENG, MARTIN TJAHJONO, D. RAJARATHNAM, LI CHUANZHAO, ILYA LYAPKALO,* DAVID CHEN, and MARC GARLAND†

Department of Chemical and Bimolecular Engineering, National University of Singapore, 4 Engineering Drive 4, Singapore 117576 (S.C., M.T., D.R., D.C., M.G.); Institute of Chemical and Engineering Sciences, 1 Pesek Road, Jurong Island, Singapore 627833 (M.T., L.C., I.L., M.G.)

A liquid-phase cycloaddition reaction near ambient temperature involving dimethyl acetylenedicarboxylate (DMAD) and cyclopentadiene (CP) as reactants was measured using a conventional Fourier transform infrared (FT-IR) spectrometer with an emission accessory. Two semi-batch experiments were performed and a total of 55 spectra were collected using a DTGS detector. Band-target entropy minimization (BTEM), a pure component spectral reconstruction technique, was applied to analyze the data set to retrieve the pure component emission spectrum from the reaction system. The estimated emission spectra of the solvent chloroform, DMAD, CP, and product, namely dimethyl bicyclo[2.2.1]-2,5-heptadiene-2,3-dicarboxylate, were all reconstructed with rather good quality. The estimated emission spectra are similar to independent FT-IR spectra of the same cycloaddition reaction. Using a least squares fit, the relative concentration profiles of the species are obtained. Because this appears to be the first time that a liquid-phase reaction has been monitored by infrared emission spectroscopy, further improvements and opportunities for general multi-phase liquid reaction monitoring are discussed.

Index Headings: **Infrared emission spectroscopy; Liquid-phase reaction; Band-target entropy minimization; BTEM; Emittance.**

INTRODUCTION

Infrared emission spectroscopy (IRES) is a rather specialized branch of infrared spectroscopy. It has been widely used for solids and solid interfaces. For example, it has been used to characterize the molecular structures of various minerals involving carbonate, sulfates, phosphates, arsenates, and chlorides as well as to study the lattice vibrations of the crystals and to investigate the vibrations of adsorbed molecules on metal surfaces and metal supported catalysts.[1–4] IRES has been particularly important for the study of heterogeneous catalysts, since in general, such solids absorb too strongly for transmission experiments. Thus, IRES is often viewed as a compliment to transmission infrared spectroscopy. In addition, time-resolved Fourier transform emission spectroscopy has proved to be a valuable tool for the study of the vibration states of gases during photolysis experiments such as N_2O, vinyl bromide, and vinyl chloride, etc.[5–8]

A large number of experimental studies on IRES have been concerned with obtaining good quality IR emission spectra for the solid samples. In particular, they have focused on overcoming optical and experimental difficulties and severe distortion effects on the measurements of IRES. Such investigations have mainly involved the modification of experimental configurations and the testing of different conditions for sampling. Several factors such as sample temperature, sample thickness, and sample arrangement (such as the tilting of the sample) could affect the emission spectrum of the solid samples.[9–14] In this context, it should also be mentioned that various chemometric techniques, such as digital filtering, pattern recognition, and multivariate calibration, are increasingly being used to treat emission spectra, particularly for pollutant monitoring and industrial stack emissions.[15,16]

In contrast to the large number of studies on the IR emission of solid and gas-phase samples, much less attention has been paid to the study of liquid samples. Recently, successful measurements of single-component thin-film liquid samples have been performed, and the results were analyzed by band-target entropy minimization (BTEM) in order to deconvolute the Planck function and instrument response function from the raw data. The resulting pure component spectra were in agreement with independent transmission spectra of the reference.[17] It can be noted that BTEM is a curve resolution algorithm that is capable of reconstructing one spectrum at a time without the use of any *a priori* data. It has been extensively used with other vibrational spectroscopies, such as IR and Raman,[17–19] and has been used to eliminate blackbody effects from high-temperature FT-Raman experiments.[20]

The measurement and analysis of a thin liquid film suggests that a similar or extended type of approach would be applicable to multi-component liquid phase organic syntheses. Such remote monitoring of a reaction, rather than experiments with infrared absorption or infrared absorption and reflection (ATR), might fulfill a particular niche analytical requirement in some types of organic syntheses. In particular, it would be potentially very useful if IRES could be performed on syntheses conducted in the vicinity of room temperature (where many organic reactions are conducted, i.e., Grignard reactions, fine chemical hydrogenations, etc.).

In the present contribution, a cyclo-addition reaction in the liquid phase is studied by IRES. Figure 1 shows the reaction between cyclopentadiene (CP) and dimethyl acetylenedicarboxylate (DMAD) to generate the product dimethyl bicyclo[2.2.1]-2,5-heptadiene-2,3-dicarboxylate (DBHD).

This reaction is successfully monitored by IRES, the pure component spectra are deconvoluted by BTEM, and first approximations of the concentration profiles during reaction are

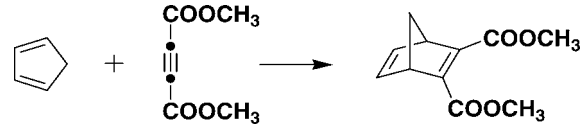

FIG. 1. The cycloaddition reaction between conjugated cyclopentadiene and a di-substituted alkyne.

Received 5 April 2007; accepted 31 July 2007.

* Current address: Institute of Organic Chemistry and Biochemistry, Academy of Sciences of the Czech Republic, Flemingovo n. 2, 166 10 Prague 6, Czech Republic.

† Author to whom correspondence should be sent. E-mail: marc_garland@ices.a-star.edu.sg.

0003-7028/07/6110-1057$2.00/0

TABLE I. Experimental design of the injections for cycloaddition reaction.

	Experiment 1		Experiment 2	
Number	Perturbation	Spectra #	Perturbation	Spectra #
1	Empty cell	1	Empty cell	29
2	Add 25 mL CHCl3	2–14	Add 25 mL CHCl3	30–32
3	Add 1 mL DMAD	15–16	Add 0.3 mL CP	33–34
4	Add 1 mL DMAD	17–18	Add 0.3 mL CP	35–36
5	Add 1 mL DMAD	19–21	Add 1 mL DMAD	37–41
6	Add 0.6 mL CP	22–24	Add 2 mL DMAD	42–44
7	Add 0.3 mL CP	25–26	Add 0.6 mL CP	45–48
8	Add 0.3 mL CP	27–28	Add 1 mL DMAD	49–55

obtained. This contribution appears to be the first detailed investigation of a liquid phase organic synthesis by IRES.

EXPERIMENTAL AND COMPUTATIONAL ASPECTS

Experimental Aspects. Both chloroform (Aldrich 99%) used as solvent, and the reactant dimethyl acetylenedicarboxylate (DMAD) (Aldrich 99%) were used as received. Cyclopentadiene (CP) was prepared from distillative dissociation of dicyclopentadiene (Aldrich). The resulting product was checked by ^{1}H nuclear magnetic resonance (NMR), found to be approximately 99% pure, and stored at −80 °C.

Two semi-batch cycloaddition reactions were performed at 308 K. Approximately 25 mL of the solvent chloroform was used in each experiment, and then various quantities of the reactants dimethyl acetylenedicarboxylate (DMAD) and cyclopentadiene (CP) were added according to the experimental design given in Table I. The two semi-batch experiments differ due to the order in which the reactants were added.

The reactions were conducted in the experimental setup shown in Fig. 2. A Schlenk tube with magnetic stirring was immersed in a cryostat set to the reaction temperature of 308 K. The liquid phase in the Schlenk tube was circulated to the emission cell using a hermetically sealed membrane pump (Cole Parmer) at the flow rate of 5 mL/min via PEEK tubes of 1/16-in. outer diameter. The temperature of the cell was maintained by a circulating water bath to 308 K. The emission spectra were measured on a Bruker Equinox-55 FT-IR spectrometer equipped with an external emission accessory. Details of the customized thermostated emission cell, with a 4 mm thickness ZnSe window, have been reported previously.[21]

To maximize signal intensity from reaction on the external bench, optical alignment was conducted before the measurements. This alignment involved both angle and distance adjustments between the emission cell and the parabolic mirror. Ten minute co-added scans were accumulated for each emission spectrum at a resolution of 6 cm^{-1} using an air-cooled DTGS detector. The raw experimental spectra were used in all calculations, and no background subtractions were performed. Emission spectra of the empty cell, the solvent, the reactant DMAD in the solvent, and the reaction after injecting the second reactant CP were all recorded. A total of 55 emission spectra were obtained from the two semi-batch experiments.

Independent cycloaddition experiments were conducted in FT-IR transmission mode in order to acquire reference FT-IR spectra of dimethyl acetylenedicarboxylate, cyclopentadiene, and dimethyl bicyclo[2.2.1]-2,5-heptadiene-2,3-dicarboxylate for comparison with the present emission results.

Band-Target Entropy Minimization for Emission Experiments. ***Measurement Model.*** Solids and solid interfaces have been used extensively in emission measurements. A Beer–Lambert type law for emission spectroscopy has been developed that is analogous to that of the Beer–Lambert IR absorbance law.[22] This is shown in Eq. 1, where $E(\nu)$ is the emittance of the sample, $\varepsilon(\nu)$ is the emissivity, ν is the particular wavenumber of electromagnetic radiation, and x is an effective thickness (i.e., analogous to product concentration × thickness in the Lambert–Beer law for IR):

$$-\log_{10}[1 - E(\nu)] = x\varepsilon(\nu) \quad (1)$$

Keresztury et al.[22] have drawn attention to the difficulties surrounding the definition and use of the emittance $E(\nu)$. They note that the intensity of emission can be measured and/or has been used in many forms, i.e., (1) single beam intensity, (2) single beam intensity ratioed to sample holder, (3) single beam ratioed to blackbody, and (4) single beam ratioed to optically opaque and thick reference sample. Although intensity forms (3) and (4) are preferred forms from a theoretical viewpoint, the single beam measurement will retain modulation due to the Planck function and instrument response function.

In the present multi-component case, where the Planck function and instrument response function are also considered to be independent spectral contributions, the single beam intensity will be used for $E(\nu)$ without any further modification. Since the emittance in the present experiments is on the order of 10^{-4}, a Taylor expansion shows that the term $-\log_{10}[1 - E(\nu)]$ simplifies to just $E(\nu) \times \log e$. Accordingly, the model for the present emission experiments for a multi-component solution can be re-written as Eq. 2 where l is the path-length,

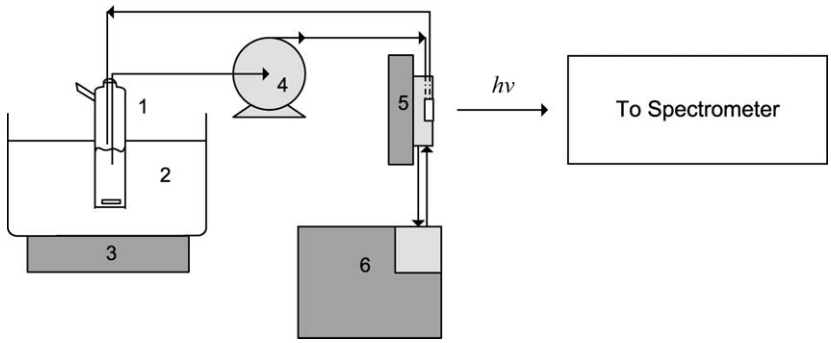

FIG. 2. Schematic configuration of the experimental setup: (*1*) Schleck tube; (*2*) Silicon oil; (*3*) IKA RCT Basic; (*4*) Pump; (*5*) Emission cell with window; (*6*) Water bath.

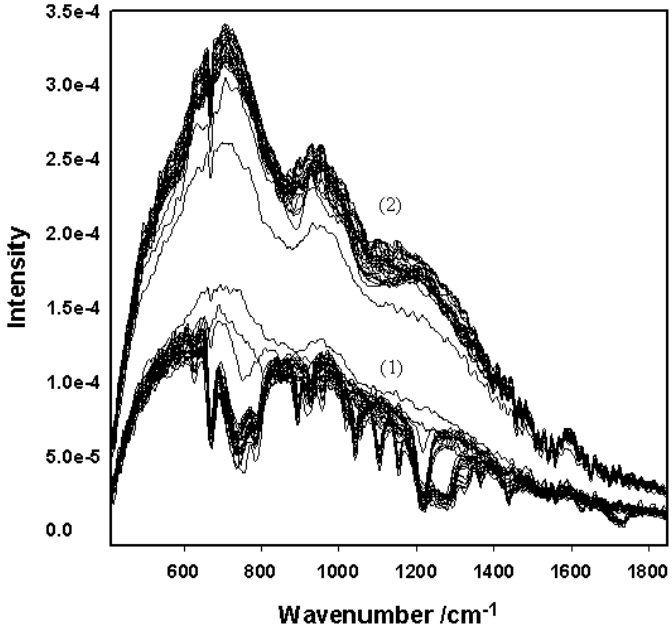

FIG. 3. Fifty-five emission spectra from two experiments: (*1*) experiment 1; (*2*) experiment 2.

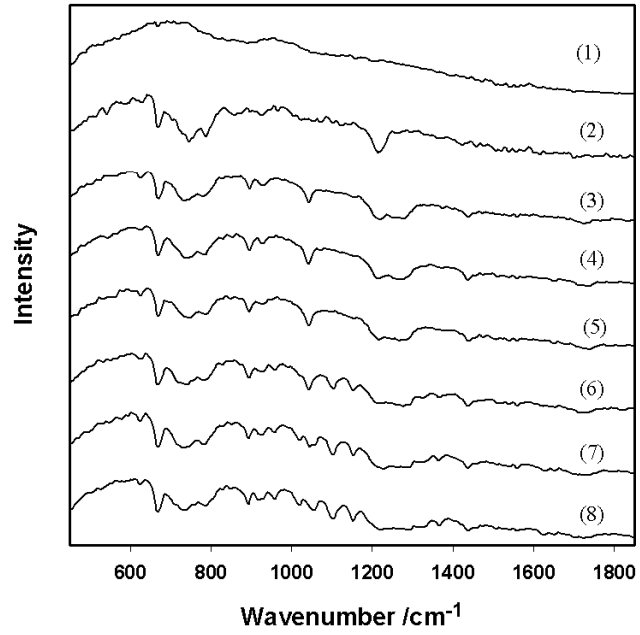

FIG. 4. The emission spectra of (*1*) the empty cell; (*2*) chloroform; (*3–5*) DMAD in chloroform; (*6-8*) CP, DMAD, and reaction in the solution.

c is the concentration, and Φ is the associated random experimental error as well as nonlinearities in the bilinear model. In Eq. 2, it is assumed that k solution measurements are made, s species are present, and ν channels of spectroscopic data are measured. Correspondence with the solution phase Lambert–Beer expression for IR spectroscopy is readily apparent. This type of simplification was used in our previous work with liquid films.

$$E(\nu)_{k\times\nu} = (l_{k\times k}c_{k\times s}\varepsilon_{s\times\nu} + \Phi_{k\times\nu}) \times (\log e)^{-1} \qquad (2)$$

If the measurements are not pure emission in nature, i.e., if they arise from absorption–emission phenomenon, then re-adsorption/self-absorption will distort the spectra and Eq. 2 will not hold exactly. As noted elsewhere,[22] "*this effect of self-absorption is due to the interplay of non-linearity of both emittance and transmittance scales and their opposite directions*". In the present contribution, Eq. 2 will simply be used as shown, in order to identify present limitations for the interpretation of multi-component reactive solutions in the vicinity of room temperature.

Band-Target Entropy Minimization. As mentioned above, the goal of BTEM is to retrieve the emissivity of the species of interest based on the single beam emission spectra from a reaction mixture in a complex system. The first step of BTEM is singular value decomposition (SVD).[23] SVD is used to decompose the experimental emission data, $E(\nu)$, into three matrices according to Eq. 3, where subscript k is the number of the spectra measured and ν is the channels of data. In this equation $\mathbf{U}_{k\times k}$ and $\mathbf{V}^{\mathrm{T}}_{\nu\times\nu}$ are the left singular vectors and right singular vectors that form an orthonormal basis, and $\mathbf{\Sigma}_{k\times\nu}$ is the corresponding singular value of the matrix.

$$E(\nu) = \mathbf{U}_{k\times k}\mathbf{\Sigma}_{k\times\nu}\mathbf{V}^{\mathrm{T}}_{\nu\times\nu} \qquad (3)$$

The primary equation for estimating the pure component emissivities by BTEM is given by Eq. 4. In the BTEM algorithm for emission spectroscopy the estimated pure component emissivity, $\hat{\varepsilon}'_{1\times\nu}$, is an optimized combination of z right singular vectors $\mathbf{V}^{\mathrm{T}}_{z\times\nu}$, where z is typically much greater than the number of species present. Further details concerning the various entropy forms used, the minimization of entropy, and the optimization of the transformation vector $\mathbf{T}$ for emission spectroscopy can be found elsewhere.[21]

$$\hat{\varepsilon}'_{1\times\nu} = \mathbf{T}_{1\times z}\mathbf{V}^{\mathrm{T}}_{z\times\nu} \qquad (4)$$

RESULTS

Experimental Data. A total of 55 emission spectra were obtained from the two semi-batch experiments and these are shown in Fig. 3. The emission spectra from experiment 1 have a considerably better signal-to-noise ratio than those from experiment 2. However, the spectra from experiment 2 have a higher overall signal intensity. The differences in the two data sets illustrate the sensitivity of emission experiments, particularly due to changes in film thickness, optical alignment, etc.

Figure 4 shows a sub-set of the data from experiment 1. Because the temperature of the reactive solution is just above room temperature and a room temperature detector is used, the spectra in Fig. 4 show mixed emission–absorption phenomena. The first spectrum shows the emission of the cell, which roughly resembles a smooth black body emission. All of the subsequent spectra show rather sharp signals due to the molecular vibrations of the species present. Thus, spectra 2–8 correspond to various steps during the addition of solvent, reactants, and then the emission of the reactive multi-component solution. The spectral range is limited to the region 400 cm^{-1} (instrumental cut-off) to approximately 1900 cm^{-1} (where emission at 308 K becomes more or less negligible).

Spectrum 2 shows bands centered at approximately 670, 740, 925, 1215 cm^{-1}, etc. These bands are consistent with chloroform's IR spectrum in the low wavenumber region. Spectra 3–5 show some significant new bands at approximately

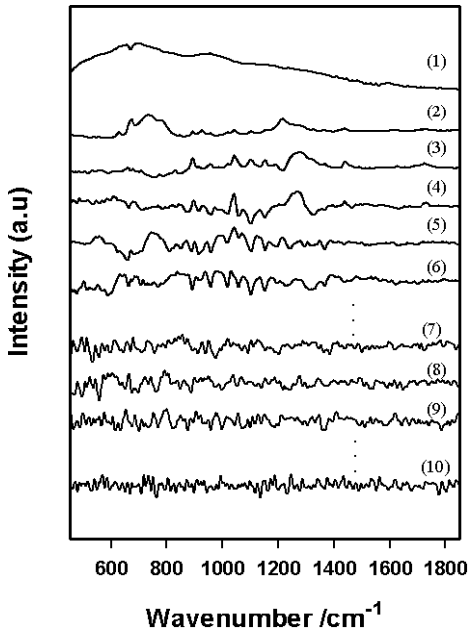

FIG. 5. Ten right singular vectors of the VT matrix for consolidated data set: (*1*–*6*) first six right singular vectors; (*7*) tenth right singular vector; (*8*) twentieth right singular vector; (*9*) thirtieth right singular vector; (*10*) fifty-fifth right singular vector.

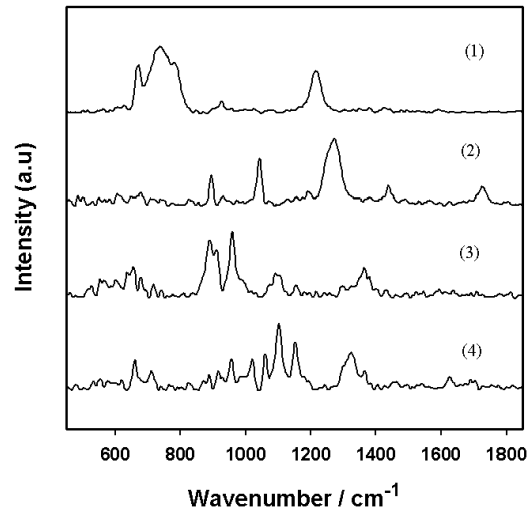

FIG. 6. Full range emittance patterns reconstructed using BTEM: (*1*) Chloroform; (*2*) DMAD; (*3*) CP; (*4*) Product.

896, 1042, 1438, and 1726 cm^{-1}, corresponding to the vibrations of DMAD. Spectra 6–8 were obtained after the introduction of CP. These spectra show several new peaks appearing at 624, 960, 1020, 1102, 1152, 1366 cm^{-1}, etc., indicating the presence of both CP and the organic product DBHD. Taken together, the spectra in Fig. 4 clearly show that meaningful spectral changes can be observed during a liquid-phase organic synthesis conducted in the vicinity of room temperature using an emission-type instrument configuration.

Singular Value Decomposition. The two sets of experimental emission spectra involving a total of 55 emission spectra were first consolidated into a single matrix $\mathbf{E}(\nu)$, which was then subjected to singular value decomposition. The first six right singular vectors, as well as the 10th, 20th, 30th, and 55th vectors are shown in Fig. 5.

The first six right singular vectors in Fig. 5 show clearly meaningful signals corresponding to the background as well as the vibrations from the species present. These vectors have rather good signal-to-noise ratios. More specifically, it can be observed that the first vector has signal due primarily to the blackbody background, the second vector has a significant contribution from the solvent chloroform, the third vector has a lot of spectral features from DMAD, and the 4th through 6th vectors also have considerable contributions from CP and the organic product. The 10th, 20th, and 30th right singular vectors still show some molecular vibrations; however, there is a considerable contribution from noise. Finally, the 55th vector is more or less white noise. Because localized and meaningful signals can still be seen in the first approximately 30 right singular vectors, these will be used in the following analysis.

Spectral Reconstruction Using Band-Target Entropy Minimization: Full Spectral Range Analysis. The right singular vectors from the two sets of emission experiment data were subjected to BTEM analysis. The first 30 vectors of the consolidated data set were employed. The results are shown in Fig. 6.

Four estimated spectral patterns could be successfully reconstructed from the BTEM analysis. As shown in Fig. 6, these spectral patterns resemble chloroform, DMAD, CP, and the product. All of the estimated spectra have quite good signal-to-noise ratio. The first estimated spectrum, having the major bands located at approximately 672, 740, 928, 1215 cm^{-1}, etc., corresponds to the chloroform emittance, where the broad and intense signal at approximately 740 cm^{-1} belongs to the C–Cl vibration. The second estimated spectrum, having bands at approximately 896, 1041, 1438, and 1727 cm^{-1}, corresponds to the DMAD emittance; the signal at 1727 cm^{-1} belongs to the C=O group. The third estimated spectrum, having major bands at approximately 656, 890, 912, 1090, 1366 cm^{-1}, etc., corresponds to the CP emittance, where the signal at 1366 cm^{-1} corresponds to the C–H bending mode. Finally, the fourth spectrum, having major bands located at approximately 1020, 1102, 1152, 1324, 1626 cm^{-1}, etc., corresponds to the product DBHD, where the signal at 1626 cm^{-1} belongs to the C=C groups and the signal at approximately 1720 cm^{-1} belongs to the C=O group.

It should be noted that a similar analysis was performed with just the data from experiment 1 (the high signal-to-noise set). This analysis did not provide spectral estimates as good as those obtained after the combination of both data sets. Indeed, different experimental designs and sequences of reagent additions were used in experiments 1 and 2 (resulting in different concentrations), and hence there was a greater signal variance in the combined data sets. Consequently, more useful basis vectors and better spectral estimates were obtained.

Spectral Reconstruction Using Band-Target Entropy Minimization: Partial Spectral Range Analysis. The full-range spectral reconstructions shown in Fig. 6 resemble the four reagents present, but they could be better. For example, it is clear from Fig. 6 that some reconstructions are sub-optimal and possess residual signal from other components. In particular, the organic product spectral estimate appears too complex in the C–C stretch region, and some of these vibrations coincide with vibrations from other reagents.

It is known that spectral artifacts similar to those mentioned

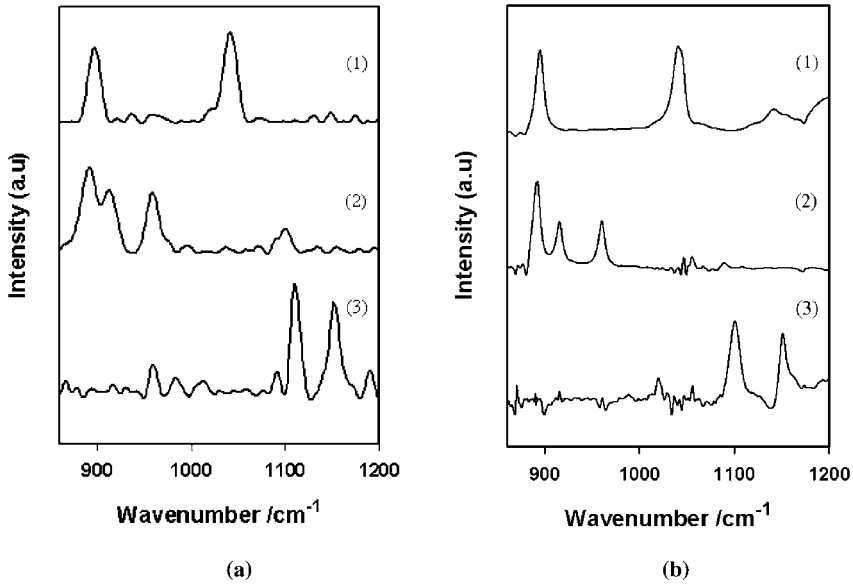

FIG. 7. Comparison of (**a**) partial range estimated emittance patterns via BTEM and (**b**) IR spectra: (***1***) DMAD; (***2***) CP; (***3***) Product.

above can arise if there is too much noise in the experimental spectra. If a wide spectral range is used, then too much noise is incorporated into the spectral estimates, and the quality frequently deteriorates. Thus, truncating the spectral range is often advantageous, because it reduces the accumulation of too much noise (and hence signal entropy) in the final estimates. Accordingly, BTEM was rerun for just the region 860–1200 cm^{-1}.

In addition, the cycloaddition reaction was performed using FT-IR spectroscopy. The resulting absorbance spectra of this cycloaddition reaction were analyzed using BTEM, and the estimated pure component spectra of the reactants were recovered. The data from the region 860–1200 cm^{-1} was used again. This was done (1) in order to have consistent spectral regions for comparison of the emission and FT-IR results, and (2) because solvent FT-IR absorbance is too large outside this spectral window (above 2 AU and hence the detector response is not so linear) and this again interferes with BTEM spectral reconstruction. Figure 7 compares the new estimated emission spectra with the estimated FT-IR spectra in the region 860–1200 cm^{-1}.

The estimated spectra for each species from both IR emission and the FT-IR experiment are quite similar. The two major bands for DMAD at 896 and 1041 cm^{-1} present in the estimated FT-IR spectra are present in the estimated emission spectra. The three major bands for CP at 890, 960, and 1090 cm^{-1} present in the estimated FT-IR spectra are present in the estimated emission spectra. Finally, the two major bands for the organic product at 1102 and 1152 cm^{-1} present in the estimated FT-IR spectra are present in the estimated emission spectra. As expected, the estimated emission spectra show some line broadening. Relatively few artifacts are present in the estimated emission spectra obtained over a partial spectral range.

Relative Concentrations of Reactants. A least squares fit of the estimated emission spectra onto the original experimental emission spectra was performed using the partial range spectral estimates from 860–1200 cm^{-1}. This results in an estimate of the relative concentration profiles of the reactants as shown in Fig. 8. The addition of the DMAD and CP can clearly be seen at spectra 15 and 22, respectively, in experiment 1. Furthermore, the decline in DMAD and the increase of DBHD due to reaction can also be clearly seen. The fluctuations in the relative concentration profiles are somewhat large due to the high noise level in the present emission spectra. The experimental data from experiment 2 was also analyzed. However, since the signal-to-noise level was very low (see Fig 3), the concentration profiles show considerable scatter.

DISCUSSION

Methodological Improvements. The present work demonstrates the possibility of remotely monitoring a liquid-phase organic synthesis near ambient temperature by infrared emission spectroscopy, thus obtaining the pure component spectral estimates of the species and first approximations to the relative concentration profiles. However, the present work also shows that experimental and numerical improvements are needed before this method can be applied more generally.

First, improvements in the signal-to-noise ratio are needed. This can probably be realized by (1) using an MCT detector cooled to liquid nitrogen temperature, and (2) using a dedicated infrared emission spectrometer (instead of the currently used multi-purpose spectrometer modified for emission experiments), thus increasing signal throughput.

Second, improvements have to be made in order to generate data of better quality for quantitative measurements. This can probably be realized by (3) carrying out the reactions in a cell where the window is also thermostated, in order to reduce any thermal gradients in the fluid and hence reduce re-absorption phenomenon, (4) optimizing the film thickness in order to obtain sharper and more resolved spectral features,[11] and (5) devising an approach whereby the inter-experimental alignment is more reproducible. In particular, a better thermostated cell should help to prevent (1) re-absorption phenomenon, which introduces various undesirable nonlinearities, as well as (2) intra-experimental baseline changes (as seen in Fig. 3) and the associated appearance of slightly negative concentration profiles (as seen in Fig. 8).

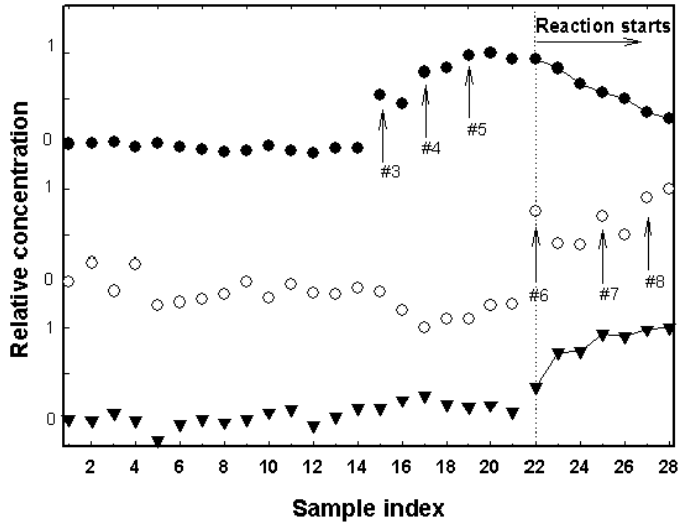

FIG. 8. The concentration profiles of DMAD (●), CP (○), and product (▼) from Experiment 1. Perturbation numbers #3–#8 correspond to the experimental designs provided in Table I.

The implementation of the above-mentioned steps should lead to much better spectral estimates and much better least square fits of the data for concentration profiles.

Future Directions. The use of infrared emission spectroscopy in the investigation of liquid-phase organic syntheses could provide some new opportunities. For example, it is common in infrared transmission spectroscopy that various spectral regions absorb too strongly (i.e., the solvent), and hence can not be used for quantitative analysis. In infrared emission spectroscopy, a wider spectral range can be utilized. Second, most organic syntheses are multi-phasic, i.e., involving solids floating in the liquid phase (i.e., salt-forming reactions, Grignard reactions, heterogeneous catalytic reactions with powdered catalysts, etc.) or having bubbles generated or even introduced into the liquid phase (i.e., hydrogenations). Infrared transmission spectroscopy has considerable problems with both cases, and infrared emission spectroscopy may represent an alternative. Third, ATR spectroscopy can be used for multi-phasic systems; however, it is an absorption-reflectance spectroscopy, which introduces additional complications.[24] Infrared emission spectroscopy, at least in its simplest form, does not possess contributions from reflection.

CONCLUSION

A liquid-phase cycloaddition reaction, performed in the vicinity of ambient temperature, was successfully measured by infrared emission spectroscopy using a room-temperature DTGS detector. Multiple perturbation experiments were performed in order to obtain data necessary for self-modeling curve resolution. The BTEM algorithm was successfully applied to the data to recover the pure component emission spectra of the solvent, the organic reactants DMAD and CP, and the organic product DBHD. These recovered emission spectra were consistent with those of independent FT-IR absorbance spectra. Furthermore, least squares analysis using these BTEM spectral estimates provided first approximations to the relative concentration profiles of the species during the course of the reaction. The present results demonstrate the potential of infrared emission spectroscopy as an analytical tool to monitor liquid-phase organic syntheses and suggest future opportunities for quantitative studies.

1. V. E. Hamilton, J. Geophysical Res. **105,** 9701 (2000).
2. R. L. Frost and A. M. Vassallo, Clays Clay Miner. **44,** 635 (1996).
3. M. D. Lane and P. R. Christensen, ICARUS **135,** 528 (1998).
4. C. Li, Q. Xin, K. L. Wang, and X. X. Guo, Appl. Specstrosc. **45,** 874 (1991).
5. D. E. Heard, R. A. Brownsword, D. G. Weston, and G. Hancock, Appl. Spectrosc. **47,** 1438 (1993).
6. L. Letendre, D. K. Liu, C. D. Pibel, J. B. Halpern, and H. L. Dai, J. Chem. Phys. **112,** 9209 (2000).
7. C. Morrell, C. Breheny, V. Haverd, A. Cawley, and G. Hancock, J. Chem. Phys. **117,** 11121 (2002).
8. A. Carvalho, G. Hancock, and M. Saunders, Phys. Chem. Chem. Phys. **8,** 4337 (2006).
9. F. J. DeBlase and S. Compton, Appl. Specstrosc. **45,** 611 (1991).
10. D. Kember and N. Sheppard, Appl. Specstrosc. **29,** 496 (1975).
11. J. Mink, "Sampling Techniques for Vibrational Spectroscopy", in *Handbook of Vibrational Spectroscopy,* J. Chalmers and P. Griffiths, Eds. (John Wiley and Sons, New York, 2002), vol. 2, p. 1195.
12. J. Mink, Appl. Specstrosc. **46,** 1747 (1992).
13. S. V. Compton, D. A. C. Compton, and R. G. Messerschmidt, Spectroscopy **6(6),** 35 (1991).
14. J. Hvistendahl, E. Rytter, and H. A. Oye, Appl. Spectrosc. **37,** 182 (1983).
15. F. W. Koehler, G. W. Small, R. J. Combs, R. B. Knapp, and R. B. Kroutil, Vib. Spectrosc. **27,** 97 (2001).
16. M. J. Mattu, G. W. Small, R. J. Combs, R. B. Knapp, and R. T. Kroutil, Appl. Spectrosc. **54,** 341 (2000).
17. C. Z. Li, L. F. Guo, and M. Garland, Organometallics **23,** 2201 (2004).
18. E. Widjaja, Y. Y. Tan, and M. Garland, Org. Proc. Res. Dev. **11,** 98 (2007).
19. E. Widjaja and J. T. Sampanthar, Anal. Chim. Acta **585,** 241 (2007).
20. Ch. Srilakshmi, E. Widjaja, M. Garland, and B. G. Anderson, J. Raman Spectrosc. **38,** 349 (2007).
21. S. Y. Cheng, D. Rajaratham, M. L. Tan, and M. Garland, Appl. Spectrosc. **60,** 521 (2006).
22. G. Keresztury, J. Mink, and J. Kristof, Anal. Chem. **67,** 3782 (1995).
23. G. H. Golub and C. Reinsch, Mum. Math. **14,** 403 (1970).
24. K. Yamamoto and H. Ishida, Vib. Spectrosc. **8,** 1 (1994).

Available online at www.sciencedirect.com
ScienceDirect
Talanta 74 (2008) 1132–1140
Talanta
www.elsevier.com/locate/talanta

The application of BTEM to UV–vis and UV–vis CD spectroscopies: The reaction of $Rh_4(CO)_{12}$ with chiral and achiral ligands

Shuying Cheng [a], Feng Gao [b], Karl I. Krummel [a], Marc Garland [a,b,*]

[a] *Department of Chemical and Bimolecular Engineering, National University of Singapore, 4 Engineering Drive 4, Singapore 117576, Singapore*
[b] *Institute of Chemical and Engineering Sciences, 1 Pesek Road, Jurong Island, Singapore 627833, Singapore*

Received 10 July 2007; received in revised form 17 August 2007; accepted 17 August 2007
Available online 23 August 2007

Abstract

Two different organometallic ligand substitution reactions were investigated: (1) an achiral reactive system consisting of $Rh_4(CO)_{12} + PPh_3 \rightleftharpoons Rh_4(CO)_{11}PPh_3 + CO$ in *n*-hexane under argon; and (2) a chiral reactive system consisting of $Rh_4(CO)_{12} + (S)$-BINAP $\rightleftharpoons Rh_4(CO)_{10}$BINAP $+ 2CO$ in cyclohexane under argon. These two reactions were run at ultra high dilution. In both multi-component reactive systems the concentrations of all the solutes were less than 40 ppm and many solute concentrations were just 1–10 ppm. In situ spectroscopic measurements were carried out using UV–vis (Ultraviolet–visible) spectroscopy and UV–vis CD spectroscopy on the reactive organometallic systems (1) and (2), respectively. The BTEM algorithm was applied to these spectroscopic data sets. The reconstructed UV–vis pure component spectra of $Rh_4(CO)_{12}$, $Rh_4(CO)_{11}PPh_3$ and $Rh_4(CO)_{10}$BINAP as well as the reconstructed UV–vis CD pure component spectra of $Rh_4(CO)_{10}$BINAP were successfully obtained from BTEM analyses. All these reconstructed pure component spectra are in good agreement with the experimental reference spectra. The concentration profiles of the present species were obtained by performing a least square fit with mass balance constraints for the reactions (1) and (2). The present results indicate that UV–vis and UV–vis-CD spectroscopies can be successfully combined with an appropriate chemometric technique in order to monitor reactive organometallic systems having UV and Vis chromophores.

Keywords: BTEM; Spectral reconstruction; $Rh_4(CO)_{12}$; BINAP; UV–vis and UV–vis CD spectroscopy

1. Introduction

Rhodium complexes are frequently used as catalyst precursors for hydroformylation, hydrogenation, cyclotrimerization, etc. [1]. This group of complexes is one of the most extensively studied in organometallic chemistry [2]. A rather large variety of achiral and chiral ligands have been used to modify the reactivity and selectivity of rhodium in catalytic reactions. In particular, mono-dentate and bi-dentate ligands are widely used to generate new mono-nuclear and poly-nuclear rhodium complexes.

The tetranuclear rhodium complex $Rh_4(CO)_{12}$ is a well known and widely used catalyst precursor [1]. It has been shown that $Rh_4(CO)_{12}$ readily reacts with 1 equivalent triphenyl phoshine at room temperature to give the corresponding mono-substituted product Eq. (1) [3]. Alternately, it is known that disubstitution can occur when 2 equivalents of triphenyl phoshine are used [3]. In the present contribution, 1 equivalent of (*S*)-BINAP, a chiral bidentate phosphine [4], will be used Eq. (2). The polynuclear metal cluster $Rh_4(CO)_{12}$ has a very strong red color and all known derivatives are also highly colored. Since it is a chiral naphthalene derivative, (*S*)-BINAP has both intense UV and UV-CD spectra.

$$Rh_4(CO)_{12} + PPh_3 \rightleftharpoons Rh_4(CO)_{11}PPh_3 + CO \quad (1)$$

$$Rh_4(CO)_{12} + (S)\text{-BINAP} \rightleftharpoons Rh_4(CO)_{10}\text{BINAP} + 2CO \quad (2)$$

Organometallics are frequently characterized by NMR [5–7] and FTIR [8–12]. NMR typically requires high solute concentrations, on the order of many milligrams per milliliter. FTIR

* Corresponding author. Tel.: +65 6796 3947; fax: +65 6316 6185.
E-mail address: marc_garland@ices.a-star.edu.sg (M. Garland).

0039-9140/$ – see front matter © 2007 Elsevier B.V. All rights reserved.
doi:10.1016/j.talanta.2007.08.019

analysis can frequently be performed at much lower concentrations or even in situ during catalytic reactions (in the ppm range). Since the molar absorptivities of chromophores in the UV–vis are typically orders of magnitude greater than fundamental vibrations in the IR, UV–vis has the potential for characterizing chromophore-containing organometallics at much lower concentrations. Electronic circular dichroism (ECD) spectroscopy, which measures the difference in absorbance of right- and left-circularly polarized light by a substance, is also a valuable tool to monitor chiral organometallic complexes, particularly complexes of biological and medical importance [13]. Since the phenomenon of electronic circular dichroism spectroscopy is normally many orders of magnitude greater than either vibrational circular dichroism or Raman Optical Activity (ROA), ECD holds the potential for detecting chiral organometallics possessing chromophores at very low concentrations.

Many techniques have been proposed for UV/UV-CD spectroscopic data analysis of multi-component solutions in order to reconstruct the pure component spectra. Basically, the main idea of these methods is to first determine the basis vectors associated with the observed UV/UV-CD spectroscopic data. The most generally used decomposition techniques include principal component analysis (PCA) [14], singular value decomposition (SVD) [15–18] and non-linear iterative partial least-squares (NIPALS) [19]. These basis vectors are then transformed to give the spectral estimates of the pure components in the mixture. Examples include; (1) a self-modelling curve resolution (SMCR) technique based on principal component analysis (PCA) and non-negativity constraints to resolve a two-component mixture system measured using UV/vis spectroscopy introduced by Lawton and Sylvester [14]. (2) A computer-assisted target factor analysis (CAT) algorithm, where SVD was applied to the abstract factor analysis and simple-to-use interactive self-modelling mixture analysis (SIMPLISMA) was applied to optimize UV–vis spectral estimates of the components [20]. (3) A singular value decomposition analysis was applied to a large set of UV-CD spectra measured from a metalloprotein [15].

Although, other SMCR methods have been proposed and implemented, some serious problems remain for spectral resolution of UV–vis data [14–20]. In particular, UV–vis spectra are normally very broad with few distinct features. Moreover, there is often a very high degree of spectral overlap between the spectra of different species. In addition, a prior information of some sort is often needed for spectral reconstruction, i.e. an estimate of the number of species present and/or an estimate of the concentrations of the species present.

In the present contribution band-target entropy minimization (BTEM) is applied to UV–vis data from reactions (1) and (2) in order to reconstruct the pure component spectra. Furthermore, BTEM is successfully applied to the UV–vis-CD data as well to reconstruct the circularly polarized pure component spectra. Although BTEM has been successfully applied to many spectroscopic data sets with non-negative localized signals, i.e. FTIR, Raman, NMR, this is the first time it has been applied to broad UV–vis data. In addition, this is the first application of BTEM to UV–vis-CD spectra which possess both positive and negative parts.

2. Computational section

2.1. Inverse problems and system identification

Both multi-component UV–vis and UV–vis CD measurements obey the Bouguer–Lamber–Beer law in the low concentration range. Consequently, they can be modeled as follows:

$$A_{k\times\nu} = l_{k\times k} C_{k\times s} a_{s\times\nu} + e_{k\times\nu} \tag{3}$$

$$\Delta A_{k\times\nu} = l_{k\times k} C_{k\times s} \Delta\varepsilon_{s\times\nu} + \left[e_{k\times\nu}\right]_{CD} \tag{4}$$

where

$$\Delta\varepsilon = \varepsilon_{\mathrm{L}} - \varepsilon_{\mathrm{R}} \tag{5}$$

In the above equations, $A_{k\times\nu}$ is an absorbance matrix, $C_{k\times s}$ a concentration matrix, $a_{s\times\nu}$ a pure component spectral matrix, ΔA the difference between absorbance of left circularly polarized (LCP) and right circularly polarized (RCP) light, ε_{L} and ε_{R} the molar extinction coefficients for RCP and LCP light, l the path length, subscript k the number of measurements (spectral pattern), subscript s the number of the observed species, subscript ν the number of data channels, subscript CD refers to polarized data and $e_{k\times\nu}$ is error, i.e. the experimental noise and model non-linearity.

In multi-component spectroscopic data analysis, there are three frequent major tasks: (1) determine the number of observable species "s" present (2) determine the pure component spectra of the observable species, i.e. $a_{s\times\nu}$ and $\Delta\varepsilon_{s\times\nu}$ and (3) determine the concentrations $C_{k\times s}$ of all observable species present. These inverse problems are typically ill posed. In order to constrain the problems and hence obtain meaningful solutions, various constraints are usually imposed. Non-negativity in concentrations and non-negativity in pure component spectra $a_{s\times\nu}$ are the most frequently used. Since CD spectra possess both positive and negative parts, a non-negativity constraint cannot be imposed on $\Delta\varepsilon_{s\times\nu}$.

2.2. Band-target entropy minimization (BTEM)

The main system identification task is pure component spectral estimation. Self-modeling curve resolution (SMCR) comprises a family of chemometric techniques which target the reconstruction of pure component spectra from mixture spectroscopic data [21–24]. Band-target entropy minimization, a SMCR technique, was developed to reconstruct the pure component spectra from mixture spectroscopic data without any a priori information such as the number of significant factors present (a priori information is indispensable for many other self-modeling curve resolution methods) [25–29]. In BTEM, the entropy minimization concept is used in the objective function and optimization is performed using Simulated Annealing to give the simplest spectral patterns. Some frequently encountered difficulties in signal processing, such as spectral nonlinearities

arising from shifting band position and changing band shapes, are easily accommodated by the BTEM algorithm. Another important advantage of BTEM is that it can be used to retrieve a pure component with very low concentration (very low signal intensity).

The first step in BTEM is to perform singular value decomposition (SVD) in order to decompose the experimental UV absorbance data, $A_{k\times\nu}$, into three matrices according to Eq. (6), where $U_{k\times k}$ and $\mathrm{V}^{\mathrm{T}}_{\nu\times\nu}$ are the left singular vectors and right singular vectors which form an orthonormal basis, and $\Sigma_{k\times\nu}$ is the corresponding singular value of matrix. The UV–vis-CD data $\Delta A_{k\times\nu}$ can be decomposed in a similar manner Eq. (7).

$$A_{k\times\nu} = U_{k\times k}\Sigma_{k\times\nu}\mathrm{V}^{\mathrm{T}}_{\nu\times\nu} \tag{6}$$

$$\Delta A_{k\times\nu} = \left[U_{k\times k}\Sigma_{k\times\nu}\mathrm{V}^{\mathrm{T}}_{\nu\times\nu}\right]_{CD} \tag{7}$$

The first several row vectors of $\mathrm{V}^{\mathrm{T}}_{\nu\times\nu}$ will consist of meaningful spectral features while the rest will consist primarily of noise. The BTEM algorithm searches the subspace of z basis vectors for the simplest underlying patterns. This is achieved by transforming the abstract right singular vectors in $\mathbf{V}^{\mathrm{T}}$ into pure component spectra estimates, $\hat{a}$ for UV–vis data and $\Delta\hat{\varepsilon}$ for UV–vis-CD data, one-at-a-time using Eqs. (8) and (9).

$$\hat{a}_{1\times\nu} = T_{1\times z}\mathbf{V}^{\mathrm{T}}_{z\times\nu} \tag{8}$$

$$\Delta\hat{\varepsilon}_{1\times\nu} = \left[T_{1\times z}\mathbf{V}^{\mathrm{T}}_{z\times\nu}\right]_{CD} \tag{9}$$

The z transformation elements $T_{1\times z}$ are determined using a non-linear optimization. The objective function Eq. (10) includes two terms: information entropy function (H) and penalty function (P) for non-negativity of the estimated spectra $A_{k\times\nu}$ and their corresponding concentrations:

$$F_{\mathrm{obj}} = H + P \tag{10}$$

In turn, the information entropy function is given by Eq. (11) where h_ν is a discrete probability distribution function and the exponent m is the degree of spectrum differentiation. In the present study, both the first and second derivative were used in the BTEM analyses. These provided good spectral reconstruction for bands having shoulders and for those with severe overlap.

$$H = -\sum h_\nu \ln h_\nu \tag{11}$$

$$h_\nu = \frac{|\hat{a}^m_\nu|}{\sum_\nu |\hat{a}^m_\nu|} \quad \text{or} \quad h_\nu = \frac{|\Delta\hat{\varepsilon}^m_\nu|}{\sum_\nu |\Delta\hat{\varepsilon}^m_\nu|} \tag{12}$$

3. Experimental

3.1. General information

All solution preparations and transfers were carried out under argon (99.999%, Soxal, Singapore) atmosphere using standard Schlenk techniques [30]. The argon was further purified before use by passing it through a deoxy and zeolite column to reduce the trace oxygen and water, respectively. The solvents *n*-hexane and cyclohexane (>99.6%, Fluka) were refluxed over sodium–potassium alloy under argon atmosphere. Purified nitrogen (99.999%, Saxol, Singapore) was used to purge the 2250 Shimadzu UV–vis spectrometer and Jasco-810 UV–vis spectropolarimeters.

The metal complex tetrarhodium dodecacarbonyl, $Rh_4(CO)_{12}$ (98%) and the chiral ligand (*S*)-(−)-2,2′-bis (diphenylphosphino)-1,1′-binaphthyl, (*S*)-BINAP (97%) from Strem chemicals (Newport, MA) and the achiral ligand triphenylphosphine, PPh_3 (>99%) from Merck were used as received.

3.2. Equipmental setup

A schematic diagram of the experimental setup is shown in Fig. 1. The two semi-batch ligand substitutions (i) $Rh_4(CO)_{12}$ with PPh_3, and (ii) $Rh_4(CO)_{12}$ with (*S*)-BINAP were performed in a Schlenk tube equipped with magnetic stirring. A rubber septum was used at the top of the Schlenk tube in order to insert transfer lines and in order to inject perturbations during the semi-batch runs. The liquid phases was circulated to a quartz cuvette with 1.0 cm path length using a Teflon membrane pump (Cole Parmer) at the flow rate of 5 ml/min via Teflon tubes of 1/16 in. outer diameter. The quartz cuvette was fixed in a stainless steel cell holder and placed in the cell chamber of UV spectrometer. For any particular experiment, either the Shimadzu UV-2550 spectrometer or the Jasco-810 spectropolarimeter was used. Experiments were run at ambient temperature circa 298 K.

The entire system was cleaned with anhydrous solvent (*n*-hexane/cyclohexane) prior to experiments. Furthermore, the reactions were carried out under argon in order to avoid of the degradation of $Rh_4(CO)_{12}$, PPh_3, (*S*)-BINAP and the resulting metal complexes.

3.3. In situ spectroscopic measurements

Fifty milliliters *n*-hexane and 50 ml cyclohexane were used as solvent for the reactions (1) and (2), respectively. Both semi-batch reactions were performed in a similar manner. For example, in the ligand substitution reaction (1) first, 50 ml of *n*-hexane was transferred to the Schlenk tube under argon and the stirrer was turned on. The pressure was controlled

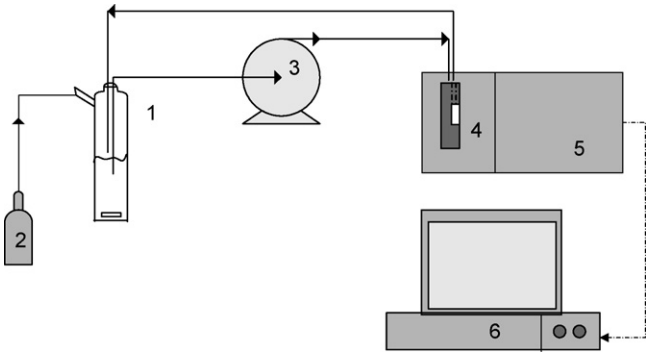

Fig. 1. Schematic of experimental configuration: (1) Schlenk tube; (2) argon tank; (3) pump; (4) quartz cell; (5) UV–vis spectrometer; (6) data acquisition.

Table 1
Experimental design for ligand substitution reaction indicating the individual perturbation steps

Index	Experiment 1: $[Rh_4(CO)_{12}]$ with PPh_3		Experiment 2: $[Rh_4(CO)_{12}]$ with (*S*)-BINAP	
	Perturbation	Spectra #	Perturbation	Spectra #
1	Solvent: *n*-hexane	1–2	Solvent: cyclohexane	1–2
2	Add 100 μl $[Rh_4(CO)_{12}]$	3–4	Add 100 μl $[Rh_4(CO)_{12}]$	3
3	Add 100 μl $[Rh_4(CO)_{12}]$	5–6	Add 200 μl $[Rh_4(CO)_{12}]$	4
4	Add 50 μl PPh_3	7–8	Add 200 μl $[Rh_4(CO)_{12}]$	5
5	Add 100 μl PPh_3	9–10	Add 50 μl (*S*)-BINAP	6-7
6	Add 250 μl $[Rh_4(CO)_{12}]$	11–12	Add 50 μl (*S*)-BINAP	8
7	Add 250 μl $[Rh_4(CO)_{12}]$	13–14	Add 50 μl (*S*)-BINAP	9
8	Add 200 μl PPh_3	15–17	Add 100 μl (*S*)-BINAP	10
9	Add 250 μl PPh_3	18–19	Add 100 μl (*S*)-BINAP	11–12

at just over 0.1013 MPa of argon. After the *n*-hexane solvent was circulated through the entire system, the UV–vis spectra in the quartz cuvette were collected. A stock solution of *n*-hexane with $Rh_4(CO)_{12}$ (ca. 27.5 mg in 20 ml) was prepared and a predetermined amount was injected into the Schlenk tube under argon. Typically, after each perturbation the solution was circulated for circa 10 min to achieve solution homogeneity. Then the UV–vis spectra of the $Rh_4(CO)_{12}$/*n*-hexane solution in the quartz cuvette were collected. A stock solution of *n*-hexane with PPh_3 (ca. 8.4 mg in 20 ml) was prepared and a predetermined amount was injected into the Schlenk tube under argon. After equilibrium, the UV–vis spectra of the reactive system were collected. The perturbation steps in each experiment correspond to the experimental design as shown in Table 1.

In a similar manner, a stock solution of 13.5 mg (*S*)-BINAP dissolved in 20 ml cyclohexane and a stock solution of 31.5 mg of $Rh_4(CO)_{12}$ dissolved in 20 ml cyclohexane were prepared for the ligand substitution reaction (2). The corresponding experimental design is also shown in Table 1.

All the UV–vis and/or CD spectra were recorded at scanning speed of 200 nm/min in the range of 800–200 nm. Since $Rh_4(CO)_{12}$ reacts with PPh_3 almost instantaneously, most of these spectra were collected under nearly full transformation of PPh_3, i.e. where the equilibrium is shifted to the far right in Eq. (1). Similarly, $Rh_4(CO)_{12}$ reacted rapidly with (*S*)-BINAP, most of these spectra were collected under nearly full transformation of (*S*)-BINAP, i.e. where the equilibrium is shifted to the far right in Eq. (2).

4. Results and discussion

4.1. Ligand substitution of $Rh_4(CO)_{12}$ with PPh_3

4.1.1. Experimental data

The ligand substitution of $Rh_4(CO)_{12}$ with the achiral ligand PPh_3 was carried out in *n*-hexane under argon atmosphere. The in situ spectroscopic measurements were performed using the Shimadzu UV-2550 spectrometer. A total of 19 UV–vis spectra were obtained from this experiment as shown in Fig. 2. These measurements show absorbance from the solvent, $Rh_4(CO)_{12}$ and the cluster. A few spectral maxima and shoulders are seen, i.e. at 305, 380 nm, etc. All spectral features are broad, as expected for UV–vis spectra. Two spectral step changes, one at 420 nm and the other at 540 nm are also observed. These are due to the optical filter changes.

4.1.2. Singular value decomposition (SVD)

The 19 UV–vis spectra were first consolidated into a single matrix. The spectra preconditioning, namely background subtraction, was performed on the consolidated absorbance data matrix and then singular value decomposition (SVD) was employed to decompose this preconditioned absorbance data matrix to obtain the right singular vectors, the orthonormal matrix V^T. The first 6 right singular vectors and 19th vector are shown in Fig. 3.

The first 3 right singular vectors in Fig. 3 show meaningful signals although the bands are quite broad. These bands are significant spectral features associated with the metal carbonyl and metal complex. The 4th and 5th right singular vectors still show some absorbance bands, however, there is a considerable contribution from noise. The 6th to the 19th right singular vectors can be considered to be primarily white noise. Since all meaningful spectral features are seen in the first five right singular vectors, only vectors 1–5 were used in the following BTEM analysis.

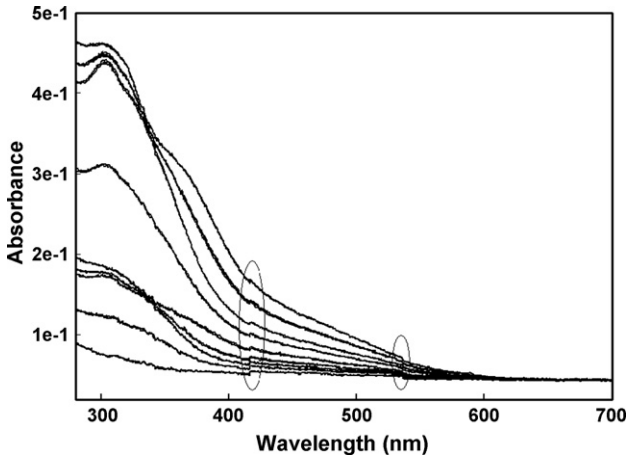

Fig. 2. UV–vis reaction spectra of the ligand substitution reaction of $Rh_4(CO)_{12}$ with PPh_3 (under argon) involving 9 perturbation steps. The ovals highlight the areas where filter changes occur.

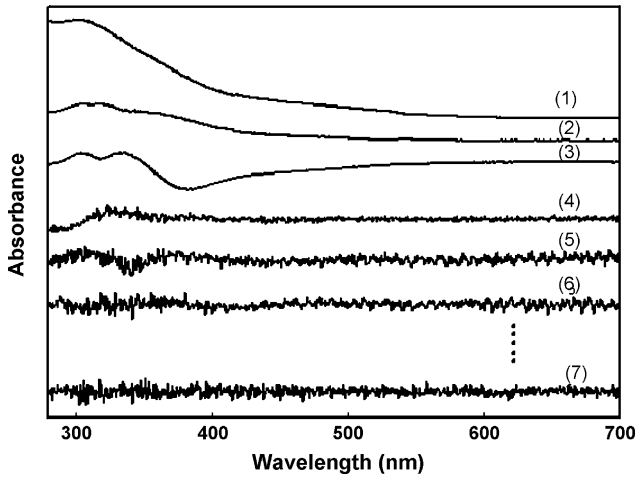

Fig. 3. Seven right singular vectors of the V^T matrix for the consolidated data set from the ligand substitution reaction of $Rh_4(CO)_{12}$ with PPh_3 (Experiment 1): (1)–(6) first six right singular vectors; (7) 19th right singular vector.

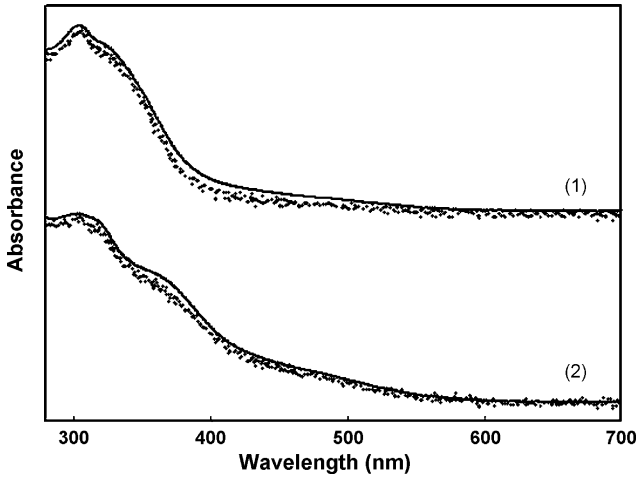

Fig. 4. Solid lines: recovered pure component spectra obtained by BTEM: (1) $Rh_4(CO)_{12}$ and (2) $Rh_4(CO)_{11}$ PPh_3; dotted lines: UV–vis experiment reference spectra: (1) $Rh_4(CO)_{12}$ and (2) $Rh_4(CO)_{11}$ PPh_3.

4.1.3. Spectral reconstruction using BTEM

The 5 right singular vectors from the experimental absorbance data were transformed to pure component spectra using BTEM analysis. Two estimated spectral patterns could be successfully reconstructed from the BTEM analysis. These are the estimated UV–vis pure component spectra of $Rh_4(CO)_{12}$ and the product $Rh_4(CO)_{11}PPh_3$. Fig. 4 compares the estimated UV–vis spectra with the experimental reference spectra. Both estimated spectra are in quite good agreement with the experimental reference spectra.

More right singular V^T vectors (up to 19 V^T vectors) were used in other analyses, however, no additional meaningful spectra patterns were obtained. Since $Rh_4(CO)_{12}$ reacts instantaneously with PPh_3 and since Eq. (1) is shifted to the far right, the analysis indicates that little or no free PPh_3 was present in these spectra (note that PPh_3 has a broad chromophore from 200 to 300 nm due to the phenyl groups).

4.1.4. Concentrations profiles

The relative concentration profiles of the reactants were calculated by a least squares fit of the estimated UV–vis spectra onto the original experimental UV–vis absorbance spectra. Since the present experiments were conducted at PPh_3:$Rh_4(CO)_{12}$ ratios less than 0.7 the presence of the di-substituted product $Rh_4(CO)_{10}(PPh_3)_2$ can be neglected [31]. Furthermore, the mono-substituted product was totally soluble in *n*-hexane in the range of concentration used in this study (less than 5 ppm). Accordingly, the mass balance from the experimental design was used as a constraint in order to determine the calibrations for both $Rh_4(CO)_{12}$ and $Rh_4(CO)_{11}PPh_3$. Fig. 5 compares the concentration profiles of $Rh_4(CO)_{12}$ and $Rh_4(CO)_{11}PPh_3$ obtained from the experimental design with those obtained from the spectroscopic measurements. It is clearly seen that satisfactory concentration profiles for both $Rh_4(CO)_{12}$ and the product $Rh_4(CO)_{11}$ PPh_3 are obtained. However, some discrepancy appears as more and more perturbations are made. This increasing discrepancy is probably due to accumulation of error during the experimental procedure, either from systematic error during injection and/or the slow loss of hexane through the septum (it is very volatile).

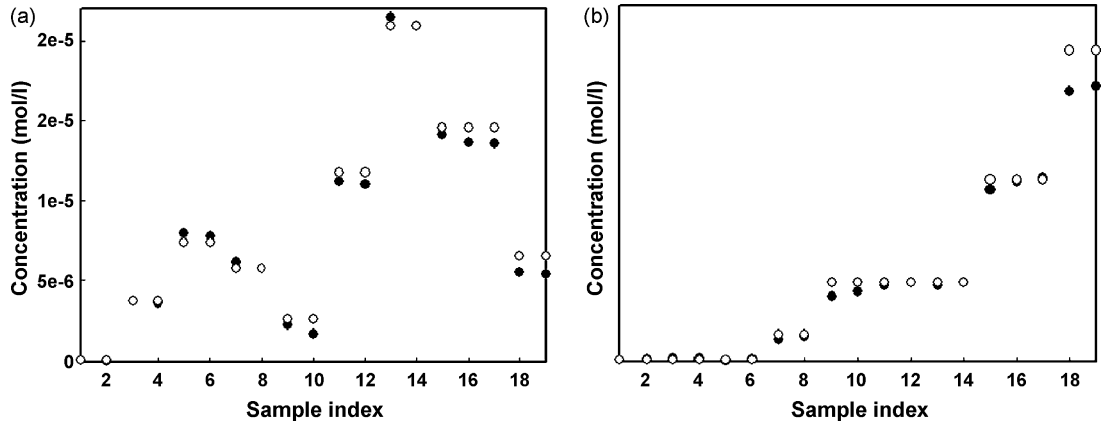

Fig. 5. Comparison of the concentration profiles from recovered UV–vis pure component spectra (●) and experiment design (◯). Profiles for (a) $Rh_4(CO)_{12}$ and (b) $Rh_4(CO)_{11}$ PPh_3.

4.2. Ligand substitution of $Rh_4(CO)_{12}$ with (S)-BINAP

The ligand substitution of $Rh_4(CO)_{12}$ with the chiral bidentate ligand (*S*)-BINAP was carried out in cyclohexane under an argon atmosphere. This reaction was carried out in a semi-batch mode by introducing perturbations of (*S*)-BINAP into reactive system. The concentrations of all the reactants involved in this reaction were less than 20 ppm and the concentration of the product $Rh_4(CO)_{10}$BINAP was less than 10 ppm. The in situ spectroscopic measurements were performed using the UV Jasco-810 spectropolarimeter. A total of 12 UV–vis spectra and 12 UV–vis-CD spectra were obtained simultaneously from the above experiment.

4.2.1. UV–vis experimental data set

4.2.1.1. Experimental data. The 12 UV–vis spectra from the above experiment in the range of 700–280 nm are shown in Fig. 6. Since all spectra are below circa 2 absorbance units, these spectra were taken in a more-or-less linear instrument response region. In the high nm range, the UV–vis spectra are rather featureless and correspond primarily to the instrument function. The primary signals of interest are all below 500 nm. At the reagent concentrations used, significant changes are seen in the region of circa 280–500 nm during the semi-batch experiment. Since none of the experimental spectra have absorbance above circa 1.5, rather strict additivity of component spectra should exist, and the bilinear form of the Bouguer–Lamber–Beer law should remain valid.

4.2.1.2. Singular value decomposition. A total of 12 UV–vis spectra were first consolidated into a single matrix. To minimize the effects of the solvent and cuvette signals on the spectral analysis, spectral preconditioning was performed. This background subtraction resulted in a new consolidated absorbance data matrix. Next, singular value decomposition (SVD) was employed to decompose this preconditioned absorbance data matrix to give the right singular vectors, the orthonormal matrix

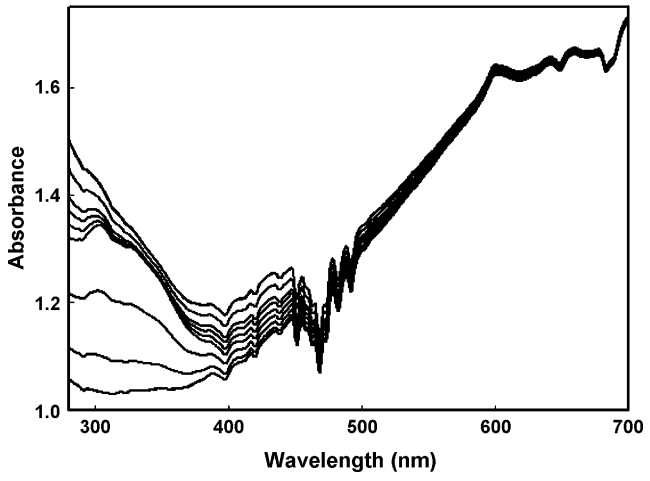

Fig. 6. UV–vis reaction spectra of the ligand substitution reaction of $Rh_4(CO)_{12}$ with (*S*)-BINAP (under argon) involving 9 perturbation steps.

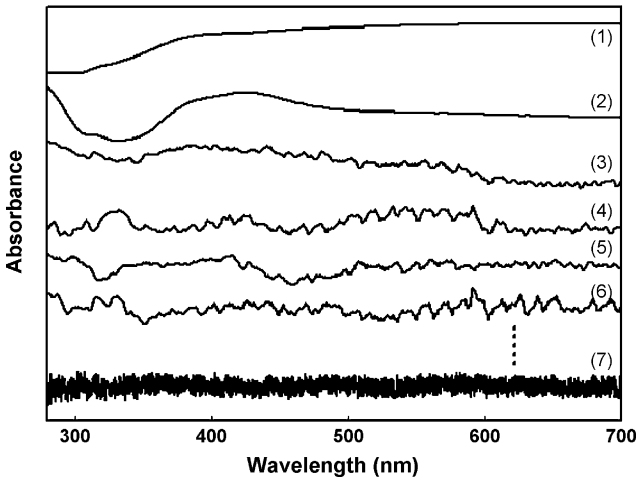

Fig. 7. Seven right singular vectors of the V^T matrix for UV–vis consolidated data set from the ligand substitution reaction of $Rh_4(CO)_{12}$ with (*S*)-BINAP (Experiment 2): (1)–(6) first six right singular vectors; (7) 12th right singular vector.

V^T. The first 6 right singular vectors and 12th vector are shown in Fig. 7.

The first 2 right singular vectors in Fig. 7 show significant spectral features with the very broad bands associated with the metal carbonyl and metal complex. The 3rd to 6th right singular vectors still show some absorbance bands, however, there is a considerable contribution from noise. The 12th right singular vectors can be considered to be white noise. Since prominent spectra features can be observed only in the first six right singular vectors, these will be used in the following BTEM analysis.

4.2.1.3. Spectral reconstruction using BTEM. BTEM analysis was performed using the first 6 right singular vectors from the preconditioned UV–vis absorbance data in order to reconstruct the pure component spectra involved in the reaction. The noticeable spectral extrema in the first 6 right singular vectors

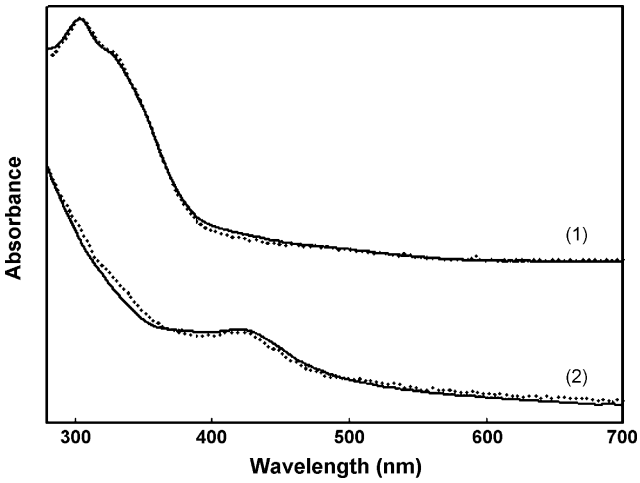

Fig. 8. Solid lines: recovered pure component spectra obtained by BTEM: (1) $Rh_4(CO)_{12}$ and (2) $Rh_4(CO)_{10}$ BINAP; dotted lines: UV–vis experiment reference spectra: (1) $Rh_4(CO)_{12}$ and (2) $Rh_4(CO)_{10}$BINAP.

were used as targets. Two estimated UV–vis spectral patterns, from $Rh_4(CO)_{12}$ and the product $Rh_4(CO)_{10}$BINAP, could be successfully reconstructed from the BTEM analysis. Fig. 8 compares the estimated UV–vis spectra with the experimental reference spectra. Both estimated spectra are in quite good agreement with the experimental reference spectra.

4.2.1.4. Concentrations profiles. An estimate of the relative concentration profiles of the reactants was calculated by a least squares fit of the estimated UV–vis spectra onto the original experimental UV–vis absorbance spectra. Further quantitative spectroscopic analysis was performed using the mass balances from the experimental design as a constraint and assuming that only reaction (2) occurs. The quantitative analysis resulted in two concentration profiles for $Rh_4(CO)_{12}$ and the product $Rh_4(CO)_{10}$BINAP as shown in Fig. 9. It is clearly seen that satisfactory concentration profiles of both $Rh_4(CO)_{12}$ and the product $Rh_4(CO)_{10}$BINAP were obtain from the quantitative analysis, at least for the first 10 steps of the semi-batch reaction.

The 10th step corresponds to a (*S*)-BINAP:$Rh_4(CO)_{12}$ ratio of circa 0.5. In the 11th and 12th step higher ratios of (*S*)-BINAP:$Rh_4(CO)_{12}$ up to 2:3 were used. In these last two steps, some discrepancy occurs between the estimated and experimental design concentrations. This result appears to indicate that some non-negligible side reactions are occurring. The formation of small amounts of a di-substituted product $Rh_4(CO)_8(BINAP)_2$ and/or a dinuclear species of the stoichiometry $Rh_2(CO)_6$BINAP are the most likely candidates.

4.2.2. UV–vis CD experimental data set

4.2.2.1. Experimental data. The 12 UV–vis CD spectra from the above experiment in the range of 225–425 nm are shown in Fig. 10. These spectra show (1) a non-flat and non-zero baseline (at least in the region of <300 nm) due to the instrument function and (2) pronounced CD features at circa 235, 265 and 320 nm. In addition, these CD spectra have considerably lower S/N ratios compared to the unpolarized UV–vis measurements.

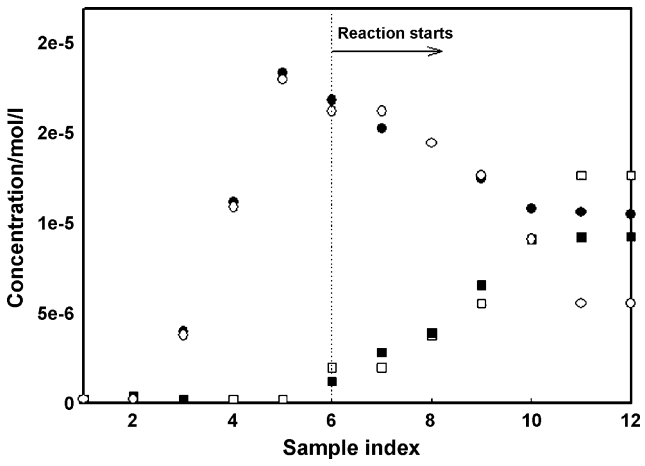

Fig. 9. Comparison of the concentration profiles from recovered UV–vis pure component spectra (solid symbols) and experiment design (open symbols). Profiles for: (●) $Rh_4(CO)_{12}$ and (■) $Rh_4(CO)_{10}$ BINAP.

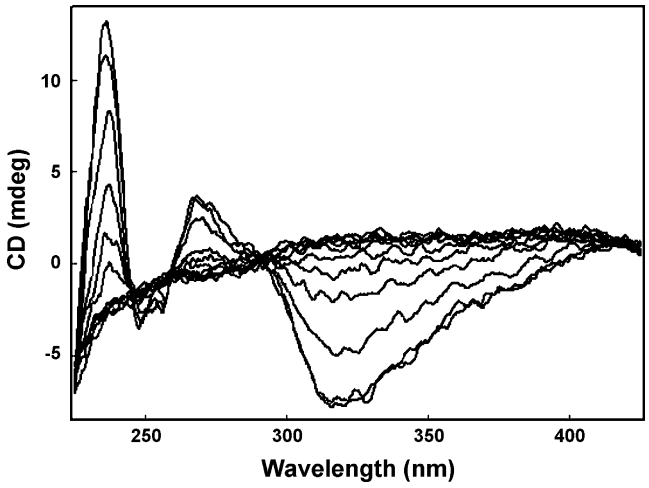

Fig. 10. UV–vis CD reaction spectra of the ligand substitution reaction of $Rh_4(CO)_{12}$ with (*S*)-BINAP (under argon) involving 9 perturbation steps.

4.2.2.2. Singular value decomposition. No base-line correction was performed with the 12 UV–vis CD spectra, however, they were smoothed with the Savitzky–Golay smoothing algorithm. Subsequently, the smoothed spectra were consolidated into a single matrix. Next, singular value decomposition was employed to decompose this CD data matrix to give the right singular vectors, the orthonormal matrix V^T. The first 6 right singular vectors and 12th vectors are shown in Fig. 11.

The first 2 right singular vectors in Fig. 11 show significant spectral features associated with the instrument function and the chiral metal complex. The 3rd to 6th right singular vectors still show some features, however, there is a considerable contribution from noise. The 12th right singular vector can be considered to be more-or-less white noise. Most of the prominent spectral features are embedded in the first six right

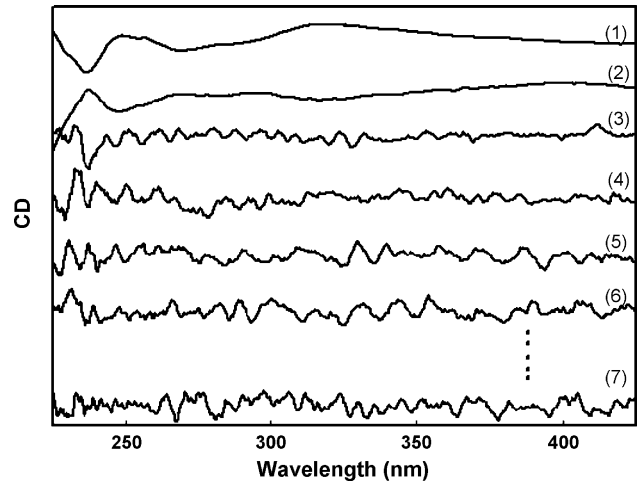

Fig. 11. Seven right singular vectors of the V^T matrix for UV–vis CD consolidated data set from the ligand substitution reaction of $Rh_4(CO)_{12}$ with (*S*)-BINAP (Experiment 2): (1)–(6) first six right singular vectors; (7) 12th right singular vector.

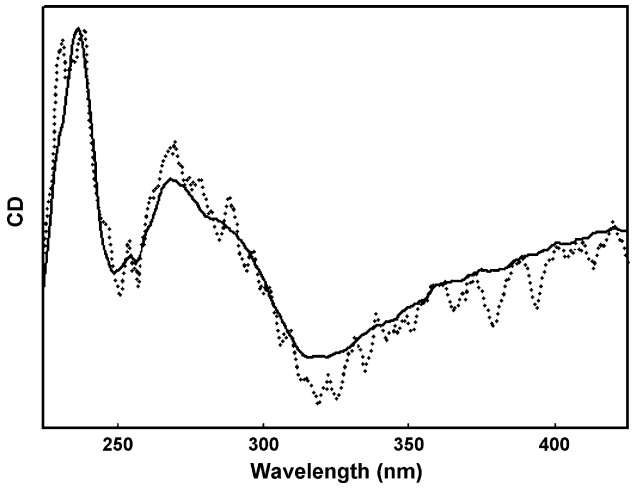

Fig. 12. Recovered pure component spectra obtained by BTEM: $Rh_4(CO)_{10}$ BINAP, solid line and UV–vis CD experiment reference spectra: $Rh_4(CO)_{10}$ BINAP, dotted line.

singular vectors and these will be used in the following BTEM analysis.

4.2.2.3. Spectral reconstruction using BTEM. The first 6 right singular vectors were used to reconstruct the pure component ECD spectrum of the chiral metal complex $Rh_4(CO)_{10}$BINAP. The noticeable spectral extrema in the first 6 right singular vectors were used as targets. Fig. 12 compares the estimated UV–vis CD spectrum with the experimental reference spectrum. This result indicates that the BTEM algorithm can be used to obtain accurate CD pure component spectra, i.e. spectra with both positive and negative parts.

4.2.2.4. Concentration profiles. The estimated relative concentration profiles of the reactants were computed by least squares fit of the estimated UV–vis CD spectra onto the original experimental UV–vis CD spectra. Further quantitative spectroscopic analysis was performed using the mass balances to constrain the numerical solution, assuming that only reaction (2) occurs. The quantitative analysis resulted in the concentration profile for the product $Rh_4(CO)_{10}$ BINAP. Fig. 13 compares the estimated concentration profile of the product $Rh_4(CO)_{10}$ BINAP obtained from (i) the UV–vis CD experimental data set with (ii) the UV–vis experimental data set and (iii) the experimental design 'real' concentration profile. The 3 concentration profiles of the product $Rh_4(CO)_{10}$ BINAP are in very good agreement. The only exception involves the last 2 steps, 11 and 12, which might be associated with the formation of small amounts of a disubstituted product $Rh_4(CO)_8(BINAP)_2$ and/or a dinuclear species of the stoichiometry $Rh_2(CO)_6$BINAP.

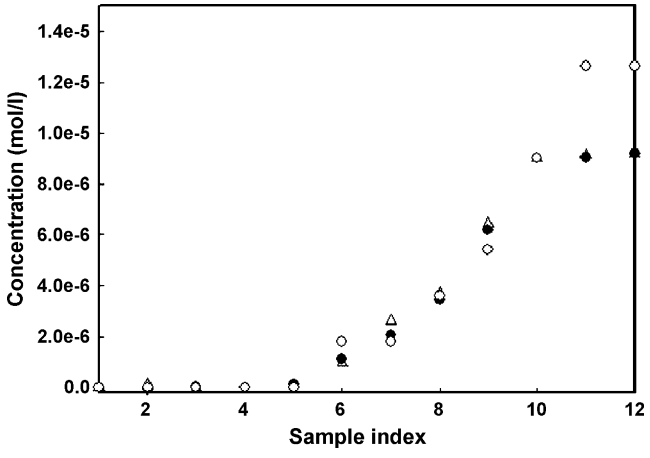

Fig. 13. Comparison of $Rh_4(CO)_{10}$ BINAP concentration profile determined from recovered UV–vis CD pure component spectra (●),UV–vis pure component spectra (△) and experiment design (◯).

5. Conclusions

The present results demonstrate that spectral reconstruction for organometallic reactive systems can be achieved by the application of UV–vis/UV–vis CD spectroscopy combined with a reliable and effective chemometric technique, namely, the BTEM algorithm. Moreover, the present results suggest that much more complex systems can be studied. Since the BTEM algorithm has been previously shown to be effective with systems containing 10 or more species (using FTIR, Raman, etc.), analysis of complex reactive systems using UV–vis/UV–vis CD spectroscopy appears possible in the near future.

Acknowledgment

The authors wish to thank the Institute of Chemical and Engineering Sciences for support of this research.

References

[1] R. Dickson, Homogeneous Catalysis with Compounds of Rhodium and Iridium, Springer, New York, 1985.
[2] J.E. Macintyre (Ed.), Dictionary of Organometallic Compounds, vol. 3, second ed., Chapman & Hall, London, 1995, pp. 3197–3397.
[3] R. Whyman, J. Chem. Soc. Dalton Trans. 13 (1972) 1375.
[4] J. Seyden-Penne, Chiral Auxiliaries and Ligands in Asymmetric Synthesis, Wiley-Interscience, New York, 2004.
[5] M. Stichelberger, D. Desbouis, V. Spiwok, L. Scapozza, P.A. Schubiger, R. Schibli, J. Organomet. Chem. 692 (2007) 1255.
[6] B.T. Heaton, L. Strona, J. Jonas, T. Eguchi, G.A. Hoffman, J. Chem. Soc. Dalton Trans. (1982) 1159.
[7] P.J. Dyson, J.S. Mclndoe, Transition Metal Carbonyl Cluster Chemistry, Gordon and Breach Science Publishers, Amsterdam, 2000.
[8] P.S. Braterman, Metal Carbonyl Spectra, Academic Press, 1975.
[9] W. Chew, E. Widjaja, M. Garland, Organometallics 21 (2002) 1982.
[10] C. Li, E. Widjaja, M. Garland, J. Am. Chem. Soc. 125 (2003) 5540.
[11] P.C. Ford, J.S. Bridgewater, B. Lee, Photochem. Photobiol. 65 (1997) 57.
[12] S.M. Massick, T. Buttner, P.C. Ford, Inorg. Chem. 42 (2003) 575.
[13] S. Eriksson, S.K. Kim, M. Kubista, B. Nordtn, Biochemistry 32 (1993) 2987.
[14] W.H. Lawton, E.A. Sylvester, Technometrics 13 (1971) 617.
[15] T. Konno, Protein Sci. 7 (1988) 975.
[16] P. McPhie, R.I. Shrager, Arch. Biochem. Biophys. (1992) 293.
[17] N. Sreerama, R.W. Woody, J. Mol. Biol. 242 (1994) 497.
[18] D.W. McMullen, S.R. Jaskunas, I.J. Tinoco, Biopolymers 5 (1967) 589.
[19] L. Antonov, G. Gergov, V. Petrov, M. Kubista, J. Nygren, Talanta 49 (1999) 99.

[20] G. Meinrath, S. Lis, Fresenius J. Anal. Chem. 369 (2001) 124.
[21] R.M. Wallance, J. Phys. Chem. 64 (1960) 899.
[22] W. Windig, J. Guilment, Anal. Chem. 63 (1991) 1425.
[23] W. Windig, Chemom. Intell. Lab. Syst. 36 (1997) 3.
[24] R. Tauler, I. Marques, E. Casassas, J. Chemom. 12 (1998) 55.
[25] C. Srilakshmi, E. Widjaja, M. Garland, B.G. Anderson, J. Raman Spectrosc. 38 (2007) 349.
[26] S.Y. Cheng, D. Rajaratham, M.L. Tan, M. Garland, Appl. Spectrosc. 60 (2006) 521.
[27] C. Li, L. Guo, M. Garland, Organometallics 23 (2004) 2201.
[28] C. Li, E. Widjaja, M. Garland, J. Catal. 213 (2003) 126.
[29] L.R. Ong, E. Widjaja, R. Stanforth, M. Garland, J. Raman Spectrosc. 34 (2003) 282.
[30] D.F. Shriver, M.A. Drezdzon, The Manipulation of Air-Sensitive Compounds, Wiley, New York, 1986.
[31] M. Tjahjono, A.D. Allian, M. Garland, Dalton Trans. 12 (2006) 1505.